A Thesis Submitted for the Degree of PhD at the University of Warwick

Permanent WRAP URL:

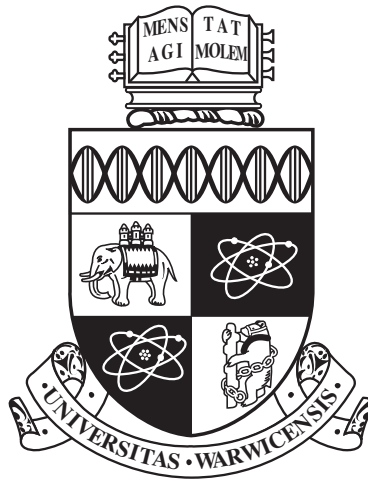**warwick.ac.uk/lib-publications**

System identification of lithium-ion battery dynamics: From characterisation to application

by

Chuanxin Fan

Thesis

Submitted to the University of Warwick

in partial fulfilment of the requirements

for admission to the degree of

Doctor of Philosophy

Warwick Manufacturing Group

February 2022

THE UNIVERSITY OF
WARWICK

Contents

List of Tables

List of Figures

Acknowledgments

I would like to give my heartfelt thanks to my primary supervisor, Dr. Dhammika Widanalage, whose encouragement, guidance and support enabled me to develop a deep understanding of my work. Without his consistent and illuminating instruction, my research work could not proceed to this stage. The research skill, writing skill and presenting skill he taught me will benefit me throughout my life. I would also like to thank my secondary supervisor, Dr. Matthew D Higgins, for his supervision and mentorship in my industrial project as well as the guidance and support he provided for writing journal and conference publications. I could not have wished for better supervisors.

I offer my regards and blessings to all of the members of Energy Storage Group at WMG, University of Warwick. I would like to express my special thanks to my friends, Dr. Liuying Li, Dr. Chen Wang, Dr. Kailong Liu for their support and friendship. My thanks also go to Mr. Kieran O'Regan and Prof. Emma Kendrick from School of Metallurgy and Materials, University of Birmingham, for collaborative work that made it possible for me to carry out this research.

Last but not least, I would like to express my deepest gratefulness to my mother Mrs. Xiuxia Wang and father Mr. Minghai Fan as well as my love Miss. Yanyu Xiao, for their encourage, support and love. I could not have done this without you!

Declarations

This thesis is submitted to the University of Warwick in support of my application for the degree of Doctor of Philosophy. It has been composed by myself and has not been submitted in any previous application for any degree. Parts of this thesis have been published by the author:

Chapter 4:

C. Fan, T. R. Grandjean, K. O'Regan, E. Kendrick, and W. D. Widanage, "Understanding non-linearity in electrochemical systems using multisine-based non-linear characterization," Transactions of the Institute of Measurement and Control, p. 01423312211045991, 2021

Chapter 5:

C. Fan, K. O'Regan, L. Li, E. Kendrick, and W. Widanage, "Frequency domain non-linear characterization and analysis of lithium-ion battery electrodes," Journal of Energy Storage, vol. 36, p. 102371, 2021

Chapter 6:

C. Fan, K. O'Regan, L. Li, M. D. Higgins, E. Kendrick, and W. D. Widanage, "Data-driven identification of lithium-ion batteries: A nonlinear equivalent circuit model with diffusion dynamics," Applied Energy, vol. 321, p. 119336, 2022

Chapter 7:

C. Fan, M. D. Higgins, and W. D. Widanage, "Real-time state of charge estimation of electrochemical model for lithium-ion battery," in 2019 IEEE Vehicle Power and Propulsion Conference (VPPC), pp. 1–6, IEEE, 2019

Abstract

To alleviate range anxiety among electric vehicle (EV) owners, the accuracy of lithium-ion battery (LIB) mathematical models in the low state of charge (SOC) range must be enhanced. A battery model that is easy to parameterise while maintaining accuracy over the entire SOC range is required in sophisticated battery management algorithms. This thesis addresses this knowledge gap via system identification methods of characterisation, identification, and application.

The level of non-linearity over different SOCs is first studied by using random phase odd-multisine signals, and applied on the Doyle-Fuller-Newman (DFN) model and a three-electrode experimental set-up of a commercial $5\,A\,h$ cylindrical 21700 LIB cell. The charge transfer coefficient is determined as the most sensitive parameter towards battery nonlinearity and with an asymmetrical Butler-Volmer kinetic the model nonlinear response provided good agreement against experimental data. The cathode even order nonlinearity is the main contributor towards the battery voltage nonlinearity while the anode starts to dominate at very low SOC.

Utilising the newly proposed characterisation method, a non-linear equivalent circuit model with diffusion dynamics (NLECM-diff), which phenomenologically describes the main electrochemical behaviours, such as ohmic, charge-transfer kinetics, and diffusion processes, is identified. Compared to the parameterisation challenge of electrochemical models, the NLECM-diff does not rely on geometrical parameter and all parameters are determined from the measured current and voltage signals. The NLECM-diff is around 50% more accurate than a conventional ECM and is comparable to the single particle model with electrolyte model (SPMe). When simulating driving cycles and long duration discharges, the dominant voltage loss changes from ohmic to the diffusion losses, and the characteristic of the negative electrode is determined as the primary reason for the low-SOC-error.

The last part of this thesis presents three case studies of model application as part of the project 'Virtually Connected Hybrid Vehicle (VCHV)'. The SPMe and the NLECM-diff models were demonstrated in Hardware-in-the-Loop (HIL) and therefore merit consideration for EV applications.

Abbreviations

BMS	Battery Management System
CC	Constant Current
CC-CV	Constant Current – Constant Voltage
CPE	Constant Phase Element
C-rate	Current Rate
DFN	Doyle-Fuller-Newman
DFT	Discrete Fourier Transform
ECM	Equivalent Circuit Model
EIS	Electrochemical Impedance Spectroscopy
EV	Electric Vehicle
FOM	Fractional Order Model
GITT	Galvanostatic Intermittent Titration Technique
HIL	Hardware-In-the-Loop
IC	Internal Combustion
ID-HIL	Internet Distributed Hardware-In-the-Loop
LCO	Lithium Cobalt Oxide
LIB	Lithium-ion Battery
LMO	Lithium Manganese Oxide
LPF	Lithium Iron Phosphate
MIF	Model Input factors
MIL	Model-in-the-Loop

NCA	Nickel Cobalt Aluminium Oxide
NFRA	Nonlinear Frequency Response Analysis
NMC	Nickel Manganese Cobalt oxide
NLECM	Nonlinear Equivalent Circuit Model
NLECM-diff	Nonlinear Equivalent Circuit Model with Diffusion Dynamics
NMC	Nickel Manganese Cobalt oxide
NEDC	New European Driving Cycle
OCV	Open Circuit Voltage
OEM	Original equipment manufacturer
P2D	Pseudo-two-Dimensional
RMS	Root-Mean-Square
RMSE	Root-Mean-Square Error
SA	Sensitivity Analysis
SEI	Solid Electrolyte Interface
SOC	State of Charge
SOH	State of Health
SOP	State of Power
SPMe	Single Particle Model with Electrolyte Dynamics
TCP	Transmission Control Protocol
UDP	User Datagram Protocol

Chapter 1

Introduction

1.1 Context

Transition from fossil fuel-based mobility to electrified is one of the greatest global challenges of the twenty-first century for society, business, and politics. Recently, the United Kingdom announced its grand challenge mission, named 'Future of mobility', with the goal of establishing the UK as a leader in the design and manufacture of zero emission vehicles and setting an ambitious target for all new cars and vans to be effectively zero emission by 2040. Additionally, as part of its enormous set of new climate and energy rules, the so-called "Fit-for-55" package, the European Commission published a proposal that would effectively outlaw the sale of petrol and diesel automobiles in the EU from 2035. Similarly, New Zealand joined the Electric Vehicles (EVs) Initiative in 2019, aiming to become a carbon-free economy by 2050 and China announces to reach peak emissions by 2030 and to achieve carbon neutrality by 2060 as a significant step in the fight against climate change.

The implementation of Electric Vehicles has been regarded as the foremost choice to replace the conventional internal combustion (IC) engine-based vehicles for eliminating all mobile emissions [5]. Currently, Lithium-ion Batteries (LIBs) are the most promising energy storage technology in electric vehicles to fulfil this goal, as its advantages such as high specific energy density (up to 250 Wh/kg), high power density (ranging from 0.5 kW/kg to 2 kW/kg), high energy efficiency (90-100%), and superior cycle performance [6, 7, 8]. However, the high demands on the LIB technology by a rapidly growing market, requires higher energy density for a longer driving range and improved battery performance for a lower electric vehicle manufacturing cost. Strategies to accomplish this goal can be the evolution of superior "next-generation" battery materials and the development of the battery

management technology. In Figure 1.1, the electrode stack level energy content of various cell chemistries, including state-of-the-art chemistries and future LIB and Li-metal technologies, is shown [9]. The roadmap of next-generation battery materials with high energy densities has been proposed conceptually. However, developing new battery materials is not an easy task and is unlikely to be accomplished in the near future. Also, transforming the novel battery material research outcomes into commercial products is also an extremely time-consuming process.
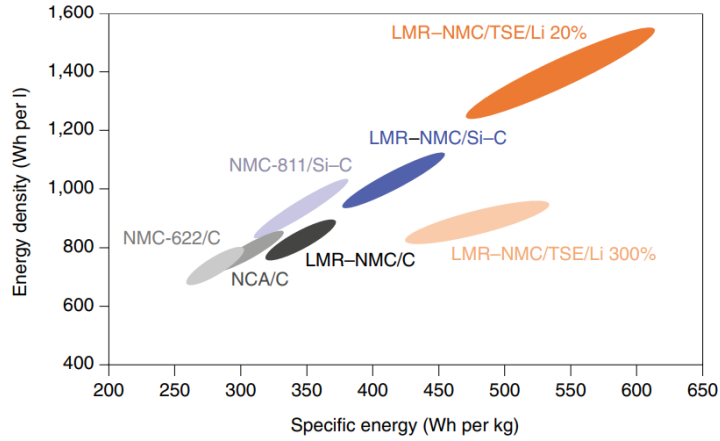
Figure 1.1: Energy density vs specific energy at electrode stack level for state-of-the-art and future battery chemistries in automotive applications. The state-of-the-art Lithium-ion battery chemistry is represented by NMC-622/graphite and NCA (lithium nickel cobalt aluminium oxide)/graphite [9].

On the other side, the development of the battery management technology has attracted considerable attention from automotive original equipment manufacturers (OEMs) in recent years. Driven by the high demands from renewable energy storage system applications, the battery management system (BMS) market is growing. The report from Market Research Future (MRFR) expects the global battery management system market to reach USD 14042.04 million at a compound annual growth rate (CAGR) of 18.59% from 2020 to 2027 (forecast period) [10]. Independent of the battery chemistry used, an effective battery management system is compulsory for electric vehicle applications to ensure that the batteries can operate safely and reliably, avoid physical damage, and handle temperature variations, minimal capacity loss, and cell unbalancing [11]. Not only does the BMS regulate the operating conditions of the battery to ensure its safety, but it also provides accurate estimation of the state of charge (SOC) and state of health (SOH) for energy management modules in electric vehicles [12]. Additionally, the BMS is critical for controlling and updating data, detecting faults, all of which are critical for achiev-

ing optimal battery utilisation [13]. By applying the advanced battery management technology, the energy can be sufficiently and smartly extracted from the batteries for a longer driving range, and the battery service life can be significantly prolonged for reducing the maintenance expenses. Thereby the battery performance can be substantially enhanced, and create a favourable environment for OEMs to deliver viable energy storage solutions at a reasonable price.

Typically, establishing a robust battery mathematical model serves as the starting point for developing advanced battery management technologies [5]. Based on the model accuracy, model-based functional applications and algorithms, such as SOC and SOH estimations, can be applied to ensure the safe and optimal battery operation in real-time [14]. In addition, a comprehensive battery model can also be utilised in predicting new battery material performance in terms of current-voltage characteristics and ageing degradation, which benefits the evolution of the next generation battery technology. Thus, a battery model that accurately represents the battery characteristics is fundamental and crucial for the development of advanced electric vehicle applications and new battery technologies.

1.2 Motivation for the Direction of Research

The research presented in this thesis is aligned with the externally funded engineering project 'Virtually Connected Hybrid Vehicle (VCHV)'. The aim of the VCHV project is to reduce time-consuming physical testing of hybrid vehicle prototype components, the development of a test rig and the physical testing of the complete system. A hybrid/electric vehicle prototype incorporates numerous subsystems, each of which must complement the others in order to function properly as a single unit. For instance, the battery configuration should be perfectly matched to the converter unit, and the motor output should be mechanically linked to the engine, in order for the entire system to perform reliably over its lifetime. In an ideal world, all subsystems would be co-located for prototype testing throughout the system's development, but this is prohibitively expensive and time-consuming, especially in the automotive industry, where they are typically developed under separate roofs and frequently by different companies/suppliers bound by confidentiality clauses. To demonstrate the feasibility of a real-time virtual powertrain testing for automotive OEMs, the VCHV project was proposed to establish a real-time internet distributed Hardware-In-the-Loop (HIL) simulation platform spread across different geographical locations. As shown in Figure 1.2, there were six UK universities working collaboratively with the common objective to develop different hybrid pow-

ertrain sub-systems distributed throughout the United Kingdom and virtually tested together in the HIL simulation, with the possibility of replacing the subsystems with virtual mathematical models.
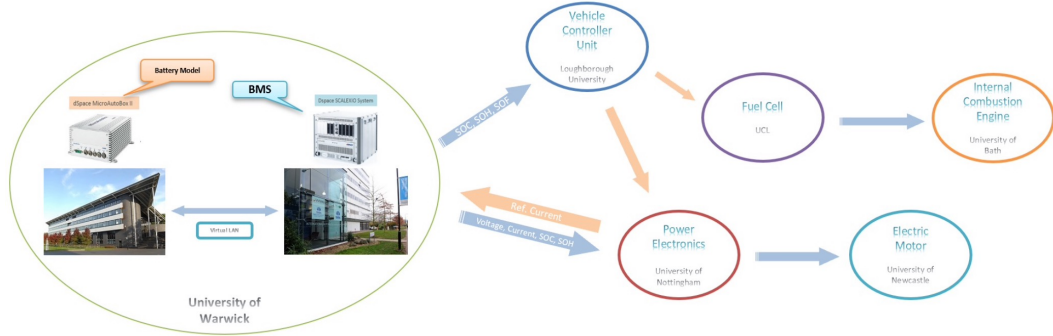
Figure 1.2: Proposal of the VCHV project.

HIL simulation is a real-time technique for developing and testing embedded control systems that are used to operate complex equipment and systems [15]. In 1936, the first attempt of HIL application is reported for (real-time) flight simulation, where the early goals were to simulate the instruments with a fixed-cockpit "linktrainer" [16]. Furthermore, HIL motion simulators were built for the dynamic testing of vehicle components since 1985 [17]. In recent years, HIL simulations for real-time onboard battery-related testing have begun to be conducted in order to develop sophisticated battery technology [18, 19, 20, 21]. In contrast to simulation software such as Simulink, the HIL simulation can execute representations (mathematical models) of the Unit-Under-Test (UUT) and process data signals in exact real time, making it perfect for integrating with actual devices or systems. Design and testing without the need to operate a real process is the key advantage of the HIL simulation, which results in a significant reduction of the cost and development time [22]. To replace the physical component of a machine or system, however, an accurate mathematical representation (model) is compulsory in the real-time HIL simulations.

As stated in the VCHV proposal, the responsibility of the author, on behalf of WMG, University of Warwick, was to develop a battery model that serves as a power supply for the virtual powertrain in the internet distributed HIL simulation platform. As illustrated in Figure 1.2, the HIL rigs from dSPACE company were employed to implement the models of a lithium-ion battery and a BMS for HIL simulations and transit the obtained data signals with VCHV partners. Because the complexity of a battery model can impact computation time, particularly for

electrical real-time HIL systems, the model fidelity has to be taken into account during the modelling process in order to decrease the computational cost [23]. Additionally, a compromise between the number parameters to identify and the model accuracy required for a specific application is not trivial [21]. In relation to model parameter estimation the infrastructure facilities of small- and medium-sized automotive OEMs may be unable to conduct sophisticated characterisation tests and physical-chemical experimental tests to extract parameters of complex lithium-ion battery models [24]. Therefore the characterisation methods supporting parameterisation of the desired battery model has to be easy-to-implement, which is also a critical objective and point of examination throughout this thesis. As mentioned above, the direction of research is determined to develop an application-oriented, easily identifiable, low computational cost lithium-ion battery mathematical model with the accomplishment of high accuracy in the real-time Hardware-in-the-Loop simulation platform.

1.3   Research Objectives

In practical electric vehicle (EV) applications, the lithium-ion battery operation is optionally restricted within a safety state-of-charge (SOC)* window by the automotive OEMs rather than taking advantage of the full range between 0% and 100% [26, 27]. From the point of view of the usage of a single lithium-ion cell, there are two main compelling reasons, in the literature, for this setup; on the one hand, some studies state that lithium-ion batteries that operate within a partial range of SOC, present excellent cycling performance with essentially reduced battery degradation. Jiang et al. investigated the effect of SOC operation ranges on LIB capacity degradation, and concluded that, when the battery is cycled in a SOC range below 25% and above 75%, the fastest capacity fade occurs [28]. Compared with full range cycles, batteries degrade slower when the SOC is limited to 30%–90% [29]. Similarly, Kostopoulos et al. suggested that EV manufacturers should limit the battery discharging-charging procedure between 20% and 80% for battery health reasons [30]. Regarding the limitations caused from the perspective of LIB ageing degradation, it can be expected to be improved by developing new battery materials and advanced optimal charging strategies in the future. On the other hand, the restricted

---

*From electrochemical perspective, the SOC of a battery is related to the Li^+ concentration amount in the particle throughout the positive electrode and negative electrode, and it is a relative quantity that describes the ratio of the remaining Li^+ concentration amount to the present maximum available Li^+ concentration amount of a battery [25]. The value of the SOC varies between 0% and 100%. If the SOC is 100%, then the cell is said to be fully charged, whereas a SOC of 0% indicates that the cell is completely discharged.

operation range is a consequence of the unreliability of the battery model voltage prediction in battery management systems within the specific SOC range, which could lead to unexpected energy exhaustion and bring considerable range anxiety to the passengers [31]. Zheng et al. state that LiBs in the low SOC range show very strong nonlinear performance that cannot be well simulated by widely used equivalent circuit battery models (ECMs), which leads significant SOC estimation error in the low SOC range [32]. Also, refer to [33, 34], the authors propose that the widely used ECMs are generally inadequate at predicting battery terminal voltage at low SOC, which considerably increases the risk associated with the urgent usage of a battery at low voltage. If an advanced battery model can provide excellent accuracy across the entire SOC range of 0 to 100%, the restriction on SOC operation range can be removed, allowing for more battery energy to be extracted for achieving a longer driving range without increasing the cost of the battery, which benefits the high demands of the growing EV market.

For fulfilling the requirements of BMS applications, two classes of existing lithium-ion battery mathematical models reviewed in Chapter 2 are developed from two distinct modelling perspectives, respectively. Note that only single battery cell models are taken into consideration in this thesis, thus the effects of cell-cell variation and temperature inhomogeneity, which is generally investigated by a module-level or pack-level model [35], cannot be represented. The class of physical model[†] has attracted the attention of the scientific community in recent years, including Doyle-Fuller-Newman (DFN) model [36] and the family of Single Particle Model (SPM) [37, 38]. This model class is renowned for its high accuracy across the entire SOC window and for its inherent physical relevance. However, the limitations, such as considerable identification and parameterisation costs and low calculation efficiency, make it unsuitable for the thesis requirements as well as HIL applications for small- and medium-sized automotive OEMs. More details will be introduced in Chapter 2. Alternatively, the class of equivalent circuit model (ECM) is commonly applied in the real-time onboard BMS applications due to the advantages of efficient computational cost [5]. However, a major issue contributing to error of SOC estimation in a BMS is reported that the poor accuracy of the conventional ECM[‡] voltage estimation in the low SOC range (e.g. at SOC less than 20%) [32]. According to the literature, it's commonly reported that a conventional ECM is able to pro-

---

[†]A physical model, also known as electrochemical model, is one that is based on principle of physics and requires a domain to be defines where the dynamics occur together with the associated material and physical properties of that domain.

[‡]A conventional ECM refers to a linear ECM that makes use of electrical components (resistors, capacitors, and DC voltage supply) to equivalently emulate the current-voltage relationship of a lithium-ion battery.

vide sufficiently accurate voltage prediction and SOC estimation in high and middle SOC ranges during discharging, but the model accuracy in the low SOC range is rarely mentioned [39]. The available SOC range was commonly determined higher than 10% in the validation experiments, e.g. 40%~70% in [40], 25%~100% in [41], 20%~100% in [42], and 10%~100% in [34]. Furthermore, some researches indicate that the fidelity of conventional ECMs typically declines at SOC lower than 20% and decreases significantly under 10% SOC during discharging [43, 44]. Refer to [39], under a set of constant-current discharge pause profiles, minor voltage error of conventional linear ECM is observed at SOC larger than 20% and no error summation is noticed. However, the lower-than-20% SOC leads to a considerable voltage error increase, which indicates that the model inaccuracy effect at low SOC is purely a SOC issue. Xiong et al. argued that the ECM inaccuracy is caused by the nonlinearity of the OCV curve, and as the OCV curve has strong nonlinearity at low SOC below 10%, the accuracy of the ECM substantially declines at low SOC during discharging but barely reduces at high SOC during charging [33]. To clarify the low-SOC-error issue, Figure 1.3 presents the voltage predictions of the 2nd order linear ECM [45] and the physical model Single Particle Model with Electrolyte Dynamics (SPMe) [38, 46] for a LG M50 21700 NMC battery cell. Additionally, accuracy and computational time comparison of two models are listed in Table 1.1. When compared to experimental data, the linear ECM shows a relatively poor accuracy with 0.172 V RMSE across the entire SOC range and specifically 0.493 V RMSE in the low SOC range (from 20% to 0% SOC) which indicates the significant low-SOC-error of the linear ECM. In contrast, SPMe achieves a high degree of accuracy with 0.048 V RMSE across the entire SOC range, and the RMSE from 20% to 0% SOC for the SPMe is 0.036 V. However, given that the massive parametersation tests and long computational time[§] of the SPMe shown in Table 1.1, this is not a suitable candidate for practical EV applications [39] and the ECM is chosen as the basis of model modification to improve the low-SOC-area performance. Thus, the accuracy of the ECM class is required to be improved to that of the physical class model, where the objective accuracy requirements are defined as 0.050 V 100%-0% RMSE and 0.060 V 20%-0% RMSE under 0.5C CC discharge profile.

The accuracy of battery models is directly related to the reliability of practical BMS applications including real-time HIL simulation mentioned in Section 1.2. However, the main reason, the existing conventional linear ECMs do not provide comparable accuracy to physical models during discharging, particularly in the low

---

[§]Note that the computational time of two models using the same PC hardware with the CPU of Intel Core i7 and 16.0GB RAM for simulation.
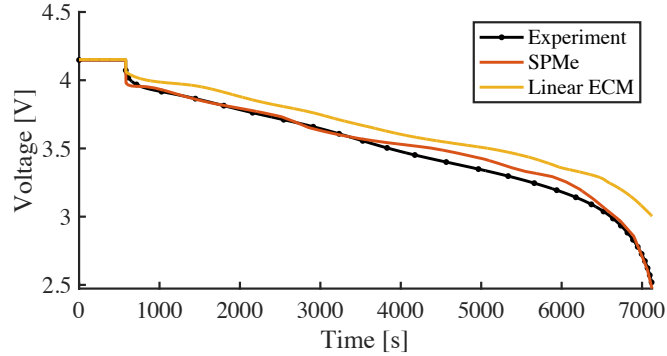
Figure 1.3: Voltage predictions of conventional linear 2nd order ECM and physical model discharged from 100% SOC to 0% SOC at 0.5C constant current load.

Table 1.1
Features of two class battery models at 0.5C constant current load.

Model	100%-0% RMSE [V]	20%-0% RMSE [V]	Parameterisation tests	Computational Time [s]
Linear ECM	0.172	0.493	2	2.30
SPMe	0.048	0.036	7	301.33

SOC range, is still an open question. On the one hand, Firouz et al. conducted experiments and analysed the input and output of the battery system from the perspective of control theory, and they stated that the ECM, as a linear approximate model, ignores the nonlinear characteristics of the battery system, which is a main reason to cause model error, especially in the low SOC range [47]. On the other hand, as reviewed in Chapter 2, some researchers developed complex physical-based electrochemical models and fractional-order models with electrochemical processes to achieve high model accuracy [48, 49]. Thus, the author asserts that the absence of interpretations of battery nonlinearity and battery dynamics are origins of the inaccuracy of linear ECMs. To improve the ECM accuracy across the entire SOC range, a unique battery mathematical model that takes these two features into consideration while also meeting the motivations outlined in Section 1.2 is necessary to be developed for academic and industrial applications. Nonlinearity of lithium-ion batteries, as a critical component of the battery model, must be captured by applying specific nonlinear characterisation methods and the results further understood. Consequently, four research objectives are defined, which determine the research work undertaken within this thesis;

(1) Design a characterisation method capable of capturing battery non-linearity.

(2) Understand the electrochemical processes contributing to nonlinearity.

(3) Develop a battery mathematical model which requires minimal identification cost while achieving a high level of accuracy over the entire SOC range.

(4) Evaluate the applicability of the proposed battery model to Hardware-in-the-Loop simulations.

1.4 Scope of the Thesis

The goal of this thesis is to develop an application-oriented, easily identifiable, low computational cost battery model capable of achieving high accuracy over the entire state-of-charge range for internet distributed Hardware-in-the-Loop applications. For this purpose, this thesis reviews existing widely-employed battery models including the class of physical models and the class of equivalent circuit models to understand the context within which such models are developed and their intended applications, as well as the nature of experiments required to characterise and parameterise models from either class. The benefits and shortcomings of both model classes are identified, and the improvements from the standpoint of system identification are proposed to address the shortcomings in terms of the difficulty in parameter determination of the physical model class and the low-SOC-error of the ECM model class.
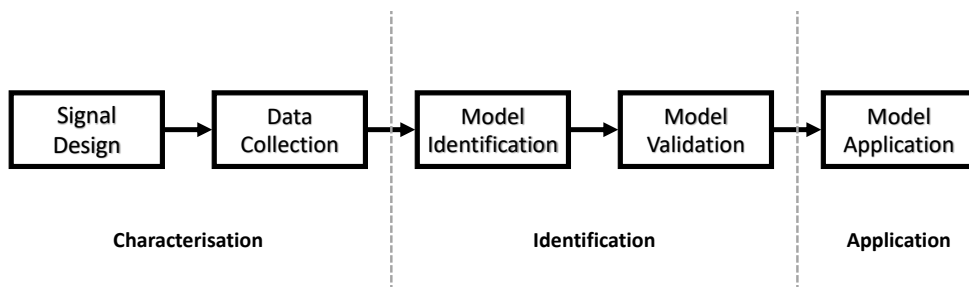
Figure 1.4: The typical system identification procedure.

This thesis is founded on the system identification approach, which is described as three battery-related features, namely characterisation, identification, and application, as depicted in Figure 1.4. To begin, dedicated excitation signals and experiments that actively excite battery cells are designed to collect essential information for building a model, which is proposed as a battery characterisation

method. In the identification part, a model structure is required to be determined to represent the system, and it should be matched with the characterised data about the system by mostly minimising a cost function that measures a goodness of the fit. The developed battery model is validated by simulations to test whether it accurately describes the available data. Last but not least, the finished model is implemented in practice to determine its suitability to the intended HIL application.

In this thesis, the research is dedicated to the discharge phase of the battery cell level at a room temperature (25°C); the charge phase as well as the module and pack levels are not considered. Given that lithium-ion batteries work at typical temperatures ranging from 10°C to 40°C and an efficient battery thermal management system can maintain the proper temperature range, temperature dependency is not taken into account. Furthermore, temperature dependency, control algorithms that operate on the HIL platform, state estimation algorithms, inclusion of battery ageing are beyond the scope of this thesis, however, such topics may benefit from the proposed characterisation method and battery model. The results of this thesis may be of high interest for the improvement of current LIB technology and battery management system design with the goal of supplying automotive original equipment manufacturers.

1.5 Thesis Structure

This thesis is structured as follows. Chapter 2 presents a critical review of existing battery mathematical models, including lithium-ion battery fundamentals and dynamic processes, applied in academia and industry. The applicability of these models for the HIL application case described in Section 1.2 is examined, thus the development of a precise equivalent circuit battery model accounting for battery nonlinearity and a large time constant dynamic is noted as a knowledge gap in the existing literature.

To identify the desired battery model, relevant characterisation tests necessary to obtain the characteristics of the battery voltage dynamic response are reviewed. Especially, to fulfil Research Objective (1), an overview of research fields in which nonlinear characterisation tests is presented in Chapter 3. Chapter 4 presents a model-based study to understand why and how electrochemical processes excite and affect battery nonlinearity by applying a frequency domain multisine characterisation technique on the pseudo-two-dimensional (P2D) model. Chapter 5 describes an experimental investigation into the nonlinear frequency responses of a full battery cell as well as individual electrodes using a three-electrode experimental set-up

of a commercial 5 A h cylindrical 21700 cell.

Chapter 6 proposes a semi-physical nonlinear equivalent circuit model taking battery nonlinearity and diffusion dynamics into consideration on the basis of the nonlinearity characterised in Chapter 5, which is validated under various EV load current profiles and compared with an electrochemical model the Single Particle Model with electrolyte dynamics (SPMe). Chapter 7 examines the applicability of the SPMe model and the NLECM-diff proposed in Chapter 6 for the internet distributed Hardware-In-the-Loop applications. Chapter 8 provides discussions and conclusions of this thesis and suggestions for future work.

Chapter 2

A Review of Lithium-ion Battery Mathematical Models

2.1 Introduction

Mathematical models of lithium-ion batteries are employed to emulate LIB voltage response for fulfilling various management demands. An accurate battery model is essential for an on-board battery management system (BMS) for assessing various battery state variables, such as state-of-charge (SOC), state-of-power (SOP), and state-of-health (SOH), which indicates the energy content, power delivery capability, and batteries 'health' condition, respectively [50, 51, 52]. Numerous efficient optimisation and control strategies to prolong battery service life are developed on the basis of comprehensive battery models [53, 54, 55, 56]. To meet these expectations for a variety of applications, researchers have developed extensive battery mathematical models to accurately predict the macroscopic physical quantities (such as voltage, temperature and current) of lithium-ion batteries.

As such, Section 2.2 introduces the fundamental knowledge of LIBs, including their basic components and operational principles, together with the commonly used commercial LIB chemistry. Section 2.3 describes the typical electrochemical processes that occur inside a LIB which are related to specific voltage losses contributing to the measured battery terminal voltage, and from the modelling point of view, the dynamic response of the electrochemical processes are classified as linear or nonlinear with regard to their mathematical representations. Section 2.4 reviews the mainstream of existing battery mathematical models employed for the practical applications, which are developed on the basis of either the mathematical representations of fundamental electrochemical processes or the phenomenological description

of the dynamic behaviour of a lithium-ion battery. Meanwhile, the advantages and limitations of these battery models are summarised in terms of model identification and computational cost, which determines the applicability of the specific battery model in the case of HIL applications. Following this review, the knowledge gap is identified for the research question in Section 2.5.

2.2 Fundamentals of Lithium-Ion Batteries

A LIB consists of a cathode (positive electrode) and an anode (negative electrode), separator, electrolyte and current collectors. Two spatially separated electrodes comprise of the electrochemically active material and inactive components such as conducting additives and binder, and are isolated by a separator, typically a micro-porous polymer membrane, that allows the transport of lithium ions but not electrons. The electrolyte of LIBs is commonly a liquid solvent mixture, e.g., carbonate-based solvents [57]. In addition to liquid electrolyte, polymer, gel, and ceramic electrolyte have also been explored for LIB applications [58]. The metal current collectors are attached to electrodes and serve as the external terminals of a LIB. Generally, copper is utilised as the material of anode current collector, and for cathodes the collector is usually an aluminium alloy. Figure 2.1 illustrates the basic working principle of the discharge and charge processes of a typical lithium-ion battery.

The basic principle of LIBs is an oxidation-reduction (Redox) reaction. The chemical equations of the charging and discharging processes are shown in the following equations for the anode and the cathode, respectively.

$$\text{Li}_x\text{C}_6 \rightleftharpoons x\text{Li}^+ + x\text{e}^- + \text{C}_6 \tag{2.1}$$

$$\text{Li}_{1-x}\text{MO}_2 + x\text{Li}^+ + x\text{e}^- \rightleftharpoons \text{LiMO}_2 \tag{2.2}$$
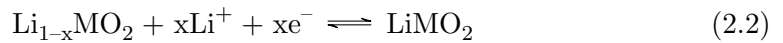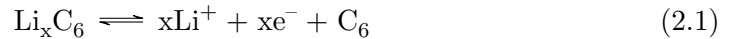
where M represents a transition metal (e.g., Co, Ni, Mn) [59]. During the charging process, the oxidation occurs at the cathode, thus the electrons are released and the lithium ions deintercalate from the cathode. The electrons pass through the external circuit, resulting in the generation of an electrical current in the opposite direction of the electron flow, as well as the lithium ions are transported to the anode by diffusion and migration through the electrolyte inside of the LIB. At the anode the lithium is reduced, in which lithium ions accept electrons and intercalate in the host structure of the anode. For the discharge process these processes occur
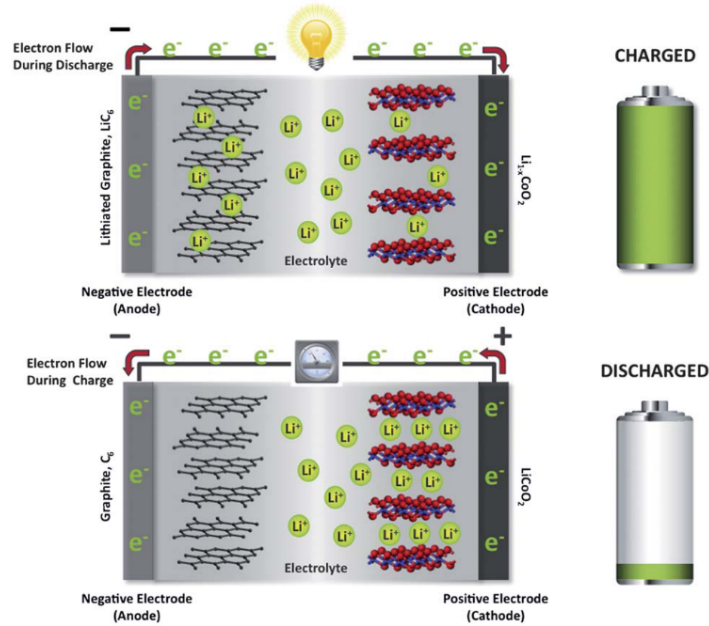
Figure 2.1: Working principle of the discharge and charge process of LIBs [59]

in the other direction.

LIB capacity is dependent on the cathode. After years of continuous development, numerous cathode electrode materials have been investigated and commercialised. Lithium Cobalt Oxide (LCO) and Lithium Manganese Oxide (LMO) were the first commercially available cathode materials in LIBs [60]. The LCO material has a layered structure that allows lithium ions to intercalate between planes. In commercial cells, this material has a voltage of $4.2\,\text{V}$ relative to lithium metal, which corresponds to the cycling of 0.5 Li^+ per $LiCoO_2$ and a capacity of 140-150 Ah/kg. Modern commercial batteries still use cobalt, but the material has significant disadvantages compared to newer alternative electrode materials, including being environmentally hazardous and highly expensive. In addition, its instability at high temperatures and susceptibility to thermal runaway during overcharging [61] make LCO less desirable for automotive applications. The LMO is different from the LCO, which has a spinel atomic structure. The material is relatively inexpensive compared to LCO, and its thermal safety characteristics are superior to those of LCO, with a greater thermal runaway temperature [62]. However, the material has a lower charge capacity, which makes it less desirable for some automotive applications. Recently, cathodes composed of a transition metal oxide mix, specifically lithium Nickel Manganese Cobalt oxide (NMC) in various ratios (1:1:1, 6:2:2, 8:1:1), have acquired popularity due to their increased cycle life and high energy density.

Literature indicates that the possible specific charge capacity of NMC ranges from 140 to 230 Ah/kg, providing it a significant energy capacity advantage over LCO. Due to its reduced cobalt content, it is significantly cheaper, less hazardous, and safer to operate and store than LCO [63]. In addition, since the practical energy density is enhanced by increasing the nickel proportion, the development of high nickel NMC cathode batteries is becoming mainstream [64]. In addition, the lithium Nickel Cobalt Aluminium oxide (NCA) is also a state-of-the-art cathode material for some applications, as NCA has a comparably high practical specific capacity. However, compared with the other cathode materials, the drawback of NCA is the severe capacity fade at elevated temperature (40-70°C) due to solid electrolyte interface (SEI) growth on the cathode and micro-crack growth at grain boundaries [65]. A detailed overview of cathode material properties is given in [60].

On the other side, the state-of-the-art anode material in LIBs are carbon-based. Graphite was commercialised as an anode material twenty years ago and is now the most widely used material due to its significant advantages, including low cost, high electrochemical and mechanical stability, and availability [66]. The lithium titanium oxide (LTO) is the other commercial anode material for high power applications and usually in combination with lithium iron phosphate (LFP) as high power cathode material. Additionally, silicon (Si) active material with impressively high theoretical capacity is used for next-generation anodes in lithium ion batteries (LIBs). However, due to the inevitable volume expansion and unstable SEI coating, pure Si is still confronted with challenges in commercialisation. To address these challenges, silicon-alloys and silicon oxide have been explored and suggested to be the future direction [67].

2.3 Dynamic processes of Lithium-Ion Batteries

Independent of the electrode materials used, each electrochemical and physical process in lithium-ion batteries leads to a specific voltage loss depending on the excitation current [48]. From the perspective of modelling, the related response can be classified as nonlinear and linear dynamics, respectively. Typical electrochemical and physical processes in LIBs consist of charge transfer reactions, diffusion processes, thermodynamics, and electrical potential, which are discussed below.

2.3.1 Charge transfer reactions

Charge transfer reactions at the electrodes, notably oxidation and reduction, are nonlinear Faradaic processes characterised by a nonlinear relationship between cur-

rent density and over-potential, which is described using the Butler-Volmer kinetics, as shown in Equation (2.3).

$$j = \frac{i_{0,\mathrm{k}}}{F} \left(\exp(\frac{\alpha_{\mathrm{a}} F}{RT} \eta) - \exp(-\frac{\alpha_{\mathrm{c}} F}{RT} \eta) \right), \quad \mathrm{k} \in \{\mathrm{n, p}\} \tag{2.3}$$

where j is the volume rate of lithium-ion generation, $i_{0,\mathrm{k}}$ is the exchange current density, k denotes the electrodes (n for anode and p for cathode), η is the over-potential, α_{a} and α_{c} are the anodic and cathodic transfer coefficients, and F, R, and T are Faraday's constant, the gas constant, and the temperature, respectively.

Equation (2.3) illustrates how the electrical current through an electrode is dependent on the voltage difference between the electrode and the bulk electrolyte for a simple, unimolecular redox reaction when both a cathodic and anodic reaction occur on the same electrode. It assumes that the concentrations at the electrode are practically equal to the concentrations in the bulk electrolyte, allowing the current to be expressed as a function of potential only. The exponential relation between j and η in Equation (2.3) is expected to result in nonlinearity contributing to the battery terminal voltage.

2.3.2 Diffusion processes

Diffusion processes occur in the solid phase and electrolyte phase of a LIB, which are caused by the difference of lithium ion concentration. In the electrode particles, solid phase diffusion process is represented by Fick's second law in spherical coordinates:

$$\frac{\partial c_{\mathrm{s,k}}}{\partial t} = \frac{D_{\mathrm{s,k}}}{r^2} \frac{\partial}{\partial r} \left(r^2 \frac{\partial c_{\mathrm{s,k}}}{\partial r} \right), \quad \mathrm{k} \in \{\mathrm{n, p}\} \tag{2.4}$$

here $c_{\mathrm{s,k}}$ is the lithium ion concentration in particles, the diffusion coefficient of lithium is $D_{\mathrm{s,k}}$, time t and the spatial coordinate r. The distribution of lithium ion concentration in spherical particles is nonlinear due to the relation to current-voltage nonlinearity via Butler-Volmer kinetic in the boundary conditions:

$$\left. \frac{\partial c_{\mathrm{s,k}}}{\partial r} \right|_{r=0} = 0, \quad \left. -D_{\mathrm{s,k}} \frac{\partial c_{\mathrm{s,k}}}{\partial r} \right|_{r=R_{\mathrm{s}}} = j_{\mathrm{k}} \tag{2.5}$$

where j_{k} is the flux of lithium ions away from the surface of the spherical particles. At the centre of the particle ($r = 0$), there is no flux, and on the surface of the particle ($r = R_{\mathrm{s}}$), the flux is equal to the consuming/producing rate of Lithium ions due to the electrochemical reaction occurring at the solid/liquid interface.

Equation (2.4) assumes that the porous electrode is made of equally sized, isotropic, homogeneous spherical particles [68]. This homogeneous description of

electrode microstructure results in smooth, uniform intercalation/de-intercalation of lithium inside the electrode and has proven to be successful in characterising discharge/charge behaviours particularly at low to moderate rates [69]. In reality, however, Li-ion electrodes are very heterogeneous structures [70]. In addition, the spherical assumption leads to the microstructure of electrode posed posed in a one-dimensional domain with spherical symmetry. This renders the model simple enough to be computationally affordable, while retaining enough of the physics to be able to accurately predict the batteries' behaviour and capture its internal states [71].

In the electrolyte, ionic transport is a result of a combination of two physical processes. The first occurs as a consequence of migration produced by a local electric field, while the second occurs as a result of ion diffusion caused by concentration gradients [72]. The species conservation in electrolyte phase can be expressed given in Equation (2.6), which assumes the electrolyte consist of a binary salt in a single solvent; however, mixtures of several non-aqueous liquids or high and low molecular weight polymers can be treated as a single solvent without significant loss of rigour [68].

$$\varepsilon_{\mathrm{e,k}} \frac{\partial c_{\mathrm{e,k}}}{\partial t} = \frac{\partial}{\partial x}\left(D_{\mathrm{e}}\varepsilon_{\mathrm{e,k}}^{b}\frac{\partial c_{\mathrm{e,k}}}{\partial x}\right) + \frac{3\varepsilon_{\mathrm{s,k}}\left(1 - t^{+}\right)}{R_{\mathrm{k}}}j_{\mathrm{k}} \qquad (2.6)$$

where involving the lithium ion concentration $c_{\mathrm{e,k}}$, the time t, the electrolyte volume fraction $\varepsilon_{\mathrm{e,k}}$, the active particles volume fraction $\varepsilon_{\mathrm{s,k}}$, the Li^{+} transference number t^{+}, the Bruggeman porosity exponent b, the lithium ion diffusion coefficient in electrolyte D_{e}, the radius of active material particles R_{k} and the net molar flux of lithium ions exiting the particle kinetic j_{k}.

As the simulation results demonstrated in [73], the impact of the ionic transport process in the electrolyte towards LIB nonlinearity is expected to be only minor. Thus, when considering the contribution of diffusion processes to LIB nonlinearity, solid diffusion processes in spherical particles can be regarded as the primary process [74].

2.3.3 Thermodynamic

Thermodynamics is the branch of physics that addresses the fundamentals of the physical and chemical behaviour of equilibrium matter [75]. In lithium-ion battery study, thermodynamics are generally illustrated using open circuit voltages (OCV) of the electrodes as a function of their stoichiometry. When it comes to battery modelling, a frequently utilised alternative is to employ a measured OCV vs. SOC curves. The OCV U_{OCV} is defined as the difference between cathode potential U_{p} and anode potential U_{n} when the two electrodes are at equilibrium, e.g., in

the absence of a current. The diagram of three potential is shown as Figure 2.2. Note that "RE" denotes a reference electrode which is embedded inside the battery to directly measure the negative and positive electrode potentials and enables a quantitative evaluation of various electrochemical aspects of the battery's internal electrochemical reactions [76]. The relationship among cathode potential, anode potential, and full cell OCV is described in Equation (2.7).

$$U_{\text{OCV}} = U_{\text{p}} - U_{\text{n}} \tag{2.7}$$
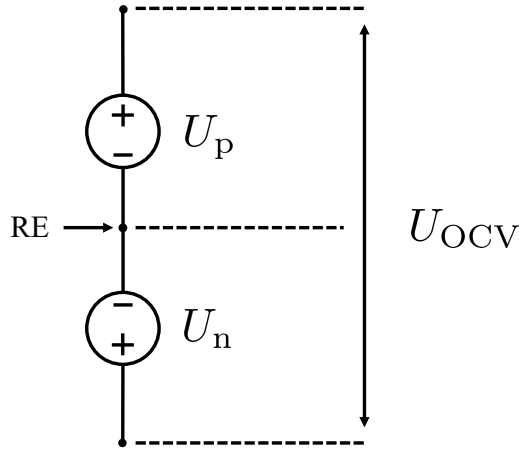
Figure 2.2: The diagram of battery three potentials.

The equilibrium electrode potential U_{k} can be measured using a reference electrode or half cell configuration in a potentiostat [24]. As such, the electrode potential incorporates thermodynamic information about the electrode, such as the number and type of phase transitions that the electrode materials undergo during charge and discharge (the majority of battery electrodes undergo multiple phase transformations), as well as the amount of lithium intercalated in each phase [77]. Mathematically, the potential of an electrode material during a phase transformation can be described using the chemical potential, which quantifies the change in internal energy caused by the variation in the concentration of ionic species. Nernst equation, as described in Equation (2.8), is commonly used to provide a linkage between equilibrium electrode potential U_{k}, and the concentration of participants in the electrode process shown in Equation (2.9):

$$U_{\text{k}} = U_{\text{k}}^0 + \frac{RT}{nF} \ln \frac{C_{\text{O}}}{C_{\text{R}}}, \quad \text{k} \in \{\text{n}, \text{p}\} \tag{2.8}$$

18

$$O + ne \rightleftharpoons R \tag{2.9}$$

with the standard equilibrium potential U_k^0, the number of electrons exchanged in the redox reaction n (n=1 for lithium-ion systems), the oxidant concentration C_O, and reductant concentration C_R [78]. In intercalation reactions, U_k^0 reflects the energy of intercalated ions in specific sites within the lattice of the host material [79].

2.3.4 Potentials

The potentials of LIBs refer to the voltage drop which are caused by the resistance to the flow of electrons in the electrodes and the movement of ions through the electrolyte and membrane. These phenomena are determined by the electronic conductivity of the electrodes and current collectors (often copper and aluminium) and the ionic conductivity of the electrolyte and membrane [80]. The relationship is summarised by Ohm's Law for electromagnetics:

$$J = \sigma E \tag{2.10}$$

where E is electric field intensity (V/m), J is the volume current density, a vector describing the current flow, having units of A/m^2; and σ is conductivity $\sigma^{-1}\text{m}^{-1}$.

In the physical model class, the potentials is described by the boundary conditions of solid phase charge conservation, as following

$$
\begin{aligned}
\sigma_{s,n}\varepsilon_{s,n}\frac{\partial \phi_{s,n}}{\partial x}\bigg|_{x=0} &= \sigma_{s,p}\varepsilon_{s,p}\frac{\partial \phi_{s,p}}{\partial x}\bigg|_{x=L} = \frac{i_{app}}{A_{surf}} \\
\sigma_{s,n}\varepsilon_{s,n}\frac{\partial \phi_{s,n}}{\partial x}\bigg|_{x=L_n} &= \sigma_{s,p}\varepsilon_{s,p}\frac{\partial \phi_{s,p}}{\partial x}\bigg|_{x=L-L_p} = 0
\end{aligned}
\tag{2.11}
$$

where $\frac{\partial \phi}{\partial x}$ is electric field intensity and $\frac{i_{app}}{A_{surf}}$ is current density. Thus, when the parameters are considered to be fixed, the potential relationship is a linear dynamic.

2.3.5 Summary

By far, main nonlinear and linear dynamic processes of lithium-ion batteries have been briefly described. From a modelling perspective, battery mathematical models are developed to simulate the current-voltage relationship of the lithium-ion battery based on either the aforementioned fundamental physical principles or empirical

19

dynamic responses. In what follows, existing battery models widely utilised in the BMS applications will be reviewed comprehensively.

2.4 Mathematical models of Lithium-Ion Batteries

Existing battery mathematical models can be classified into two categories in terms of modelling approaches: electrochemical or physical models that are based on fundamental electrochemical theory as well as equivalent circuit models which exploit a combination of data and analogies with other physical systems. Note that, due to the amount of data required for modelling, Machine Learning (ML) models, which apply statistical algorithms to learn from data directly, are out of scope in this thesis.

2.4.1 Electrochemical models

Electrochemical models, starting from the physical geometries and electrochemical mechanisms in the electrodes and electrolyte, have been proposed to describe the lithium-ion battery behaviours over the past few years.
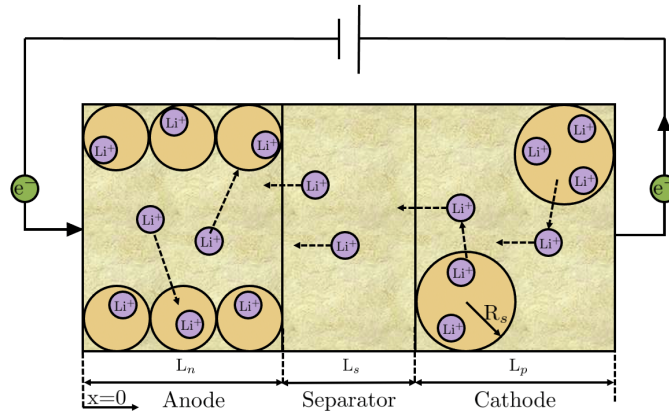
Figure 2.3: The schematic diagram of the pseudo-two-dimensional (P2D) model

Doyle et al. proposed the porous electrode theory in 1993 to describe lithium-ion cells and described the widely used physics-based electrochemical model, named as pseudo-two-dimensional (P2D) model [36, 68, 81]. The schematic diagram of the pseudo-two-dimensional model is shown in Figure 2.3. In the x dimension, the cell is divided into three regions to respectively represent the negative electrode, the separator, and the positive electrode. Lithium ions (Li-ions) exist in both solid and liquid phases in the electrodes, but only in the liquid phase within the separator.

Table 2.1
Governing equations of the P2D model.

Description	Equation	Boundary conditions
Mass conservation	$\frac{\partial c_{s,k}}{\partial t} = \frac{D_{s,k}}{r^2}\frac{\partial}{\partial r}\left(r^2\frac{\partial c_{s,k}}{\partial r}\right)$	$\left.\frac{\partial c_{s,k}}{\partial r}\right|_{r=0} = 0,\ -D_{s,k}\left.\frac{\partial c_{s,k}}{\partial r}\right|_{r=R_s} = j_k$
Charge conservation	$\frac{\partial}{\partial x}\left(\sigma_{s,k}\varepsilon_{s,k}\frac{\partial \phi_{s,k}}{\partial x}\right) = \frac{3\varepsilon_{s,k}F}{R_k}j_k$	$\sigma_{s,n}\varepsilon_{s,n}\left.\frac{\partial \phi_{s,n}}{\partial x}\right|_{x=0} = \sigma_{s,p}\varepsilon_{s,p}\left.\frac{\partial \phi_{s,p}}{\partial x}\right|_{x=L} = \frac{i_{app}}{A_{surf}}$ $\sigma_{s,n}\varepsilon_{s,n}\left.\frac{\partial \phi_{s,n}}{\partial x}\right|_{x=L_n} = \sigma_{s,p}\varepsilon_{s,p}\left.\frac{\partial \phi_{s,p}}{\partial x}\right|_{x=L-L_p} = 0$
Mass conservation	$\varepsilon_{e,k}\frac{\partial c_{e,k}}{\partial t} = \frac{\partial}{\partial x}\left(D_e\varepsilon_{e,k}^b\frac{\partial c_{e,k}}{\partial x}\right) + \frac{3\varepsilon_{s,k}(1-t^+)}{R_k}j_k$	$\left.\frac{\partial c_{e,n}}{\partial x}\right|_{x=0} = \left.\frac{\partial c_{e,p}}{\partial x}\right|_{x=L} = 0$
Charge conservation	$\frac{\partial}{\partial x}\left(\kappa\varepsilon_{e,k}^b\frac{\partial \phi_{e,k}}{\partial x} - \kappa\varepsilon_{e,k}^b\frac{2(1-t^+)RT}{F}\frac{\partial \ln c_{e,k}}{\partial x}\right) = -\frac{3\varepsilon_{s,k}F}{R_k}j_k$	$\left.\frac{\partial \phi_{e,n}}{\partial x}\right|_{x=0} = \left.\frac{\partial \phi_{e,p}}{\partial x}\right|_{x=L} = 0$
Butler-Volmer	$j_k = \begin{cases} \frac{i_{0,k}}{F}\left(\exp\left(\frac{\alpha_a F}{RT}\eta\right) - \exp\left(-\frac{\alpha_c F}{RT}\eta\right)\right), & k \in \{n,p\}, \\ 0, & k = s. \end{cases}$	
Exchange current	$i_{0,k} = k_k c_e^{\alpha_a} \cdot \left(c_{s,k,max} - c_{s,k}|_{r=R_k}\right)^{\alpha_a} \cdot \left(c_{s,k}|_{r=R_k}\right)^{\alpha_c}$	
Overpotential	$\eta = \phi_{s,k} - \phi_{e,k} - U_k(c_{s,k}|_{r=R_k}), \qquad k \in \{n,p\}$	
Terminal Voltage	$U(t) = \phi_{s,p}(L,t) - \phi_{s,n}(0,t) - \frac{R_f^k}{A_{surf}}i_{app}(t)$	

In the solid phase, Li-ions intercalate into / deintercalate from the solid-phase material, which is represented by spheres with radius R_s. In the liquid phase, Li-ions exist in a dissolved state in the electrolyte. The intercalation and deintercalation of Li-ions between the solid particles in the cathode and anode define the charging and discharging processes of a lithium-ion battery. The governing equations and boundary conditions of the P2D model are listed in Table 2.1. The readers can refer to [36] for more details of the P2D model. It is worthy to note that the nonlinear dynamic processes mentioned in Section 2.3 are taken into account in this electrochemical model, which enables the P2D model to give accurate voltage predictions. The model is able to not only predict the macroscopic current-voltage relationship of the battery but also directly simulate the battery internal microscopic information such as particle concentration distribution. Furthermore, taking advantage of emulating microscopic dynamic processes in electrodes, the P2D model offers the ability

to couple with parasitic reactions for modelling ageing mechanisms such as SEI formation and lithium plating [82, 83]. However, due to its algebraic constraints and coupled interactions, the P2D model takes a significant amount of computational cost and time to solve, which is deemed prohibitive for on-board BMS applications [84, 85].

To reduce the complexity of the electrochemical model for real-time and control-oriented applications, simplifications of the P2D model have been proposed in recent years. The approach for simulating the motion of ions in and out of the electrodes using a number of spherical particles is proposed [86], and later it has been extended to lithium-ion batteries. The single particle model (SPM) is one of the most commonly used simplified electrochemical battery model [37, 82, 87, 88]. The SPM describes the LIB thermodynamics, the diffusion of lithium in the active material of individual electrodes, and the charge-transfer kinetics of the Li-ions intercalation/deintercalation reaction at the solid/liquid interface. In contrast with the P2D model [36], it assumes the molar flux (from the solid active material to the electrolyte) is uniform along each electrode and idealises each electrode as a single spherical particle, as well as electrolyte dynamics are ignored all together. The results show that the computational time and cost of SPMs are significantly less than those of the rigorous P2D model. However, due to the lack of Li^+ concentration distribution and the potential distribution in the electrolyte phase, the model accuracy can hardly be maintained when the electric current is larger than 1C[*] [88]. Thus, an extended type of SPM, which comprises of the solid phase and the electrolyte phase dynamics, termed as single particle model with electrolyte dynamics (SPMe), was derived in [38]. The assumption of the SPMe model leads to a linear relationship between molar ion flux j and the input current I as follows Equation (2.12),

$$j_n^-(t) = \frac{I(t)}{Fa^-L^-}, \quad j_n^+(t) = \frac{I(t)}{Fa^+L^+} \tag{2.12}$$

Note that here positive current stands for discharging, and negative current for charging in [38].

Then the PDEs in the P2D model become decoupled, as shown in Figure 2.4. The dynamics of lithium concentration in the solid and electrolyte phases are given below. Note that $\{+, sep.-\}$ stand for the positive electrode (PE), separator, and negative electrode (NE) domain, respectively [38].

The evolution of lithium concentration in the solid phase follows Equation

---

[*]In the battery literature, the electrical current input is commonly denoted as a C-rate, which is a value of current normalised by the rate capacity of a battery cell. Such that the discharging duration is 1 h when a cell is discharged by 1C current from 100% to 0% SOC.
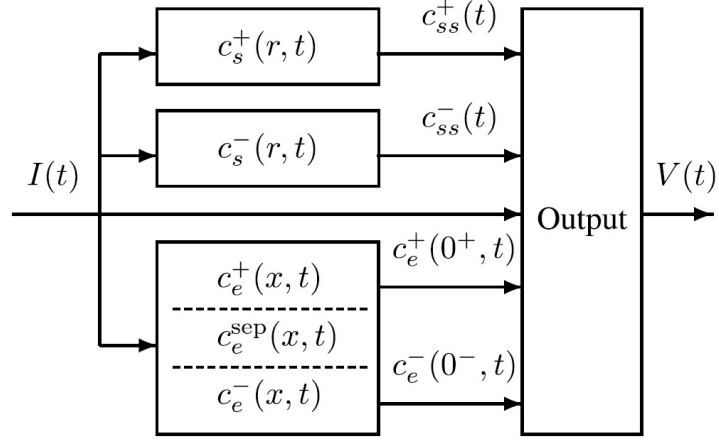
Figure 2.4: The block diagram of the SPMe [38].

(2.13),

$$\frac{\partial c_{\mathrm{s}}^{\pm}}{\partial t}(r,t) = \frac{1}{r^2}\frac{\partial}{\partial r}\left[D_{\mathrm{s}}^{\pm}r^2\frac{\partial c_{\mathrm{s}}^{\pm}}{\partial r}(r,t)\right] \tag{2.13}$$

with boundary conditions in Equation (2.14),

$$\frac{\partial c_{\mathrm{s}}^{\pm}}{\partial t}(0,t) = 0, \quad \frac{\partial c_{\mathrm{s}}^{\pm}}{\partial t}(R_{\mathrm{s}}^{\pm},t) = \pm\frac{1}{D_{\mathrm{s}}^{\pm}Fa^{\pm}L^{\pm}}I(t) \tag{2.14}$$

The evolution of lithium concentration in the electrolyte phase follows Equation (2.14), (2.15), and (2.16),

$$\varepsilon_{\mathrm{e}}^{-}\frac{\partial c_{\mathrm{e}}^{-}}{\partial t}(x,t) = \frac{\partial}{\partial x}\left[D_{\mathrm{e}}^{\mathrm{eff}}(c_{\mathrm{e}}^{-})\frac{\partial c_{\mathrm{e}}^{-}}{\partial x}(x,t)\right] + \frac{1-t_{c}^{0}}{FL^{-}}I(t) \tag{2.15}$$

$$\varepsilon_{\mathrm{e}}^{\mathrm{sep}}\frac{\partial c_{\mathrm{e}}^{\mathrm{sep}}}{\partial t}(x,t) = \frac{\partial}{\partial x}\left[D_{\mathrm{e}}^{\mathrm{eff}}(c_{\mathrm{e}}^{\mathrm{sep}})\frac{\partial c_{\mathrm{e}}^{\mathrm{sep}}}{\partial x}(x,t)\right] \tag{2.16}$$

$$\varepsilon_{\mathrm{e}}^{+}\frac{\partial c_{\mathrm{e}}^{+}}{\partial t}(x,t) = \frac{\partial}{\partial x}\left[D_{\mathrm{e}}^{\mathrm{eff}}(c_{\mathrm{e}}^{+})\frac{\partial c_{\mathrm{e}}^{+}}{\partial x}(x,t)\right] - \frac{1-t_{c}^{0}}{FL^{+}}I(t) \tag{2.17}$$

with boundary conditions in Equation (2.18),

$$\frac{\partial c_{\mathrm{e}}^{-}}{\partial x}(0^{-},t) = \frac{\partial c_{\mathrm{e}}^{+}}{\partial x}(0^{+},t) = 0 \tag{2.18a}$$

$$D_{\mathrm{e}}^{-,\mathrm{eff}}(c_{\mathrm{e}}(L^{-}))\frac{\partial c_{\mathrm{e}}^{-}}{\partial x}(L^{-},t) = D_{\mathrm{e}}^{\mathrm{sep,eff}}(c_{\mathrm{e}}(0^{\mathrm{sep}}))\frac{\partial c_{\mathrm{e}}^{\mathrm{sep}}}{\partial x}(0^{\mathrm{sep}},t) \tag{2.18b}$$

$$D_{\mathrm{e}}^{\mathrm{sep,eff}}(c_{\mathrm{e}}(L^{\mathrm{sep}}))\frac{\partial c_{\mathrm{e}}^{\mathrm{sep}}}{\partial x}(L^{\mathrm{sep}},t) = D_{\mathrm{e}}^{+,\mathrm{eff}}(c_{\mathrm{e}}(L^{+}))\frac{\partial c_{\mathrm{e}}^{+}}{\partial x}(L^{+},t) \tag{2.18c}$$

$$c_e(L^-, t) = c_e(0^{\text{sep}}, t) \tag{2.18d}$$

$$c_e(L^{\text{sep}}, t) = c_e(L^+, t) \tag{2.18e}$$

Finally, the terminal voltage output is a nonlinear function of the PE and NE surface lithium concentrations ($c_{\text{ss}}^+(t)$ and $c_{\text{ss}}^-(t)$), the electrolyte lithium concentrations at the positive and negative current collectors ($c_e(0^+, t)$ and $c_e(0^-, t)$, respectively), and the input current $I(t)$, as in Equation (2.19):

$$
\begin{aligned}
V(t) = {}& U^+(c_{\text{ss}}^+(t)/c_{\text{s,max}}^+) - U^-(c_{\text{ss}}^-(t)/c_{\text{s,max}}^-) \\
& + k_{\text{conc}} \left[\ln\left(c_e(0^+, t) \right) - \ln\left(c_e(0^-, t) \right) \right] \\
& + \left[\frac{L^+ + 2L^{\text{sep}} + L^-}{2\bar{\kappa}} - \left(\frac{R_f^+}{a^+ L^+} + \frac{R_f^-}{a^- L^-} \right) \right] I(t) \\
& + \frac{RT}{aF} \left[\sinh^{-1}\left(-\frac{I(t)}{2a^+ L^+ i_0^+(t)} \right) - \sinh^{-1}\left(\frac{I(t)}{2a^- L^- i_0^-(t)} \right) \right]
\end{aligned}
\tag{2.19}
$$

where $i_0^{\pm}$ represents the exchange current density, and

$$i_0^{\pm}(t) = k^{\pm} \left[c_{\text{ss}}^{\pm}(t) \right]^{\alpha_c} \times \left[c_e(0^{\pm}, t)(c_{\text{s,max}}^{\pm} - c_{\text{ss}}^{\pm}(t)) \right]^{\alpha_a} \tag{2.20}$$

The readers can refer to [38] for more details of the derivation of the SPMe equations.

To solve the SPMe equations, the same procedure in [38] is followed here. The evolution of lithium concentration in the electrode and electrolyte domains were solved separately.

For the electrode concentration dynamics, the average lithium concentration in the electrode, or bulk concentration, is an integration of the current [89],

$$\frac{\overline{C_s^{\pm}}(s)}{I(s)} = \pm \frac{3}{R_s^{\pm} a^{\pm} F L^{\pm}} \frac{1}{s} \tag{2.21}$$

where $\overline{C_s^{\pm}}(s)$ is the Laplace transformation of $\overline{c_s^{\pm}}(t)$, and $I(s)$ is the Laplace transformation of the current $I(t)$. Similar notations will apply hereinafter.

Define the difference between the electrode surface concentration and bulk concentration as $\Delta c_s^{\pm}(t) = c_{\text{ss}}^{\pm}(t) - \overline{c_s^{\pm}}(t)$. Then according to the transcendental transfer function proposed in [89] as following,

$$\frac{\Delta C_s^{\pm}(s)}{I(s)} = \frac{R_s^{\pm}}{D_s^{\pm}} \frac{\left[(\beta^{\pm})^2 + 3 \right] \tanh(\beta^{\pm}) - 3\beta^{\pm}}{(\beta^{\pm})^2 \left[\tanh(\beta^{\pm}) - \beta^{\pm} \right]} \tag{2.22}$$

where $\beta^{\pm} = R_s^{\pm}\sqrt{s/D_s^{\pm}}$. Equation (2.22) can be reformulated into the partial fraction expansion, neglecting the high frequency dynamics above a cut-off frequency (here $10\,\mathrm{Hz}$),

$$\frac{\Delta C_s^{\pm}(s)}{I(s)} \approx Z_s^{\pm} + \sum_{k=1}^{n_s^{\pm}} \frac{r_k^{\pm}s}{s - p_k^{\pm}} \tag{2.23}$$

The readers can refer to [89] for more details. Next, Equation (2.23) can be readily put into state-space form as

$$\dot{x}_s^{\pm}(t) = A_s^{\pm}x_s^{\pm}(t) + B_s^{\pm}I(t)$$
$$\Delta c_s^{\pm}(t) = C_s^{\pm}x_s^{\pm}(t) + D_s^{\pm}I(t) \tag{2.24}$$

where $x_s^{\pm}(t)$ is a vector representing the concentration $c_s^{\pm}(x,t)$ at the discrete nodes.

In addition, the electrolyte concentration dynamics in Equation (2.14), (2.15), and (2.16) is discretised by finite element method, yielding

$$\dot{x}_e^{\pm}(t) = A_e x_e(t) + B_e I(t)$$
$$c_e(0^+, t) = C_e^+ x_e(t), \quad c_e(0^-, t) = C_e^- x_e(t), \tag{2.25}$$

where $x_e(t)$ is a vector representing the concentration $c_e(x,t)$ at the discrete nodes. Equation (2.25) can be further simplified by removing the pole/zero cancellation at the origin, as shown in [89].

In the SPMe model, the solid-phase Li concentration in each electrode is assumed to be constant in spatial coordinate x, uniformly in time; the exchange current density is approximated by its averaged value, which is independent of x; and the total moles of lithium in the electrolyte and in the solid phase are assumed to be conserved, allowing the fluxes to be written as proportional to input current. The terms of the ohmic potential drop due electrolyte conductivity and the electrolyte concentration overpotential are added in the SPMe voltage expression to improve the voltage accuracy for larger currents than the SPM. Similarly, the models in [90, 91, 25] also take the dynamics of electrolyte into account. Notably, although electrochemical models can achieve relatively high accuracy and are widely used in scientific community, there are still limitations in the physics described and simplifications made as ideal mathematical representations, such as the assumption of uniform current density and the idealisation of the battery active material into uniform spherical particles in Fick's law of diffusion [92].

25

The primary advantage of SPMs is that the uniform molar flux assumption allows the concatenation dynamics and potentials to be decoupled and solved in isolation and therefore requires minimum computational effort compared to the P2D model (which is a fully coupled system of nonlinear PDE equations). SPMs have therefore been widely used for many purposes such as online estimation and life modelling of lithium-ion batteries. For example, Han et al. developed a simplified physics-based electrochemical model to estimate lithium-ion battery SOC [93]. Li et al. proposed a SPM coupled with chemical/mechanical degradation physics model to estimate lithium-ion battery SOH [94]. Reniers et al. reviewed and compared various degradation models implemented within a SPM framework and their behaviour [95]. In recent years, to support on-broad applications, model order reduction algorithms, such as residue grouping [89, 96], balanced truncation [97], Padé approximation [98], have been used to reduce the complexity of electrochemical models while retaining the appropriate level of accuracy. Although these methods result in some information loss in the simplified reduced-order models, it is more desirable for real-time battery applications.

However, a challenge with aforementioned physics-based electrochemical models is the model parameterisation of the various dynamics in each electrode and electrolyte. A total of 35 parameters are required to in the P2D model which increases the difficulty of parameterisation procedure [24]. Characterisation tests in Chapter 3 are used to elucidate the thermodynamic and kinetic properties of the materials and electrodes and provide essential information for electrochemical models. For example, Galvanostatic intermittent titration technique (GITT) was used to ascertain the open circuit voltage (OCV) of the LIB, and the diffusion coefficient at different states of charge (SOC) [99]. Electrochemical impedance spectroscopy (EIS) is applied to calculate the exchange current density for each electrode and their activation energy from the Arrhenius equation, and subsequently the reaction rate was determined [100]. Apart from the necessary characterisation methods, to obtain a comprehensive parameter set for electrochemical models, a few advanced experimental tests have to be applied to collect essential physical property information, such as SEM for electrodes morphology, inductively coupled plasma optical emission spectroscopy (ICP-OES) and energy-dispersive X-ray spectroscopy (EDS) for elemental composition, X-ray diffraction for the material crystal structure and theoretical density [24]. Such tests and analysis introduce obstacles into electric vehicle applications and cannot be easily achieved within an engineering framework outlined in Chapter 1. Thus, to achieve the objectives of the VCHV project, a different category of battery models, which is more suitable for real-time applications due

to its simple structure and easy identification, will be reviewed in the next section.

2.4.2   Equivalent circuit models

Taking advantage of the lower computational load and fewer parameters than electrochemical models, the equivalent circuit models (ECMs) have gained wide attention and practical applications. The ECMs utilise a number of simple electrical circuit components, such as a voltage source (indicating open circuit voltage), resistors (indicating the difficulty of electron and ion movement), and resistor-capacitor (RC) in parallel branches (indicating the polarisation inside the battery) to imitate the current-voltage characteristics and transient behaviour of a lithium-ion battery [92]. In the literature, existing ECMs are commonly classified into two types: the time-domain ECMs*, known as the conventional integer-order models, and the frequency-domain ECMs†, including fractional order models and nonlinear equivalent circuit models.

Time-domain ECM
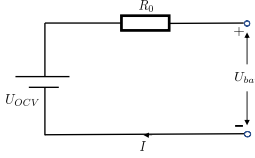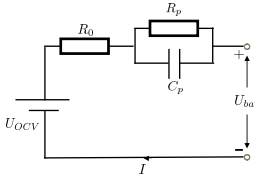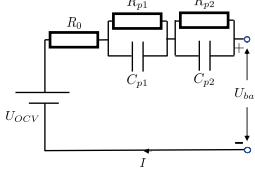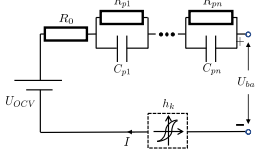
The time-domain ECM comprises of voltage source, resistor, capacitor, inductance, and other circuit components to emulate the battery terminal voltage and current characteristics. The basic time-domain equivalent circuit models are shown in Table 2.2. The simplest time-domain ECM only has a resistor which is connected in series with a voltage source. It is designed to describe the open circuit voltage of batteries, also known as the Rint model [101]. This model is easily identified and implemented into battery simulation, however, it does not account for any electrochemical process dynamics of a battery which results in a poor accuracy under slow dynamic profiles [102]. To improve the model accuracy and involve battery dynamics, a parallel RC branch is added in the circuit of the Rint model, named the Thevenin ECM [103]. The polarisation between electrode and electrolyte can be reflected in this model, and the battery dynamic behaviour is described more accurately. In order to separately take into account the electrochemical polarisation and concentration polarisation, He et al. added an extra RC branch to the Thevenin model, also called the DP model [104]. Multiple RC branches can be added in ECMs for a superior accuracy, however, as the number of RC branches increases, the mathematical representation of the model become more complex, which makes

---

*A time-domain ECM is a model that is based on time-domain current and voltage measurements.

†A frequency-domain ECM refers to a model that is identified through related data captured by frequency-domain characterisation methods.

the model parameter identification more difficult and not applicable for practical applications. Thus the number of RC branches in the ECM is recommended to be limited and is less than four in the literature [105].

Table 2.2
Schematic diagram of various time-domain equivalent circuit models

Models	Model Structure	Model equations and Features
Rint model		$U_{\text{batt}} = U_{\text{OCV}} - I \cdot R_0$ where U_{batt} is the terminal voltage, U_{OCV} represents the open circuit voltage, I is the input current, and R_0 is the battery Ohmic resistance.
Thevenin model		$U_{\text{batt}} = U_{\text{OCV}} - U_{\text{p}} - I \cdot R_0$ where R_{p} is the polarisation resistance, C_{p} is the polarisation capacitance, and U_{p} is the voltage of RC branch.
DP model		$U_{\text{batt}} = U_{\text{OCV}} - U_{\text{p1}} - U_{\text{p2}} - I \cdot R_0$ where R_{p1}, R_{p2} are the polarisation resistance, C_{p1}, C_{p2} are the polarisation capacitance, and U_{p1}, U_{p2} are the voltage of RC branches.
RCH model		$U_{\text{batt}} = U_{\text{OCV}} - U_{\text{p1}} - \cdots - U_{\text{pn}} - I \cdot R_0 + h_{\text{k}}$ where R_{p1}, R_{pn} are the polarisation resistance, C_{p1}, C_{pn} are the polarisation capacitance, U_{p1}, U_{pn} are the voltage of RC branches, and h_{k} is the hysteresis voltage

In addition, the RC ECMs are sometimes integrated with dedicated elements depicting the battery hysteresis behaviour, which is named as the RCH model and shown in Table 2.2, e.g., the first-order RC model with hysteresis [106, 107, 108] and third-order RC model with hysteresis [109]. Hysteresis, the phenomenon by which the OCV of the battery is inconsistent between charging and discharging processes, is a basic thermodynamic characteristic of a LIB [110]. Depending on cell chemistries, the level of hysteresis varies. Nejad et al. compared the hysteresis levels obtained after a one-hour rest period for the LiPO_4 and NMC cell chemistries, and the results present that the hysteresis levels for the LiPO_4 chemistry is considerably higher than that for the NMC chemistry. Moreover, in the medium SOC range (around 20%-80%), the OCV curve for the LiPO_4 chemistry is fairly flat, which

indicates that, in the SOC estimation applications, even a small error in the voltage measurement within this range can result in a large deviation from the actual SOC value [111]. Thus, a model structure with the cell's hysteresis behaviour for the $LiPO_4$ chemistry is more necessary than that for the NMC chemistry. Hu et al. systematically compared the practicality of twelve commonly used ECMs in terms of model complexity and accuracy, and concluded that the first-order RC branch ECM is preferred for NMC cells, while the first-order RC ECM with one-state hysteresis is the best choice for $LiPO_4$ chemistry cells [40].

The advantage of the ECMs is the simple model structure and easy identification as such these models are widely applied in BMS applications, such as various states estimation [112, 113]. For state of charge (SOC) estimation, the ECMs are integrated with a algorithm like an Extend Kalman Filter (EKF) [114, 115, 14], a fuzzy-logic system [116], a least squares technique [117], a luenberger observer [118], and a sliding mode observer [119]. State of health (SOH) estimation is also investigated using the ECMs in battery management systems. Since the SOH cannot be directly measured in practice, the advanced algorithms are utilised to estimate the variation of degradation indicators, such as battery capacity and internal resistance, for determining ageing states. For example, Tong et al. improved the SOH and SOC estimation by using the EKF and recursive least squares to optimise the battery capacity [120]. In addition, Kim et al. designed an EKF to identify the internal resistance for SOH estimation [121]. Similarly, the genetic resampling particle filter is applied to identify the battery pack internal resistance for SOH estimation [122]. Pei et al. employed the double EKF to simultaneously identify SOP and the Thevenin model parameters in real time [123]. In the literature, the ECMs and the Kalman filter family tests have been widely used for battery states estimation in EV applications [50].

However, a general disadvantage is that a time-domain ECM cannot directly associate an electrical circuit component to a certain battery physical phenomena, which limits the detailed insight of lithium-ion battery behaviours and the employment for interpreting physical processes such as battery ageing [124]. Additionally, due to the limitation of electrical circuit components which hardly exhibits nonlinear characteristics of a lithium-ion battery, most conventional ECMs with constant parameters are linear models and can only remain relatively higher fidelity at middle-to-high (larger than 20%) SOC regions and at low current load. For instance, refer to [39], the DP model provides accurate results between 20% and 100% SOC with the error within $\pm 10\,\text{mV}$ under a 0.5C constant-current discharge pause profiles (DPP)[‡]

[‡]The DPP is determined as a two-period cycle in which the battery undergoes constant-current

test. Starting from the test with SOC lower than 19.5%, the estimated voltage show larger deviation from the real value with maximum 60 mV underestimation, which indicates that model fidelity declines in the low SOC range. Additionally, when the current load increases, the ECM RMSE[§] results 3 mV at 75.9% SOC and 25 mV at 11.5% SOC in 0.5C DPP case increase to 24 mV at 75.9% SOC and 42 mV at 11.5% SOC in 2C DPP case, which indicate that the model fidelity decreases rapidly when the current load increases. Similarly, Xiong et al. demonstrated that RMSE of the Thevenin model under DST[¶] working condition rapidly grows from 5 mV at 80% SOC to 17 mV at 10% SOC [33]. Therefore, linear ECM models are inadequate for the objective of this thesis, which is to improve model accuracy at low SOC range.

Frequency-domain ECM

On contrary to the aforementioned time-domain ECMs, the frequency-domain ECMs, which are analysed and designed with data obtained by frequency domain characterisation tests, have attracted growing attention for modelling electrochemical power sources in the last few years. The frequency response of lithium-ion batteries have distinct characteristics, such as the impedance response captured by electrochemical impedance spectroscopy (EIS) which will be discussed in Section 3.3, and the frequency-domain ECMs offer a significant advantage to model the non-local and heterogeneous phenomena prevalent in electrochemical systems, such as nonuniform potential distribution [126]. This type of model is therefore considered an effective candidate in many fields of battery management, including frequency domain modelling for health diagnosis and battery heating, as well as time domain modelling for BMS applications including SOC and SOH estimations and fault diagnosis [124]. According to the identification approaches utilised, the frequency-domain ECMs can be further classified into two categories: the fractional order model (FOM) and the nonlinear equivalent circuit model (NLECM).

The fractional-order model (FOM) was first proposed for NiMH batteries in [127], in which the parameters were identified based on impedance data in the frequency domain [128]. However, due to the lack of appropriate numerical approaches

---

discharge in the first period and rests in the second period, cycling from a fully charged condition to the discharge voltage limit. The purpose of the extended constant-current discharge period is to imitate stable driving conditions with generally constant speed and power consumption, whereas the purpose of the rest period is to test the accuracy of voltage estimate during the depolarisation process.

[§]The voltage RMSE is computed using the mean voltage error during the discharge period of each DPP cycle, and the SOC value is regarded as the mean SOC during each entire discharge period.

[¶]The DST test is a widely used dynamic driving profile to evaluate the performance of the vehicle, and is also used to validate model accuracy or algorithm efficiency [125].

for implementing the frequency-domain model back into the time domain at that time, the model was rarely implemented. Recently, the development of the FOM is prompted by the application of fractional-order calculus as well as new elements, which exhibit memory effects, by the circuit analysis theory [129, 130, 131]. A common feature of electrochemical battery system is that multiple dynamic processes mentioned in Section 2.3 occur simultaneously during operation and inherently exhibit different time scales [124]. Faster physical processes show smaller time constants than slower processes, which can be distinguished by characterising the impedance over wide frequency ranges in electrochemical impedance spectroscopy (EIS) [132]. Note that the EIS will be introduced as one of the conventional characterisation tests in Chapter 3. The fractional-order behaviour of battery impedance spectra has been widely reported in the literature, leading to the design of constant phase element (CPE).

The modelling principles of the FOMs is to design an equivalent circuit with the goal to fit the experimentally measured impedance data obtained from EIS using circuit elements, as demonstrated in Figure 2.5. Apart from the circuit elements in the conventional ECMs mentioned in Section 2.4.2, a CPE initially proposed in [133] is utilised into the circuit to describe the phenomenon of capacitance dispersion in LIBs, and its frequency domain electric impedance Z_{CPE} is expressed as

$$Z_{\mathrm{CPE}}(\omega) = \frac{1}{C_{\mathrm{CPE}}(j\omega)^{\alpha}} = \frac{1}{C_{\mathrm{CPE}}(\omega)^{\alpha}} \left(\cos \frac{\alpha\pi}{2} - j \sin \frac{\alpha\pi}{2} \right), \quad for \quad \alpha \in (-1, 1), \tag{2.26}$$

where the exponent α is a fractional-order related to capacitance dispersion, C_{CPE} is the capacity coefficient, j is the imaginary unit, and ω is the angular frequency. The CPE element can be considered as a generalised electrical element with constant-phase angle of $\alpha\pi/2$. Similarly, various conventional elements can be represented by setting corresponding phase shifts, such as resistance ($\alpha = 0$), capacitance ($\alpha = 1$), and inductance ($\alpha = -1$). In the Nyquist plot, a CPE is a straight line with a slope of $-\tan(\alpha\pi/2)$, and thus the straight line in the low frequency range can be emulated, which cannot be achieved with an ideal resistance or capacitance. In this case, the CPE is commonly named as the Warburg element, which is expressed as following [126]:

$$Z_{\mathrm{W}}(\omega) = Z_{\mathrm{D}} \frac{\tanh \sqrt{j\omega/\omega_{\mathrm{D}}}}{\sqrt{j\omega/\omega_{\mathrm{D}}}}, \tag{2.27}$$

where ω_{D} and Z_{D} represent characteristic frequency and diffusion resistance, respec-

tively.

To model the semi-circle in the mid-frequency range, the Z_{arc} element, i.e., a parallel connection of a CPE and an ideal resistance, denoted by R//CPE, is commonly utilised and expressed as

$$Z_{\mathrm{arc}}(\omega) = \frac{R}{1 + RC_{\mathrm{CPE}}(j\omega)^\alpha}.$$ (2.28)

By eliminating ω, one obtains

$$\left(Z'_{\mathrm{arc}}(\omega) - \frac{R}{2}\right)^2 + \left(Z''_{\mathrm{arc}}(\omega) - \frac{R}{2}\cot\frac{\alpha\pi}{2}\right)^2 = \left(\frac{R}{2}\csc\frac{\alpha\pi}{2}\right)^2,$$ (2.29)

which represents a circle whose centre is $(R/2, R\cot(\alpha\pi/2)/2)$, and the radius is $R\csc(\alpha\pi/2)/2$, as shown in Figure 2.5. With the presence of the CPE, the depressed semi-circle in the middle frequency range can be modelled [124]. Thus, taking advantage of fractional-order calculus, the CPEs can significantly improve the feasibility of FOMs for EIS fitting that can be used to link impedance variation and battery status for frequency domain applications, such as health diagnosis [134] and alternating current (AC) heating [135].
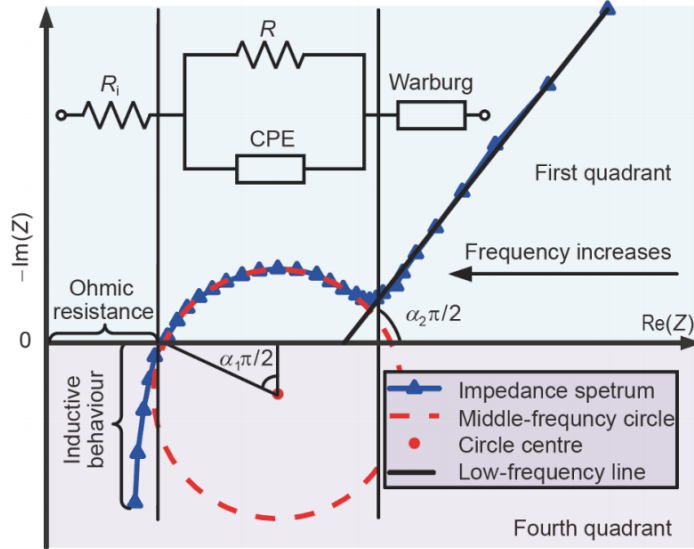
Figure 2.5: Example of fractional order based EIS fitting [124].

To apply FOMs in the time-domain BMS applications, the CPE element has to be implemented in the time domain. The fractional-order operator for a

CPE in Equation 2.26 is mathematically defined by $\mathcal{D}_t^\alpha(\cdot) = \frac{d^\alpha(\cdot)}{dt^\alpha}$. An equation with $\mathcal{D}_t^\alpha$ describes dynamic processes with infinite dimension. To facilitate analysis and numerical implementation, three different definitions have been proposed for the description of the fractional order derivatives, namely, Grunwald-Letnikov (GL), Riemann-Liouville (RL), and Caputo [136]. The definition of GL provides an intuitive discretisation form, and its expression can be directly used in numerical calculation [137]. The GL fractional derivative is defined as

$$\mathcal{D}_t^\alpha f(t) = \lim_{T \to 0} \frac{1}{T^\alpha} \sum_{k=0}^{t/T} (-1)^k \binom{\alpha}{k} f(t - kT), \qquad (2.30)$$

where T is the sampling time interval, t/T is the maximum integer lower than or equal to t/T, and $\binom{\alpha}{k}$ represents the Newton binomial term defined as

$$\binom{\alpha}{k} = \frac{\Gamma(\alpha + 1)}{\Gamma(k + 1) \cdot \Gamma(\alpha - k + 1)}, \qquad (2.31)$$

where $\Gamma(\cdot)$ is the gamma function, also known as Euler second integral, which is a generalisation of factorial functions in real and complex fields, defined as

$$\Gamma(\alpha) = \int_0^\infty \xi^{\alpha-1} e^{-\xi} d\xi. \qquad (2.32)$$

A comprehensive description of these definitions as well as their peculiarities has been presented in [136, 138]. For battery modelling, α is commonly in the range of [0,1], and a fractional α can depict a memory effect in terms of $f(t)$. In lithium-ion batteries, such memory effects is attributed to electrochemical processes, such as charge transfer reactions and diffusion. These processes entail time-domain voltage memory and can be modelled using fractional derivatives. Technically, with CPEs, the plate hypothesis underlying the real electrodes can be relaxed, and non-uniform boundary and distributed intercalation/deintercalation processes within porous electrodes can be described [139].

Taking advantage of the fractional calculus, numerous FOMs have recently been explored for LIB modelling. Typical FOMs for a lithium-ion battery cell is shown in Figure 2.6. Zou et al. proposed an infinite-dimensional model for LIB by simply replacing the ideal capacitance in the RC branch of the Thevenin model to a CPE, as presented in Figure 2.6a. However, a complex approximation algorithm, named Oustaloup recursive approximation [140], has to be applied to transfer the fractional equations to ordinary difference equations for handling numerical calculation, which may affect the model's accuracy due to the determination of frequency

bounds. To achieve higher accuracy, by taking into account the diffusion process, a Warburg element (W) is added in series with the charge-transfer resistor (R_1) of an FOM, as shown in Figure 2.6b [128]. This FOM shows a high accuracy in voltage prediction to experiment results in the time domain by applying the GL fractional derivative, as well as this model is utilised to study the experimental impedance spectra of a LFP cell [141]. In Figure 2.6c, a Warburg element is set in series with the R//CPE branch to describe LIB dynamics [142]. The FOM with two R//CPE branches in series in Figure 2.6d has also been employed and is expected to be more robust to uncertainties [143].
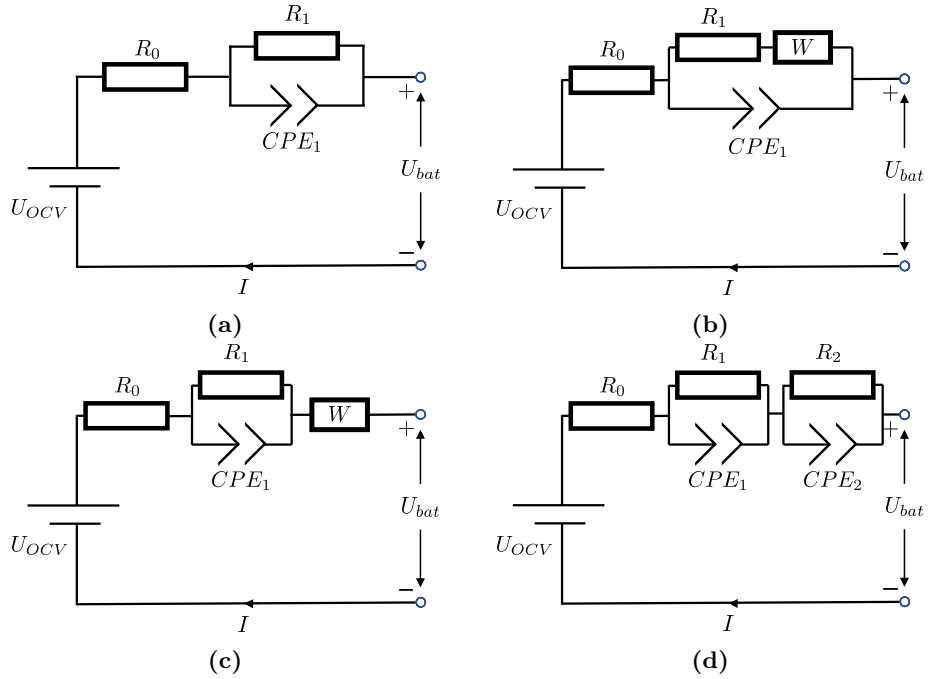
Figure 2.6: Typical fractional-order circuit models for a Li-ion cell.

The FOM has demonstrated its advantages in terms of high accuracy and physical phenomena depiction, however, as a relatively new model, the model identification limits the practical applications of the FOMs and is likely to be investigated further. The approaches for the FOMs reported in the literature can be categorised into two main groups, namely offline identification and online identification. In the frequency-domain offline identification, according to the FOM modelling principle, researchers extract the FOMs parameters directly by fitting EIS test results, which avoids the complex time-domain calculation caused by CPE elements [124]. Andre et al. parameterised a FOM to investigate the impedance spectra of NMC batteries obtained from EIS tests as well as to simulate the battery voltage [43]. The results

shows that the FOM has a better estimation fidelity than a third order conventional ECM. However, for parameterising the FOMs in the frequency domain, the time-consuming EIS tests have to be conducted, which hinders the FOMs from being employed in the time domain [144]. Moreover, the requisites of a valid EIS test restrict the amplitude of excitation current signal to a relatively small value [132], which results that this offline identification method can only model the impedance of the battery cell at pesudo-linear status, such that the nonlinearity of lithium-ion batteries excited by large loads is unfortunately neglected. Additionally, in the time domain, the widely used evolutionary algorithms, e.g., genetic algorithm (GA) [145] and particle swarm optimisation (PSO) [146], are applied for identifying FOM parameters based on the current and voltage response. However, the determination of the model order is the main difficulty of the parameter identification. The differential orders of CPEs can be determined by fitting the EIS impedance curve in the frequency domain, unfortunately, in the pure time-domain algorithm, no information can be used for the order determination before the parameterisation procedure, thus the identification is a nonlinear optimisation problem and hardly solved by simply gradient-based evolutionary algorithms. For instance, a Warburg-like element, which is used to characterise the diffusion impedance, has no fixed differentiation order in the FOMs [147]. Furthermore, the high computational cost of these evolutionary algorithms for CPEs is not trivial.

Compared with offline identification, online identification is desirable for existing BMSs to maintain model fidelity with the fast-changing battery states, but the limited computational resources have to be taken into consideration. Most online identification methods, especially the evolutionary algorithms, cannot be integrated into existing BMSs, as considerable computational efforts are required for online identification to adapt to dynamic profiles. Instead, recursive least squares and variants of the Kalman filters are reported as the efficient online identification methods and expected for further investigations and applications in the future work [124]. Concerning the research objectives in Chapter 1, the fractional-order models are not suitable for this work until the identification methods with low computational cost are further addressed. Additionally, the absence of an explicit interpretation of the battery nonlinearity may render the FOMs ineffective for investigating the low-SOC-area error problem [43].

Contrary to the fractional-order models, the non-linear equivalent circuit model (NLECM), which is a subcategory of nonlinear models identified using a frequency domain approach, takes into account the above limitations. The approach follows system identification methodologies, which have a rich foundation in experi-

mental design and identifying non-linear dynamics. Nonlinear system identification has attracted the attention of scientists and engineers due to its flexibility and the fact that the majority of practical systems are intrinsically nonlinear. In the past, nonlinear models were commonly developed for modelling complex mechanical systems with hysteresis distortions, such as the wet-clutch [148], the switched reluctance motor [149], and the hysteresis system [150]. In the recent few years, nonlinear models have been introduced in the field of electrochemical battery systems in several publications [151, 152, 153]. It is worth to note that, the nonlinear models in this thesis interpret the battery nonlinearity with explicit mathematical functions, rather than the linear parameter varying (LPV) type nonlinear models for the batteries in Ref. [154, 155, 156].

To establish a nonlinear model, the magnitude of nonlinearity is necessary to be characterised by specific nonlinear characterisation tests. Note that the nonlinear characterisation tests will be reviewed in Chapter 3. In system identification the notion of a "best linear approximation" (BLA) is proposed by Schoukens et al. to detect, qualify, and quantify nonlinearities (of a nonlinear dynamical system) in the frequency domain using periodic multisine perturbation signals [157, 158, 159]. In the case of lithium-ion batteries, the BLA analysis on NMC pouch cells were performed such that the linear impedance as well as nonlinearities can be captured [47]. However, only nonparameteric models in the frequency domain were developed in these work, which are not employed in the BMS applications. For model parameterisation, several popular nonlinear model structures can be found in the literature, such as nonlinear state space models [160], block-oriented nonlinear models [161], and nonlinear autoregressive exogenous models (NARX) [162]. Among those systems, the block-oriented nonlinear model are used for its simplicity as the nonlinear dynamic behaviour is separated into a linear time invariant (LTI) dynamical block and a static nonlinearity block (SNL) [163]. Furthermore, a significant advantage of this structure is the ability to link to the physical phenomena of the system, which is especially important for modelling electrochemical systems [152, 151]. The typical series block-oriented structures in the literature is presented in Figure 2.7. In this type of model, the whole system is distributed in linear blocks (shown in red colour with capital letter) and nonlinear blocks (shown in blue colour with lower-case letter) with configurations such as parallel, series, feedback, or feed-forward. Considering the model simplicity and efficiency for practical applications, Hammerstein and Wiener configuration systems are widely used in nonlinear system identification [151, 164, 165, 152].

In the case of battery system modelling, the block-oriented NLECMs have
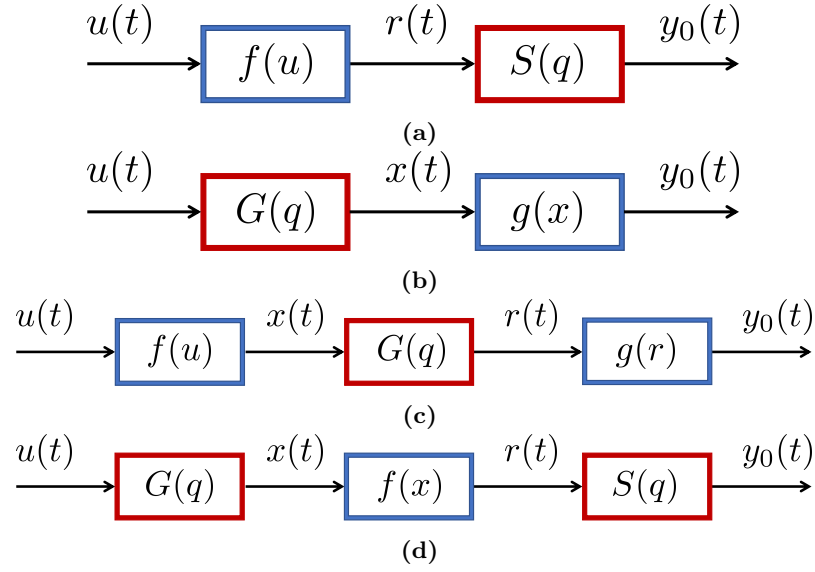
Figure 2.7: Series block-oriented nonlinear models in form of (a) Hammerstein, (b) Wiener, (c) Hammerstein-Wiener and (d) Wiener-Hammerstein systems [163].

been investigated in only few papers. Widanage et al. proposed a Wiener configuration NLECM, as shown in Figure 2.8, for a lithium-ion NCA battery on the basis of the experimental results obtained using a pulse-multisine identification excitation [152]. In this NLECM, the linear ECM block represents the electrical behaviour on the internal ohmic resistance and short time constant polarisations, and the nonlinear over-voltage block describes the non-linear dependence of the voltage on the current due to transport limitations, as well as the OCV and hysteresis model block depicts the battery open circuit voltage including thermodynamic information. As such the physics phenomena of batteries can be related to its linear and non-linear parts, which provides valuable information that a conventional linear ECM cannot contain. The validation results show that the NLECM exhibits lower root mean square error (RMSE) and peak error than a conventional linear ECM [152]. However, the validation of the NLECM under an entire SOC range load profile is not involved and the energy type battery used in this study only exhibits weak nonlinearity. Allafi et al. implemented an online parameter estimation algorithm for the NLECM and reported that, as the NLECM can also keep minimum calculation load and low parameter identification cost, it is qualified as a suitable candidate for practical BMS applications [153]. For the stronger nonlinearity cases, Firouz et al. developed a Hammerstein-Wiener structure non-linear model for all-solid-state batteries. However, the multiple nonlinear blocks increase the computational cost and the difficulty of identification [151].
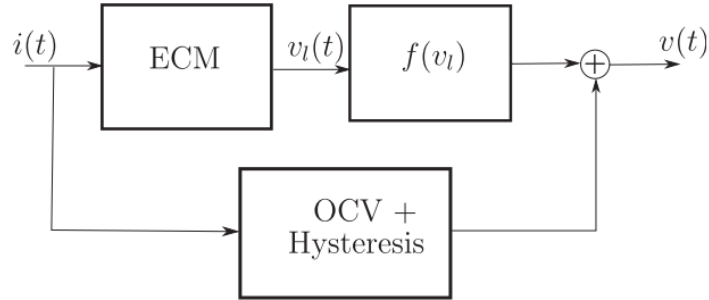
Figure 2.8: Structure of Li-ion battery NLECM. The overall model consists of a linear ECM followed by a non-linear over-voltage function and a parallel OCV and hysteresis model block [152].

Given that the NLECM was introduced into the battery field very recently, the relevant research is in its infancy. Existing literature reports on the performance of NLECMs exclusively in the context of short-term dynamic tests with minor SOC variations. However, as the NLECM's performance is not examined across the entire SOC range, the model's accuracy in the low SOC region, as well as the impact of battery nonlinearity to model performance, is still unknown. Additionally, only the limited frequency range (e.g., $0.01\,\mathrm{Hz} < f < 1\,\mathrm{Hz}$) was examined in these studies for capturing electrochemical dynamics. Unfortunately, dynamic processes corresponding to larger or smaller time constant dynamics, such as diffusion and charge-transfer processes, are neglected during modelling, resulting in an incomplete phenomenological description of battery dynamics in the NLECMs.

2.5   Summary

This chapter has critically reviewed the fundamentals of LIB operation, the typical dynamic processes, as well as the existing body of literature regarding mathematical models of lithium-ion batteries. To summarise, the key features of the battery models employed in the existing literature, such as the number of parameters and equations, the relevant characterisation tests, as well as nonlinearity interpretation are listed in Table 2.3. It is emphasised that electrochemical models are computationally expensive due to the large number of equations when the governing equations are discretised for solving. In addition, the characterisation experiments (around 7) leads to the difficulty of extracting 35 parameters. On the contrary, equivalent circuit models have the advantages of having a low computational cost and requiring minimal characterisation tests for parameterisation, which makes them more

preferable for practical EV applications.

Table 2.3
Overview of battery models in literature

Model	Number of Parameters	Number of Equations	Characterisation Tests	Nonlinearity Interpretation	Ref.
DFN	35 (including electrode OCVs)	8*	FIB-SEM, GITT, EIS, ICP-OES, EDS, OCV, Capacity test	Yes	[24]
SPM	24	4*	Same as DFN**	Yes	[37]
SPMe	30	6*	Same as DFN**	Yes	[38]
ECM	4 (assuming 1st order)	7 (including interpolation functions)	HPPC, OCV	No	[40]
FOM	5 (assuming 1st order)	7 (increases once implemented)	EIS, OCV	No	[139]
NLECM	8 (assuming 2nd order)	9	Multisine test, OCV	Yes	[152]

*Note that the number of equations increases up to hundreds when the governing equations are discretised for solving.
**Note that physical parameters of electrochemical models can be shared.

Regarding the low-SOC-error issue raised in Chapter 1, the electrochemical models commonly show superior accuracy than the equivalent circuit models. Because of the mathematical representations of physical laws implemented in the electrochemical models, both nonlinearity and typical diffusion dynamics of a lithium-ion battery are inherently interpreted, which leads to the high accuracy achieved by electrochemical models through the entire SOC range. However, nonlinearity is rarely taken into account in the ECMs. Ouyang et al. stated that the reason for battery model low-SOC-area inaccuracy is due to the strong nonlinearity of a lithium-ion battery at low state of charge range [39]. Currently, the understanding of the battery nonlinearity is limited to its theoretical definition that is used to describe the intensity of the non-proportional variation relationship between battery terminal voltage and current excitation. As the nonlinearity is difficult to be characterised by traditional battery characterisation tests, the source of battery nonlinearity is seldom investigated in existing publications. Additionally, the absence of a specific dynamic may also result in the error of model voltage prediction. As a phenomenological model, the ECM is developed to describe the voltage dynamic response of a LIB. However, the description cannot directly associate an electrical circuit component to a certain battery physical phenomena, which limits the detailed insight of lithium-ion battery behaviours. Due to the limitations of traditional model parameterisation approaches, the voltage losses that the ECMs can only account for are those with limited time constant (tens of seconds), such as the ohmic loss and small time constant polarisation loss [45, 166]. In comparison to the linear ECM, the NLECM can not only account for ohmic loss and small time constant polarisation loss by RC branches, but it can also interpret charge-transfer kinetics by a nonlinear function, which provides the opportunity to associate particular components to battery physical dynamics [45]. Recent research suggests that the ECM model

accuracy is rather low due to the limitation of linear circuit elements in ECMs. By taking nonlinearity into account, the NLECM model of the 18650 Li-ion NCA battery results in lower RMSE and lower max voltage error (13%-25% and 52%-62% respectively) in comparison to the first-order linear ECM. In addition, the results indicate that including the non-linear over-voltage function improves both the RMSE and peak error when operating below room temperature [45]. Although the NLECM is developed with nonlinearity in mind, the model's performance across the entire SOC range is overlooked in the existing literature. However, the large time constant (thousands of seconds) loss caused by diffusion dynamics is absent from both the ECM and NLECM models, which requires further investigation. Thus, due to its superior accuracy and capability of physical dynamics interpretation, the NLECM, as the state-of-the-art battery model, serves as the starting point for this thesis.

Figure 2.9 provides a summary of the literature review in Chapter 2 (blue rectangles) and Chapter 3 (orange rectangles), highlighting both advantages and downsides of corresponding techniques. In this thesis, a non-linear equivalent circuit model with diffusion dynamics (NLECM-diff), which consists of the OCV curve, impedance linear block, nonlinearity block, and diffusion dynamic block, is developed to improve the model accuracy at low SOC range. Thus, the nonlinearity of battery systems and large time constant dynamics are required to be captured for modelling by applying specific characterisation techniques. In the next chapter, the characterisation tests, which are employed to provide necessary information of battery dynamic behaviour for establishing NLECM-diff model, are introduced. Furthermore, an overview of nonlinear characterisation methods is presented as one of the research objectives of this thesis.
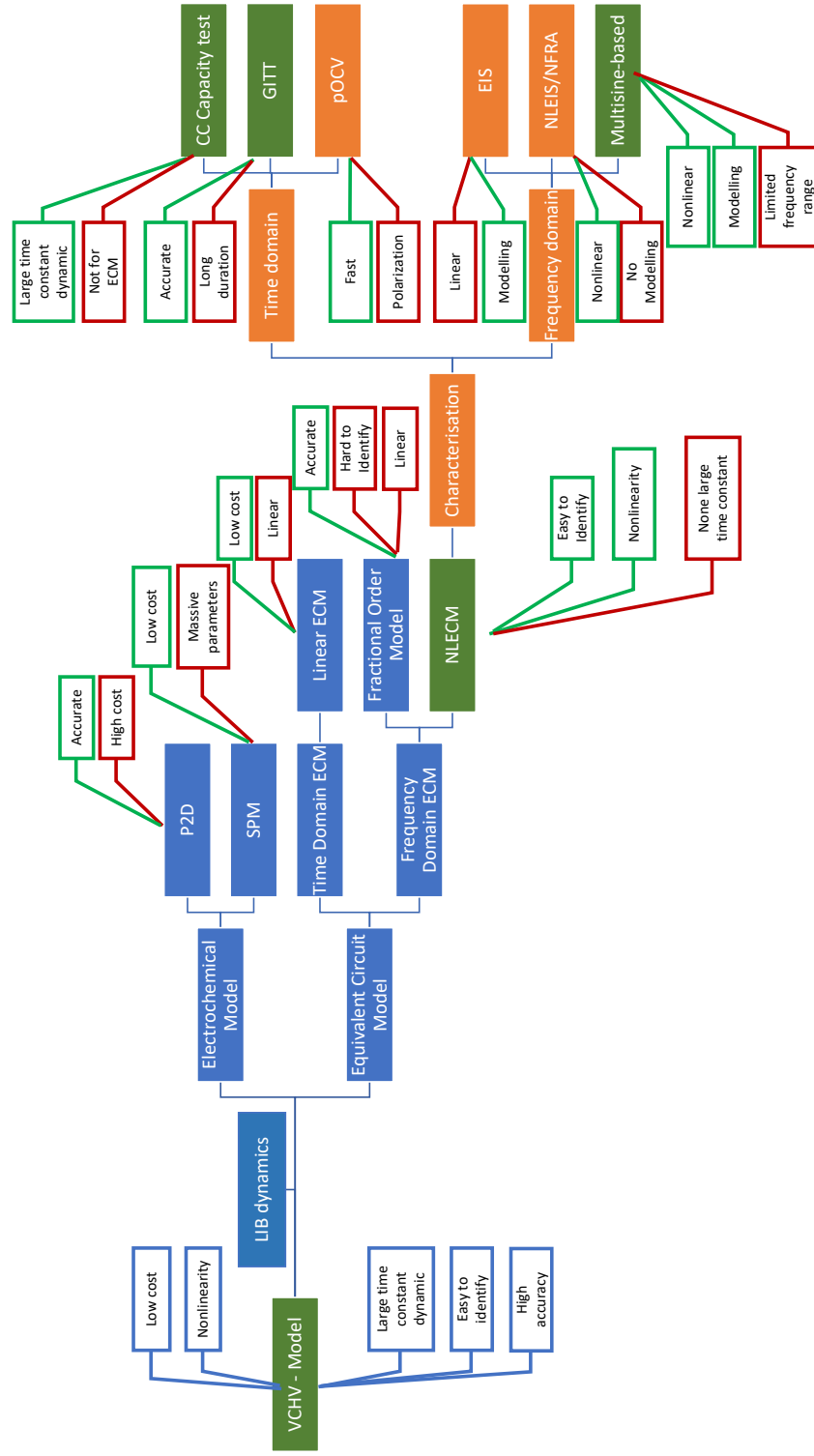
Figure 2.9: The structure of literature review in Chapter 2 and Chapter 3. Note that the green and red line callout indicate the advantage and disadvantage of the corresponding technique.

Chapter 3

A Review of Lithium-ion Battery Characterisation Tests

3.1 Introduction

Characterisation tests of lithium-ion batteries refer to the broad and general procedures by which the characteristics and properties of a LIB are probed and measured. In the field of battery technology, characterisation tests are employed to analysis the LIB performance as well as to identify and quantify battery degradation, such that novel electrode material, electrolyte and cell design can be benefited and further developed. In addition to the LIB properties and dynamic responses obtained by specific characterisation tests, researchers and engineers are able to design mathematical models and extract relevant parameters to accurately emulate the relationship of current and voltage [24]. Therefore, it is of great significance to develop efficient characterisation tests when developing battery models for BMS applications.

Current battery characterisation tests can be classified to invasive [167] and non-invasive [166] tests. Invasive tests are commonly performed on the torn-down battery cells for the analysis of material physical and chemical properties. For instance, scanning electron microscopy (SEM) is employed to monitor the morphology and uniformity of electrode micro-structures, which can be used to measure physical characteristics such as the particle size of the active materials, particle surface film formation, and mechanical changes within the electrode materials [167]. In terms of the chemical and material properties, X-ray diffraction (XRD) can be used to determine the elemental composition of active materials, as well as the crystal structure and theoretical density of the materials. As such, invasive tests enable

the investigation of LIBs and the parameterisation of electrochemical models, as detailed in Ref.[24]. However, these are destructive tests which result that the characterised tests cannot be repeatable on the same LIB for tracking the evolution of LIB characteristics. Additionally, the sophisticated preparation required, such as cell deconstruction, is challenging for battery engineers without the relevant training on handling hazardous materials. Thus, the use of invasive tests is out of the scope of this thesis.

In contrast to the invasive tests, non-invasive tests are devised based on the battery electrical input-output relationship, and non-destructively measuring of lithium-ion cell characteristics is accessible for both industrial engineers and academic researchers [166]. With these tests, comparing the LIB performance and tracking the evolution of performance over a LIB life are achievable, such that the degradation of LIBs can be quantified in terms of energy capacity fade and impedance rise [168]. Furthermore, concerning battery modelling, a range of tests can be employed to elucidate the linear and nonlinear dynamic processes of LIBs mentioned in Section 2.3. According to the specific analysis approach, the common characterisation tests related with battery modelling are classified into time domain and frequency domain tests, which will be explained in the following.

3.2 Time Domain Characterisation tests

By employing specialised experimental rigs, the designed current/voltage demand signals and battery voltage/current response are captured as digital data points with regard to time, which can be directly analysed in the time domain. Because no additional procedures, such as Fourier transforms, are required, this type of test is easy to perform and incorporate into real applications. From the viewpoint of battery models in the BMS, capacity is related to SOC that directly determines values of parameters in battery models, and OCV curve is the backbone of battery models, determining approximately 90% of the voltage profile. In this section, typical time domain characterisation tests for battery modelling are reviewed, such as constant current tests for obtaining cell capacity information and open circuit voltage (OCV) tests for OCV vs. SOC curves.

3.2.1 Constant current capacity tests

The definition of capacity is a measure of the total electric charge stored in a battery, which is determined by the amount of active material available in electrodes for intercalation [169]. As the capacity of the cell is directly related to the lithium

inventory and/or active material, the cell capacity is a convenient indicator for defining the state of health (SOH) of a lithium-ion battery and a fundamental parameter for battery modelling.

The common characterisation method to measure a LIB's capacity is to first charge the cell until fully charged state and then discharge the cell until the lower voltage limit, as shown in Figure 3.1. During charging the battery cell, the constant-current constant-voltage (CC-CV) method is commonly employed in practical tests. The method consists of a constant current charge until the cell voltage reaches a threshold value (typically the maximum specified voltage of 4.2V), followed by a constant voltage charge until a low current approaches the cut-off (typically less than 20% of the constant-current value) [170]. In the discharge step, the constant current (CC) profile is utilised to get the discharge curves, and by Coulomb counting, which integrate the current in A h with regard to time, is applied to obtain the capacity value of the battery cell. This measurement method is used for several advantages, such as the simplicity of interpreting the results, repeatability, and high accuracy of current measurement (over constant power profiles) [166].
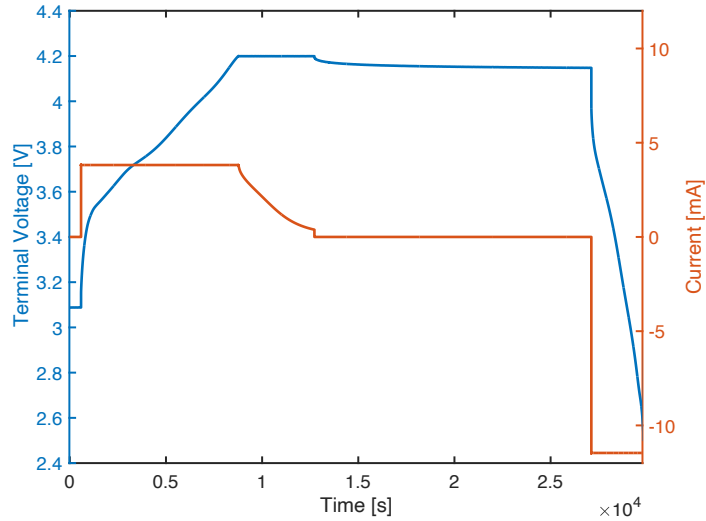
Figure 3.1: An example of CC-CV charge and CC discharge profile with 0.3C charge and 1C discharge rate. Note that 1 C-rate is 11.5 mA for the battery cell utilized in this test.

The measured capacity of a battery is dependent on the operational conditions in terms of the charge-discharge current rates and temperature. As mentioned in Section 2.3, the reaction in the electrodes is governed by the Butler-Volmer framework, the overpotential increases when a higher rate current is applied on a cell. Since the equilibrium potential decreases and the internal resistance of the

cell increases as SOC reduces, the overpotential at a low SOC gradually increases, resulting in a cell's voltage to reach the lower limit before all the stored charge is extracted. Thus, the accessible capacity of a cell reduces when a higher current rates is applied [171]. This phenomenon is frequently observed when a variety of constant current loads are used for discharging, which will be shown in Chapter 6. In addition, the reaction rate of lithium ion intercalation depends on temperature. As higher temperatures result in faster ion movement and an improvement of solid phase diffusion, the internal resistance and overpotential of a battery cell decrease. As such, more capacity can be extracted from a cell before the lower voltage limit is reached, and the opposite is true for lower temperatures. Since cell capacity is dependent on testing conditions, the test parameters must be kept consistent throughout the testing period.

Concerning battery modelling, the constant current load tests are commonly used to extract parameters by fitting discharge curve data for the electrochemical models [172]. While the large number of unknown parameters in electrochemical models may raise issues about the unique identifiability of model parameters, CC tests can efficiently achieve less than 2% relative error when validating the parameterised model under driving cycle loads [173]. In contrary, this method is seldom applied for parameterisation of equivalent circuit models which use the electrical elements, such as resistor, capacitors, and a voltage source, to form a circuit network to analogously describe a battery behaviour. As described in Chapter 2, these elements are influenced by the measurement timescale and is only suitable for emulating small time constant dynamics. However, the typical timescale of constant-current capacity tests is around 3600 s (for a 1C load case), which is too large for the combinations of resistors and capacitors within ECMs. The author believes that, the CC tests can be employed to parameterise ECMs which are coupled with proper large time constant dynamic representations, such that the scope of ECM type models can be extended for the applications with similar load profiles.

3.2.2   Open circuit voltage tests

Open circuit voltage (OCV) plays a crucial role in battery models, it is the battery thermodynamic equilibrium potential when not under a current load and is commonly in the form as a function of the SOC. It functions as an ideal yet changeable (e.g. with SOC) voltage source in the model to which over-potential is added. As mentioned in Section 2.3, the OCV vs. SOC curve of the full-cell is defined by the open circuit voltage of the positive electrode and the negative electrode. In the case of battery modelling the electrode OCV curves are integrated in both electrodes of

electrochemical models and the full-cell OCV curve is added in equivalent circuit models for full-cell level dynamics. Additionally, the path dependence of OCV is a distinctive characteristic of lithium-ion batteries which is termed as OCV hysteresis. From a thermodynamics perspective, the origins of OCV hysteresis can be clarified: first, hysteresis is primarily induced by the multi-particle effect [174], which consists of the non-monotonic potential of many single particles [175]. Second, during the process of lithium insertion/extraction, mechanical stress and microscopic deformation will cause the active electrode material to undergo a two-phase change. Lastly, the Shrink-core model [176] illustrates that phase juxtaposition at any SOC depends on the charging and discharging history of the battery material [177]. Due to the OCV hysteresis, the cell OCV during charge is different from discharge at the same SOC. The importance of hysteresis in model accuracy and SOC estimation has been shown in Ref. [178]. In the literature, the maximum hysteresis was found in a LFP cell (38 mV) and lowest in the LTO cell (16 mV) [179]. As a result, the hysteresis may be used in battery models. The level of OCV hysteresis, which presents along with OCV curves, can also be characterised by OCV tests. To measure OCV vs. SOC curves, the most common method is based on the galvanostatic intermittent titration technique (GITT) or pseudo-OCV test (pOCV) in the time domain. In what follows, the tests for measuring OCV and the associated hysteresis are discussed.

Galvanostatic intermittent titration technique (GITT)

Galvanostatic intermittent titration technique (GITT), popularised in the late 1970s, is a method that provides both kinetic and thermodynamics information of an electrochemical system under investigation [180, 181, 99]. GITT entails the application of a current transient to adjust the cell's SOC, followed by prolonged relaxation period during which no current flows through the cell. The relaxation period is defined as a specified duration or until an equilibrium condition is satisfied (i.e., when $dE/dt \sim 0$) [24]. This procedure is repeated until the desired threshold voltage has been reached. The voltages at the end of the relaxation periods are extracted and plotted to obtain the cell's OCV, denoted here as the GITT-OCV. The time and current of the discharge/charge step and the relaxation period are determined by the cell temperature and the desired accuracy [166]. Barai et al. proposed the optimal trade-off between accuracy and test duration is to measure OCV for every 1% SOC increment with a relaxation period of 4 h [179]. In this work, the 4 h is suggested as a sufficient period for LIBs to reach a pseudo-equilibrium state, at which point any further variations in voltage typically less than 1 mV cannot be successfully recorded

using standard cell characterisation equipment [179].

GITT has been widely applied in modelling, from extracting model parameters for electrochemical models to directly using the OCV data in equivalent circuit models. Birkl et al. developed an OCV estimation model, which can account for temperature dependence and voltage hysteresis, to be integrated in to a full cell model in a BMS [79]. The model is fitted to OCV data recorded from a NMC LIB at various temperature conditions and yields the accuracy of better than $5\,\mathrm{mV}$ [79]. However, the short relaxation periods (around $1\,\mathrm{h}$) in this work are relatively short and may result in a larger error of the model, as literature reported that a relaxation period of $1\,\mathrm{h}$ is acceptable for LFP batteries [182], but this is unlikely to be long enough for other LIB chemistries to reach electrochemical equilibrium [183, 179, 184]. Mao et al. performed an improved GITT test with varying pulse currents and relaxation periods to measure the OCV curve for developing a multi-particle electrochemical model. The simulation results demonstrate that the model is applicable in all scenarios and more precise for the case of smaller current pulse discharge rate with a longer relaxation period [185]. Delacourt et al. applied GITT to validate the single-particle model and study the diffusion coefficient of a $\mathrm{Li}_y\mathrm{FeSO}_4\mathrm{F}$ electrode [186]. Furthermore, GITT is employed to estimate Li^+ transport and diffusion parameters to support the modelling of a layer transition metal-oxide positive electrode in Ref. [187]. Chen et al. employed GITT to obtain the thermodynamic OCV curves for parameterisation of multi-scale lithium-ion battery models [24]. In Ref. [188], GITT is also applied to build models for the electrochemical kinetics of lithium ions.

GITT has been recognised as a powerful technique in the scientific community that can provide valuable information to significantly improve model performance. A drawback of this method is perhaps the lengthy testing duration which could be up to two weeks (i.e., 17 days for a GITT test in Ref. [179]). Thus further research is likely required to reduce the GITT test duration.

Pseudo-OCV test (pOCV)

Due to the lengthy duration (several weeks) of a GITT experiment, a pseudo-OCV (pOCV) is frequently obtained through low rate galvanostatic cycling, which lasts over a comparatively short period of testing time. Typically a C/25 or lower constant charge/discharge rate is applied in low-rate cycling tests, which is employed to minimise kinetic contributions, lower the electrode polarisation and reduce ohmic heat generation [166]. In the case of low-rate cycling tests, the ohmic loss contributing to cell voltage is very low [189], as well as no ohmic heat is assumed to

be generated. Furthermore, a single voltage profile can be generated by averaging the low rate charge and discharge voltage curves [190]. As the definition of an open circuit voltage is the voltage which is measured when there is no current, the averaged voltage profile obtained from low-rate cycling is more correctly named as pseudo-OCV. Figure 3.2 presents an example of the pOCV (red curve) of a LFP cell at $20°C$.
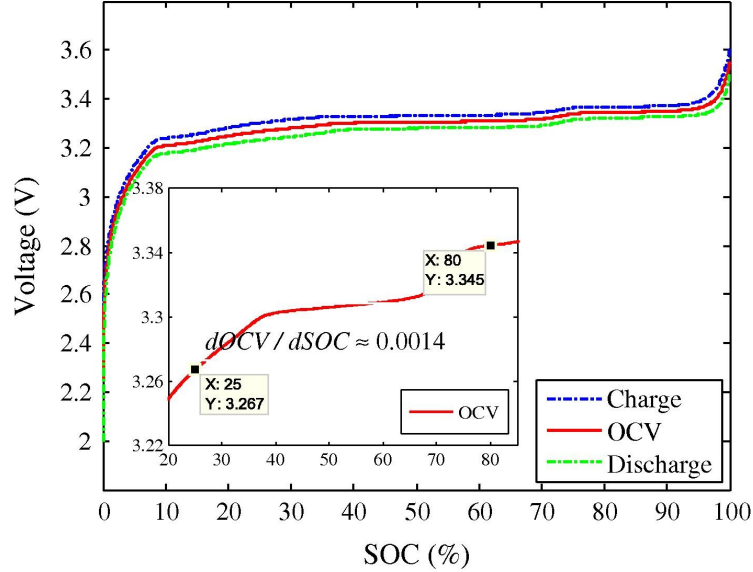
Figure 3.2: An example of the pOCV (the average OCV) of a LFP cell at $20°C$ [191] and a flat pOCV slope between 25% and 80% SOC is emphasised in the small plot.

Due to the simplicity and ease of implementation of low-rate cycling tests, the pOCV has been widely employed for battery modelling [190, 192]. Xing et al. generated pOCV profiles by averaging the C/20 charge and discharge voltage curves at different temperatures, and developed a temperature-related SOC estimation algorithm with this pOCV which yields high accuracy [191]. Less et al. experimentally determined the pOCV by charging and discharging the cell with a current rate of C/50 for the parameterisation of a micro-scale model [193]. Barai et al. suggested that the pOCV seems to be the best compromise between time and accuracy [166].

So far time domain characterisation tests for measuring OCV curves have been reviewed. According to the aforementioned literature, both GITT and pOCV tests are widely employed in the battery modelling studies. However, Chen et al. argued that the OCV obtained from GITT and pOCV are distinct [24]. With a slow galvanostatic cycle for recording pOCV, polarisation caused by the cell resistance will be observed, even at low C-rates. In addition, the phase transition voltage will be observed in the pOCV tests rather than the pure thermodynamic, such that

the cell hysteresis is convoluted with the cell overpotential and a larger hysteresis voltage is observed than in GITT tests [194]. Furthermore, in a recent research, the authors observed that the relaxation to OCV of a NMC811/graphite-SiO$_x$ cell at low SOC is not accurately described in the case of the pOCV profile, which is another drawback of the OCV from the pOCV tests [24]. Taking everything into account, the OCV curve from the GITT experiments is chosen for use in this thesis to improve model performance, despite that the barrier of the long test duration still exists.

3.3   Frequency Domain Characterisation tests

In recent years, frequency domain characterisation tests have also been developed with the increased LIB applicability. Contrary to the tests in the time domain, the measured LIB voltage data and designed excitation current data are transformed into the frequency domain for further analysis. As the characteristic frequency range of each electrochemical dynamic is inherently distinct, more insight about LIB dynamics, which are inaccessible in the time domain, can be analysed. In addition, from Electrochemical Impedance Spectroscopy (EIS) to Nonlinear Frequency Response Analysis (NFRA), researchers' attention are extended from linear dynamics to non-linear dynamics for comprehensive understanding and analysis of lithium ion batteries.

3.3.1   Internal impedance tests

Electrochemical impedance spectroscopy (EIS)

The Electrochemical Impedance Spectroscopy (EIS) is a widely applied frequency domain characterisation technique employed to investigate the fundamental electrochemical dynamics within a LIB. The working principle of EIS is show in Figure 3.3. The detailed guide and theory of this tests can be referred to [132]. With EIS, the linear response of a battery over a wide frequency range from mHz to MHz is investigated and analysed. A sinusoidal excitation current, that is, alternating current (AC), is excited by galvanostatic equipment and applied on the system and the alternating voltage response of the system is measured (galvanostatic measurement). Alternatively, the system can be excited with a sinusoidal voltage and the sinusoidal current response measured (potentiostatic measurement). In an ideal case, both scenarios would provide identical results. Using a Fast Fourier Transformation (FFT), the excitation and response signal are transformed to the frequency domain
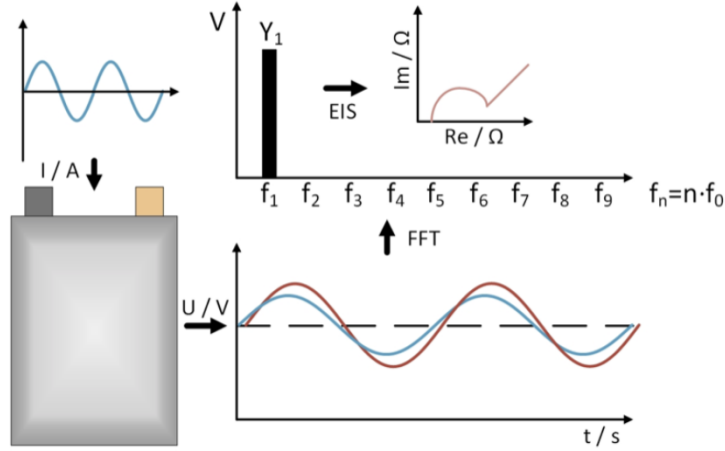
Figure 3.3: Working principle of Electrochemical Impedance Spectroscopy (EIS) [74].

from the time domain. Prior to further analysis, the quality of EIS results has to be examined. Referring to [195], if the prerequisites a) causality, b) time-invariance, c) stability and d) linearity, are fulfilled, then the results of EIS is considered valid. Also the Kramers-Kronig relation can be applied to examine the validity of EIS [196]. However, as shown in Figure 3.4, a lithium-ion battery, as an electrochemical system, shows a pseudo-linear current-voltage relationship only at specific situations, e.g. at a steady-state operation point using an input current with a small amplitude. Thus, in the case of galvanostatic measurements, an excitation current I_{AC} with a small amplitude of approximately C/20 is applied for valid EIS tests [197].

In a linear or pseudo-linear system, the voltage response to a sinusoidal current is sinusoidal at the same frequency (ω) with a scaled amplitude but the phase (φ) is shifted, as shown in Figure 3.3. The small amplitude sinusoidal excitation current can written in the frequency domain as following:

$$I_{AC}(\omega) = I_0(\omega)\exp(j\varphi_1(\omega)) \tag{3.1}$$

where I_0 is the amplitude of the current. The angular frequency ω is defined as:

$$\omega = 2\pi f \tag{3.2}$$

The sinusoidal voltage response $V(\omega)$ of the system with a phase shift of Φ when the angular frequency is ω is given as:

50
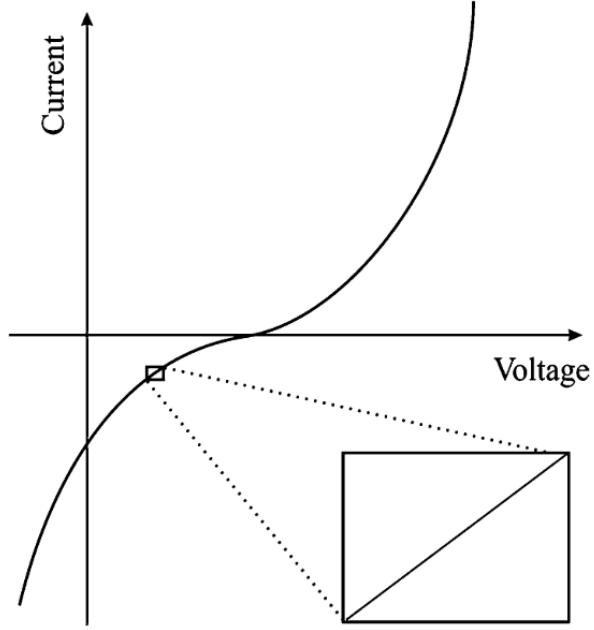
Figure 3.4: Example of a current-voltage relation for a pseudo-linear LIB [198].

$$V(\omega) = V_0(\omega) \cdot \exp(j \cdot \varphi_2(\omega)) \tag{3.3}$$

$$\varphi_2 = \varphi_1 + \Phi \tag{3.4}$$

According to the definition of impedance, the complex impedance $Z(\omega)$ of a LIB is calculated in analogy to Ohm's law as:

$$Z(\omega) = \frac{V(\omega)}{I_{\mathrm{AC}}(\omega)} = \frac{V_0(\omega) \cdot \exp(j \cdot \varphi_2(\omega))}{I_0(\omega) \cdot \exp(j \cdot \varphi_1(\omega))} = |Z_0| \cdot \exp(j \cdot \Phi(\omega)) = |Z_0|(\cos\Phi + j \cdot \sin\Phi) \tag{3.5}$$

Thus, the impedance of a LIB can be plotted as a Nyquist-Plot with the real $Re(Z(\omega))$ part and the imaginary $Im(Z(\omega))$ part, as shown in the following equations:

$$Re\{Z(\omega)\} = |Z_0| \cdot \cos\Phi \tag{3.6}$$

$$Im\{Z(\omega)\} = |Z_0| \cdot \sin\Phi \tag{3.7}$$
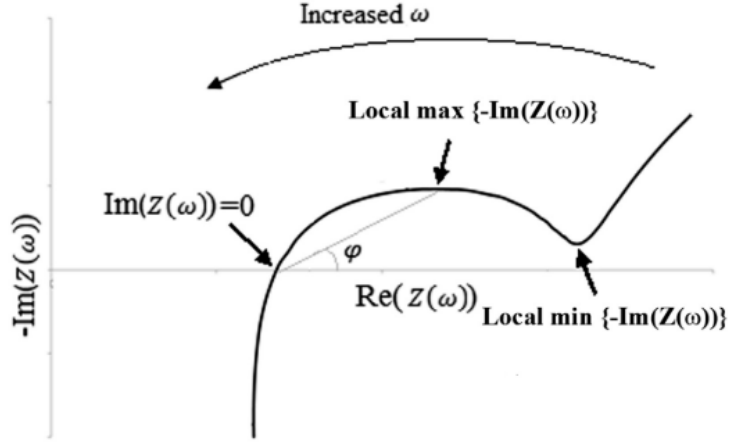
Figure 3.5: A typical Nyquist plot representing the impedance spectrum of a LIB. Indicated are a number of characteristic points that define the dynamic behaviour of a LIB [166].

A typical impedance Nyquist plot of a LIB is shown in Figure 3.5 which plots the real part on the x-axis against and the negative imaginary part on the y-axis of the Nyquist presentation. LIB dynamic processes can be separated and attributed to particular characteristic frequency ranges [199]. In Figure 3.5, some widely used mark points are plotted in the impedance spectrum to characterise a LIB. The point $Im(Z(\omega)) = 0$ is the junction between a capacitive behaviour and an inductive behaviour and only an almost pure ohmic resistance (R_0) is observed at this point. In the frequency range higher than this point, termed as high frequency range, the inductive reactance of the battery caused by the cable connections and the current collector can be observed [200]. The semi-circle between $Im(Z(\omega)) = 0$ and local min $-Im(Z(\omega))$ corresponds to the charge-transfer process at the solid electrolyte interfaces which typically shows capacitive and resistive behaviour, and this frequency range is termed as the medium characteristic frequency range. The frequency at local maximum $-Im(Z(\omega))$ is defined as the $1/RC$ time constant, which indicates the voltage response speed rate of the LIB corresponding to current changes [200]. The characteristic frequency range lower than the frequency at local min $-Im(Z(\omega))$ corresponds to diffusion processes in the active material of the electrodes. In the literature, dynamic characterisation with EIS is widely applied for several critical topics of LIBs, such as state-of-charge (SOC) estimation, temperature estimation, ageing determination, and battery modelling [166]. [201] reported that the low frequency data from an EIS test is able to be used to predict the SOC of a LIB. Similarly, the EIS is employed as a diagnostic tool to estimate the LIB

SOC [202]. Furthermore, the temperature of a LIB can be associated with the frequency of the point which is the intersection of the Nyquist plot with the real axis [203]. The results show that the frequency changes corresponding to the temperature variation. A more recent study of EIS has been extended to internal temperature on-line estimation [204]. In addition, as impedance of a LIB changes with ageing degradation, researchers apply EIS to quantify LIBs ageing. For example, Waag et al. reported that the SEI growth is one of the ageing mechanisms from EIS results [200]. Pastor et al. employed EIS along with other characterisation tests to quantify the degradation modes (DMs) in LIBs, such as conductivity loss (CL), loss of active material (LAM) and loss of lithium inventory (LLI) [197]. From a perspective of battery modelling, the general modelling methodology with EIS is to fit a fractional-order model (FOM) to EIS Nyquist results to extract the ECM parameters of a LIB [139, 43]. More details about FOMs have been introduced in Chapter 2.

Although EIS has been widely employed in the battery field, the preconditions of valid EIS, such as linearity of the system, limits analysis to the linear frequency response and therefore a LIB has to be analysed under the assumption of linearisation. Such that nonlinear LIB dynamics introduced in Section 2.3, such as the charge-transfer reactions at the electrodes representing by Butler-Volmer kinetics, cannot be sufficiently excited and captured under a small amplitude sinusoidal excitation current. As a result, the valuable information about battery nonlinearity is unavailable and generally neglected in regard to characterisation and modelling. To fulfil this gap, in recent years, nonlinear characterisation tests have been developed and applied on lithium-ion batteries, which will be explained in the next section.

3.3.2   Non-linear characterisation tests

To gain nonlinear insight into lithium-ion battery dynamics, an extension to EIS is to apply moderate or high amplitude excitation to drive the battery into a weakly or strong nonlinear currant-voltage relation that can be mathematically considered as a nonlinear transfer function. Figure 3.6 illustrates how a general nonlinear transfer function responds when excited by a sinusoidal excitation signal. Due to the nonlinear transfer function, when an excitation signal of symmetrical amplitude to each side is applied, the output response in the time domain exhibits different positive and negative amplitudes, but retains the same fundamental frequency as the excitation signal. The output response to a single-frequency sinusoidal excitation

current generates higher harmonics[*] of the fundamental frequency in the output Fourier spectrum.
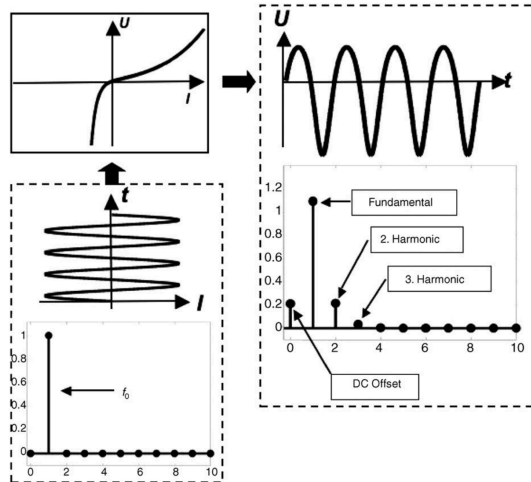
Figure 3.6: The origin of harmonic oscillations for a nonlinear transfer function with a sinusoidal excitation signal [206].

Before the nonlinear analysis idea developed in the battery field, harmonics in the voltage response were treated as by-products which lead to errors in impedance measurement and even to invalid EIS results [207, 206]. However, in recent year, researchers have noticed that, with the right framework for interpretation, harmonics can provide insight about the system's internal state [208].

Total harmonic distortion (THD) analysis

Early study on characterising the nonlinearity of electrochemical systems utilising alternating current concentrated on detecting variations in the impedance response as the amplitude of the perturbation increases [207, 209, 210, 211, 212, 213, 214, 215]. Particular topics are to determine corrosion current and charge-transfer coefficients by quantifying the distortion of the fundamental frequency impedance spectrum [211, 212]. More recently, Total Harmonic Distortion (THD) analysis, which is commonly used in acoustics research for noise detection [216], has been utilised for characterising electrochemical systems such as fuel cells [217, 218, 219]. Figure 3.7 shows an example of the voltage response of a direct methanol fuel cell to an input current of sinusoidal excitation of large amplitudes. The THD of fuel cell systems

---

[*]In general, any periodic signal can be represented by a superposition of several sinusoidal oscillations with multiples of the excitation frequency, and these so-called 'harmonics' can be determined using Fourier transformation [205]

can be defined as the ratio of the sum of the amplitude of the voltage response of all higher harmonic frequencies ($k \geq 2$) to that of the fundamental frequency (k=1):

$$\mathrm{THD} = \frac{\sqrt{\sum_{k=2}^{\infty} |Y_k|^2}}{Y_1} \tag{3.8}$$

According to variation of THD value through the frequency range, the specific electrochemical processes can be identified. Mao et al. reported that the THD has better performance than EIS in identification of methanol oxidation kinetics and methanol concentration monitoring for direct methanol fuel cells [217, 218]. The THD was applied on proton exchange membrane fuel cells to demonstrate the difference between oxygen reduction reaction mechanisms and to identify the closer one to the reality [219]. However, at that time, the analysis of nonlinear frequency response behaviour by THD spectroscopy was limited in the fuel cell area.
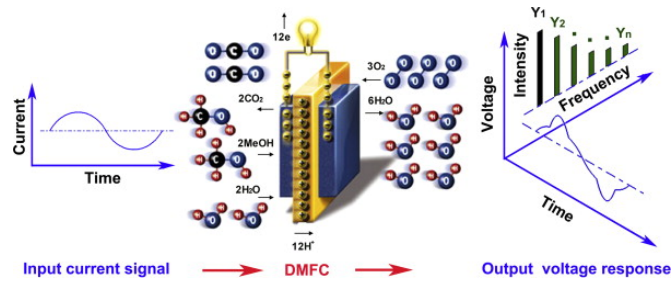
Figure 3.7: Schematic diagram for the voltage response of a direct methanol fuel cell to a sinusoidal input of current in both time domain and frequency domain [218].

At the present time, two state-of-the-art nonlinear characterisation tests for lithium-ion batteries are proposed according to the amplitude selection of the perturbation current, such as Nonlinear Electrochemical Impedance Spectroscopy (NLEIS) with a moderate-amplitude sinusoidal current and Nonlinear Frequency Response Analysis (NFRA) with a large-amplitude sinusoidal current.

Nonlinear electrochemical impedance spectroscopy (NLEIS)

Murbach et al. proposed an analytic-numerical approach with the pseudo-two-dimensional model to evaluate EIS and NLEIS impedance spectra [220]. Murbach et al. performs a full-frequency NLEIS test for LIBs using commercially available cells, and the results show that the second harmonics NLEIS spectra is sensitive to degradation in charge transfer symmetry whereas linear EIS is mainly sensitive

to changes in charge transfer rates [221]. To integrate physics-based analysis into NLEIS analysis, an open-software platform, named Impedance Analyzer, is developed in [222].

Nonlinear frequency response analysis (NFRA)

Almost at the same time, nonlinear frequency response analysis (NFRA), a large-amplitude perturbation method, has been employed on lithium-ion batteries for higher harmonics characterisation. Figure 3.8 illustrates the working principle of NFRA. Similar to NLEIS, NFRA investigates higher harmonics, such as Y_2, Y_3, ..., Y_n, to characterise a battery and analyse nonlinear processes. Harting et al. applied NFRA on lithium-ion batteries and correlated NFR spectra with EIS impedance spectra to investigate contributions of nonlinear processes [223]. Then NFRA is applied on both fresh and aged cells to analyse the harmonic spectra for lithium plating identification and state-of-health (SOH) estimation [224, 225, 226]. To verify the experimental results obtained, NFRA was applied with the pseudo-two-dimensional model and single particle model for frequency response analysis [73, 227]. Wolff et al. presented a model-based analysis of the NFRA technique to understand the source of higher harmonics and the impact of parameter variations on battery non-linearities. The simulation results demonstrate that, in a whole battery model, the nonlinearities generated by charge transfer reactions and solid diffusion processes are superimposed in corresponding characteristic frequency ranges [228].
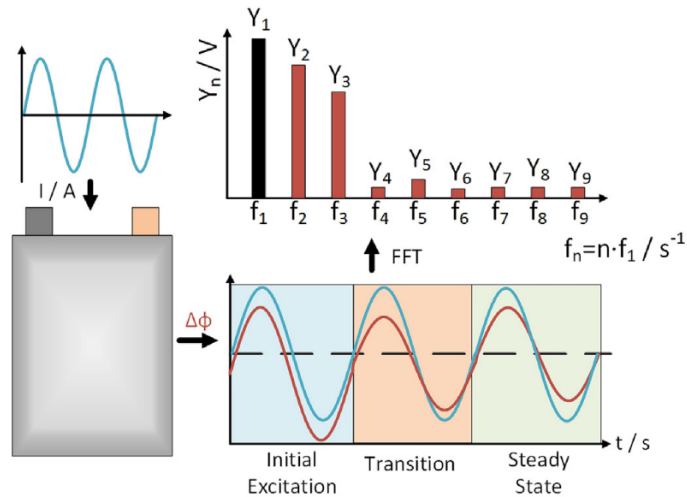
Figure 3.8: Working principle of Nonlinear Frequency Response Analysis (NFRA) [227].

Taken together, both NLEIS and NFRA show promising performance in

providing comprehensive analysis of battery nonlinear processes and can be considered as important additional dynamic analysis methods for lithium-ion batteries in terms of state estimation and ageing determination. However, the measurement of the nonlinear response over the full frequency spectrum results in extremely lengthy experiment durations, up to a few hours, which limits these methods to the laboratory environment. Furthermore, while these nonlinear characterisation tests have demonstrated their capacity to physical parameter estimation and ageing mechanism identification, however, there is no evidence from the existing literature that the methods can be used for battery system identification. Given that the required battery model for this thesis necessitates the identification of both a dominant linear response and battery nonlinearity, but the NLEIS and NFRA methods are nonlinearity-restricted, these methods are not utilised in this thesis.

Multisine-based nonlinear characterisation tests

From the perspective of signal design, a successive single sweep sinusoidal signal over a broad frequency range is applied in the aforementioned nonlinear characterisation tests, which leads to extremely time-consuming testing for low frequency experiments. Recently, inspired by frequency domain system identification theory, several preliminary studies have been proposed to capture battery linear and nonlinear dynamics with various multisine excitation signals, which can significantly shorten testing duration and provide the potential for on-board applications. The fundamentals of the multisine-based nonlinear characterisation technique are briefly explained below.

To undertake the multisine-based nonlinear characterisation technique, the multisine excitation signal is required to be designed as the first step. As a periodic broadband signal (a signal that repeats), the multisine signal is designed by summing sinusoids, which provides flexibility in the design of its amplitude spectrum and harmonic content [229]. A general multisine excitation signal can be expressed as Equation (3.9)

$$u(n) = \sum_{k=1}^{K} A_k \sin\left(2\pi n k f_s / N + \varphi_k\right) \qquad n = 0, ..., N-1, \qquad (3.9)$$

where N is the number of samples per period, K denotes the highest harmonic number of the signal, f_s is the sampling frequency, A_k is the amplitude and φ_k is the phase of the kth harmonic. The N of a multisine can be flexibly determined and the frequency resolution is set to $f_0 = f_s/N$ Hz. From Shannon sampling theorem, the highest possible harmonic K has to be less than or equal to $N/2$.

Thus, the highest possible frequency of the multisine signal can be obtained as the product $f_0 \times K$, and should span the characteristic frequency range of the battery for characterisation. To ensure a steady-state behaviour (equilibrium state in the case of batteries) during the characterisation duration, the DC frequency, which is $n = 0$ harmonic, is suppressed for obtaining a zero-mean current signal.

When a multisine signal is applied to a nonlinear system (for e.g. a battery), some energy injected at the excited harmonics in the excitation signal will be transferred and observed at the other harmonic positions in the output spectrum, which indicates the system nonlinearity [230]. To characterise the nonlinearity of a battery, the harmonic content f_k, amplitude spectrum A_k, and harmonic phases φ_k are the key factors to be determined in the signal design procedure. For the harmonic content f_k, the excited and suppressed harmonics of a multisine signal can be selected within the bandwidth considered according to specific objectives. The set of excited harmonics is denoted as H_{exc} and the sets of suppressed harmonics as $H_{\text{supp,odd}}$ and $H_{\text{supp,even}}$ with respect to the odd and even harmonics. The motivation of suppressing harmonics is that the suppressed odd and even harmonics can be utilised for detecting the odd and the even order nonlinearities, respectively [231].

Theoretically the amplitude A_k can be flexibly determined to drive a system into a nonlinear state. Various amplitudes lead to different level of system nonlinearity [47]. Nevertheless, for simplicity, a flat spectrum, which sets the amplitude of all the excited harmonics to unity, is generally applied in the signal design. Then the root-mean square (RMS) value of the designed multisine signal can be scaled in the time domain for a specific amplitude.

The phases of the excited harmonics φ_k can be set to obtain different amplitude distributions to excite the dynamics around a certain operating point [232, 233]. Depending on the technical constraints imposed by the tester's current and voltage limits, as well as safety concerns (cell temperature, over and under voltage), large peaks in a designed signal should be minimised, and thus the multisine may require to be optimised by minimising a phase-related criterion known as the crest factor (CF) [234].

An example of a random-phase multisine signal in both time domain and frequency domain is shown in Figure 3.9. The time domain multisine current signal is applied to a battery at preset conditions (e.g., temperature and SOC), and the voltage response is recorded for analysis. The input current $i^{[p]}(t)$ and output voltage $v^{[p]}(t)$ data are then recorded in time domain as follow:
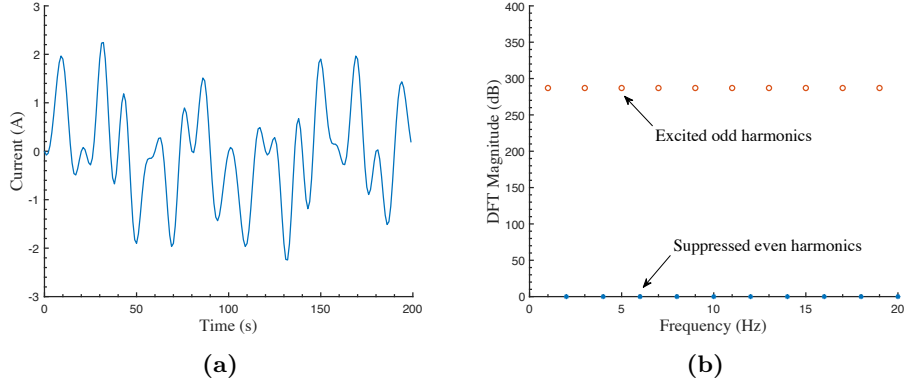
Figure 3.9: An example of a random-phase multisine, with $f_\text{s} = 200$, $N = 200$, $A_\text{k} = 1$. (a) The multisine signal in the time domain, (b) DFT magnitude of multisine showing excited and suppressed harmonics. H_exc: all odd harmonics up to 20 Hz.

$$i^{[p]}(n), \quad v^{[p]}(n) \qquad p = 1, 2, ..., P \quad n = 0, ..., N - 1, \tag{3.10}$$

where p indicates the pth period of the input signal $i(n)$ and of the output voltage response $v(n)$ and P denotes the total number of periods at each condition. By Discrete Fourier Transform (DFT), the discrete time domain data can be transformed to the frequency domain, as input and output spectra:

$$I^{[p]}(k) = \sum_{n=0}^{N-1} i^{[p]}(n)e^{-2j\pi kn/N}, \quad V^{[p]}(k) = \sum_{n=0}^{N-1} v^{[p]}(n)e^{-2j\pi kn/N}, \quad k = 0, ..., N - 1, \tag{3.11}$$

where $I^{[p]}(k)$, $V^{[p]}(k)$ in Equation (3.11) denote the spectrum of $i^{[p]}(n)$, $v^{[p]}(n)$ at the kth harmonic.

In the frequency domain, the spectrum of measured voltage output data can be separated out into the excited (H_exc) and suppressed harmonic sets ($H_\text{supp,odd}$ and $H_\text{supp,even}$) as:

$$V^{[p]}(k) = V_0^{[p]}(k) + V_\text{S}^{[p]}(k) + N_V^{[p]}(k) \qquad k \in H_\text{exc}, \tag{3.12a}$$

$$V^{[p]}(k) = V_\text{S}^{[p]}(k) + N_V^{[p]}(k) \qquad k \in H_\text{supp,odd} \cup H_\text{supp,even}, \tag{3.12b}$$

where $V_0^{[p]}(k)$ is the linear voltage response of a battery that only appears on the excited harmonics, $V_\text{S}^{[p]}(k)$ indicates the battery nonlinearity, and $N_V^{[p]}(k)$ indicates the noise distortion from practical environment and measurement hardware in the voltage output spectrum [233].

Based on the voltage output spectra $V^{[p]}(k)$, the mean spectrum $\bar{V}(k)$ can be estimated by averaging over the P periods to reduce the effect of noise ($N_V^{[p]}(k)$), as shown in Equation (3.13a). Note that the P here indicates the measured periods when the battery reaches a steady-state. Further, according to Equation (3.13b), the corresponding variance $\hat{\sigma}^2_{\bar{V}_{(k)}}$, which suggests the uncertainty of $\bar{V}_{(k)}$, can be calculated. Statistically, the uncertainty is related to the noise of environment and hardware equipment, and the smaller variances indicates the higher reliability of characterisation results. It is worth mentioning that all calculated results are shown in decibels by directly using the MATLAB command 'dB'.

$$\bar{V}(k) = \frac{1}{P} \sum_{p=1}^{P} V^{[p]}(k) \tag{3.13a}$$

$$\hat{\sigma}^2_{\bar{V},k}(k) = \sum_{p=1}^{P} \frac{\left| V^{[p]}(k) - \bar{V}(k) \right|^2}{P(P-1)} \tag{3.13b}$$

In theory, the output response of a linear system will retain the same harmonics as the input signal, and only the different amplitude and phase will vary. However, for a non-linear system, intermodulation of the input signal leads to additional harmonic components at non-excited harmonic positions in the output spectrum. Thus, odd and even order nonlinearities $\bar{V}(k)$ can be observed and quantified according to the energy shown at the suppressed harmonics $k \in H_{\text{supp,odd}}$ and $k \in H_{\text{supp,even}}$ in the voltage response spectrum.

There are only few publications in the literature that discuss capturing battery dynamics using multisine signals. Zappen et al. designed and performed multisine excitation signals as a fast characterisation technique to gather impedance information [234]. However, the research only focuses on the linear dynamics of a battery. Widanage et al. designed pulse-multisine signals as the identification excitation to characterise the battery linear and nonlinear dynamic behaviour for battery modelling [45]. The concept of the pulse-multisine is to excite the battery over a higher frequency, which combining the advantage that the signal has sufficient power. Unfortunately, the battery system nonlinearity was not explicitly analysed in terms of odd and even non-linear distortions in the study. In addition, the characteristic frequency range was selected to be less than $1\,\text{Hz}$, as such the higher frequency range electrochemical processes were ignored. Relan et al. employed a random phase multisine to characterise the battery electrical response for developing a data-driven polynomial nonlinear state-space battery model [235], and Firouz et al. applied random phase multisine signals with multiple realisations which allows

separating the nonlinear distortion variance and noise variance from the linear part of battery [47]. Multisine excitation signals require a short testing time in comparison with conventional single sine sweep measurements. However, multiple signal realisations for characterising random phase nonlinear distortion will prolong the testing duration and increase computation of signal design procedure. Up to now, the multisine signal is rarely employed to capture battery dynamics as a specialised nonlinear characterisation method.

Compared with single-sine sweep nonlinear characterisation tests, the multisine-based method have shown great potential and superiority. Firstly, the testing duration is significantly reduced from few hours to hundreds seconds with same frequency range [47]. Furthermore, the odd and even order nonlinearities can be characterised by the multisine-based method. According to findings of the NFRA, the nonlinearity can provide detailed insight into the ageing status and degradation mechanism [225, 224]. Given these two features, it is thought that the multisine-based method has the potential to be used as on-board characterisation tests in the future. In addition, a significant advantage of the multisine-based method is the simultaneous capture of linear and nonlinear dynamics, which is difficult to achieve with other standard nonlinear characterisation tests. For example, the NFRA is frequently combined with the EIS test to obtain a comprehensive description of the dynamics [223]. Eventually, as mentioned previously, the origin of multisine signals is as the perturbation signal which serves for nonlinear system identification [233]. Thus, on the basis of results from the multisine-based method, the battery models, which reflect the linear and nonlinear dynamics of the battery, can be identified in a frequency domain identification approach [152]. Taking all of these factors into account, the multisine-based nonlinear characterisation technique is determined to be employed in this thesis for investigating battery nonlinear dynamics as well as for developing an advanced battery model.

3.4   Summary

In this chapter, a range of characterisation tests which are commonly used for battery modelling and nonlinearity analysis have been introduced. The spectrum of these non-destructive methods is provided and tabulated in Table 3.1. Note that, since the research objective of establishing the NLECM-diff model has been determined in previous chapters, only the characterisation tests that can provide relevant information are in the scope of this chapter. As described in Chapter 2, the NLECM-diff model is composed of four components: a diffusion dynamic block, an OCV curve, an

impedance linear block, and a nonlinearity block; thus, the corresponding characterisation tests for these blocks are determined. Firstly, the constant current capacity test is believed as an ideal method to extract parameters linked to diffusion processes, due to the ability to capture large time constant dynamics. In addition, the GITT is determined to be applied in this work for obtaining the OCV vs. SOC curve, as the OCV without polarisation is unavailable by the pseudo-OCV test. Regarding the linear and nonlinear blocks, it is determined that the multisine-based test is employed in this thesis to collect cell impedance and nonlinearity, and a frequency domain system identification approach can be used to establish the mathematical models. Details of battery modelling will be demonstrated in Chapter 6.

Table 3.1
Summary of characterisation test methods, data provided, test duration, and applicability of methods in the literature.*

Test method	Data extracted	Test duration (h)	Modelling application	Nonlinearity analysis
CC Capacity test	Cell capacity	3-20	✓	Not considered
GITT	Actual OCV vs. SOC	>100	✓	Not considered
Pseudo-OCV test	pOCV vs. SOC	25-100	✓	Not considered
EIS	Cell Impedance	2-4	✓	×
THD	Nonlinear distortion	2-4	×	✓
NLEIS	Cell nonlinearity	2-4	×	✓
NFRA	Cell nonlinearity	2-4	×	✓
Multisine test	Cell impedance and nonlinearity	<1	✓	✓

*Note that only the characterisation tests required for establishing the NLECM-diff model described in Chapter 1 are reviewed.

Taking advantage of the ability to capture battery nonlinearity, the multisine tests can also be applied as a specialised nonlinear characterisation method. According to the existing literature on NFRA, battery nonlinearity has demonstrated promise for estimating SOH and identifying ageing mechanisms, which has significant implications for BMS design. Unfortunately, the protracted measuring time of single-sine sweep methods is an obstacle to practical EV applications. In contrary, the testing duration of multisine-based tests is significantly shorter than that of the single-sine sweep methods with same frequency range, which is preferred for on-board applications. However, there is no systematic investigation of battery nonlinearity captured by the multisine-based method in the existing literature. Thus, there is a knowledge gap in insufficient understanding of battery nonlinearities in terms of the source of the nonlinearity and the major electrochemical process that contributes to the nonlinearity.

In the next chapters, an enhanced random phase odd multisine nonlinear characterisation method that utilise a single realisation is devised to capture battery

nonlinearity while simultaneously obtaining the information required for battery modelling. Furthermore, a model-based analysis and an experimental investigation are performed to further understand the battery nonlinearity in Chapter 4 and 5.

Chapter 4

A Model-based Investigation of Lithium-ion Battery Nonlinearity[†]

4.1 Introduction

To understand the origins of lithium-ion battery nonlinearity, for further practical applications including modelling, an efficient nonlinear characterisation method is required. As detailed in Section 3.3.2 existing approaches are either hindered by the lengthy experimental process or are not employed as a particular characterisation technique to systemically investigate the nonlinearity [47, 223]. Thus, these methods need to be improved further for nonlinearity analysis to meet "**Research Objective (2):** Understand the electrochemical process contributing to nonlinearity." The most exciting aspect of multisine signals is the flexibility that allows in choosing the harmonics, phases, amplitudes and frequency range [233]. As such, the author asserts that, by employing a multisine signal with specially modulated harmonics, it may be feasible to characterise the nonlinearity of a battery cell while reducing the test duration. As a part of this study, a novel multisine signal is designed to partially fulfil "**Research Objective (1):** Design a characterisation method capable of capturing battery nonlinearity."

By applying the proposed multisine-based method, nonlinearity of lithium-ion batteries can be characterised for subsequent analysis. Prior to this work, analysis of battery nonlinearity by multisine-based methods has not been theoretically analysed. To fulfil this knowledge gap, a model-based investigation, conducted on

---

[†]Parts of this chapter have been published in [1]

a comprehensive electrochemical mathematical model, is performed in this chapter, as the physical parameters that directly attribute to corresponding processes can be identified and studied. Note that, in order to avoid the effect from environment, temperature dependency and heat generation are disregarded in this work. The most recognised electrochemical model is the Doyle Fuller Newman (DFN) model [36], despite the DFN model's limitations to fully retrieve all phenomena, as described in Chapter 2. Its framework is extensively used in the battery field and has remained mostly unchanged over the last two decades. For example, charge-transfer coefficients in the Butler-Volmer equation can be related to the charge-transfer kinetics on the electrode and electrolyte interface, and diffusion coefficients in the equation of Fick's second law is linked to diffusion processes in the electrode active material [236]. By tuning the specific parameters of interests, variations in observed nonlinearity (via the multisine characterisation approach) can be linked to the effect of the underlying processes. In addition, refer to [73], Nonlinear Frequency Response Analysis (NFRA) is performed on the DFN model to identify which processes can be observed with NFRA and how the processes affect individual higher harmonics and their sum. Measurements of three different cell types, a commercial 18650 cell with a capacity of $800\,\mathrm{mA\,h}$ and two hand-made pouch cells from the Battery LabFactory Braunschweig with a capacity of around $35\,\mathrm{mA\,h}$ (Lithium Manganese Oxide ($LiMn_2O_4$) for pouch cell A and Nickel Manganese Cobalt ($Ni_{1/3}Mn_{1/3}Co_{1/3}$) for pouch cell B), show that characteristic frequency ranges can be detected for all cells, though the cell spectra strongly diverge. Amplitude and the progression of individual higher harmonics strongly differs between cells type and chemistry. Wolff et al. concluded that the model-based analysis is indeed essential to get a deeper understanding of the nonlinear response and the underlying processes and as such to interpret experimental studies. Furthermore, the linear and nonlinear physics of the DFN model is employed to evaluate the fundamental and higher harmonic response of a $LiCoO_2|LiC_6$ cell subject to NLEIS method [220]. It is therefore believed that the influence of each electrochemical process to battery nonlinearity can be determined and understood correspondingly by using the DFN model.

To evaluate the influence of parameters on a model output, sensitivity analysis (SA) methods can be used. The SA approach quantifies the uncertainty in a mathematical model's output, which is attributed to the uncertainty of model input factors (MIFs), e.g. assumptions, errors in the data, resolution, and parameters [237]. To date, several studies have focused on the SA of various battery models in the time domain to investigate how sensitive the model output voltage is to changes in its parameters. Lai et al. investigated the sensitivities of a 2RC (resistor-

capacitor) branch model with one-state hysteresis (2RCH) to determine the crucial parameters to reduce the cost of SOC estimation and retain the results accuracy [238]. Deng et al. analysed the parameter sensitivity of a typical physics-based model for an all-solid-state battery model and proposed a joint estimation method of model parameters and states [239]. The results show that the maximum and minimum lithium-ion concentrations have the greatest influence on the model output. Grandjean et al. identified that the most sensitive parameters of a single particle model with electrolyte (SPMe) using the Morris screening method are the anode diffusion coefficient and cathode diffusion coefficient [240]. Most of the existing SA studies focus on the effect of parameters on the voltage output of battery models, however, very few researchers investigated the battery nonlinear response by sensitivity analysis methods. The effect of parameters on nonlinear voltage response of the P2D model and simple fundamental models are respectively analysed by using NFRA method [73, 228]. In these two studies, only one parameter was examined while keeping the other parameters at their nominal values at a single time, which is termed as the local sensitivity analysis method. However, it is unable to detect the presence of interactions between parameters of interests [241]. Compared to the local SA method, global SA methods consider the sensitivity across the whole MIF space and study all the possible parameter combinations to evaluate the effect from parameters interactions [238]. Therefore, global SA methods are universally recognised as more comprehensive methods for sensitivity analysis. It's worth emphasising that, in this chapter, the MIFs are defined as the parameters with physical significance, while the battery nonlinearity (in the frequency domain, which is elaborated in the subsequent sections) is specified as the model output. According to the SA results, the most sensitive parameter contributing to battery nonlinearity can be determined, and thus the electrochemical process associated with this parameter is recognised as having the greatest influence towards the battery nonlinear response. As a result, the most sensitive parameter can be estimated by fitting data captured by the multisine-based nonlinear characterisation when applied to a battery (rather than a mathematical model), which can save extra cost of experimental approaches for parameterisation.

The remainder of this chapter is structured as follows: The methodology to understand battery nonlinearity with a model-based approach is detailed in Section 4.2. Section 4.3 presents the sensitivity analysis results to attribute the effect of electrochemical processes to the nonlinear response. Conclusions of this research are given in Section 4.4.

4.2 Methodology

This section presents the methodology for determining the sensitivity of the DFN model parameters to battery nonlinearity in the frequency domain to investigate the electrochemical processes that contribute to voltage dynamic response. Firstly, the design of random phase odd multisine signal is explained for nonlinear analysis. Secondly, nonlinearities of the DFN model with published parameters are characterised and compared to experimental data from a 11.5 mA h three-electrode configuration cell, which was related to a commercial NMC811 cathode Graphite-SiO_x anode cylindrical 21700 cell with 5 A h capacity. Thirdly, the most sensitive parameter contributing to battery nonlinearities is determined by applying a global sensitivity analysis (GSA) method. Finally, a value of the most sensitive parameter that produces the closest nonlinear response to the commercial battery is estimated by minimising the root mean square error (RMSE) of the characterised nonlinearity. To clarify, the success of the methodology is not dependent on the correctness of parameter values, as the sensitivity analysis method is focus on investigating how sensitive the model output is to the parameters variation [237] and the parameters could be unrealistic within the possible range, for example, 0.3 charge-transfer coefficient in [228] and 0.5-1.5 parameter range in [238]. Nonetheless, the valid model parameters can lead to an intuitive understanding of the nonlinearity difference between the battery model and actual cell. Note that, in this chapter, the design of multisine signals, model simulation and sensitivity analysis, as well as data collection and analysis, were the author's original work. The three-electrode configuration experimental cell was provided by collaborators from University of Birmingham.

4.2.1 Multisine signal design

A random phase odd multisine signal, which is specifically designed for this thesis to meet **Research Objective (1)**, is explained in this section. The background theory of multisine signal has been introduced in Chapter 3, and this section demonstrates the selection of critical parameters, such as frequency range, harmonics, phases, and amplitudes, in the signal design. These critical parameters for battery nonlinear characterisation should be determined by considering the battery dynamics, hardware/software limitation, safety concerns and specific objective [47].

Frequency range of signal

As described in Section 2.3, the dynamic response of a lithium-ion battery is governed by diffusion processes, thermodynamics, and charge-transfer kinetics [48].

Each process has a distinct characteristic frequency range that allows it to be identified in the frequency domain. For instance, Harting et al. concluded that, for a NMC pouch format cell used in [223], the low frequency range from 0.02 Hz to 1 Hz is for thermodynamics and diffusion processes, the medium frequency range from 1 Hz to approximately 200 Hz is for porous electrode reactions, such as double-layer capacitance and charge transfer kinetics, and the high frequency range from approximately 200 Hz to 10 kHz is for faster processes such as ionic transport between SEI and electrolyte. As the ionic transport processes have been proved to contribute only minor nonlinearity (around 10^{-2} times than the other processes), the high frequency range can reasonably be neglected for nonlinearity characterisation and analysis. In addition, limitations of the hardware sampling frequency needs to be taken into consideration. According to Shannon sampling theorem the maximum frequency of the multisine signal has to be less than $f_s/2$. Referring to [228], results of the NFRA simulation conducted on the DFN model show that the nonlinearity related to the charge-transfer kinetics decreases monotonously as the characteristic frequency increases, the smallest part of the medium frequency range is sufficient to evaluate the magnitude of nonlinearity related to the electrode reactions.

Thus, in this study, the maximum frequency f_{max} of the multisine signal was set as 10 Hz to include the low and partial mid characteristic frequency ranges, such that the nonlinearities caused by both diffusion and charge-transfer kinetics behaviour can be characterised. The frequency range was determined by the same experimental process as described in [228] which was based on the EIS result on the actual experimental cell. Furthermore, the sampling frequency f_s was set as 50 Hz to avoid signal aliasing. The number of sample per period N was set to $N = 5000$ giving a signal period of $T = N/f_s = 100$ s and the minimum frequency $f_{\min} = 10$ mHz. In addition, the frequency resolution was obtained as $f_0 = f_s/N = 0.01$ Hz.

Harmonics, phases, and amplitudes of signal

After determining the frequency range of the signal, the harmonics, phases, and amplitudes of the multisine signal were determined in order to detect the nonlinearity in the frequency domain; this is referred to as a random phase odd multisine signal. The fundamental (DC) frequency, which is $n = 0$ harmonic, was suppressed for obtaining a zero-mean current signal to ensure the cell has no net charge or discharge from the application of the signal. To detect even order nonlinear distortions, all even harmonics within the considered frequency range of the designed signal were suppressed, termed as even detection harmonics $H_{\text{supp,even}}$. Furthermore, some odd harmonics were randomly suppressed by considering three consecutive odd harmon-

ics and randomly suppressing one harmonic from each group. Denoted as odd detection harmonics $H_{\text{supp,odd}}$, the suppressed odd harmonics detect odd order nonlinear distortions. As described in Chapter 3, energy appearing at the suppressed even harmonics in the voltage spectrum are caused by even order nonlinearity and the energy appearing at the suppressed odd harmonics are due to odd order nonlinearity [233]. In this signal example, a total of 334 odd harmonics out of all $K = N/2 = 2500$ harmonics were excited giving $H_{\text{exc}} = \{1, 5, 7, 9, 13, 15, 21, 23, ..., 999\}$ within the bandwidth (10 mHz to 10 Hz).

In addition the phase φ_{n} of the excited harmonics (H_{exc}) was a uniformly distributed random variable between 0 to 2π in order to make the signal has generality and randomness. The odd only excited harmonics and random phases assigned to them classifies the signal as *random phase odd* multisine. For simplicity, the amplitude of the harmonics was identical to unity across all excited harmonics (a flat spectrum). According to the literature, different levels of battery nonlinearity can be excited depending on signal amplitudes, e.g. referring to [223], a signal with 1.5 C-rate is sufficient to excite battery nonlinearity of 32 mA h $NMC|C$ lithium-ion batteries in the pouch format for NFRA, and 0.2/0.27/0.33 C-rate signals are applied for NLECM analysis on commercially available Samsung 1.5 A h $NMC|C$ cells (INR 18650-15M) [221]. To obtain sufficient nonlinearity for analysis, the multisine signal in this work was formalised in the time domain, and its root mean square (RMS) was scaled to 1.5 C-rate. As the battery model employed in this study was parameterised to an experimental cell with 11.5 mA h rated capacity, the RMS of the multisine signal was set as 17.25 mA. Given that the peak value of the signal was relatively small in comparison to the hardware constraint and safety range, the crest factor optimisation problem was not required for this study. Furthermore, to improve the robustness of the characterisation results, the multisine signal $u(n)$ was repeated $P = 10$ times and thus the total duration was $T_{\text{total}} = P \times 100\,\text{s} = 1000\,\text{s}$ for each operational condition.

4.2.2 Experimental setup and measurements

In this work, a three-electrode configuration cell, which was related to a commercial 5 A h cylindrical 21700 cell, was constructed and termed as Cell3. The voltage response of the full-cell was measured at 10%, 50%, and 90% SOC in order to compare it to the electrochemical model simulation results under the same operating conditions. These three SOC levels were chosen for the following reasons: first, to consistent with the existing experimental procedures that both NFRA and NLECM are performed at 50% SOC [223, 221], 50% is also selected for this work. In addition,

in order to understand the nonlinearity at low and high SOC levels, 10% and 90% SOC, which are symmetrical with respect to 50%, are determined. The detailed experimental setup and measurements, including the construction of three-electrode configuration cell and the design of experimental plan, will be presented in Section 5.2.

4.2.3 Electrochemical model

The DFN model, which was introduced in Chapter 2, is applied in this work, and the readers can refer to [36] for more details. In this work, the electrochemistry-based battery modelling toolbox proposed in [242], which allows the user to easily select simplifications to make the desired trade-off between model accuracy and computation time, was employed to perform simulations in MATLAB R2019b environment. Furthermore, the validated parameters used in the DFN model were referred to [24], in which parameters for the electrochemical model are extracted by using experimental techniques.

To investigate the effect of the parameters towards the nonlinear response, some nonlinearity-related physical parameters were determined for sensitivity analysis. Theoretically, nonlinearity can be attributed to inherent nonlinear equations or time-varying parameters in linear equations during operation. As described in Section 2.3, the electrochemical processes in a lithium-ion battery, which are represented by nonlinear partial differential equations (PDEs) or nonlinear differential algebraic equations (DAEs), contribute to the nonlinearity of the battery terminal voltage dynamic response. For example, the Butler-Volmer equation, which describes the charge-transfer kinetics on electrodes, is a typical nonlinear equation in the DFN model system. Given that this equation is inherently nonlinear, small changes in the parameters result in variations in the system's nonlinearity. Therefore, the charge transfer coefficients α and the reaction rate coefficients k are considered as MIFs for the sensitivity analysis in this study. Note that, as one of the assumptions of the SPMe model is "define molar ion flux as proportional to current," which results in an "open-loop" overpotential representation, the nonlinearity within charge-transfer kinetics may not be observable. Thus, the SPMe may not be a suitable candidate to be used for nonlinearity analysis study. In contrast to the majority of modelling research, which assumes that the anodic and cathodic charge transfer coefficients (α_a and α_c) are equal to 0.5 by default, this study evaluates system nonlinearities when α_a was randomly selected within a range around the nominal value point 0.5 and α_c equals to $1 - \alpha_a$. Note that the charge transfer coefficients for the cathode and anode are assumed to be equal to 0.5 in this study.

To simulate the DFN model, spatial discretisation has to be applied on the governing PDEs in Table 2.1, and the resulting set of linear original differential equations (ODEs) describes the diffusion processes of lithium-ion concentration and phase potential. In many modelling literature, the parameters of the solid diffusion coefficient $D_{s,k}$, electrolyte diffusion coefficient D_e and ionic conductivity κ are assumed as constant values for simulation simplicity. However, referring to [24], the experimental results show that these parameters are functions of lithium-ion concentration during battery operation. Thus, the variation of these concentration-dependent parameters also act as a source of non-linearity towards the voltage response, and these parameters are taken into account in this SA study.

As tabulated in Table 4.1, seven nonlinearity-related parameters were determined for the analysis of sensitivity, and a sufficiently wide range of parameters was chosen under the condition that the DFN model can function properly to emulate the behaviour of a physical lithium-ion cell. Note that this work is limited by the fact that its parameter range is not physical, which could result in the model output to be mathematically fitted but based on unrealistic parameter values. Given that the success of this work's methodology is not dependent on the correctness of parameters, this work can be used for sensitivity analysis, however, a physical parameter possible range merits additional investigation in the future. The other parameters in the DFN model assume to have negligible effect on battery nonlinearity, which will be verified in the following sections.

Table 4.1

Nonlinearity-related parameters of the DFN model and their possible ranges.

Parameters	Unit	Nominal Value[*]	Possible range
α_a	$-$	0.5	$[0.4-1.6]*$ Nom.
κ	Sm^{-1}	0.9487	$[0.5-1.5]*$ Nom.
$D_{s,n}$	m^2s^{-1}	3.3×10^{-14}	$[0.5-1.5]*$ Nom.
$D_{s,p}$	m^2s^{-1}	4×10^{-15}	$[0.5-1.5]*$ Nom.
D_e	m^2s^{-1}	1.7×10^{-10}	$[0.5-1.5]*$ Nom.
k_n	$Am^{2.5}mol^{-1.5}$	6.48×10^{-7}	$[0.5-1.5]*$ Nom.
k_p	$Am^{2.5}mol^{-1.5}$	3.42×10^{-6}	$[0.5-1.5]*$ Nom.

[*]Note Nom. is the abbreviation of Nominal Value.
[*]All parameters used in the DFN model are refereed to [24].

To consistent with the procedure of existing nonlinearity analysis [223, 221], battery voltage response at 50% SOC was considered. Under the assumption that the DFN can fully replicate battery dynamics, the nonlinearity of the DFN model should be close to that of an actual battery cell once a good agreement was reached

between the voltage response of the model and the cell. Moreover, considering that the DFN model with constant parameters was commonly regarded as providing sufficient accuracy across the whole SOC range, identical findings are expected for SOC levels of 10% and 90%. Figure 4.1 presents the validation result of the DFN model on the experimental battery cell Cell3, at 50% SOC, while the 1.5 C-rate multisine signal is applied. Note that the relevant information of the experimental cell will be provided in Chapter 5. A good agreement between the terminal voltage of the experimental data and of simulation is observed in Figure 4.1a. Furthermore, a 10 s segment is randomly selected and locally amplified, and it shows that the DFN model has a minor overestimation of 0.12 V at peak voltage. Figure 4.1b shows the voltage error which is determined as the model value subtracted by the measured voltage value. The black dashed lines in Figure 4.1b include the 0.050 V and −0.050 V error boundaries, and most of the voltage error is within the boundaries. Additionally, the voltage root mean square error (RMSE) of the DFN model was calculated over the entire testing period and it equals to 0.049 V, which indicates the DFN model can predict the battery voltage response and provide sufficient accuracy (within the accuracy requirement proposed in Section 1.3). Due to the fact that the majority of physical class models do not account for SOC-dependent parameter variations [24, 243], the same set of parameters is expected to be valid for the other SOC levels. Sensitivity analysis is more meaningful when a high fidelity validated model is used, as the nominal values of the parameters are realistic for the commercial cell. In this work, the parameterised model was not a fully validated model due to the limitations of the DFN model and unrealistic parameters. However, because the output is mathematically fitted to experimental data, this work could give plausible global sensitivity analysis results.

4.2.4 Sensitivity analysis method: Morris method

For sensitivity analysis, nonlinearities of the DFN model with nominal values were characterised by the multisine-based method and quantified. As shown in Equations (3.11) and (3.12), the time-domain voltage response is converted to the frequency-domain spectrum by applying DFT. The mean spectrum V_k is calculated by taking the average over P periods. The root mean square of the odd order nonlinearity $V_{rms,odd}$ and the even order nonlinearity $V_{rms,even}$ are calculated as model outputs in this work, as shown in Equation (4.1).
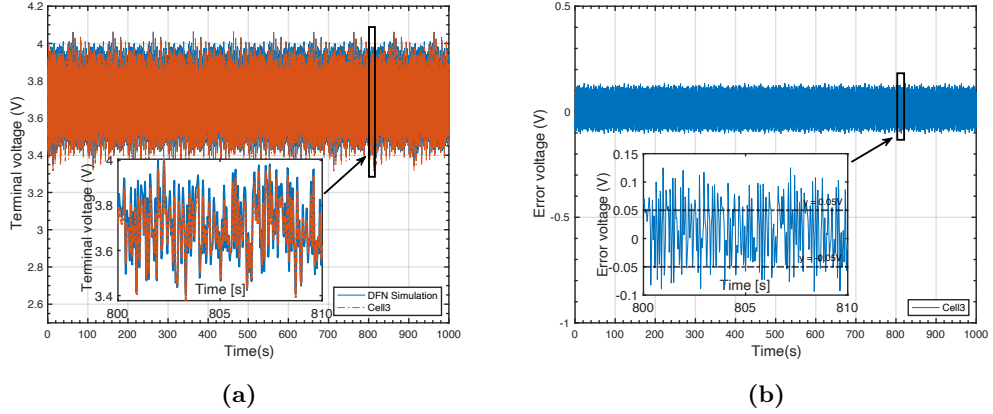
Figure 4.1: DFN model prediction vs experimental data at 50% SOC under 1.5C multisine signal. (a) Terminal voltage between the DFN model and Cell3; (b) Error voltage between the DFN model and Cell3. The simulation result of the DFN model has a good agreement with the experimental result, which indicates the high accuracy of the parameterised DFN model in this study.

$$V_{\text{rms,l}}\left(\bar{\theta}_{\text{j}}\right) = \sqrt{\frac{\sum_{\text{k}}\left(V_{\text{k}}\left(\bar{\theta}_1, ..., \bar{\theta}_{\text{j}}, ..., \bar{\theta}_{\text{m}}\right)\right)^2}{Cardinal(k)}},$$
$$k \in \begin{cases} H_{\text{supp,odd}}, & \text{l} = \text{odd} \\ H_{\text{supp,even}}, & \text{l} = \text{even} \end{cases} \tag{4.1}$$

Here $V_{\text{rms,l}}$ is the root mean square of nonlinearities at detection harmonics (suppressed odd or even harmonics), $\bar{\theta}$ denotes the nominal value of parameters, subscript j is the jth parameter, and $Cardinal(k)$ indicates the total number of odd or even detection harmonics. The root mean square is a well-known measure in engineering, also for nonlinearity analysis in total harmonic distortion, and it gives a mean value of the overall nonlinearity of a system [228, 217].

The global sensitivity analysis method proposed by [244], which is recognised as the simplest but effective method, is utilised in this work. The Morris method overcomes the limitation of the local SA by performing partial derivative calculations in different locations of the input variable domain of variation. The method is global because the input variables can vary over their entire domain of definition [245]. It has been utilised to research the SPM [240] and DFN model [246] and this method was favoured as it is fast, requires fewer simulation samples and its qualitative ranking of variable sensitivities is close to more complex SA methods. The approach, however, cannot be utilized to quantitatively assign relative importance [247]; it simply provides insight into whether characteristics are more or

less significant. It is consequently appropriate for tasks such as sorting parameters based on their sensitivities or picking subsets of unimportant or difficult-to-identify parameters [248]. The Morris method enables the classification of inputs into three categories: inputs with negligible effects, inputs with large linear effects but without interactions, and inputs with large non-linear and/or interaction effects. The method entails discretising the input space for each variable, followed by a predetermined number of "One At a Time" (OAT) designs in which each input is varied while fixing the others [249]. These experimental designs are picked at random from the input space, and the variation direction is also random. It allows elementary effects for each input to be estimated by repeating these processes, and sensitivity indices are derived from these effects [250].

Suppose each parameter θ_j, $j = 1, 2, ..., d$ in the DFN model is independent, and the input space is discretised into a d-dimensional grid per input. Denote r as the number of OAT designs. The elementary effect (EE) of the jth parameter obtained at the ith repetition, is defined as,

$$EE_j^{(i)} = \left| V_{\mathrm{rms},l}\left(\bar{\theta}_j^{(i)} + \Delta_j^{(i)}\right) - V_{\mathrm{rms},l}\left(\bar{\theta}_j^{(i)}\right) \right|, \quad i = 1, 2, ..., r \qquad (4.2)$$

where $\bar{\theta}_j^{(i)}$ denotes the nominal parameter values in the ith repetition, $\Delta_j^{(i)}$ denotes the random perturbation value from a standard uniform distribution on the open interval (0,1) and $\bar{\theta}_j^{(i)} + \Delta_j^{(i)}$ is always within the corresponding possible range as listed in Table 4.1. In this study, the Morris method is applied for nonlinearity analysis with $r = 15$ repetitions and $d = 7$, which requires $n = r(d+1) = 120$ model calls.

Indices of elementary effect (EE) distribution are calculated to evaluate the sensitivity of parameters, as follows:

$$\mu_j = \frac{1}{r} \sum_{i=1}^{r} EE_j^{(i)} \qquad (4.3a)$$

$$\sigma_j = \sqrt{\frac{1}{r-1} \sum_{i=1}^{r} \left(EE_j^{(i)} - \mu_j\right)^2} \qquad (4.3b)$$

where μ_j is mean of the elementary effects and σ_j is standard deviation of the elementary effects.

The interpretation of the indices is as following, μ_j is a measure of influence of the jth input on the output. A large μ_j indicates a high contribution of the jth input to the dispersion of the output. σ_j is a measure of nonlinear and/or interaction

effects of the jth input. If σ_j is small, elementary effects have low variations on the support of the input. Thus, a perturbation has the same effect throughout the support, implying a linear relationship between the analysed input and output. On the other hand, the large σ_j indicates that the linearity hypothesis is less likely. Thus a variable with a large σ_j value is regarded to have nonlinear effects or to have interactions with at least one other variable. A plot linking μ_j and σ_j allows the three groups to be distinguished. More details can be found in [240, 250].

4.3 Results and discussions

To understand the nonlinearity of lithium-ion battery systems, the multisine-based method was applied on the DFN model and the three electrode cell at 10%, 50% and 90% SOC levels. The measured voltage response were transformed into the frequency domain, and the frequency spectrum of the measured voltage was compared to that of the DFN model and analysed. Furthermore, the Morris method (Section 4.2.4) was employed for sensitivity analysis and the most sensitive parameter towards battery nonlinearities and the linear response was evaluated respectively. The detailed results and discussions are presented in the following sections.

4.3.1 Comparison of battery frequency response

In this section, the results analysis and discussion focus on the nonlinearity of the DFN model and the experimental cell at 10% SOC. The motivation is that, as mentioned in [47], the battery nonlinearities of both $NMC|C$ are much stronger at low SOC levels than at higher SOC levels. The terminal voltage spectrum of the DFN model (with nominal parameters) and the experimental cells at 1.5 C-rate 10% SOC, characterised by the multisine-based method (Section 4.2.1), are plotted in Figure 4.2. As mentioned in the signal design section, the energy shown at the excited harmonics (blue curve) indicates the dominant linear response spectrum (Equation 3.13a with $k \in H_{\text{exc}}$) at the operating point (10% SOC). In the non-excited detection harmonics, the level of nonlinear contributions (termed as the battery nonlinearity) can be separated to odd (red circle) and even (yellow triangle) order, respectively (Equation 3.13a with $k \in H_{\text{supp,even}}$ or $H_{\text{supp,even}}$). The purple points indicates the noise standard deviation from measurement and environment error (Equation 3.13b). It can be noticed that the dominant linear response spectrum (blue) and the noise floor (purple) in the DFN model agrees well with the experiment results. However, there are significant differences in the nonlinear contributions in the DFN model compared to the experimental results (4.2a vs 4.2b). The dominant non-

linearity in the DFN model is the odd nonlinearity over the whole characterisation frequency range, while it is the even nonlinearity in the experiment data. Given that the DFN model is commonly used in model-based nonlinearity investigation work [220, 227, 228], it is assumed that the DFN model covers the nonlinearity-related battery dynamics of a lithium-ion battery, although the DFN model's limitations, such as its mathematical approximation and lack of non-homogeneity interpretation, still exist and may affect the model's nonlinear response. In this study, it is considered that the DFN model is suitable for interpreting nonlinear dynamics, thus, inspired by model parameterisation procedure, the inconsistent nonlinearity results between the experimental data and model simulation are attributed to the incorrect parameters in the model, which motivates further investigation employing sensitivity analysis.
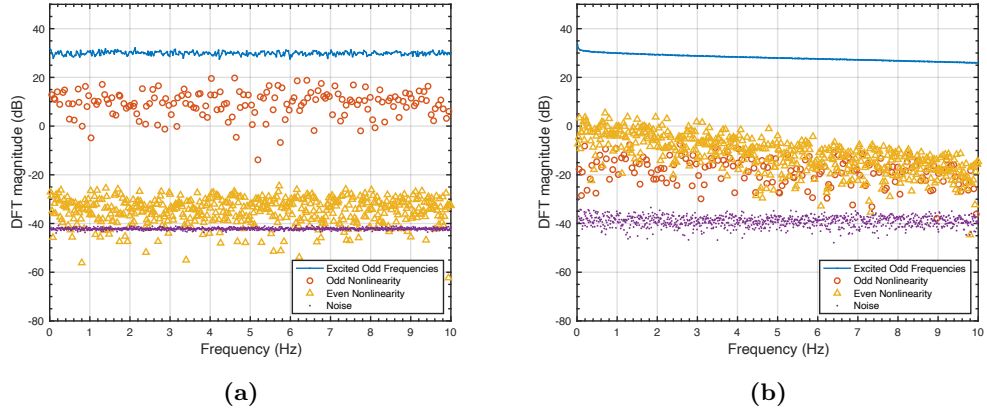
Figure 4.2: Comparison of terminal voltage spectrum at 1.5 C-rate 10% SOC. (a) Voltage spectrum of the DFN model; (b) Voltage spectrum of experimental data.

4.3.2 Analysis of parameter sensitivity towards nonlinearities

Figure 4.3a depicts the parameter sensitivity analysis results to battery odd nonlinearity (plotting equations 4.3b vs equation 4.3a) at 1.5 C-rate 10% SOC. In the SA results, the value of μ and σ can be classified into three categories, such as large, average, and minor. The MIF (Table 4.1), which has the largest μ and σ, is deemed as the most sensitive factor and marked with a diamond. The minor level, marked with a dot, is when the value of μ and σ are less than 1/10 of the most sensitive factor, and the MIFs can be considered insensitive. The remaining factors between 'large' and 'minor' levels are defined as average sensitivity MIFs and marked with a

square. Therefore, it is observed that the charge transfer coefficient α^* is the most sensitive parameter and has strong non-linear effects and/or interactions effect (large μ and large σ). It's noted that, in the Morris method, the sensitivity of MIF is qualitatively ranked, thus the higher sensitivity of one parameter value does not imply that the others do not contribute to nonlinearity. The anode reaction rate constant k_n has average non-linear effects and/or interactions effect (average $\mu = 3.49\,\mathrm{dB}$ and average $\sigma = 3.05\,\mathrm{dB}$). The remaining parameters, such as ionic conductivity κ, cathode reaction rate constant k_p, cathode diffusion coefficient $D_\mathrm{s,p}$, anode diffusion coefficient $D_\mathrm{s,n}$, and electrolyte coefficient D_e, are insensitive towards the odd distortions observed in the spectrum, since the value of μ and σ of these MIFs are one order of magnitude smaller than the most sensitive parameter ($\mu < 0.47\,\mathrm{dB}$). The sensitive parameters α and k fulfil their roles in the Butler-Volmer equation, which indicates that any slight variation of the charge transfer behaviour can lead to considerable change in the battery nonlinear response. Since the Butler-Volmer kinetic is an odd symmetric function (between the over-potential and current density) and shows point symmetry in the nonlinear current voltage relation with $\alpha_\mathrm{a} = \alpha_\mathrm{c} = 0.5$, it's reasonable to observe the variation of battery nonlinearities when the α_a is no longer 0.5 and the Butler-Volmer kinetics is not symmetric anymore.

To further validate the nonlinearity related parameters, the sensitivity of an extended physical parameters space was analysed at the same condition, as shown in Figure 4.3b. This extended parameter space consists of the 7 aforementioned nonlinearity related parameters and 14 extra physical parameters (See Table 4.2) which are normally taken into account in electrochemical model SA studies. Consistent with Figure 4.3a, the most sensitive parameter in the extended parameters case is still the charge transfer coefficient α followed by the anode reaction rate constants k_n, which means the selection of nonlinearity related parameters is reasonable and the major source of battery nonlinearities is the charge transfer reaction. Furthermore, Figure 4.3b verifies that the extended physical parameters have a negligible effect towards battery nonlinearities compared to the non-extended parameter set (See Table 4.1). From a computational perspective, applying the global sensitivity analysis method on the DFN model is relatively costly, for instance, a total of 5188 s operation time was required for the 7 parameters case using a standard laptop. Given that the most sensitive parameter is included in both cases, the 7 parameters case for subsequent analysis was utilised in this work, rather than the extended 21 parameters, to reduce computational cost by two-thirds.

---

*The charge transfer coefficient α in the legend denotes the anodic charge transfer coefficient α_a.
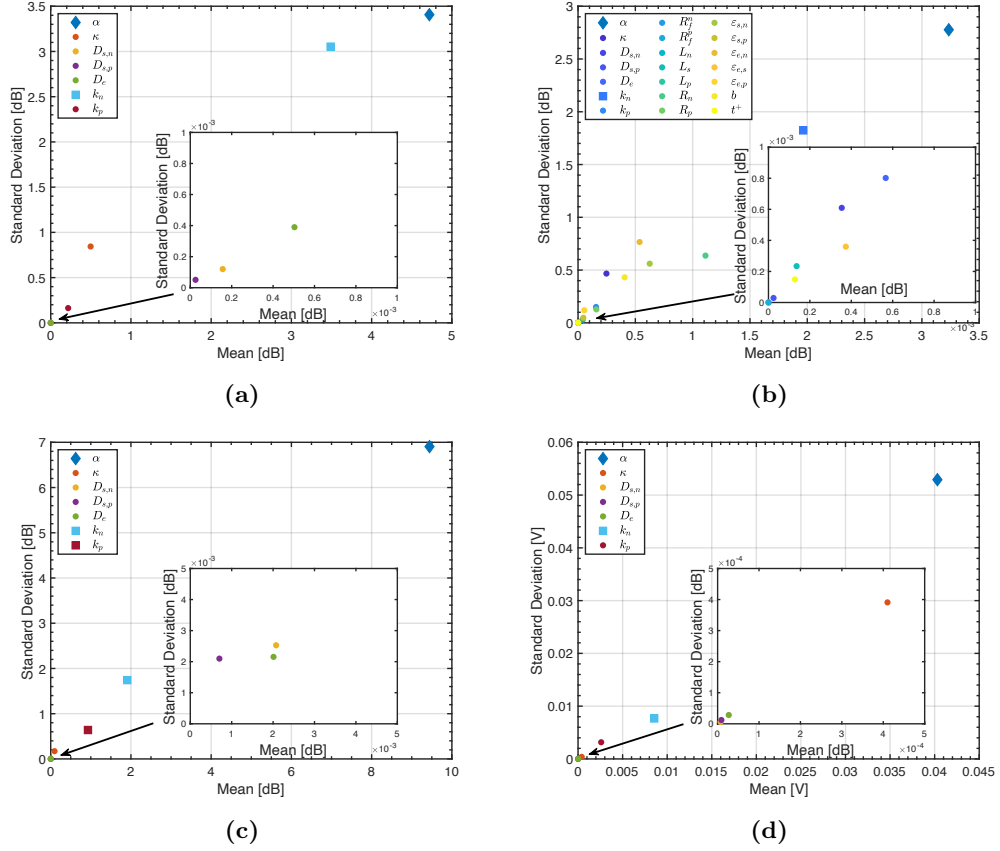
Figure 4.3: Parameters sensitivity analysis results of the DFN model based on the Morris screening method at 1.5 C-rate 10% SOC. (a) Sensitivity of nonlinearity related parameters to odd nonlinearity; (b) Sensitivity of extended physical parameters to odd nonlinearity; (c) Sensitivity of nonlinearity related parameters to even nonlinearity; (d) Sensitivity of nonlinearity related parameters to terminal voltage.

The sensitivity analysis results of nonlinearity related parameters to battery even nonlinearity are shown in Figure 4.3c. It is observed that the sensitivity of the charge transfer coefficient α is again the greatest, followed by those of anode reaction rate constant k_n and cathode reaction rate constant k_p, and the other parameters are insensitive.

The sensitivity of the parameters towards the terminal voltage were analysed by the same method and is shown in Figure 4.3d. The results show that the charge transfer coefficient α is the most sensitive parameter to terminal voltage, followed by anode reaction rate constant k_n and cathode reaction rate constant k_p. The charge transfer coefficient α has strong interaction effects (large μ and large σ). The anode reaction rate constant k_n and cathode reaction rate constant k_p have average non-linear effects and/or interactions effects (average $\mu = 5.57\,\mathrm{mV}$ and average

Table 4.2
Extended model input factors (MIFs) - 14 extra physical parameters for the extended sensitivity analysis.

Parameters	Dimension	Nominal Value*	Possible range
R_f^n	$\Omega \times m^2$	10^{-4}	$[0.5 - 1.5] * \text{Nom.}$
R_f^p	$\Omega \times m^2$	10^{-4}	$[0.5 - 1.5] * \text{Nom.}$
L_n	m	0.9487	$[0.5 - 1.5] * \text{Nom.}$
L_s	m	3.3×10^{-14}	$[0.5 - 1.5] * \text{Nom.}$
L_p	m	4×10^{-15}	$[0.5 - 1.5] * \text{Nom.}$
R_n	m	1.7×10^{-10}	$[0.5 - 1.5] * \text{Nom.}$
R_p	m	6.48×10^{-7}	$[0.5 - 1.5] * \text{Nom.}$
$\varepsilon_{s,n}$	$\%$	0.75	$[0.5 - 1.5] * \text{Nom.}$
$\varepsilon_{s,p}$	$\%$	0.665	$[0.5 - 1.5] * \text{Nom.}$
$\varepsilon_{e,n}$	$\%$	0.25	$[0.5 - 1.5] * \text{Nom.}$
$\varepsilon_{e,s}$	$\%$	0.47	$[0.5 - 1.5] * \text{Nom.}$
$\varepsilon_{e,p}$	$\%$	0.335	$[0.5 - 1.5] * \text{Nom.}$
b	$-$	1.5	$[0.5 - 1.5] * \text{Nom.}$
t^+	$-$	0.2594	$[0.5 - 1.5] * \text{Nom.}$

*Note Nom. is the abbreviation of Nominal Value.
*The nominal value of parameters are refereed to [24].

$\sigma = 5.41 \,\text{mV}$). The remaining parameters, such as cathode diffusion coefficient $D_{s,p}$, anode diffusion coefficient $D_{s,n}$, electrolyte coefficient D_e, and ionic conductivity κ, are deemed to have no effect since they are one order of magnitude smaller than α ($\mu < 0.41 \,\text{mV}$). Furthermore, compared to the literature which analyses the sensitivity to model voltage output in the entire SOC window [240], the sensitivity of the solid diffusion coefficients D_s (in this analysis) is insensitive. The reason may be due to the variation of SOC is negligible during a multisine-based characterisation test, which leads to the effect of diffusion behaviour to terminal voltage being minor.

Furthermore, Figure 4.4 presents the sensitivity results of nonlinearity related parameters to the odd and the even order nonlinearity at 50% and 90% SOC levels. In the Morris method, as the perturbation Δ_i of a MIF in Equation (4.1) is randomly selected from the corresponding possible range, the sensitivity results of a MIF varies within a certain extent. However, overall, the sensitivity of each nonlinearity related parameter is still consistent with the 10% SOC case.

The results shown in Figure 4.3 and Figure 4.4 reveal that the charge transfer coefficient α is the most sensitive parameter to nonlinearities of a lithium-ion battery. Moreover, the sensitivity analysis results indicate that the charge-transfer reaction plays a vital role in the lithium-ion battery dynamic response at a SOC level.
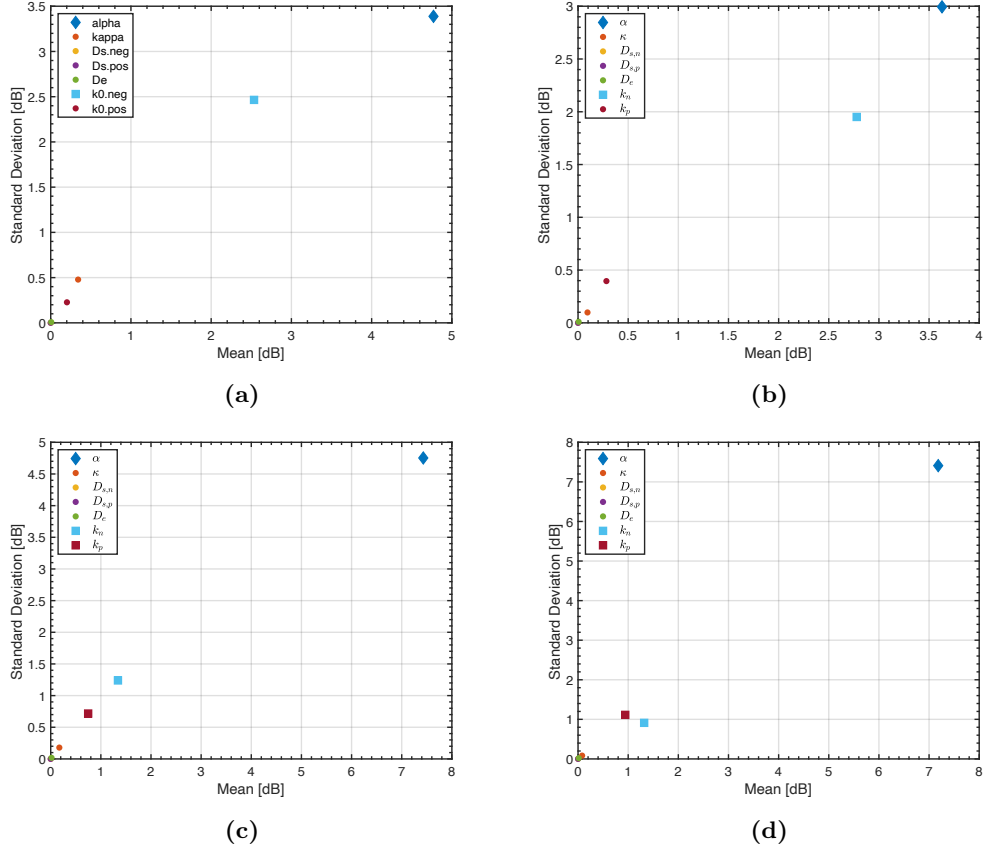
Figure 4.4: Sensitivity results of nonlinearity related parameters to nonlinearities at various SOC levels of; (a) Odd nonlinearity at 50% SOC, (b) Odd nonlinearity at 90% SOC, (c) Even nonlinearity at 50% SOC, and (d) Even nonlinearity at 90% SOC .

4.3.3 Effect of charge-transfer coefficient towards battery nonlinearities

Based on the sensitivity analysis results, the charge transfer coefficient α has been identified as the most sensitive parameter towards the battery nonlinearity and terminal voltage response at a specific SOC level. To further understand the effect of charge transfer coefficient α, the nonlinearities of the DFN model with various charge transfer coefficients α were characterised and compared to each other in this section (Figure 4.5). The nominal values of the anodic charge transfer coefficient α_a and cathodic charge transfer coefficient α_c are 0.5, and the level of nonlinearity at nominal values are the yellow lines in Figure 4.5a and Figure 4.5b. The anodic charge transfer coefficient α_a is varied by multiplying the nominal value by a gain factor, where the range of gain factors is defined from 0.6 to 1.8. It leads to the anodic charge transfer coefficient α_a examined in this section to vary between 0.3

and 0.9. Then, the corresponding cathodic charge transfer coefficients α_c can be obtained by $1 - \alpha_a$. While for a simple one electron transfer reaction, the sum of α_a and α_c equals to 1 is rational [251].
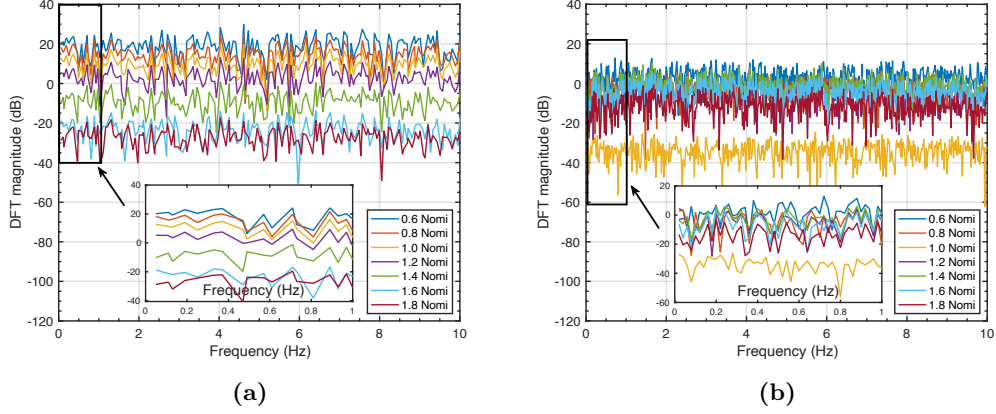
Figure 4.5: Nonlinearities comparison at various α_a values at 1.5 C-rate 10% SOC. (a) Odd nonlinearity comparison with various α_a; (b) Even nonlinearity comparison with various α_a.

The battery odd nonlinearities to the varying α_a (with a 1.5 C-rate odd random phase multisine current) when at 10% SOC are compared in Figure 4.5a. It clearly shows that the odd nonlinearity shifts in the interval from around $-30\,\mathrm{dB}$ to $20\,\mathrm{dB}$ in accordance with the variation of α_a. As α_a increases from the nominal value of 0.5 ("1.0 Nomi" yellow line) in Figure 4.5a), the magnitude of the odd nonlinearity simultaneously decreases. Moreover, when α_a decreases from the nominal value the odd nonlinearity increases. Unlike the effect towards the odd nonlinearities, the even nonlinearities excited by the same charge transfer parameters do not increase or decrease continuously with the decrease or increase in α_a, as shown in Figure 4.5b. The DFN model with the nominal value excites the weakest even nonlinearity which is at around $-35\,\mathrm{dB}$. Furthermore, the even nonlinearities of all the other cases are stronger than the nominal value case and vary between $-10\,\mathrm{dB}$ to $20\,\mathrm{dB}$. This interesting phenomena of the even nonlinearity was also noticed in [228] when the NFRA was applied on the Butler-Volmer equation. When α_a is not 0.5, the perfectly symmetric charge-transfer reaction will not exist, thereby leading to an increase of the even nonlinearity.

To get a further understanding of charge transfer symmetry in the linear and nonlinear voltage response, a Taylor series expansion can be carried out to the Butler-Volmer equation,

$$j = \frac{i_{0,\mathrm{k}}}{F}(\exp(\frac{\alpha_a F}{RT}\eta) - \exp(-\frac{\alpha_c F}{RT}\eta)), \quad \mathrm{k} \in \{\mathrm{n}, \mathrm{p}\}, \tag{4.4}$$

81

and the first three dominant terms are contained for a comprehensive analysis of even and odd order higher harmonics,

$$
\begin{aligned}
j = &\frac{i_{0,\mathrm{k}}}{F} \left[\left(\frac{(\alpha_{\mathrm{a}} + \alpha_{\mathrm{c}})F}{RT} \right) \right] \eta + \frac{i_{0,\mathrm{k}}}{F} \left[\left(\frac{(\alpha_{\mathrm{a}}^2 - \alpha_{\mathrm{c}}^2)F^2}{2!R^2T^2} \right) \right] \eta^2 \\
&+ \frac{i_{0,\mathrm{k}}}{F} \left[\left(\frac{(\alpha_{\mathrm{a}}^3 + \alpha_{\mathrm{c}}^3)F^3}{3!R^3T^3} \right) \right] \eta^3 + \mathcal{O}(\eta^4)
\end{aligned}
\tag{4.5}
$$

where $i_{0,\mathrm{k}}$ is the exchange current density, η is the overpotential, α_{a} and α_{c} are the anodic and cathodic transfer coefficients, and F, R, and T are Faraday's constant, the gas constant, and the temperature, respectively. In this Taylor series expansion, the first three terms in the right-hand side of Equation (4.5) can be classified into the linear term, the even nonlinear term, and the odd nonlinear term which are related to linear response as well as even and odd nonlinearities with respect to the order of the independent variable η [233], and the reminder term $\mathcal{O}(\eta^4)$ is neglected. Given that the assumption $\alpha_{\mathrm{a}} + \alpha_{\mathrm{c}} = 1$, the change of α_{a} and α_{c} will not affect the first linear term. However, the variation of charge transfer coefficients will influence the second and third terms in Equation (4.5), especially the second term which is related to the even nonlinearity. For many electrochemical model studies using the values $\alpha_{\mathrm{a}} = \alpha_{\mathrm{c}} = 0.5$ indicate a symmetric charge-transfer kinetic, and the even nonlinear term in Equation (4.5) is eliminated, which explains the extremely minor magnitude of even nonlinearity in the DFN model simulation in Figure 4.2a. In the case of $\alpha_{\mathrm{a}} \neq \alpha_{\mathrm{c}}$ caused by an asymmetric charge-transfer reaction, the even nonlinear term appears and leads to the even nonlinearity in the results of the nonlinear characterisation observed in the experimental data (Figure 4.2b). As the difference between α_{a} and α_{c} increases, the factor $(\alpha_{\mathrm{a}}^2 - \alpha_{\mathrm{c}}^2)$ of the even nonlinear term will increase, which will excite a greater even nonlinearity as shown in Figure 4.5b. Compared to the even nonlinear term, the odd nonlinear term in Equation (4.5) will always be present due to the summation of α_{a}^3 and α_{c}^3. However, the physical interpretation of the even and odd nonlinearities is still an open question which requires further research.

Referring to Figure 4.5, the nonlinear response of the DFN model could approach the experimental results by tuning the charge transfer coefficients to an appropriate value. For example, Figure 4.6 shows the terminal voltage spectrum of the DFN model with various α_{a} values at 10% SOC. To highlight the effect of α_{a} values, the voltage spectrum of DFN model with $\alpha_{\mathrm{a}} = 0.5$ and the experimental result shown in Figure 4.2 are represented as Figure 4.6c and 4.6d. In Figure 4.6a, the odd and even nonlinearities are overlapped over the whole characterisation fre-

quency, which is consistent with the experimental data especially at high frequency range 6 Hz to 10 Hz (Figure 4.6d). On the contrary, it is noticed that the level of odd and even nonlinear contributions in the low frequency range from 10 mHz to 4 Hz are roughly comparable to the experimental case shown in Figure 4.6d. Further, the even nonlinear is now the dominant nonlinearity in the DFN model which is the opposite of the case with $\alpha_a = 0.5$ (See Figure 4.6c). However, there are still differences in the trend of the nonlinearities and the linear response level of the DFN model in both Figure 4.6a and Figure 4.6b compared to the experiment results (Figure 4.6d), such as the overlapping of the odd and even distortions in the high frequency range and the trend of the linear response and nonlinearities decreasing as frequency increases over the whole frequency range, which are observed in the experimental data but not in the simulations.
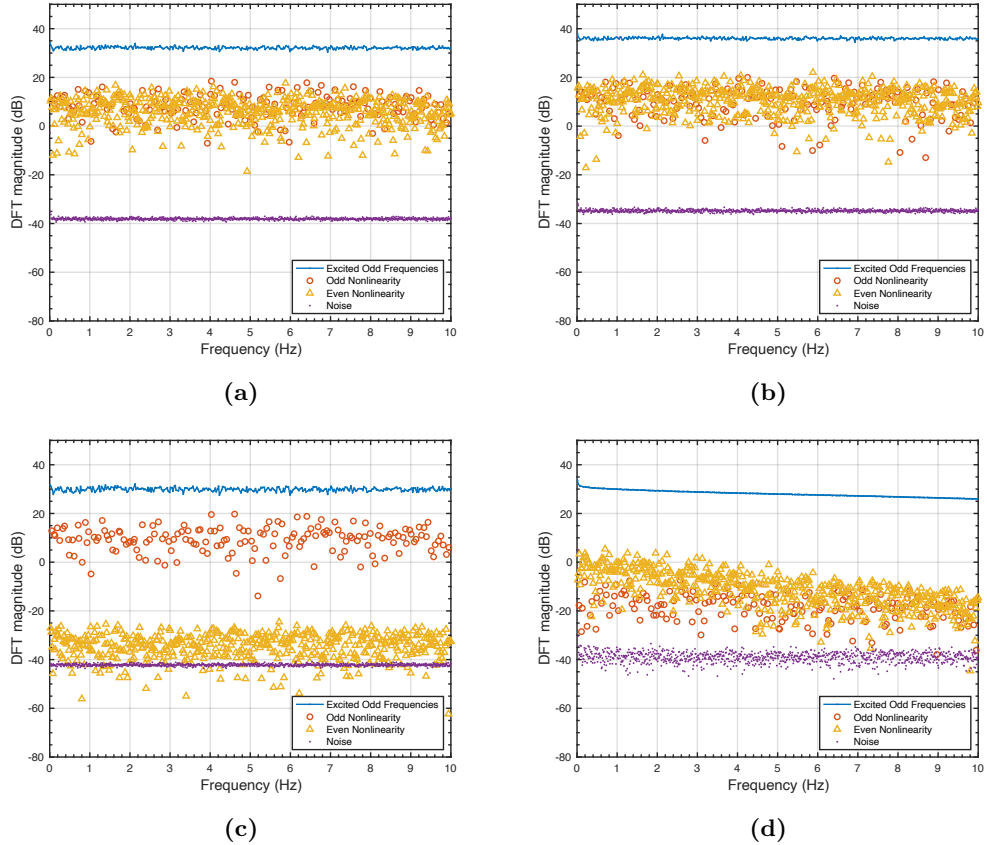
Figure 4.6: Terminal voltage spectrum from DFN model at 1.5 C-rate 10% SOC when (a) α_a is set at 0.8; (b) α_a is set at 0.9; (c) α_a is set at 0.5; (d) Voltage spectrum of experimental data. Note that (c) and (d) are adapted from Figure 4.2 for comparison.

To determine the α_a value that will lead to a comparable experimental result,

the RMSE of the odd and even nonlinearity of the DFN model with various α_a values were calculated and listed in Table 4.3. The nonlinearity error between the model and experimental result shows that with the nominal $\alpha_a = 0.5$ value the DFN model's odd nonlinearity RMSE is 29.15 and at medium error level, as well as the even nonlinearity RMSE (22.20) is the largest among all various α_a value cases. This information is consistent with the results shown in Figure 4.5. According to Table 4.3, a value of $\alpha_a = 0.8$ results in the smallest odd nonlinearity RMSE and with $\alpha_a = 0.9$ leads to the least even nonlinearity RMSE. Compared with the nominal case, both 0.8 and 0.9 could reduce the RMSE by more than a half, which indicates that these two cases lead to a non-linear voltage response that is closer to the experimental data.

Table 4.3
The odd and even nonlinearity RMSE with various α_a values, while the DFN model is at 10% SOC and under 1.5 C-rate multisine signal.

α_a	Odd Nonlinearity RMSE [dB]	Even Nonlinearity RMSE [dB]
0.3	38.37	15.27
0.4	34.03	8.79
0.5*	29.15	22.20
0.6	22.53	8.33
0.7	10.48	11.33
0.8	3.98	7.87
0.9	7.80	0.41

*The nominal value of α_a referred to [24].

4.3.4 Effect of charge-transfer coefficient towards a battery linear response

Different from the results in Figure 4.6c (with the nominal DFN parameter values of Table 4.1), Figure 4.6a and 4.6b present that the odd and even nonlinearities of the DFN model with α_a values 0.8 and 0.9 are overlapped, which is consistent with the experimental results shown in Figure 4.6d. However, the smooth "ramp-shaped" curve of measured linear response shown in Figure 4.6d, which gradually decreases in magnitude as frequency increases throughout the whole frequency range, is not observed. This section investigates the effect of charge transfer coefficient α towards a battery linear response.

Figure 4.7 shows the linear responses at various α_a values when the DFN model is at 10% SOC. Firstly, the linear response of the full cell over the whole
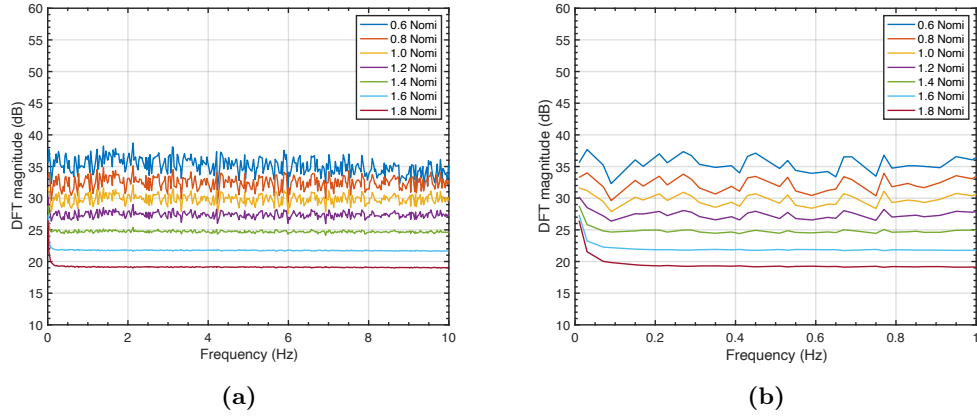
Figure 4.7: Dominant linear responses at various α_a values at 1.5 C-rate 10% SOC. (a) 'Fluctuating' and 'smooth' dominant linear responses in the whole characterisation range; (b) 'Ramp-shaped' dominant linear responses at low frequency range.

characterisation frequency range is plotted in Figure 4.7a. An interesting phenomena is, when the value of α_a is selected from 0.3 (0.6 * Nomi) to 0.6 (1.2 * Nomi), the linear response curve exhibits fluctuations from the input multisine current. On the contrary, with larger α_a values, such as 0.7, 0.8, and 0.9, a relatively flat linear response curve is obtained, which is more close to the experimental results in Figure 4.6d. Considering that the change of α_a leads to an asymmetrical charge-transfer reaction, it could act as a bandpass or low pass filter which affects the overpotential on the solid electrolyte interfaces. In addition, compared with the experimental linear response in Figure 4.6d which decreases from around 30 dB to 25 dB, the magnitude of the linear response in Figure 4.7a remains almost unchanged over the bandwidth. However, as shown in Figure 4.7b, a decreasing 'ramp' shape trend exist when α is large enough like 0.8 and 0.9, but only in the low frequency range (less than 0.2 Hz), compared to the experimental linear response which occurs over the full characterised frequency range. The reason for this difference still requires further research. From the perspective of the linear response, it is also therefore reasonable to use an α_a value between 0.8 to 0.9 rather than 0.5 to minimise the difference when compared to the experimental data at 10% SOC case.

4.4 Conclusion

In this work, a random phase odd multisine nonlinear characterisation method was developed to capture battery nonlinearities, and the Morris method was employed to perform a global sensitivity analysis on the DFN model to evaluate the effect

of physical parameters in the frequency response. By applying the multisine-based method, the linear response, odd and even nonlinearities of the parameterised DFN model were compared with experimental data. The significant nonlinearity difference between the DFN model and experimental cells suggests that the nominal values of DFN model parameters may not be realistic. The most sensitive parameter is determined as the charge transfer coefficient α, and thus the charge-transfer kinetic is determined as the main contributor to the nonlinearities of a lithium-ion battery. Furthermore, effect of α on the frequency domain nonlinear response was investigated by comparing the dynamic responses of the DFN model with various values of α. The DFN model simulation results indicate that, as α_a increases from 0.3 to 0.9, the magnitude of odd nonlinearity decreases correspondingly, but the even nonlinearity does not increase or decrease consistently with the decrease or increase in α_a. Results of the nonlinearity RMSE show that, rather than the commonly used value of 0.5, α_a set as 0.8 or 0.9 provides a good model agreement with the experimental data while the commercial cell is at 10% SOC, whereas the LIB cell exhibits significant nonlinearity leading to poor accuracy of ECM battery models. This phenomenon indicates that the charge-transfer reactions in a lithium-ion battery is an asymmetrical behaviour, rather than the commonly assumed perfect symmetrical reaction, which is consistent with the conclusions in [220, 228]. The physical implication of the asymmetrical charge transfer reactions is asymmetry in oxidation and reduction on both electrodes; i.e. the magnitude of the kinetic overpotential is not identical during charge and discharge. It's worthy to note that there is no intrinsic reason to assume charge transfer symmetry or asymmetry on either electrode. A difference in α_a and α_c for either electrode would reflect asymmetry in the charge transfer processes on that electrode, which deserves further investigation on individual electrodes in the future work. Lastly, this study demonstrates the ability of the multisine-based characterisation method to determine the optimal value of the charge transfer coefficients to achieve a good agreement with experimental results by relying on the battery nonlinearities in the frequency domain. Overall, this chapter demonstrates the feasibility of the developed nonlinear characterisation method, which is based on random phase odd multisine signal to capture and separate odd and even nonlinearities, in the analysis of battery nonlinearity, which fulfils the requirement of "**Research Objective (1):** Design a characterisation method capable of capturing battery nonlinearity." In addition, this chapter enhances the understanding of lithium-ion battery nonlinear dynamic response through the model-based investigation that charge transfer kinetic is the most sensitive to battery nonlinearity at a SOC level, which indicates that lack of charge

transfer kinetic interpretation could lead to inaccuracy of battery model. Thus this work provides a theoretical basis for the development of the new accurate battery model in Chapter 6.

In future work, the multisine-based nonlinear characterisation method can be performed on lithium-ion batteries in different health status to analysis the variation of the nonlinear responses. Due to the advantages of the short testing duration, it is worthy to investigate the capability of the method as an on-broad characterisation technique for battery state-of-health estimation. Furthermore, though $\alpha_a = 0.8$ and $\alpha_a = 0.9$ gives a smaller nonlinearity RMSE to the experimental results by about $20\,\mathrm{dB}$ while the cell is at 10% SOC, the nonlinearity magnitude reduction over the frequency range observed in the experimental data is still an open question. To investigate this inconsistency in the future, it will be necessary to take into account not only the charge-transfer coefficients, but also the other nonlinearity-related physical parameters, such as diffusion coefficients, as the trend of nonlinearity magnitude reduction is observed in the low characteristic frequency range, which is associated with battery diffusion dynamics [47]. The DFN model that achieves a good agreement with experimental results on both the nonlinearity root mean square error (RMSE) and the slope of nonlinearity magnitude reduction in the diffusion characteristic frequency range will be obtained through the application of an optimisation technique that permits multiple input variables. If the physical parameter values are within a reasonable range and the voltage response spectrum of the model overlaps the experimental results over the entire characterisation range, the origin of the nonlinearity magnitude decrease may be recognised, and the understanding of battery nonlinearity can be extended.

Chapter 5

An Experimental Investigation of Lithium-ion Battery Nonlinearity†

5.1 Introduction

This chapter presents an experimental investigation to fulfil "**Research Objective (2):** Understand the electrochemical processes contributing to nonlinearity." As presented within Chapter 4, the simulation study demonstrates how the proposed multisine-based method characterises battery nonlinearity, and the findings show that the charge-transfer reactions have the greatest effect to battery nonlinearities. However, the preceding chapter only experimentally examined battery nonlinearities at a specific operating condition, 10% SOC, which is insufficient for a thorough nonlinear analysis of lithium-ion batteries. Thus, based on the multisine-based method developed in Chapter 4, this chapter presents nonlinear characterisation tests performed on an experimental set-up of a commercial 5 A h cylindrical 21700 cell at diverse operating conditions to understand the electrodes contributing to any observed non-linear responses.

To extend the understanding of nonlinearity from a full lithium-ion battery cell to individual electrodes, a three-electrode configuration experimental cell was assembled and employed in this study. Previous nonlinear analysis research was conducted on full-cells with a variety of different cell geometry and chemistries; as a result, non-linear voltage responses of the individual electrodes have not been decoupled and attributed to relevant electrochemical processes taking place on each

---

†Parts of this chapter have been published in [2]

electrode. In addition, the contribution of nonlinearity from anode and cathode is still an open question and not fully understood. Thus, the intervention of novel techniques are required to deconvolute the voltage dynamics of the individual electrodes from a full-cell in order to conduct nonlinear characterisation tests presented in Chapter 4 for each electrode. In the literature, the deconvolution of individual electrodes is generally achieved by using half-cell configurations, where a lithium metal electrode is utilised as both the counter and reference electrode [252]. However, the use of a lithium metal counter electrode means the behaviour does not closely resemble the commercial battery [253, 254]. In comparison to half-cell arrangements, the three-electrode configuration is a potential alternative since it closely resembles a commercial cell arrangement, which makes the conclusions more relevant to practical applications [255, 256, 257, 258]. In [255], the insertion method with a pure metallic lithium reference electrode enables direct observation of voltage responses of the individual electrodes. Moreover, for assigning the entire cell behaviour into individual electrodes, Wunsch et al. proposed an experimental method to depict the separation of individual electrodes through impedance spectra [258]. The author asserts that the three-electrode configuration is a promising experimental set-up for investigating battery nonlinearities, as it provides the accurate and realistic voltage response of both a full-cell stage and individual electrode.

This chapter is structured as follows: In Section 5.2, the experimental setup and measurements are discussed. In Section 5.3, the frequency domain analysis, which has been applied on the simulation study in Chapter 4, is performed on measurements of the experimental cells, and the odd and even order nonlinearities of the full-cell and individual electrodes are analysed and discussed. Overall conclusions of this study are given in Section 5.4.

5.2 Experimental setup and measurements

To quantify the nonlinearities, measurement of voltage response of the full-cell and individual electrodes is required. Taking advantage of three-electrode configuration cell, both voltage measurements relating to a commercial 5 A h cylindrical 21700 cell can be simultaneously achieved over several operating conditions by employing a variety of multisine signals. The detailed experimental setup and measurements, including the construction of three-electrode configuration cell, the determination of characteristic frequency range, and the design of multisine signal and experimental plan, are presented in the following sections. Note that, in this chapter, the design of multisine signals, as well as data collection and analysis were the author's original

work. Assembly of three-electrode configuration experimental cells and characterisation tests were provided by collaborators from University of Birmingham.

5.2.1 Three-electrode configuration experimental cell

The experiments were conducted using a three-electrode configuration to determine the cathode and anode behaviour from the full cell potential. Note that, as three-electrode configuration experimental cells were provided by collaborators from University of Birmingham, the experiment battery parameters were same as those used in [24]. The PAT-Cell setup of the EL-Cell is comprised of a 21.6 mm FS-5P separator (EL-Cell), 100 μL of R&D281 electrolyte (Soulbrain), and the extracted positive and negative electrodes punched into 18 mm disks [259]. This three-electrode configuration cell design is constructed as shown in Figure 5.1. The electrodes (anode/cathode) were harvested from a fresh 21700 LGM50 cylindrical cells following the reported teardown procedure [24]. Note that the fresh cylindrical cells from the manufacturer and stored in a fridge ($5°C$) until they were discharged to 2.5 V and then disassembled. The cell's interior is comprised of a housing, in which a fibreglass separator is clamped and encased by an annular lithium reference electrode. The reference electrode purchased from EL-Cell comprise of a stainless steel ring that had lithium metal deposited on it, and applied to a reed contact. This enables the reference electrode to be connected to the cell's inner contacts and therefore to the battery tester. As a result, the reference is located outside the anode and cathode's real active region, and so has no effect on the diffusion routes or internal resistance of the test cell. The lithium reference electrode is positioned horizontally between the electrodes in the separator frame. This results in the formation of a symmetrical field distribution. The upper and lower sides of the enclosure can be fitted with electrode stampings of 18mm diameter (area $2.54\,cm^2$) and secured with appropriate plungers. The advantages of this method include the reproducible contacts of the individual potentials (anode, cathode, and reference) across the cell's underside [258]. The extracted NMC811 cathode and bi-component Graphite-SiO_x anode had the coating on one-side removed to allow testing in a small format cell. The electrode is generally double-sided in a commercial cell and to make it in a coin cell or an EL-Cell, the electrode was removed from one current collector. In addition, to remove it without damaging the other electrode, the electrode was taped on a glass plate and the electrode was exfoliated with a sponge. Detailed methods for cell tear down, cell assembly and characterisation are referred to [260]. Furthermore, the composition of Soulbrain R&D281 is ethylene carbonate (EC):ethylmethyl carbonate (EMC) 3:7 v/v + 1 wt% vinylene carbonate (VC). The nominal rated capacity

of an EL-Cell in this study is 11.5 mA h, which also decides the magnitude of the 1 C-rate (1C) as 11.5 mA.
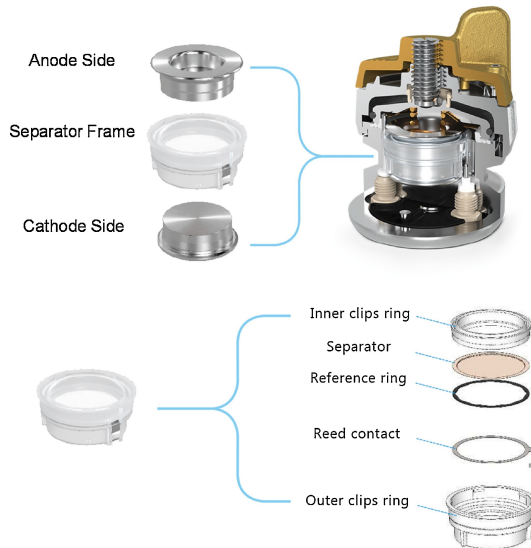
Figure 5.1: The exploded view of three-electrode configuration PAT-CELL and separator frame by EL-CELL [258].

Before the multisine signals were applied to the assembled cells, a formation protocol was used to ensure that the solid electrolyte interphase (SEI) had reformed [261]. Extraction of the electrodes and using a different electrolyte meant this step was required to ensure cell longevity. Refer to [24], this formation protocol for three electrode configuration cell consisted of two cycles at C/10 constant current constant voltage (CC-CV) charge and constant current (CC) discharge between the recommended voltage window 2.5-4.2 V. The CV step was terminated when the current decayed to C/50. The signals were programmed using the 'Batch Mode' function in the EC-Lab software (Bio-Logic®).

5.2.2 Characteristic frequency range of experimental cell

As mentioned in Chapter 4, the characteristic frequency range of lithium-ion battery cells may be not identical for different geometries. In this study, the instrument configuration setup of the three-electrode experimental cells causes an increase in cell impedance, which may result in distinct characterisation frequency ranges. Thus, the potentiostatic electrochemical impedance spectroscopy (PEIS), as described in Section 3.3.1, was performed on the experimental cells at 50% SOC to separate and identify the electrochemical processes in the frequency domain. In the PEIS experiment design, the AC perturbation signal was limited to 10 mV for minimising

non-linear effects, and also the PEIS frequency range was controlled between $10\,\text{mHz}$ and $100\,\text{kHz}$.
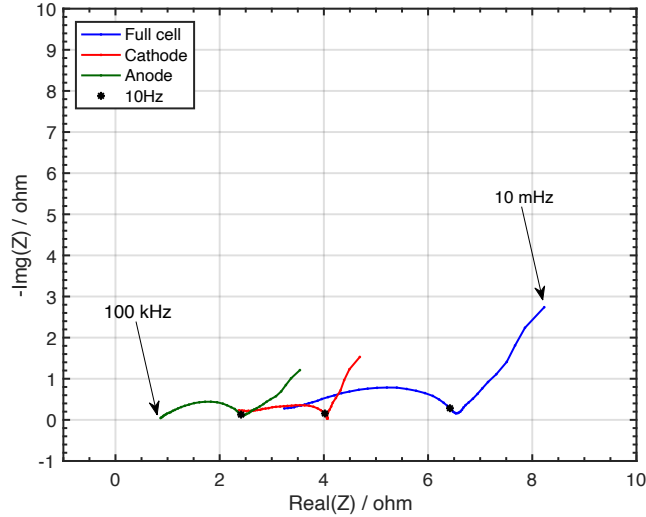
Figure 5.2: PEIS Nyquist plot of the NMC EL-Cell at 50% SOC. Note that the frequency range of PEIS was from $10\,\text{mHz}$ to $100\,\text{kHz}$.

Figure 5.2 presents the impedance spectra of the cathode, anode and full-cell. The measured impedance can be divided into two distinct parts for low frequency range $10\,\text{mHz}$ to $4\,\text{Hz}$ and a semi-circle for medium frequency range $4\,\text{Hz}$ to $100\,\text{kHz}$. As described in Chapter 3, the low frequency range represents the frequency response of diffusion process and the medium frequency range corresponds to charge-transfer reactions. In general, the EIS plot of a commercial cell format (rather than a PAT-cell) at $100\,\text{kHz}$ and above would surpass the real axis [166, 262, 197]. However, no such response is presented in any of the impedance spectra of Figure 5.2. The reason of such phenomenon is the low inductive internal structure caused by the optimised voltage measurement and contacting of the three-electrode cell configuration [258]. In addition, it's worthy to note that, due to the uneven current distribution within the experimental cells, the three-electrode configuration measurements with reference electrode occasionally show artefacts, such as inductive loop [263], however, this artefact was not observed in this work. Furthermore, the impedance value of the anode is lower than the cathode at the same frequency. In the anode spectrum, the impedance at the highest frequency almost reaches the real axis, which is commonly considered as the beginning of the high frequency part of lithium ion battery impedance. However, the cathode impedance at the same frequency is still in the semi-circle of the medium frequency range. Such phenomena are consistent with the

results in [258], and the reason can be interpreted as the higher electrical resistances of the cathode NMC material than the anode graphite material.

5.2.3 Multisine signal and experimental plan

To analyse the battery nonlinearity over several operating conditions, the multisine excitation signal was revised accordingly and the experimental plan was designed in this section. Refer to [47], battery nonlinearity varies according to the signal amplitude and the SOC of the battery cell. Thus, in this study, the multisine signal was scaled to various C-rates and applied on the battery cell over a wide range of SOC levels, as given in Table 5.1. The bandwidth of the designed signal was from $10\,\mathrm{mHz}$ to $10\,\mathrm{Hz}$, and the period length was $100\,\mathrm{s}$. A total of 334 odd harmonics out of all $K = N/2 = 2500$ harmonics were excited giving $H_{\mathrm{exc}} = \{1, 5, 7, 9, 13, 15, 21, 23, ..., 999\}$. The sampling frequency f_{s} was set as $50\,\mathrm{Hz}$. Readers can refer to Section 4.2.1 for further details. The designed multisine current signals were applied to fresh three-electrode cells, and the RMS amplitude of the multisine signals were set as $2.3\,\mathrm{mA}$, $5.75\,\mathrm{mA}$, $11.5\,\mathrm{mA}$, $17.25\,\mathrm{mA}$, and $23\,\mathrm{mA}$, corresponding to 0.2C, 0.5C, 1.0C, 1.5C and 2.0C, respectively. In addition, each input signal was repeated at different SOC levels (2%, 10%, 50%, and 90%) for all EL-Cells (see Table 5.1). The state of charge is defined exclusively by the discharge voltage to avoid the SOC uncertainty caused by voltage hysteresis and cell capacity variations. To attain the desired SOC, the battery cell was charged to maximum voltage limit $4.2\,\mathrm{V}$ at $C/10$ CC-CV ($C/50$ current cut-off) profile, then discharged by $C/10$ constant current, via predetermined voltages*, to each of the desired SOCs in descending order, i.e. 90% - 50% - 10% - 2% SOC, as in Figure 5.3 shown.

The 2.0C multisine signal at 50% and 90% SOCs resulted in large voltage drops associated with the high current being applied, and the anode voltage dropped below $0\,\mathrm{V}$ during experiments which indicates the ageing mechanism, known as lithium plating, taking place on the anode [264]. These two operating conditions were therefore excluded from the investigation to prolong cell longevity and minimise undesirable consequences associated with lithium plating. In addition, it was also observed that, at 2% SOC, the voltage data samples didn't occur around the zero mean value and the average terminal voltage of the EL-cell in each period remained decreasing, which indicates that the dynamic voltage response of an EL-Cell did not reach a steady-state behaviour within 10 periods. Thus, the testing was extended to 20 periods from 10 periods to drive the cells into a steady-state behaviour and

---

*The predetermined voltages associated to each SOC levels are decided by Coulomb counting using $C/10$ constant current discharge before the multisine tests.

Table 5.1

Test matrix of studied multisine experiments for EL-Cells at ambient temperature 25 °C. Tested combinations of SOC and C-rate are marked by an 'x' for 10 periods and an '△' for 20 periods.

SOC	C-rate				
	0.2C	0.5C	1.0C	1.5C	2.0C
2%	△	△	△	△	△
10%	x	x	x	x	x
50%	x	x	x	x	
90%	x	x	x	x	

reduce the influence of any transient behaviour for further analysis [152].

As an example, Figure 5.4 presents the averaged measured data (averaged over the 10 periods) of input current and voltage response at 0.2 C-rate excitation and 90% SOC. The positive current value implies a charge process in Figure 5.4a and negative current for a discharge. Furthermore, the error between the measured current and the designed signal is shown in Figure 5.4b which indicates the current error generated by the Biologic VMP3 hardware. In this manuscript, all experiments in this study were conducted in a thermal chamber at room temperature (25°C) and the SOC variation due to the multisine experiment was estimated by the Coulomb counting method [50]. It shows that, for 0.2 C-rate testing, less than 0.01% SOC change occurs over a particular period (refer to Figure 5.4b), and a maximum of 1% SOC change occurs for all other experiments. On the basis of this constraint, the SOC can be treated as a constant throughout the analysis, and the OCV variation during the multisine tests can be neglected [151].

When an excitation signal is applied the initial response of the battery is known as the transient response. After a period of time, the steady state response occurs and is employed for the subsequent analysis [45]. A transient error analysis can be applied to determine whether the battery system has reached steady state. For the calculation of transient error, the last measured voltage period of each experiment was considered, and the transient error was obtained by comparing the voltage response against the previous periods. In this study, after the first 3 periods, the battery system can be considered to have fully passed through the transient stage. Therefore, the first 3 periods were excluded from all datasets in the following data analysis processes to ensure the transient error can be neglected. It is worth noting that, for the 2.0% SOC experiment which requires 20 periods,
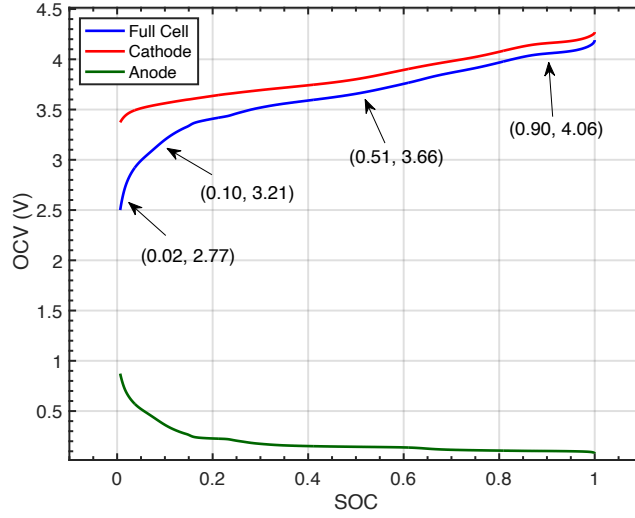
Figure 5.3: Discharge voltage profiles for the anode, cathode and full cell. Annotations illustrate the voltages that correspond to the SOCs 2%, 10%, 50%, and 90%

the first 13 periods were eliminated to reach steady state. Since the input current was designed as a zero-mean signal, the cell system can remain in steady state after passing through the transient stage. As a result, the irregular number of periods has no discernible effect on the interpretation of the data.

In the following section, the battery nonlinearity will be characterised for a full cell and individual electrodes in an three-electrode configuration experimental battery cell, following Equations (3.10), (3.11), and (3.12) in Section 3.3.2. The behaviour of each electrode can be quantified and analysed, which helps to understand the internal behaviour of lithium-ion batteries at various operating conditions.

5.3 Results and discussions

In this section, the frequency domain analysis is performed on the multisine input current and measured output voltage data of the full-cell and individual electrodes obtained from the three-electrode cell. At various SOC and excitation current levels, the electrode responsible for the nonlinearity observed in the full-cell voltage is investigated. Starting with the full-cell voltage, the nonlinearities are analysed across the different SOCs and C-rates, and are separated into odd and even order distortions to evaluate if a particular form of nonlinearity is prevalent in battery dynamics, which can be considered as the basis for nonlinear battery system identification in Chapter 6. Finally, the magnitude of the anode and cathode nonlinearities are studied to
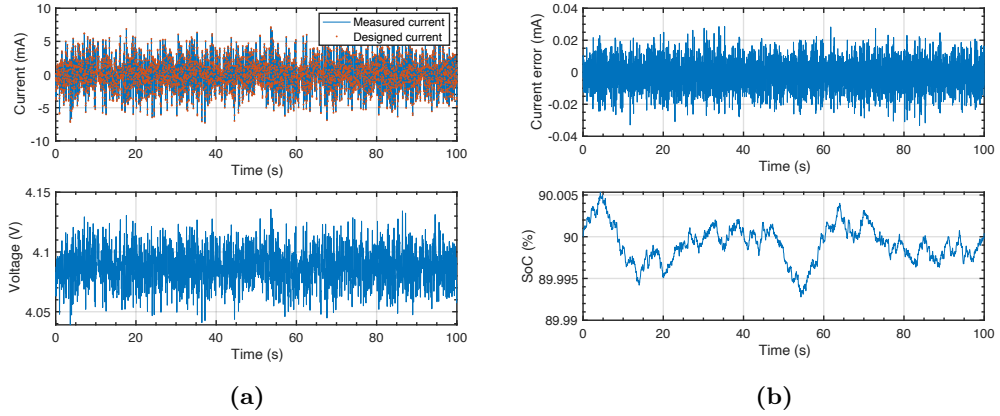
Figure 5.4: One period (averaged over the periods) of the measured current and voltage data at 0.2 C-rate 90% SOC: (a) averaged measured current and voltage, (b) averaged measured current error and estimated SOC.

identify which electrode contributes to the overall nonlinear battery behaviour.

5.3.1 Multisine current input spectrum

In Figure 5.5, the spectrum of the measured current signals for all SOC levels is plotted in the frequency domain. It shows the flat spectrum of the excited harmonics, the signal generator disturbances at the non-excited odd and even harmonics and standard deviation of the noise level. As described in Section 3.3.2, the measured current signal has a flat amplitude spectrum over the excited odd harmonics within 10 mHz to 10 Hz for 0.2C, 0.5C, 1.0C and 1.5C, respectively. Furthermore, the noise spectrum is around 90 dB lower than the excited frequencies spectrum. Note that the MATLAB® function dB was used to calculate the magnitude of the energies in this study. This indicates that the noise impact is minimal for the nonlinearity characterisation, which can be ignored in the following analysis.

As mentioned in Chapter 4, the input current signal was designed with all even and several odd harmonics suppressed. However, in practise, the VMP3 signal generator is unable to provide a near-perfect current signal, thus the harmonic content of the generated or measured current signal is distorted and extra energy is added to the non-excited harmonics. The separation of energy (in the measured current signal) into the non-excited harmonics reveals the type of nonlinearity generated by the signal generator at the excited harmonics. Additionally, in comparison to the energy detected in the excited harmonics, the nonlinearities (odd and even) are relatively low and shift upward as the amplitude of excitation signal increases. The error between the designed and measured current signals, which is shown in

Figure 5.4b, can also be observed in the frequency domain in Figure 5.5. Taking advantage of the nonlinear characterisation method, the error caused by the signal generator is observed and separated into the signal nonlinearities at even and odd non-excited harmonics, while the error induced by environmental noise is seen at all harmonics.
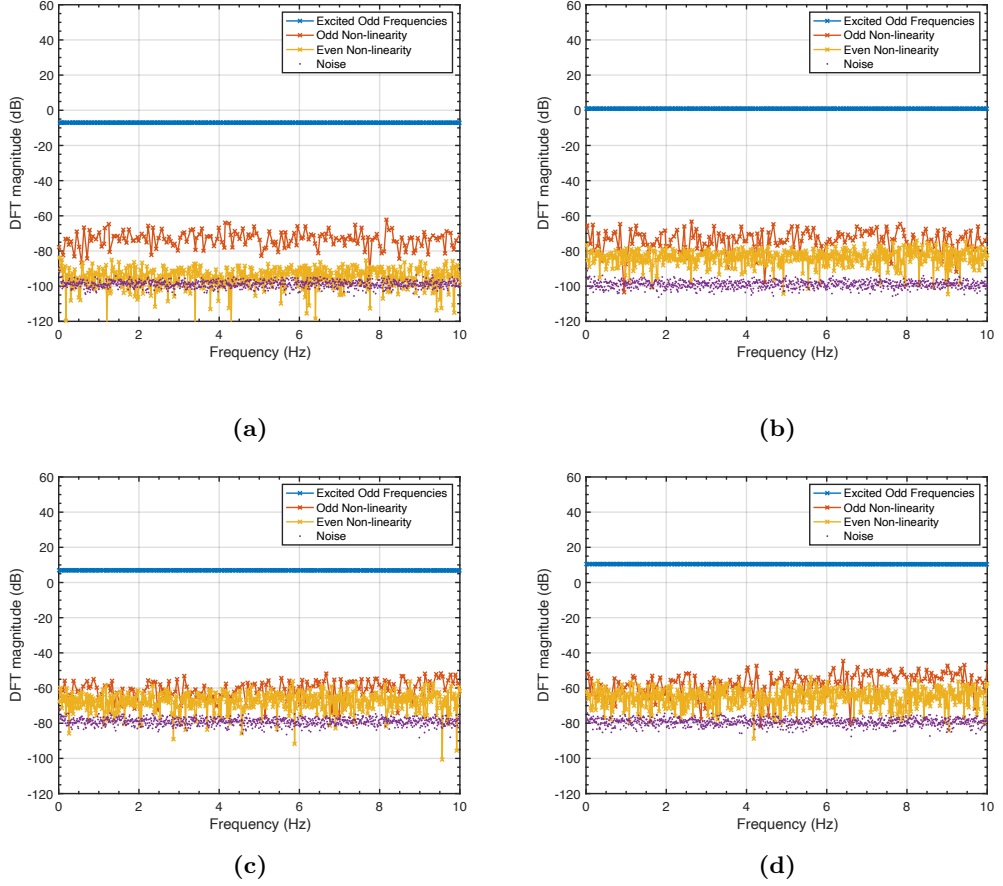
Figure 5.5: Current input spectrum while C-rate is: (a) 0.2C, (b) 0.5C, (c) 1.0C and (d) 1.5C

5.3.2 Dominant nonlinearity analysis - Full-cell

Figure 5.6 presents the full-cell voltage spectrum at the excited harmonics, the battery nonlinearities and the standard deviation of the noise when the multisine signal was at 1.5 C-rate and the cell was set at different SOC levels (90% SOC, 50% SOC, 10% SOC and 2% SOC). Considering the fluctuations of voltage spectrum on various frequencies within the frequency range, the battery voltage spectrum was plotted using the same method as in [47] rather than using mathematical evidence.

The results show that the battery nonlinearities at low SOC levels, such as 10% SOC and 2% SOC, are stronger than at higher SOC levels, and the difference in the even-order nonlinearity between 2% case and 90% case is at most 40 dB. This phenomena demonstrates that the battery exhibits more nonlinear behaviour at lower SOC levels. Furthermore, Figure 5.6 shows that there is no clear separation of the magnitude of even and odd-order nonlinearities within the frequency range when at 90% and 50% SOC, but a clear nonlinearity magnitude separation can be observed at 10% and 2% SOC. In addition, the amplitude of the even order nonlinearity is larger than the odd order nonlinearity. At 10% SOC, the separation is only noticed during the low frequency range and the nonlinearities are of similar magnitude in medium frequency range. However, at 2% SOC, the separation is clear over the whole testing frequency range. Moreover, contrary to the flat noise distortion floor in the other SOC levels, the noise standard deviation at 2% SOC shows a downward slope-type curve, which gradually decreases from -10 dB to -30 dB, indicating some non steady-state behaviour in the voltage response.

Based on the nonlinear behaviour at 10% SOC level, Figure 5.7 shows the variation of the full-cell voltage spectrum when the input current level increases from 0.2 C-rate to 1.5 C-rate, which indicates the effect of C-rate on battery nonlinearities. At 0.2 C-rate, both even and odd order nonlinearities are at the noise level, which means the battery cell was performing linearly. When the current level increases, the nonlinearities shift upwards and separate from the noise floor. Therefore, the upward shifting of nonlinearities indicates that the battery behaviour gradually changes from a linear to nonlinear behaviour. Furthermore, the magnitude of the even order nonlinearity is greater than odd at the low frequency range, especially at the higher current levels. This shows the dominance of the even nonlinearity over the characteristic frequency range of diffusion processes, which is consistent with [47]. Wolff et al. also concluded that the even harmonic is more sensitive than odd harmonic for diffusion processes based on simulation results [228].

From these results it can be concluded that significant nonlinearity occurs at the lowest SOC level and the highest current level. The nonlinearities in the low frequency range vary significantly at various operating conditions, while the even nonlinearity is dominant in the lithium-ion battery. From the aspect of electrochemical reaction processes, since the low frequency range mainly reflects the dynamic response of solid diffusion processes, the results reveal that the diffusion process of solid particles is sensitive to the battery SOC and excitation current, which is consistent with [47]. However, there is currently no theoretical electrochemical explanation of this results.
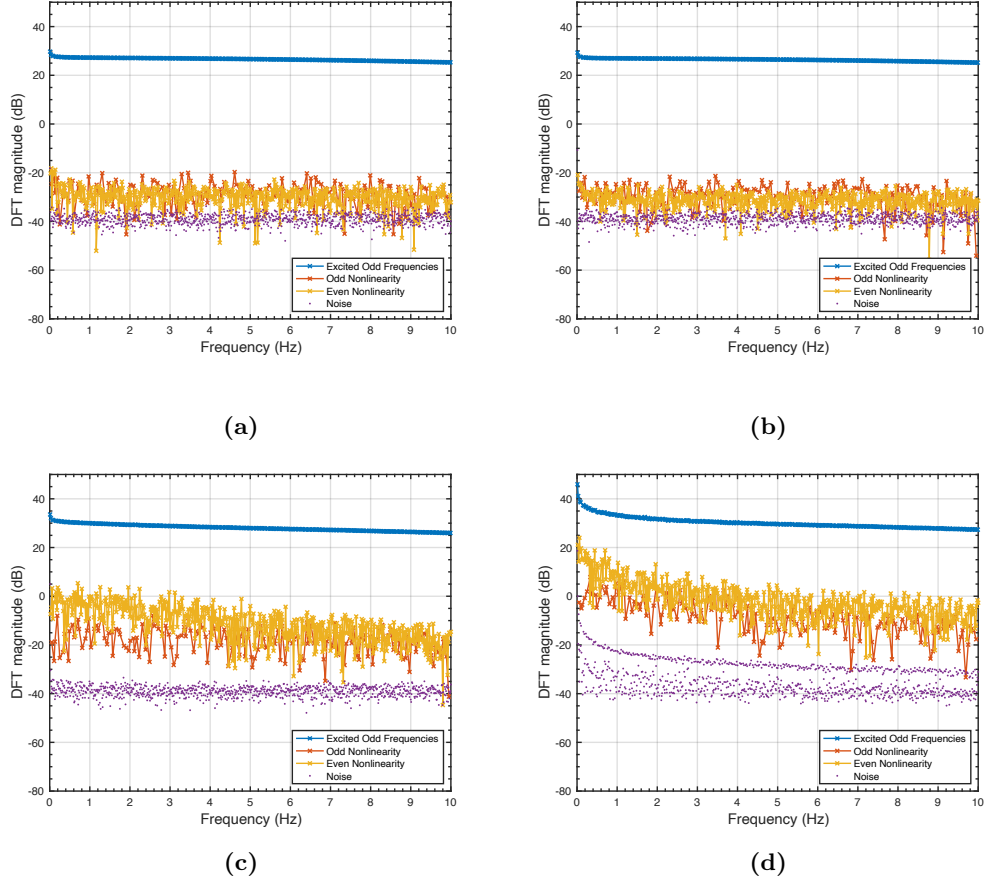
Figure 5.6: Full cell voltage output spectrum at 1.5 C-rate while SOC is: (a) 90% SOC, (b) 50% SOC, (c) 10% SOC and (d) 2% SOC

Compared with the simulation results shown in Figure 4.6, the nonlinearities in the low frequency range in Figure 5.6 exhibits a greater magnitude and a 'ramp' shape (especially at 2% SOC), which could be due to the linear diffusion PDEs utilised in the model but the actual diffusion processes are non-linear. Furthermore, according to the finding in Chapter 4 that the asymmetrical charge transfer coefficient is related to the nonlinearities at middle frequency range and the variation of charge transfer coefficient leads to the changes of nonlinearity magnitude shown in Figure 4.5, the increased magnitude of nonlinearities at 10 Hz indicates that the asymmetry of the experimental cell charge transfer reactions may vary throughout four SOC levels, and it may imply that the magnitude of the kinetic overpotential is not identical and varies during charge and discharge at various SOC levels.
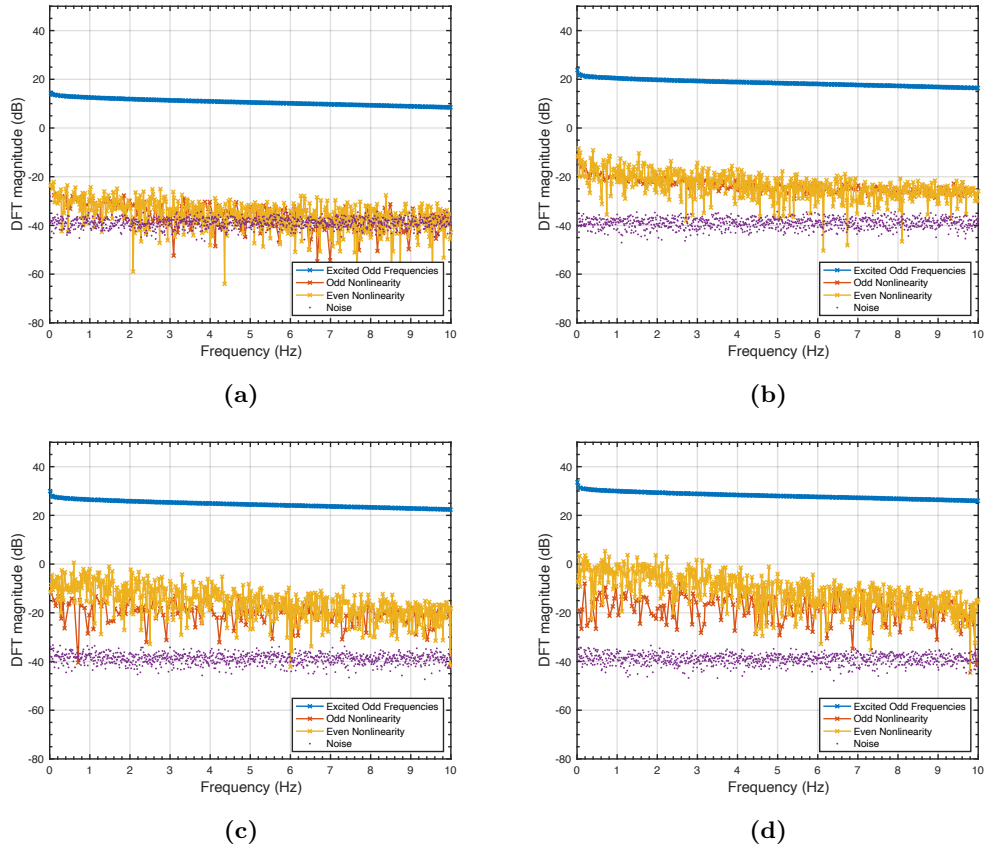
Figure 5.7: Full cell voltage output spectrum at 10% SOC while current signal is: (a) 0.2C, (b) 0.5C, (c) 1.0C, and (d) 1.5C

5.3.3 Dominant nonlinearity Analysis - Electrodes

Taking advantage of the three-electrode configuration experimental cell, the voltage response of the anode and cathode is also recorded while the full-cell data is being captured. Applying the same theory as in the last section, the voltage spectrum of the cathode and anode can be plotted to evaluate the contribution of electrodes to the nonlinearities that have been identified at the full-cell level. The odd and even order nonlinearities of the cathode and anode at two extreme operating conditions (90% SOC/0.2 C-rate and 10% SOC/1.5 C-rate) are extracted and plotted in Figure 5.8 to determine the electrode that contributes the most nonlinearity, which can be considered as the basis for modelling individual electrode system in Chapter 6. For instance, if the cathode provides the most nonlinearity and the anode contributes little nonlinearity, a decoupled-electrode battery model consisting of a nonlinear cathode model and a linear anode model can be developed for greater accuracy. Corresponding to the conclusion of the previous section there is a low level of non-

100

linear distortion at high SOC and low C-rate (90% SOC/0.2C-rate in Figure 5.8a and Figure 5.8b) and a high nonlinearity case when at low SOC and high C-rate (10% SOC/1.5C-rate in Figure 5.8c and Figure 5.8d). In Figure 5.8a and Figure 5.8b, both the cathode and anode nonlinear distortion levels are around the full-cell level, regardless of even or odd order. In contrast, the low SOC and high current rate level (10% SOC/1.5 C-rate) shows a considerable level of nonlinearity in Figure 5.8c and Figure 5.8d. It's clear that the cathode is the major contributor towards the full-cell nonlinearity, as both odd and even nonlinearities of the cathode almost overlap on the full-cell level. Furthermore, the magnitude of the cathode even order nonlinearity is around 20 dB larger than the anode even nonlinearity, and the cathode's odd order nonlinearity is around 15 dB higher than that of the anode. There is a special case when at 2% SOC where the anode nonlinearities start to dominate in the full-cell for the high C-rate currents, which will be discussed in Section 5.3.6.
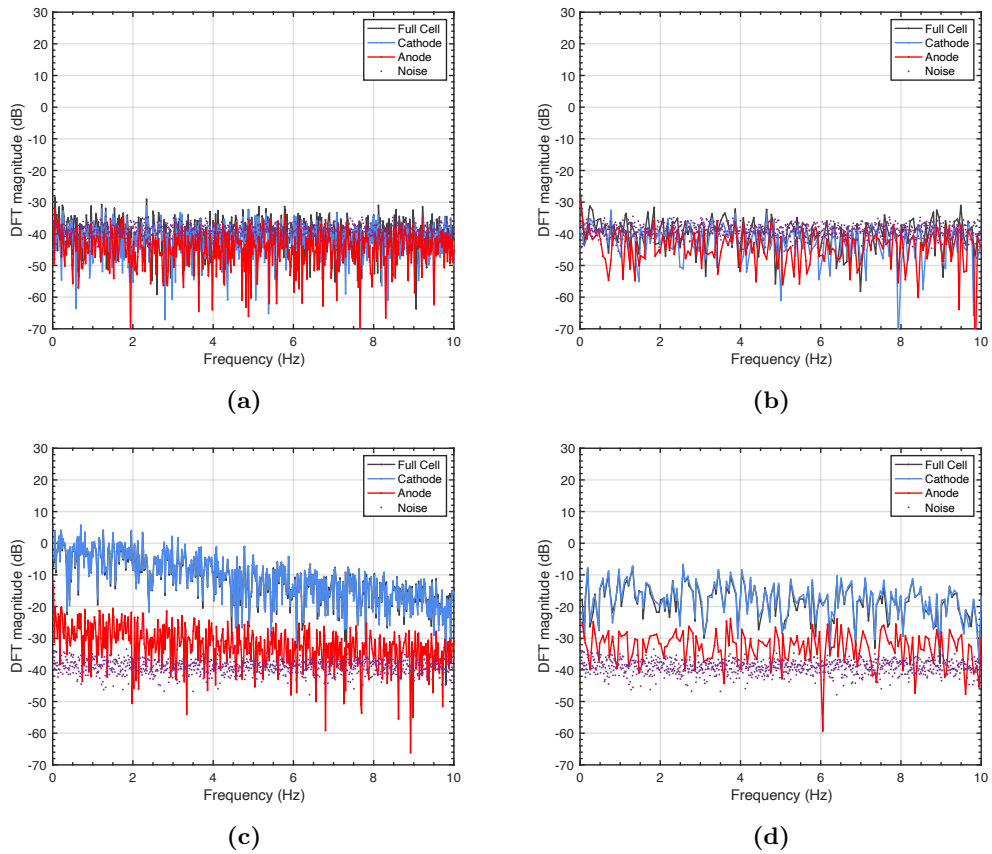
Figure 5.8: Even and odd order nonlinearities of the three-electrode configuration battery cell at: (a) Even order nonlinearity at 90% SOC 0.2C-rate, (b) Odd order nonlinearity at 90% SOC 0.2C-rate, (c) Even order nonlinearity at 10% SOC 1.5C-rate, and (d) Odd order nonlinearity at 10% SOC 1.5C-rate

101

In conclusion, even-order nonlinear distortions from the cathode have been identified as the major contributor towards the full-cell nonlinearity. Therefore, the full-cell nonlinear dynamic behaviour can be better understood by investigating the variation of cathode even non-linearity. In the following sections, the SOC dependency and C-rate dependency of the even nonlinearity of the cathode will be studied.

5.3.4 SOC dependency of cathode even non-linearity

Figure 5.9 shows the even nonlinearity of the cathode at various SOC levels when different C-rate multisine signals are applied. As the SOC level decreases, the magnitude of nonlinearity monotonously increases, which is consistent with [47]. For example, in Figure 5.9d, the cathode even nonlinearity at $10\,\text{mHz}$ raises from $-30\,\text{dB}$ to around $15\,\text{dB}$ when the SOC level decreases from 50% to 2%. Nevertheless, from 90% to 50% SOC, no noticeable increase is observed in the level of nonlinearity. Referring to [228], the exponential trend is also obtained at low frequency range by simulating the model of Fick's law for diffusion process. Therefore, the nonlinearity variations in the low frequency range indicate that the battery nonlinearity caused by diffusion processes depends on the SOC level of a lithium-ion battery. From the minimum frequency $10\,\text{mHz}$ to the maximum frequency $10\,\text{Hz}$, the magnitude difference of the cathode nonlinearity between 2% SOC and 90% SOC decreases from $45\,\text{dB}$ to around $5\,\text{dB}$ correspondingly. It appears that the nonlinearity associated with diffusion processes is susceptible to SOC. Furthermore, given that the conclusion in Chapter 4, the results suggest that, at the same current excitation, the variation in nonlinearity caused by asymmetrical charge-transfer reactions is less substantial than that related by the diffusion process at different SOC levels.

It is also observed (in Figure 5.9) that the cathode even nonlinearity at 2% and 10% SOC substantially increases when the excitation signal C-rate level enhances. However when at 50% and 90% SOC, the level of nonlinearity is low and fairly constant across the frequency range with no clear separation at all four C-rate levels. This suggests that at high SOC levels, the nonlinear behaviour is not as sensitive to the amplitude of the excitation current as it is at low SOC levels. This will be investigated further in the next section.

5.3.5 C-rate dependency of cathode even non-linearity

As a lithium ion battery exhibits different intensities of non-linearity at various C-rates, to investigate the C-rate dependency, the cathode even nonlinearities are
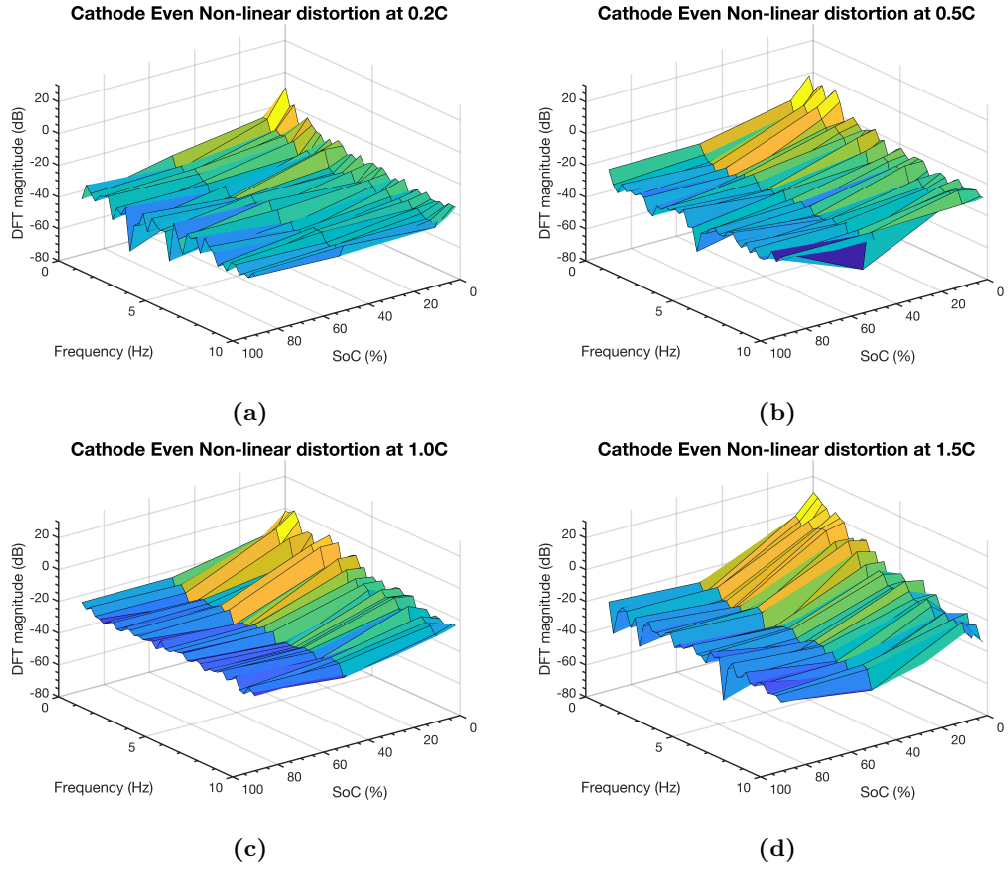
Figure 5.9: Cathode even nonlinearities at various SOC levels while current signal is: (a) 0.2C, (b) 0.5C, (c) 1.0C and (d) 1.5C

shown against each SOC level in Figure 5.10. Consistent with the previous section, the amplitude of the nonlinearity at high SOC levels is similar regardless of the C-rates, as evidenced by a fluctuation of less than 10 dB at 0.01 Hz shown in Figure 5.10a (90%) and Figure 5.10b (50%) but around 30 dB variation at 0.01 Hz (10%) shown in Figure 5.10c. Such results indicate both charge-transfer reactions and diffusion process are not sensitive to different excitation C-rate levels at higher SOC. At lower SOC levels (Figure 5.10c and Figure 5.10d), the even nonlinearity of diffusion processes monotonously increases in the lower frequency range as the C-rate increases. The overall trend of nonlinearity variation rises monotonically with increasing C-rate, which is consistent with [47]. Such results indicate that the diffusion processes show stronger nonlinear behaviour at low SOC regions when the C-rate increases.

However, Figure 5.9d shows an anomaly that the nonlinearity level at 2% SOC is lower than 10% over the medium frequency range with the 1.5C multisine
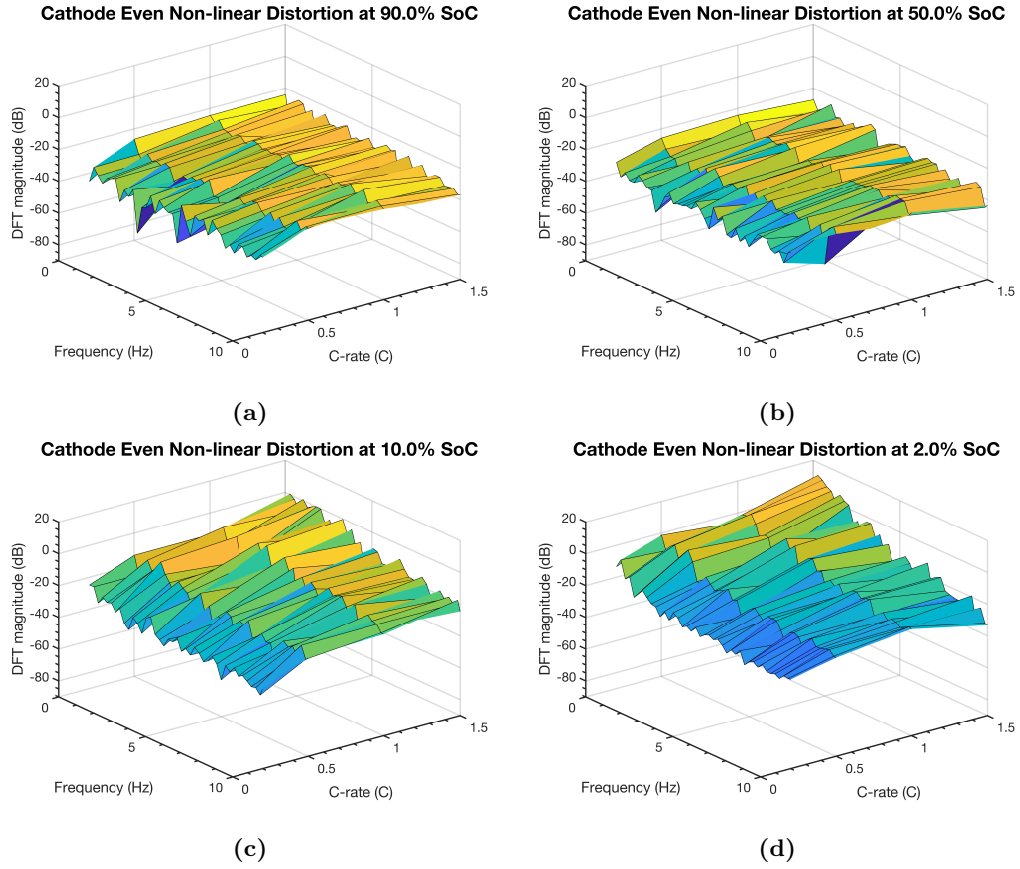
Figure 5.10: Cathode even nonlinearities at various C-rates while SOC is: (a) 90% SOC, (b) 50% SOC, (c) 10% SOC and (d) 2% SOC

current input. This phenomenon does not conform to theory that a higher C-rate excites stronger nonlinearity. In the next section, the special case of dynamic response at 2% SOC will be analysed.

5.3.6 Frequency response at 2% SOC

It's supposed that the 2% SOC dynamics are different due to the extreme distribution of lithium ion concentration between cathode and anode. Therefore, to investigate this behaviour, the even and odd nonlinearities of the cathode and anode at 10% and 2% SOC levels are plotted in Figure 5.11. Overall, the even nonlinearity is still the dominant contributor in either the anode or cathode, and is about 10 dB larger than the magnitude of odd nonlinearity. However, Figure 5.11c shows that the major contributor towards the even nonlinearity shifted from the cathode to anode around 2 Hz at low SOC (2%), which suggests that the anode's dynamics changed under low SOC levels and that a "empty" anode behaved more nonlinearly

than a "full" anode. However, there is currently no electrochemical explanation for the observed results.
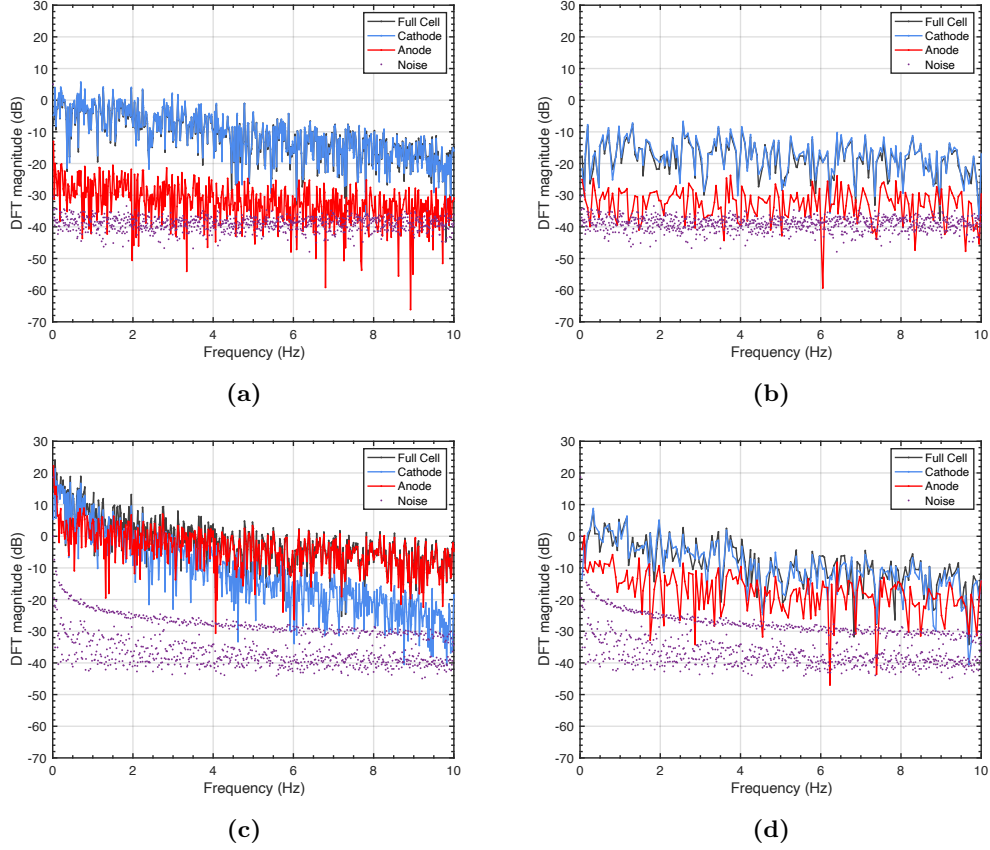
Figure 5.11: Nonlinearities of the experimental cell at 1.5 C-rate: (a) even nonlinearity at 10%, (b) odd nonlinearity at 10% SOC, (c) even nonlinearity at 2%, and (d) odd nonlinearity at 2% SOC

Focusing on this low SOC condition, the even and odd nonlinearities at 2% SOC when excited by different C-rates signal are shown in Figure 5.12 and Figure 5.13, respectively. Consistently, the cathode remains as the dominant contributor towards the odd nonlinearity between individual electrodes at every current level (see Figure 5.13). However, as the C-rate increases, the anode's even nonlinearity increased substantially and became dominating. The variation of the cathode even nonlinearity magnitude increased by around 20 dB from 0.5 C-rate to 2.0 C-rate, nevertheless, there was almost a 30 dB magnitude rise for the anode. Referring to [228], the simulation results show that, as the asymmetry of charge-transfer kinetics varies, the nonlinearity of even harmonic is significantly excited, which is also corroborated in Chapter 4. Therefore, the low lithium ion concentration in anode and

high C-rate may generate a large kinetic overpotential change on the anode during charge and discharge at 2.0% SOC. As the 2.0% SOC here is the average SOC level at equilibrium state of battery, as opposed to the 10% SOC situation, while the battery at 2% SOC was excited by a high C-rate current, the surface SOC on the anode particles may reach below 0% and over-discharge due to polarisation, thereby increasing the even nonlinearity. Hence, when analysing non-linear behaviour, the 2% SOC level should be paid attention as a special case.
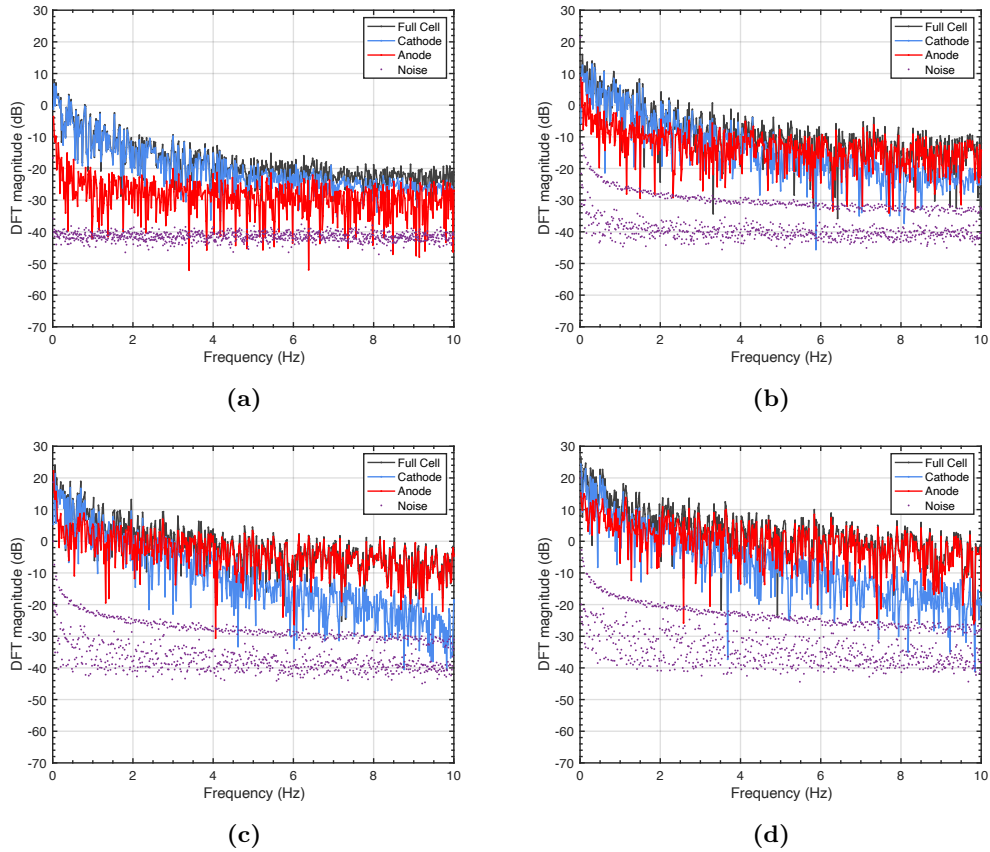
Figure 5.12: Even nonlinearities of the experimental cell at 2.0% SOC while at : (a) 0.5C, (b) 1.0C, (c) 1.5C and (d) 2.0C

5.3.7   Reproducibility of multisine method

To verify the reproducibility of the multisine nonlinear characterisation method, two additional EL-cells, termed as Cell 2 and Cell 3, were constructed using the same manner as described in Section 5.2.1 and characterised by the multisine signal. Frequency voltage response and nonlinearities of three experimental EL-Cells at 1.5 C-rate current signal are presented in Figure 5.14. Note that the results of
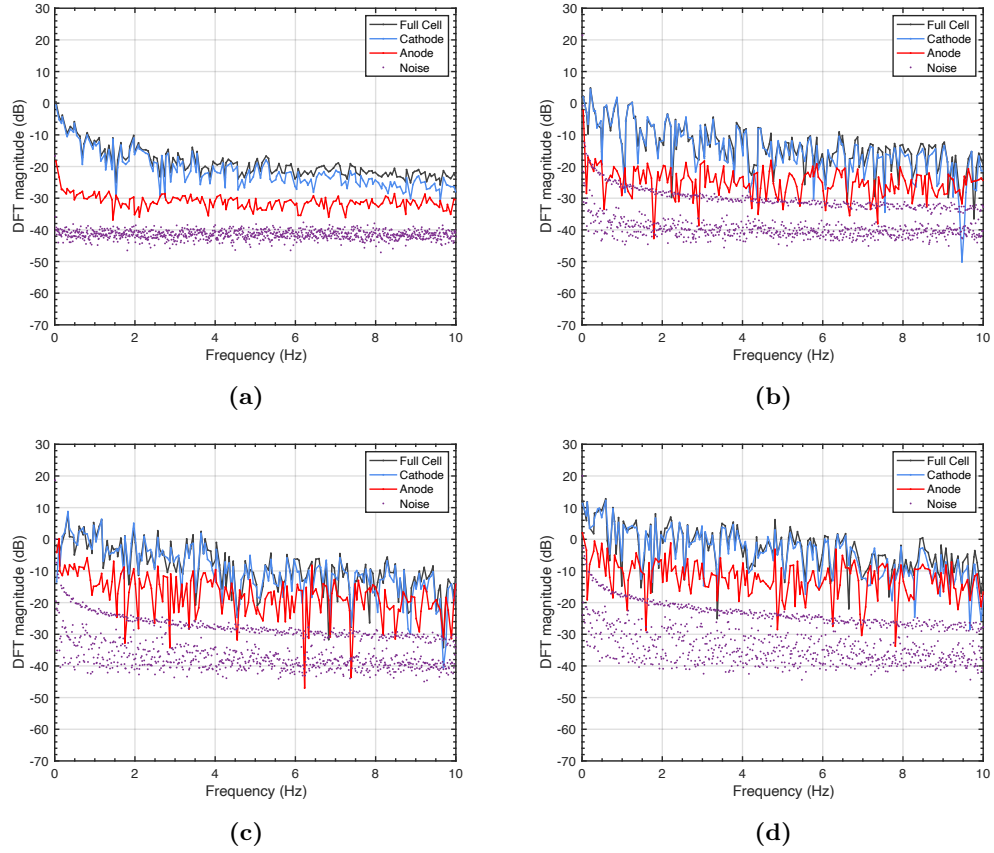
Figure 5.13: Odd nonlinearities of the experimental cell at 2.0% SOC while C-rate at: (a) 0.5C, (b) 1.0C, (c) 1.5C and (d) 2.0C

Cell 1, which are shown in Figure 5.14a, 5.14d, and 5.14g, have been analysed in previous sections. As presented in 5.14, it is evident that all three cells exhibit consistent frequency voltage responses and nonlinearities, which suggests that the characteristics of Cells 2 and 3 are comparable to those of Cell 1, and results of the multisine method can be reproduced with different battery cells.

Furthermore, the multisine method was applied on two commercial 5 A h LGM50 21700 cells, termed as LGM50 Cell1 and LGM50 Cell2, for nonlinear characterisation. The same hardware configuration as in previous sections was employed for signal generation and recording measurement, and a 10 A current booster was interfaced to the VMP3 to scale the multisine signal for commercial cells. In this case, due to the limitation of maximum current amplitude, the RMS of the multisine signal was scaled to 5 A (1.0C) for LGM50 cells. Figure 5.15 presents that frequency voltage responses and nonlinearities of two commercial LGM50 21700 cells at 1.0C. It is obviously to observe that the results of LGM50 Cell1 are consistent with those of
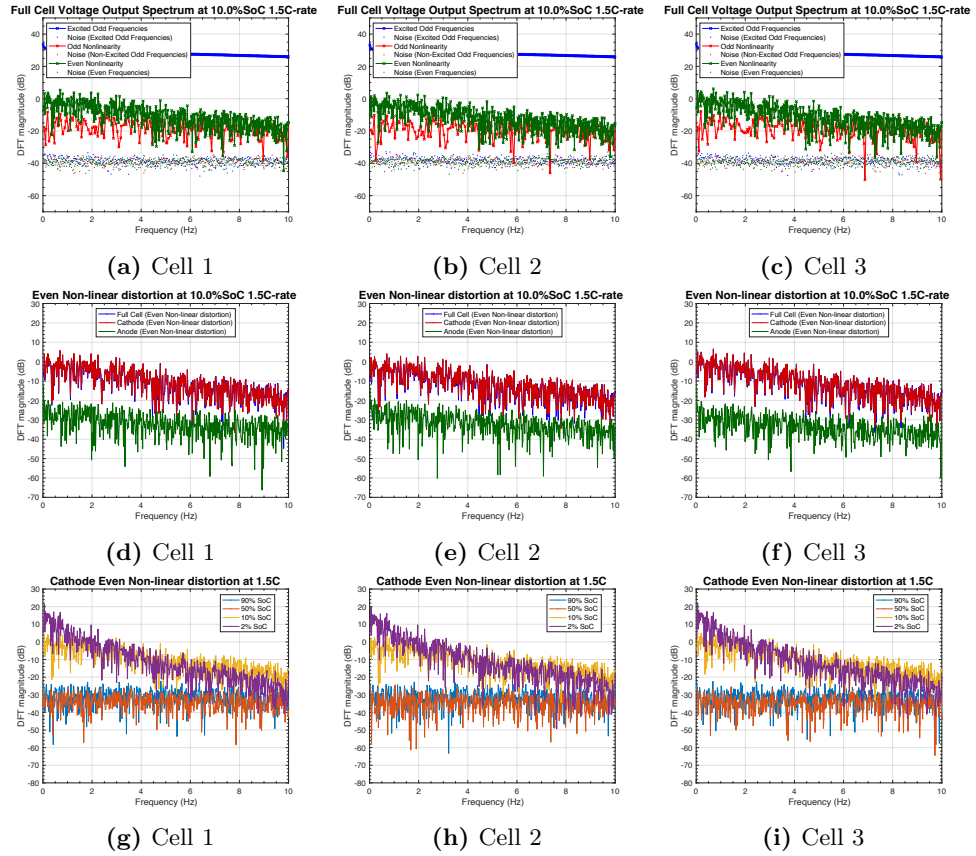
Figure 5.14: Frequency voltage response and nonlinearities of three experimental EL-Cells while current signal is 1.5 C-rate: (a), (d), (g) Cell 1, (b), (e), (h) Cell 2, and (c), (f), (i) Cell 3

LGM50 Cell2. In Figure 5.15a and 5.15b, the frequency voltage response spectrum at 10% SOC are plotted. The linear response and even and odd order nonlinearities are separated. Consistent with the nonlinearities of experimental EL-cells, the even nonlinearity is dominant in the low frequency range. Two noise levels (purple dots) with a magnitude greater than the nonlinearities are visible in the spectrum, indicating that the experimental setting is not optimal. Such results may be a result of the current booster's introduction, which requires more optimisation in the future work. In addition, the even and odd order nonlinearities at various SOC levels are presented. It shows that the even order nonlinearity at low SOC (10%) is larger than those at higher SOC levels, and odd order nonlinearities exhibit comparable magnitude at various SOC levels. These findings are congruent with those obtained using experimental EL-cells, indicating that the multisine method is reproducible and suitable for commercial battery cells.

(a) LGM50 Cell1

(b) LGM50 Cell2

(c) LGM50 Cell1

(d) LGM50 Cell2

(e) LGM50 Cell1
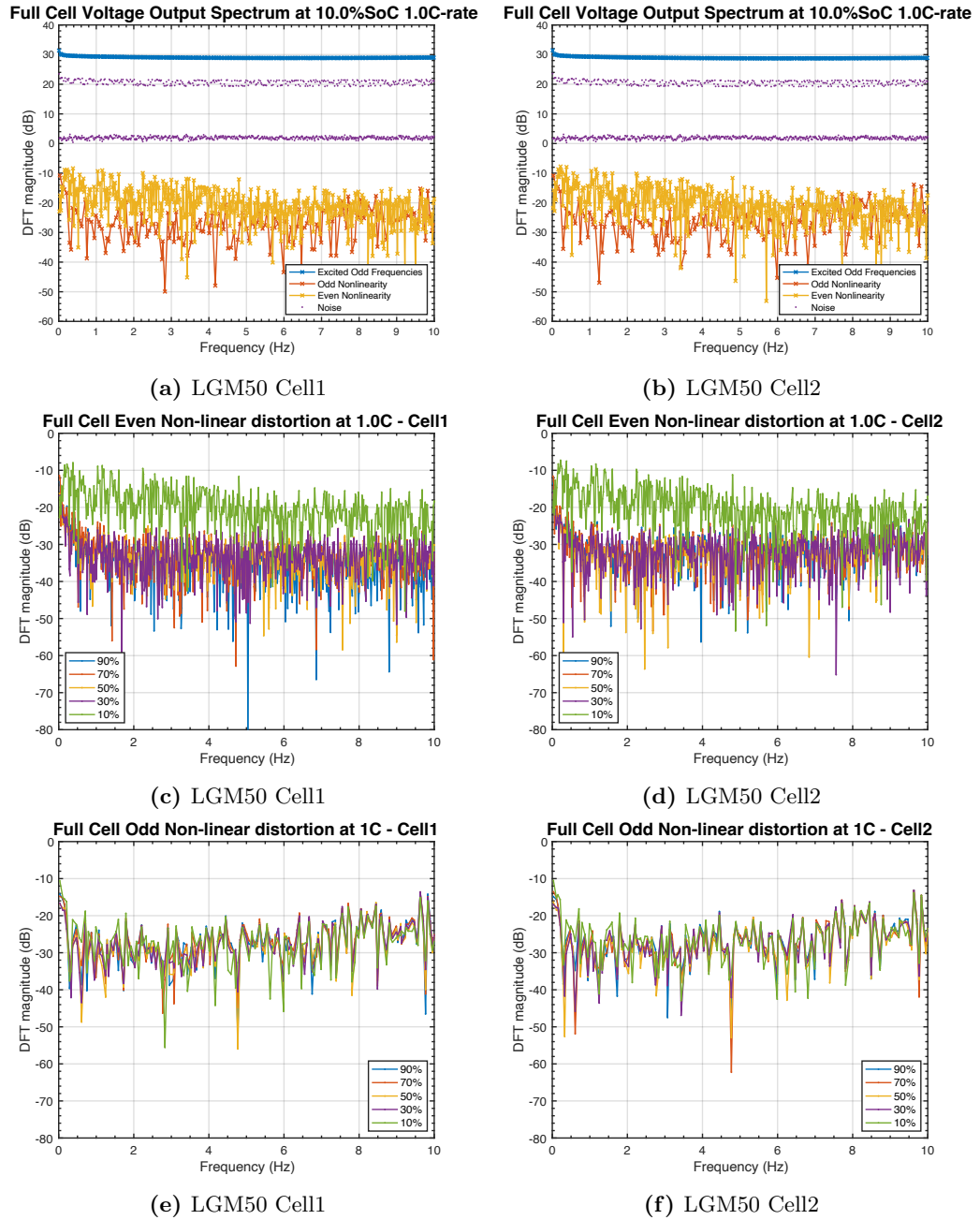
(f) LGM50 Cell2

Figure 5.15: Frequency voltage response and nonlinearities of two commercial LGM50 21700 cells while current signal is 1.0 C-rate: (a), (c), (e) LGM50 Cell1, and (b), (d), (f) LGM50 Cell2

5.4 Conclusion

In this chapter, non-linear distortions of NMC lithium-ion three-electrode configuration cells have been experimentally characterised using the multisine-based method proposed in Chapter 4. These distortion analysis was performed over a wide range of excitation signal amplitudes and SOC levels. The random phase odd multisine with all even and several odd harmonics suppressed were employed as an excitation input current signal, which leads to a 8 times faster characterisation procedure of the battery nonlinearity than the NFRA technique. The analysis, which focused on the diffusion processes and charge-transfer reactions of the cathode, anode and full-cell, was performed by analysing the non-excited harmonics in the voltage output spectrum, which provides valuable information for contributing to knowledge of battery nonlinearity at cell level. Currently, there is no evidence that nonlinear characterisation methods can be used as on-board techniques for commercial battery modules or packs. This may be because BMS hardware cannot provide sufficient current or voltage excitation signals for large-scale battery modules and packs.

Overall conclusions of this chapter are summarised as following: First, it can be concluded that nonlinearities are very low at high SOCs ($>10\%$), as such the battery current to voltage relationship is behaving linearly in these regions. From the perspective of battery modelling, a linear model suffices to emulate the current-voltage relationship of a lithium-ion battery at the high SOC region. Moreover, at low SOCs ($\leqslant 10\%$), the nonlinearities of a lithium-ion battery significantly increase, and the even nonlinearity originating from the cathode was determined as the dominant contributor of a lithium-ion battery. Possible sources for this nonlinearity include the considerable change of electrode open circuit voltage that occurs at low SOC for the cathode, and the diffusion processes due to the high concentration of lithium ion in the cathode. The open circuit voltage is an important factor for this phenomenon, however, at the moment, the multisine characterisation method can only capture battery nonlinearity related to diffusion process and charge-transfer kinetic, however, the contribution related to the thermodynamic (open circuit voltage) has not been separated and analysed. Thus, it merits further investigation to decouple the contribution of thermodynamic towards battery nonlinearities. Additionally, the dominance of the even nonlinearity indicates that an even order nonlinear characteristic function may be required for modelling non-linear behaviour of a lithium-ion battery. Lastly, the dynamics of the anode changes when at 2% SOC and starts to contributes with a significant even-order nonlinear distortion comparable to that of the cathode. Overall, this chapter experimentally investi-

gates the contribution of battery diffusion process and charge transfer kinetics to nonlinearity by employing the developed multisine-based nonlinear characterisation method, which fulfils the requirement of "**Research Objective (2):** Understand the electrochemical processes contributing to nonlinearity." In addition, this chapter concludes that diffusion process mainly contributes nonlinearity at low SOC range, which indicates that lack of interpretation of diffusion process could be the reason of linear ECM models' inaccuracy in the low SOC area. Thus this chapter suggests the nonlinearity-related diffusion process merits to be modelled during the battery system identification in Chapter 6.

As proposed in Chapter 1, strong nonlinearity of battery is defined as a factor that the existing linear ECM models could hardly provide accurate voltage and SOC results in low SOC range, and an overestimation of SOC could lead to battery energy exhaustion before expectation and force the EV into limp-home status [39]. As a result, a certain part of battery energy needs to be reserved in real-world applications by technically setting a relatively large SOC cut-off, and the battery energy could hence not be fully implemented and the EV driving range is restricted. If a sophisticated model can be developed to account for these nonlinearities then the model accuracy at low SOCs can be improved, thus the artificially set cut-off can be released and the driving range of EV can be extended without additional cost. From the perspective of frequency domain system identification theory, the nonlinearity of the battery has to be captured and quantified in advance. Furthermore, according to the characterised level of the nonlinearity, it can be accounted for using an appropriate nonlinear function (e.g. sigmoid, neural nets or polynomials) and coupled with linear equivalent circuit models to improve model accuracy, as the nonlinear equivalent circuit models introduced in Chapter 2. Therefore the multisine current signal and voltage response, is not limited to nonlinear characterisation, but can also be used to model the voltage losses and necessary time-constants in the voltage dynamics. In addition, the voltage response and nonlinearity of individual electrodes are captured by using the three-electrode cell configuration in this chapter, and the cathode is determined as dominant nonlinearity contributor. Thus, an decoupled-electrode battery model, which consists of a nonlinear cathode model and a linear anode model, can be developed, and it will have the advantage of providing the voltage response of each electrode and can be validated with widely-used electrochemical models (such as an SPMe which explicitly account for anode and cathode losses) to evaluate the accuracy at low SOC levels. The identification procedure and validation of the developed battery model is presented and discussed within Chapter 6.

Chapter 6

A Nonlinear Equivalent Circuit Battery Model with Diffusion Dynamics[†]

6.1 Introduction

This chapter presents an unique equivalent circuit battery model and corresponding system identification procedure to fulfil "**Research Objective (3):** Develop a battery mathematical model which requires minimal identification cost while achieving a high level of accuracy over the entire SOC range." As introduced in Chapter 2, a conventional linear equivalent circuit model (ECM) utilises a number of simple electrical circuit components, such as resistors, capacitor and inductors, to imitate the current and voltage relationship of a lithium-ion battery [40]. Taking advantage of the lower computational load and fewer parameters than electrochemical models, the ECM is widely employed in battery management systems for model-based state-estimation methods [14, 114, 115]. However, there are numerous restrictions that may result in the model being inaccurate and limit future applicability; An ECM is a phenomenological description and cannot directly associate an electrical circuit component to a certain battery physical phenomena, which limits the detailed insight of lithium-ion battery behaviours. Additionally, ECMs are Linear Parameter Varying models. The model parameters (ohmic resistance and time constants) can vary with SOC and temperature, but the current to voltage relationship is linear for any given operation condition, and then nonlinear behaviour of batteries is absent from conventional ECMs. Furthermore, ECMs are typically at most 2nd order (2

[†]Parts of this chapter have been published in [3]

RC pairs) and usually parameterised via HPPC pulses [40]. The losses, which is accounted for by the model, are the Ohmic loss (via the series resistor) and the polarisation loss (via the 2 RC branches). These are low time constant ($\sim$ 10s of seconds) losses, and an ECM therefore does not account for large time constant ($\sim$ 1000s of seconds) losses due to diffusion dynamics. Although Warburg elements are used to account for emulating large time constant behaviour, however, as mentioned in Chapter 2, these elements currently are only applied in frequency domain ECMs, which are hard to be implemented in practical BMS applications, due to the difficulty in identification and the lack of appropriate numerical approaches for implementation. These limitations must be addressed in order to increase the fidelity of ECMs.

From a modelling standpoint, the probable sources of low-SOC-area error, which are identified in Chapter 1 as battery nonlinearity and large time constant dynamics, are required to be integrated into the conventional ECMs to improve model accuracy. As described in Chapter 4 and 5, battery nonlinearity has been firstly characterised and analysed by applying the proposed multisine-based nonlinear characterisation method. The experimental results presented demonstrate that lithium-ion batteries exhibit a stronger nonlinear current-voltage relationship at the low SOC region, which is consistent with the hypotheses regarding probable sources of considerable low-SOC-area error proposed in [39]. However, it remains an open question whether properly interpreted nonlinearity can increase the accuracy of equivalent circuit battery models. Note that additional degrees of freedom for interpreting nonlinearity is not considered in this work, as it is seldom studied in ECM modelling literature [33, 152]. In addition, large time constant dynamics due to diffusion processes are also necessary to be taken into consideration for modelling. On contrary to electrochemical models, the effect of diffusion processes in a lithium-ion battery is seldom considered in the ECMs, which leads to poor accuracy in long time (low frequency) operational cases [265]. To the best of the author's knowledge, there is only few literatures took into account the diffusion processes in the ECM modelling. Wang et al. proposed to incorporate the effect of diffusion processes as a resistance into an one resistor-capacitor (RC) pair model to improve the power prediction [265]. However, the diffusion resistance is assumed as an additional conventional resistance in the RC pair and is not considered during the ECM parameter estimation. To enhance the model accuracy at the low SOC range, Ouyang et al. proposed an extended equivalent circuit model (EECM) to represent the effect of diffusion processes to terminal voltage by considering the SOC difference in electrode particles calculated from two RC branches [39]. Unfor-

tunately, the charge-transfer kinetic is still hidden in the two RC branches which are in essence linear components and cannot capture battery nonlinearity, and the number of EECM parameters that needs to be estimated increases from six to ten for addressing the diffusion effect only. In [266], the authors incorporated three distinct diffusion models, such as using a common Resistor-Capacitor (RC) circuit element and using a diffusion equation in an idealised particle with or without the parameter indicating the open circuit voltage curve dependency on SOC, into conventional linear ECMs, respectively. The results show that the diffusion models improved the voltage prediction capabilities when compared to a ECM not including any diffusion. However the performance of the suggested ECM with diffusion was evaluated by comparing it to convention ECMs under dynamic current loads rather than including the physical-based electrochemical models, as well as the performance over a long time constant current charge or discharge was not considered. In [49], a fractional-order model is proposed to interpret dynamics in a lithium-ion battery including an electrochemical impedance spectroscopy (EIS) sub-model for mid-high frequency dynamic. However, transformation of EIS model elements into the time domain for real-time applications is not trivial. Thus, an advanced model with a high computational efficiency and ease of implementation that can also capture the physical meaning and nonlinearity of batteries is still missing and would be beneficial to develop for real-world applications.

In this chapter, an advanced non-linear equivalent circuit model with diffusion dynamics, termed as NLECM-diff, is established by employing a data-driven identification approach, and the model can explicitly interpret the essential physical phenomena in a lithium-ion battery such as ohmic, charge-transfer kinetics, and diffusion dynamics. In the NLECM-diff, a non-linear equivalent circuit model (NLECM) encompassing a linear block for ohmic impedance and a non-linear block for charge-transfer kinetics is identified by applying the multisine-based nonlinear characterisation method on a 21700 LGM50 NMC three-electrode configuration experimental cell. Note that the characterisation method and experimental cell are identical to those utilised in Chapter 5. In addition, a lumped diffusion model inspired by the single particle model using a SOC equation in an idealised particle is incorporated into the NLECM for interpreting the large time constant losses due to diffusion dynamics in the terminal voltage on the cell level [266]. The NLECM-diff model is fully parameterisable with voltage and current data without the need to perform specific experiments to get geometric, transport and kinetic parameters. Additionally, taking advantage of the experimental cell with a stable reference electrode, NLECM-diff models for cathode and anode are also identified to estimate

the internal electrode potential variable. The accuracy of the NLECM-diff models are compared to that of the single particle model with electrolyte dynamic (SPMe) proposed in [38] when validation experiments including both a long time constant discharge and charge profile and a strong dynamical driving cycle are conducted.

The remainder of this chapter is organised as follows: Section 6.2 explains the modelling approach of the non-linear equivalent circuit battery model with diffusion dynamics (NLECM-diff), including a frequency domain identification method for the NLECM and a parameterisation process for the diffusion model. The advantage of the proposed model over the reference model NLECM is also evaluated and analysed in Section 6.3. The model validation and performance comparison to the electrochemical model are discussed in Section 6.4. Section 6.5 presents the conclusion of this research.

6.2 Methodology of model identification

As demonstrated in Chapter 5, a lithium-ion battery is a nonlinear system exhibiting a non-linear voltage response caused by electrochemical behaviour when at different SOC levels and excitation input cases. However, for conventional ECMs, any nonlinearity is commonly neglected and the interpretation of physical phenomena are discarded. This chapter tries to develop a unique model, as shown in Figure 6.1, to associate the electrochemical behaviours in a lithium-ion battery, which consists of a linear equivalent circuit model for ohmic and polarisation losses, a nonlinear sigmoid function for the nonlinear current-voltage relationship caused by the charge-transfer kinetics, an OCV-SOC block, and a simplified SOC dependent diffusion block for voltage loss caused by diffusion processes.

6.2.1 Experimental setup and identification procedure

Figure 6.2 shows the experimental setup for battery testing, which includes the three-electrode experimental EL-Cell, a charge and discharge test equipment (VMP3), a thermal chamber and a programmable upper computer. The battery was mounted in a thermal chamber at 25 °C for maintaining the cell surface temperature, and a VMP3 hardware was utilised to control the cell and record experimental data.

In addition, the data-driven identification procedure and corresponding battery tests presented in Figure 6.3 were performed to fully characterise and validate the NLECM-diff model, including a OCV test for the OCV-SOC curve, multisine tests for the linear ECM and nonlinear sigmoid function, and a fully 0.5C constant current (CC) discharge test for the SOC dependent diffusion block. Following that,
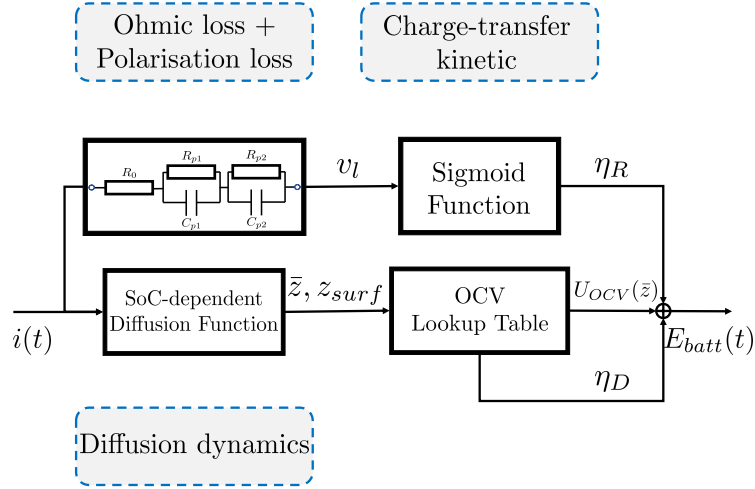
Figure 6.1: Lithium-ion battery NLECM-diff structure. The overall model consists of a linear ECM followed by a non-linear over-potential function, a parallel OCV block, and a parallel diffusion block.

0.3C/0.5C/1.0C CC discharge and CC-CV charge tests, as well as a NEDC test, were performed to validate the proposed model. In this study, 0.3C, 0.5C, and 1.0C correspond to low, medium, and high current conditions, respectively. To evaluate the model accuracy at low and high C-rates conditions, the medium 0.5C CC discharge test was used for system identification. The following subsections describe the identification steps of the corresponding model blocks in detail. Note that, in this chapter, the design of identification methodology and characterisation tests, data collection and analysis, as well as model validation were the author's original work. Three-electrode configuration experimental cells and the driving cycle (NEDC) profile were provided by collaborators from University of Birmingham.

6.2.2 Impedance estimate and equivalent circuit transfer function

For a lithium-ion battery, its impedance is commonly recognised as the linear part of battery dynamics response [152]. In the first step, an linear equivalent circuit model (ECM) is estimated by fitting the model parameters based on the best linear approximation from the measured current and voltage dataset. With the assistance of the periodic characteristic of multisine signal, a non-parametric function of battery impedance estimate can be obtained [233]. The multisine tests were conducted at 2%, 10%, 30%, 50%, 70%, and 90% SOC levels and $P = 10$ successive periods multisine signal for each SOC levels in this study. To acquire an impedance estimate under steady-state conditions, the first three periods of the measured dataset were reserved for validation, and Period 4-10 were used for parameterisation. Consider-
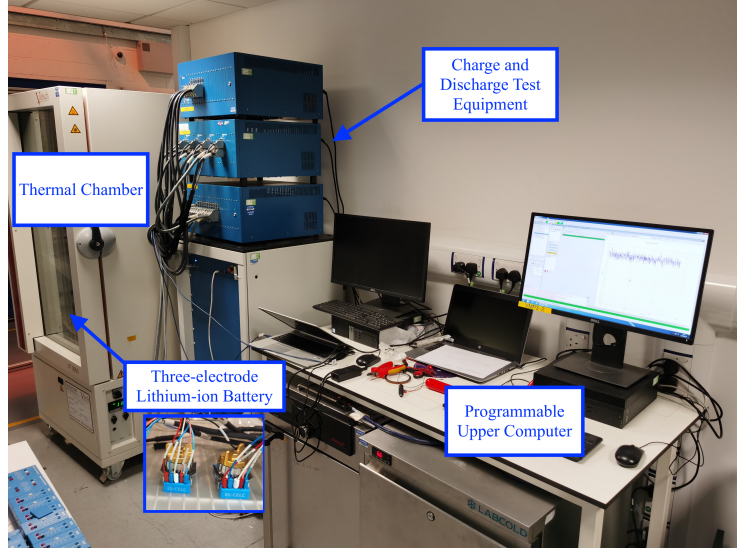
Figure 6.2: Experimental setup of data-driven identification and validation.

ing the discretised current and voltage measurement data in the remaining $P - 3$ periods, the averaged data over periods can be obtained as:

$$\bar{i}(n) = \frac{1}{P-3} \sum_{p=4}^{P} i^{[p]}(n), \quad \bar{v}(n) = \frac{1}{P-3} \sum_{p=4}^{P} v^{[p]}(n) \qquad n = 0, 1, ..., N-1 \quad (6.1)$$

where p indicates the pth period of the current $i(n)$ and the voltage data $v(n)$ measured at a given SOC.

As the thermodynamics would be accounted for by the OCV block and the diffusion process has no effect on voltage output during each multisine test when the SOC change is minimal, the *over-potential*, denoted as $\bar{v}_0(n)$, can be calculated by removing the mean voltage at the corresponding SOC from $\bar{v}(n)$ prior to estimating the impedance [152].

$$\bar{v}_0(n) = \bar{v}(n) - \frac{1}{N} \sum_{n=0}^{N-1} \bar{v}(n) \qquad (6.2)$$

Then, by the Discrete Fourier transform (DFT), the time domain measured data can be transformed to frequency domain, termed as current and voltage spectra of pth period:

$$I(k), \quad V(k) \qquad k = 0, 1, ..., N-1 \qquad (6.3)$$

117
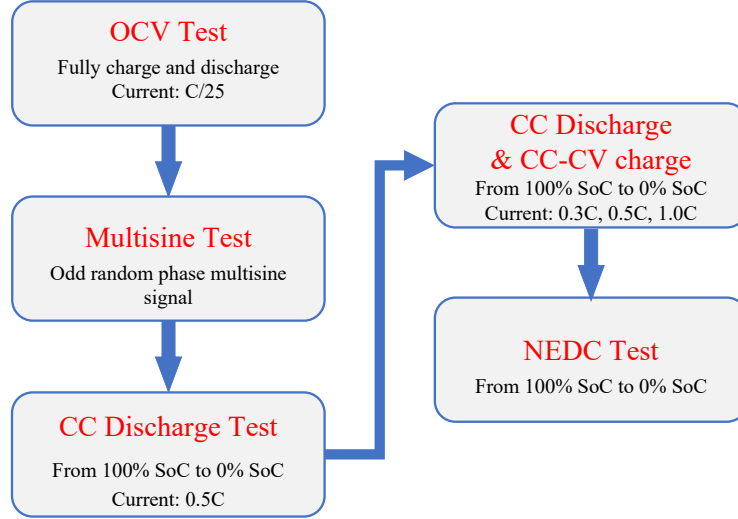
Figure 6.3: Flowchart of the data-driven identification procedure and the corresponding battery tests.

where $I(k)$, $V(k)$ in Equation (6.3) denote the DFT of $\bar{i}(n)$, $\bar{v}_0(n)$ at the kth harmonic.

In the frequency domain, the relationship between DFT voltage $V(k)$ and the DFT current $I(k)$ through the battery impedance $Z(k)$ is

$$V(k) = Z(k) \times I(k) + E(k) \tag{6.4}$$

where $E(k)$ indicates the summation of error from any practical environment and distortion from non-linear battery behaviour.

The spectrum of over-potential $V(k)$ in the frequency domain at 10% SOC with 1C multisine current input is shown in Figure 6.4a. Odd random phase multisine enables us to separate and quantify the odd and even nonlinearities through suppressed harmonics $H_{\text{supp,odd}}$ and $H_{\text{supp,even}}$, which can provide further insight about lithium-ion battery non-linear behaviour. Details on the non-linear characterisation method can be found in Chapter 5. Given $V(k)$ in Figure 6.4a and $I(k)$ in Figure 5.4, both the impedance $Z(k)$ and standard deviation $E(k)$ can be estimated by minimising the error term using the local-polynomial method (LPM) [152, 267], as shown in Figure 6.4b. The estimated impedance to standard deviation ratio was more than 25 dB, which indicates the high confidence of this impedance estimation.

Then, a transfer function was fitted to the estimated impedance.

$$Z_{\text{m}}(k) = \frac{b_{\text{nb}}(j\omega_{\text{k}})^{nb} + ... + b_1 j\omega_{\text{k}} + b_0}{(j\omega_{\text{k}})^{nb} + ... + a_1 j\omega_{\text{k}} + a_0} \tag{6.5}$$
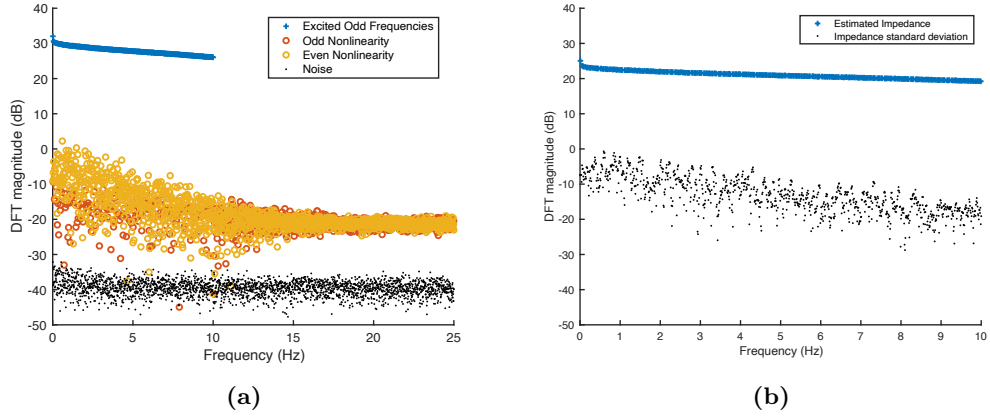
Figure 6.4: (a) Over-potential spectrum and (b) Estimated impedance and standard deviation at 10% SOC of an experimental cell.

where $Z_{\mathrm{m}}(k)$ denotes a transfer function model, $\omega_{\mathrm{k}} = 2\pi k f_{\mathrm{s}}/N$ is the discrete angular frequency at harmonic k, and nb is the model order. The coefficients of Equation (6.5) can be identified by minimising the error between the transfer function output and the estimated impedance. In this work, the Frequency domain System Identification Toolbox in Matlab® is applied to estimate transfer function coefficients [268].

Figure 6.5 shows the 1st and 2nd order transfer function fits of the impedance which indicates that the 2nd order model has a better agreement between the estimated impedance and fit than the 1st order, which shows the advantage of multisine signal that it can assist in deciding an appropriate ECM model order and structure in the form of a transfer function which can be fitted to obtain the ECM model parameters [152]. Note that both fits cannot perfectly match the impedance at few extreme low frequencies, which might be a limitation of the wide bandwidth multisine excitation. Unlike the previous literature [152, 151] only focusing on the extreme low frequency range ($\leq 1\,\mathrm{Hz}$), the bandwidth in this work was extended to 10 Hz to comprise characteristic frequency ranges of both diffusion process and charge transfer kinetics. A rapid decrease in the impedance magnitude and a peak in the phase at low frequency range are shown in Figure 6.5, which is a phenomenon that has not been found in previous work, i.e. in [152], the magnitude response of the impedance with a decreasing gain at low frequencies and the phase response with a increasing trend as the frequency increases are observed. Such difference should be due to the limitation of the bandwidth ($\leq 1\,\mathrm{Hz}$) in [152] which only captures the response attributed to the diffusion process [269], but in this study a wider bandwidth ($\leq 10\,\mathrm{Hz}$) is applied and the response due to charge-transfer kinetic can
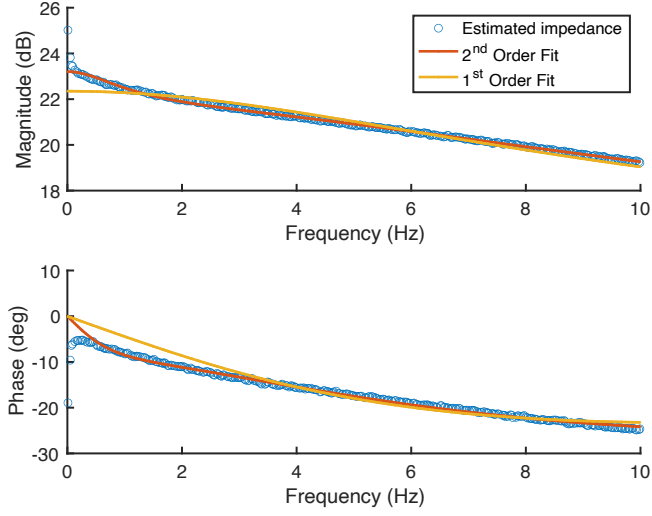
Figure 6.5: 1st and 2nd order transfer functions for impedance estimated of the cell at 10% SOC.

also be captured. Although it leads the difficulty to fit all frequencies using 1st and 2nd order transfer function, a diffusion block would subsequently be introduced and coupled to comprise the influence caused by the phenomenon.

In addition, using orders greater than two generally generated better fits, however, the higher order model in this work resulted in positive poles which indicates an unstable system, and conjugate negative poles which is not possible to be implemented in practical applications [152]. Therefore, the model order was selected as two in this work, and the corresponding ECM is shown in Figure 6.1. Furthermore, in order to get the circuit parameters of an equivalent circuit model, the transfer function has to be expanded by a partial fraction expansion as shown in Equation (6.6).

$$Z_{\mathrm{m}}(k) = -R_0 - \frac{R_{\mathrm{p1}}}{\tau_1 j\omega_{\mathrm{k}} + 1} - \frac{R_{\mathrm{p2}}}{\tau_2 j\omega_{\mathrm{k}} + 1} \tag{6.6}$$

where R_0 denotes the internal ohmic resistance, R_{p1} and R_{p2} the polarisation resistances and τ_1 and τ_2 the time constants. The capacitances shown in Figure 6.1 can be obtained as $C_{\mathrm{p1}} = \tau_1/R_{\mathrm{p1}}$ and $C_{\mathrm{p2}} = \tau_2/R_{\mathrm{p2}}$.

Thus, the linear voltage losses $v_{\mathrm{l}}(t)$ due to the ohmic and polarisation can be simulated with the corresponding 2nd order ECM with respect to a time-dependent current load $i(t)$ as Eq.(6.7).

$$v_{\mathrm{l}}(t) = \mathrm{ECM}[i(t)] \tag{6.7}$$

120

6.2.3 Non-linear over-potential function

The non-linear over-potential function $f(v_l)$ shown in Figure 6.1 is inspired by the charge-transfer kinetics in electrochemical reactions. The Butler-Volmer equation, which relates the over-potential η_{ct} of an electrode to the current density $I_{batt}(t)$, is commonly utilised to represent the charge-transfer kinetics in electrochemical models [36, 38], as shown in Equation (6.8).

$$\eta_{ct} = \frac{2RT}{F} \sinh^{-1} \left(\frac{I_{batt}(t)}{2i_0} \right) \tag{6.8}$$

where R is the molar gas constant, F is Faraday's constant, T the temperature and i_0 the exchange current. Equation (6.8) represents the non-linear relation between current and over-potential, which is seldom interpreted in conventional battery ECMs. By plotting the measured over-potential $\bar{v}_0$ against the modelled ECM output $v_l(t)$ at each SOC, the presence of any non-linear deviations can be examined and captured through a non-linear function [152].

The over-potential data points and non-linear function fitting of the battery at 10% SOC are plotted in Figure 6.6. The blue "curve" formed by compact data points represents the non-linear characteristic of over-potential which shows a weak non-linear dependence in this study. Such a phenomenon is expected because, refer to [152], the strong non-linear dependency is only shown at low temperature (i.e. $0\,°C$) while a linear dependence is observed at $25\,°C$, which might be the reason that many conventional linear ECMs neglect the non-linearity during modelling. However, according to the nonlinearity characterisation results on the same three-electrode configuration cell in Chapter 5, nonlinearity of the cell exists at 10% SOC level. A non-linear function is used to estimate such phenomena, and the good agreement between the data points and the fit indicates non-linear deviations are well captured.

Given that the "S"-shape characteristic of the ideal Butler-Volmer kinetics (using symmetry anodic and cathodic charge-transfer factors equal to 0.5), a sigmoid function was used to model the non-linear characteristic as its bounded and differentiable features can ensure the function convergence. Note that, refer to 4, the anodic and cathodic charge-transfer factors may be not symmetrical in a practical lithium-ion battery, which leads to more possibilities including the polynomials and logistic functions that should be considered to model the non-linear phenomena. Impact of model function selection is still an open question and will be studied in the future work.

In this study, the non-linear voltage loss $\eta_R(\bar{v}_l)$, caused by ohmic, polarisation
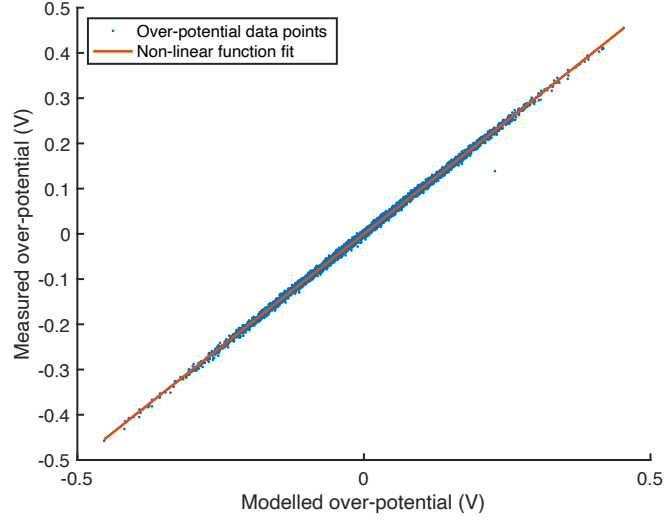
Figure 6.6: The non-linear characteristic and non-linear function fitting at 10% SOC and 25 °C.

and possible dynamic non-linear effects was obtained by the following sigmoid function, which was used to fit the measured ($\bar{v}_l$) against modelled linear over-potential ($\bar{v}_l$) data

$$\eta_R(\bar{v}_l) = \frac{c_1 \bar{v}_l}{\sqrt{1 + c_2 \bar{v}_l^2}} \tag{6.9}$$

where c_1 is the linear and c_2 is the non-linear sigmoid coefficients in Equation (6.9). The *lsqcurvefit* function from the Matlab® Optimisation Toolbox was used to estimate two sigmoid coefficient at each SOC. Then, a linear look-up table of the estimated coefficients at each SOC was built up for model simulation.

6.2.4 Open circuit voltage (OCV)

From electrochemical point of view, the battery open circuit voltage U_{OCV} accounting for thermodynamic is related to the potential of the cathode $U_c(\bar{c}_c)$ and anode $U_a(\bar{c}_a)$, as shown in Equation (6.10), which depends separately on the bulk average lithium concentration of individual electrode particles ($\bar{c}_c$ and $\bar{c}_a$).

$$U_{OCV} = U_c(\bar{c}_c) - U_a(\bar{c}_a) \tag{6.10}$$

For modelling purposes, the single particle model (SPM) assumes the size and dynamics of electrode particles to be identical within an electrode; consequently,

the cathode and anode can be treated as two electrode particles [38]. Thus, the battery macroscopic SOC is defined as the ratio of the average usable lithium ion concentration $\bar{c}$ to the maximum usable lithium ion concentration in the electrode particle in Equation (6.11)

$$\bar{z} = \frac{\bar{c}_{\mathrm{c}} - \bar{c}_{\mathrm{c},0\%}}{\bar{c}_{\mathrm{c},100\%} - \bar{c}_{\mathrm{c},0\%}} = \frac{\bar{c}_{\mathrm{a}} - \bar{c}_{a,0\%}}{\bar{c}_{\mathrm{a},100\%} - \bar{c}_{a,0\%}} \tag{6.11}$$

where $\bar{c}_{100\%}$ indicates the battery is full (100% SOC) and $\bar{c}_{0\%}$ indicates the battery is empty (0% SOC). Then, the open circuit voltage U_{OCV} can be related to the average SOC $\bar{z}$ which is represented as a $\bar{z}$-U_{OCV} curve in battery models. Given that the NMC cell, which exhibits minor hysteresis [40], was employed in this study, an extremely low current (typically C/25) was used to fully charge and discharge the battery to acquire the battery pOCV curves, which potentially can minimise battery kinetics to reduce battery hysteresis. Then the $\bar{z}$-U_{OCV} curve can be estimated by averaging the measured charge and discharge pOCV curves [270]. In this work, the three-electrode cell was employed to record not only the OCV of the full-cell (U_{OCV}) but also that of the cathode and anode (U_{c}, U_{a}). Then a *Look-Up Table* was used to archived each OCV curve to act as the open circuit voltage block in the model.

Up to this point in the paper, an NLECM similar to proposed in [152], consisting of a linear ECM block, a non-linear over-potential block, and an OCV block with respect to the macroscopic SOC achieved by current integration method, has been identified and parametrised by applying a multisine excitation at each SOC, and the performance of the NLECM will be reported and used for comparison in Section 6.3.

6.2.5 SOC dependent diffusion block

When a battery is in operation, due to the diffusion processes, the distribution of lithium ion concentration in the particle is not uniform [48]. Thus, the open circuit voltage $U(t)$ is directly reflected by the lithium ion concentration at the particle surface ($c_{\mathrm{c,surf}}$ and $c_{\mathrm{a,surf}}$), i.e. cathode surface potential $U_{\mathrm{c}}(c_{\mathrm{c,surf}})$ and anode surface potential $U_{\mathrm{a}}(c_{\mathrm{a,surf}})$, in which the potential subtraction is noted as $\triangle U_{\mathrm{surf}}$. Refer to [39], in order to design the proposed model more suitable for BMS applications, the relationship between the potential subtraction $\triangle U_{\mathrm{surf}}$ and the particle surface lithium concentration c_{surf} during operation can be approximated by the $\bar{z}$-U_{OCV} curve with the surface SOC, noted as z_{surf}, as the input. Thus $\triangle U_{\mathrm{surf}}$ can be represented as shown in Equation (6.12)

$$\triangle U_{\text{surf}} = U_{\text{c}}(c_{\text{c,surf}}) - U_{\text{a}}(c_{\text{a,surf}}) = U_{\text{OCV}}(z_{\text{surf}}) \tag{6.12}$$

Furthermore, the voltage loss η_{D} related to the difference of average concentration and surface concentration in diffusion processes can be written as Equation (6.13).

$$\eta_{\text{D}} = U_{\text{OCV}}(\bar{z}) - U_{\text{OCV}}(z_{\text{surf}}) \tag{6.13}$$

However, the conventional linear ECM commonly neglects the diffusion process inside particles and only represents the open circuit voltage by using a DC power source, which results in poor model accuracy over the whole SOC range [44]. Therefore, a simplified SOC dependent diffusion block was introduced in this section to account for the voltage loss η_{D} caused by the diffusion process. It is noted that the aforementioned ECM and nonlinear function were identified by multisine characterisation testing that was designed to minimise battery SOC change to a minimum during operations, thus no voltage loss caused by the diffusion process was taken into account. Such that the large time constant dynamics associated with the diffusion process and the small time constant dynamics associated with ohmic and charge-transfer kinetics were decoupled for easy identification.

To interpret the variation in average and surface SOC caused by diffusion process using a simplified mathematical representation, the diffusion equation solving SOC variable z for a battery particle, refer to [266], is defined on a one-dimensional geometry, using a dimensionless variable x ranging from 0 (centre of the particle) to 1 (surface of the particle) according to the following partial differential equation

$$\tau_{\text{D}}\frac{\partial z}{\partial t} - \frac{\partial^2 z}{\partial x^2} = 0 \tag{6.14}$$

where τ_{D} is a time constant which is related to the diffusion coefficient determined by battery chemical materials and manufacturing process.

The boundary conditions are

$$\left.\frac{\partial z}{\partial x}\right|_{x=0} = 0, \qquad \left.\frac{\partial z}{\partial x}\right|_{x=1} = \frac{\tau_{\text{D}}i(t)}{Q} \tag{6.15}$$

where Q is the parameter corresponding to the battery capacity. The diffusion block was only implemented in the Cartesian coordinate system in this work, and the other coordinate dimensions were not studied here, but, refer to [266], only a minor impact is shown when using different coordinate systems.

To solve Equation (6.14) with low computational cost, a Chebyshev pseudo

spectral method, termed as the discrete Chebyshev-Gauss-Lobatto (CGL) orthogonal collocation method, was applied in this work [271]. Unlike the finite difference method in [272] and the finite element method in [236] which require very a high spatial resolution, the pseudo–spectral method is a global method which uses all available function values to construct the necessary approximations to simplify calculation [273]. With the orthogonal collocation method, it is possible to find the SOC variable $z(t, 0 \leq x \leq 1)$ at the grid points $x_{\mathrm{j}} = (1 + \cos(j\pi/N))/2, j = 0, ..., N$, which distributes in the battery particle from the centre to the surface, by solving the following system of $(N + 1)$ differential algebraic equations (DAEs):

$$\begin{cases} \dfrac{\partial z_{\mathrm{j}}(t)}{\partial t} = 4 \sum\limits_{k=0}^{N} b_{jk} z_{\mathrm{k}}(t), & j = 1, ..., N - 1 \\ z_0(t) = 0 \\ z_N(t) = \dfrac{\tau_{\mathrm{D}} i(t)}{Q} \end{cases} \tag{6.16}$$

where $D^2 = D \cdot D = (b_{jk})_{0 \leq j \leq N, 0 \leq k \leq N}$ is the square of the derivative matrix D, and N is arbitrarily selected as 6 in this study. Details on the CGL orthogonal collocation method are found in [274], while a brief description of the procedure is presented in Appendix A.

In the diffusion block, the surface SOC z_{surf} can be directly obtained from Equation (6.14) while the grid point at surface is selected, as well as the average SOC $\bar{z}$ of the battery particle in this work can be obtained by

$$\bar{z} = \int_0^1 z \partial x \tag{6.17}$$

The voltage loss of SOC dependent diffusion block η_{D} in Equation (6.13) has been available for the NLECM-diff model.

To estimate Q and τ_{D} of the diffusion block, a global optimisation method, named simulated annealing (SA) algorithm proposed by Kirkpatrick [275], was applied here for the model parameterisation. Simulated annealing (SA) is a random-search strategy that utilises an analogy between the annealing process and the search for a minimum in a more general system. SA's advantage over other methods is its ability to avoid becoming locked in local minima. The approach performs a random search that accepts changes that reduce the objective function (assuming a minimisation problem), but also some modifications that raise it. Simulated annealing is considered as reliable and universal method that can deal with highly nonlinear models, chaotic and noisy data and many constraints [276]. In this work, two unknown parameters τ_{D} and Q in the NLECM-diff model were estimated by the simulated

annealing approach which obtains the optimised parameters by minimising the cost function (J) defined in Equation (6.18) as the sum of the weighted squared error between voltage measurement and the NLECM-diff model output voltage.

$$J = \sum \left| \frac{v(t) - v_{\mathrm{m}}(t)}{\sigma_{\mathrm{v(t)}}} \right|^2 \tag{6.18}$$

In Equation (6.18), $v(t)$ is the voltage measurement, $v_m(t)$ is the model-calculated voltage, and the $\sigma_{v(t)}$ is the standard deviation of the voltage measurement. Given that the diffusion process is long time operation [265], a parameterisation process under a long time profile (separate and in addition to the multisine characterisation experiments) is required for the NLECM-diff model. Thus, the optimisation is based on a 5.75 mA (0.5C) constant current (CC) discharge experiment (from 4.2 V to 2.5 V) followed by a 4 h relaxation at 25 °C, and the optimised model fit will be reported in Section 6.3. During the optimisation process, the results show that the voltage response during the discharge period, especially the ending estimated voltage value, depends on the time constant τ_{D}. Furthermore, the final estimated voltage value in the relaxation is strongly related to Q, and in this work the Q is determined to equal to 0.0113 which is close to the rated capacity of the battery 0.0115 A h .

By coupling the identified NLECM and the SOC-dependent diffusion block, the NLECM-diff model, which accounts for key battery dynamics, including the ohmic response, the charge-transfer kinetics, and the diffusion processes, has been accomplished. The model defines time-dependent voltage E_{batt} when subject to a time-dependent battery current load using the Equation (6.19), and overall nine parameters of the proposed model are listed in Table 6.1.

$$E_{\mathrm{batt}} = U_{\mathrm{OCV}}(\bar{z}) + \eta_{\mathrm{R}} + \eta_{\mathrm{D}} \tag{6.19}$$

6.3   Comparison between NLECM-diff and NLECM

To quantify the advantage over an NLECM, the accuracy of the proposed NLECM-diff model and the NLECM was compared under different load profiles in this section. The reasons to use the NLECM rather than a multiple RC linear ECM (e.g., 4RC ECM) for comparison are as follows: Refer to [40], over-fitting characteristics of high order multiple RC model (higher than 2nd order) declines the accuracy of the model, the 4RC ECM may show worse accuracy than the 2RC ECM, and the 2RC linear ECM is thus preferred to be used as a reference model in many literature

Table 6.1

Overall 9 parameters in the NLECM-diff model.

Parameters	Description	Unit
R_0	Ohmic resistance	Ω
R_{p1}	Resistance of the first polarization process	Ω
τ_1	Time constant of the first polarization process	s
R_{p2}	Resistance of the second polarization process	Ω
τ_2	Time constant of the second polarization process	s
c_1	Linear coefficient of sigmoid function	$-$
c_2	Non-linear coefficient of sigmoid function	$-$
Q	Parameter corresponding to the battery capacity	A h
τ_D	Time constant of diffusion process	s

[33, 39, 152]. Furthermore, the accuracy of NLECM has been demonstrated superior than the 2RC linear ECM in [152], which indicates the NLECM could be a better reference model from the perspective of accuracy. In addition, the NLECM-diff model is developed from the NLECM; the purpose of comparing between NLECM-diff and NLECM is to evaluate the advantage of the NLECM-diff model over the NLECM reference model.

Figure 6.7a and Figure 6.7d show the voltage estimation and voltage error results under a multisine excitation current when the battery is at 50% SOC. Note that, consistent with [151], the measured multisine dataset here is not the ones used for the model identification, and the average of first three periods measured data was used for validation. The results show that the voltage estimation of the two models almost overlap the experimental data and that most of voltage error is less than ± 0.02 V. Furthermore, the goodness-of-fit R^2 and voltage root mean square error, which are widely used metrics for model performance evaluation, of the NLECM and NLECM-diff under the two testing profiles are listed in Table 6.2. The R^2 value of the NLECM-diff result is 99.67% which is 0.01% higher than the NLECM, while the RMSE value of NLECM-diff is 0.0006 V less than that of the NLECM. The high R^2 and small RMSE value indicate both the NLECM and the NLECM-diff have great precision under the multisine test, while the minor difference between these two metrics imply that the accuracy of two models are really close. In addition, Figure 6.7b and Figure 6.7e present the voltage estimation and voltage error results under a multisine excitation current when the battery is at 10% SOC.

Both NLECM and NLECM-diff still demonstrate comparable accuracy. However, in Table 6.2, compared with the results in 50% SOC case, two models show less R^2 and greater RMSE value in 10% SOC case, which is due to the battery stronger nonlinearity introduced in Chapter 5. Furthermore, it is important to notice that the NLECM-diff model is more accurate than the NLECM model in two multisine tests, indicating the improvement of the NLECM-diff than the reference model.
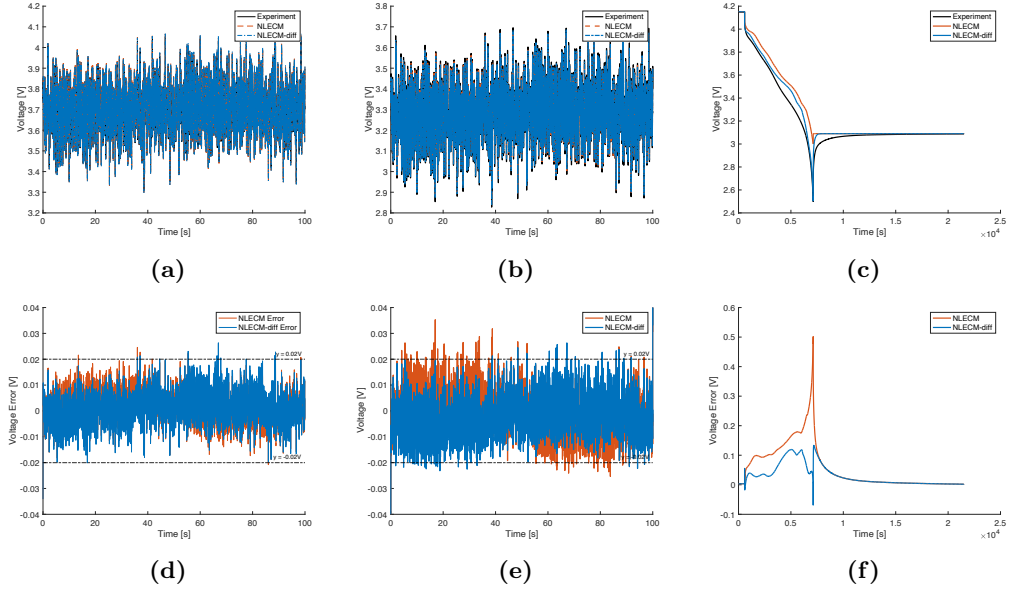
Figure 6.7: Comparison between NLECM and NLECM-diff under different load profiles. (a, d) Voltage estimation and voltage error results when subjected to a multisine current at 50% SOC, (b, e) Voltage estimation and voltage error results when subjected to a multisine current at 10% SOC, and (c, f) Voltage estimation and voltage error results under a 0.5C constant current discharge followed by a 4 h relaxation.

Furthermore, the accuracy of two models was evaluated using a 0.5C constant current discharge with relaxation profile, as illustrated in Figure 6.7c. Compared with the significant deviation of the NLECM results, a good agreement between the NLECM-diff results and the experimental data is clearly observed. The reason leading to significant error of minimum voltage for the NLECM model is due to the lack of diffusion process interpretation. In this work, the input current for simulation was identical to the experimental current excitation. In a battery there is a voltage loss caused by the solid diffusion process and leads to the terminal voltage reaching the minimal voltage limit (2.5 V in this case) before the average SOC calculated by Coulomb counting reduces to 0. As the NLECM uses average SOC to determine the value of OCV and disregards the interpretation of diffusion process, the NLECM terminal voltage at the end of the validation test is significantly worse than that of

the NLECM-diff model. Moreover, when the discharge profile ends, the NLECM-diff can smoothly transit into the relaxation status (as black array shown), which is a typical diffusion behaviour. However, the NLECM voltage response directly changes to a flat straight line after an instant ohmic voltage recovery, which is not consistent with physical reality. Additionally, as shown in Figure 6.7f, although the voltage error slightly increases at the low SOC range during the discharge profile, the maximum voltage error is less than 0.15 V and the final voltage value converge to the experimental result in the relaxation process, which indicates the high accuracy of the NLECM-diff through the whole SOC range. In contrary, the NLECM results deviated from the experimental data from the beginning of discharge and the error increases to around 0.5 V, which illustrates the drawback of the NLECM, especially in the low SOC range. Such phenomena demonstrate the NLECM-diff's advantage of capturing diffusion dynamics and the importance of a diffusion process block in a battery model for long time discharge operation. In addition, according to Table 6.2, the NLECM-diff could reduce the voltage RMSE by more than 49.6% and improve the R^2 value by 4.6% when compared to NLECM, which indicates the significant accuracy improvement of NLECM-diff compared to the traditional NLECM in the 0.5C CC discharge test.

Table 6.2

Goodness-of-fit (R^2) and voltage RMSE comparison of NLECM and NLECM-diff in the multisine and 0.5C CC discharge tests.

	Multisine 50%SOC		Multisine 10%SOC		CC Discharge	
	R^2 [%]	RMSE [V]	R^2 [%]	RMSE [V]	R^2 [%]	RMSE [V]
NLECM	99.66	0.0018	99.50	0.0093	94.05	0.0930
NLECM-diff	99.67	0.0012	99.56	0.0087	98.65	0.0469

From a parameterisation point of view, only two extra parameters were added in the NLECM-diff model, resulting in relatively limited increase of the cost in parameter identification. No experimental methods and chemical analysis were involved in the identification of the NLECM-diff model which provides a promising modelling pattern for the battery management system (BMS) developers without specific electrochemical techniques. Furthermore, the introduction of the diffusion processes block accounts for the potential variation inside the battery electrode particles, such that an evident accuracy improvement under long time operation profiles could be made by the NLECM-diff model, in contrast to the NLECM and even the traditional ECM only contains the OCV block with respect to the average SOC.

6.4 Model validation: Results and Discussions

In this section, the voltage estimation accuracy of the NLECM-diff model, which was identified using the methodology presented in Section 6.2, was validated under various load profiles. Taking advantage of the reference electrode instrumentation, the NLECM-diff model was developed not only for the full cell to emulate the battery terminal voltage dynamics, but also for the individual electrodes, labelled as NLECM-diff (PE) for the positive electrode and NLECM-diff (NE) for the negative electrode. Section 6.4.1 presents that the applicability of the NLECM-diff model on the prediction of the electrode potential response, which was compared to the single particle model with electrolyte dynamics (SPMe) proposed in [38] with a constant current (CC) discharge and constant current-constant voltage (CC-CV) charge tests. Furthermore, to validate the model effectiveness for a full cell in a variety of operational scenarios, the aforementioned CC discharge CC-CV charge tests and the New European Driving Cycle (NEDC) experimental test were conducted in the validation procedure to examine and compare the accuracy of the NLECM-diff model and the SPMe in Section 6.4.2 and 6.4.3, respectively. Note that, in this study, the partial differential equations in the SPMe were solved by the finite difference method, as well as the parameters in the SPMe were obtained from [24] for LGM50 21700 NMC cells, which were same as the cells used in this study. Lastly, the dominant battery phenomenological behaviours in terms of voltage losses under different load profiles were found by the NLECM-diff and reported in Section 6.4.4.

6.4.1 CC discharge and CC-CV charge profiles - Electrodes

An essential feature of electrochemical models is that the dynamic response of individual electrodes can be predicted, which can be employed to estimate internal potential variables for practical applications, such as charging strategy optimisation. For instance, the cells' current can be controlled during charging in a way to maintain the potential of negative electrode constantly above $0\,\mathrm{V}$ vs. $\mathrm{Li/Li^+}$ to prevent lithium plating [277]. However, the extensive parameterisation procedure, related to the geometrical and kinetic dynamics, of electrochemical models introduce difficulty for practical applications. Using three-electrode configuration experimental cells with a lithium reference electrode, the positive and negative electrode potential can be measured simultaneously. On the basis of the measured electrode potential and excitation current signal, the NLECM-diff model can be more easily developed (as discussed in Section 6.2) for individual electrodes to achieve same objectives by using electrochemical models. This section evaluates the potential response accuracy

of decoupled electrode NLECM-diff models in comparison with the experimental measured data and the potential estimation from the SPMe.

The performance of the NLECM-diff was evaluated under a set of constant current (CC) discharge and constant current-constant voltage (CC-CV) charge profiles. The profile was determined as a two-period cycle, in which the battery experiences constant current discharge until the lowest cut-off voltage followed by a relaxation for 4 h in the first period, and, in the second period, a $0.3C$ constant current charge was applied at the beginning and when the voltage reaches a threshold value, followed by the CV phase where the voltage is held constant (at 4.2 V) and the current reduces accordingly as SOC increases. The long constant-current discharge period was used to simulate stable driving conditions with relatively constant speed and demand, the rest period was used to verify the accuracy of the voltage estimation during the depolarisation process, and the CC-CV charge period was used to evaluate the model's performance under a widely used battery charging strategy. Three different current discharge tests were conducted, that include 3.83 mA (0.3C), 5.75 mA (0.5C), and 11.5 mA (1C), to discharge the battery from 4.2 V (Max rated voltage) to 2.5 V (Min rated voltage) in order to examine the impact of discharge rates on model accuracy throughout the whole voltage window, and the other parts of the profiles remain consistent.

Figure 6.8 shows the results of the model voltage and voltage error of the SPMe and the NLECM-diff models for the positive electrode (PE) and negative electrode (NE) in comparison with experimental measurements in CC discharge and CC-CV charge tests with different discharging current rates. It is worth noting that the model simulations use the same excitation current signal as recorded in the experiments. The measured experimental data (black line) of the positive electrode potential for 0.3C, 0.5C, and 1C discharging scenarios are plotted in Figure 6.8a, 6.8b and 6.8c. Both SPMe (PE) in blue line and NLECM-diff (PE) in red line can obtain a high degree of agreement with the experimental PE potential over the entire validation profiles. In the relaxation periods with no current excited, the gradually increasing potential of the positive electrode is observed in both models, and the model estimations at steady state are overlapped on the measured results. Furthermore, Figure 6.8d, 6.8e and 6.8f present the model estimations and measured data of the NE potentials under the various discharging profiles. It can be observed that the NLECM-diff (NE) model in green dash line is consistent with the SPMe (NE) in yellow dash line among the three scenarios, there is however an overestimation from SPMe (NE) at the end of discharge in 6.8e. The voltage error of the NLECM-diff model is in good agreement with the SPMe results for each electrode and is mostly

within the boundary range, which indicates that the accuracy of the NLECM-diff model is as high as the SPMe for electrode potential estimation. However, contrary to the accurate potential estimations obtained for positive electrode, the model estimated results of the negative electrode potential show the relatively large error in comparison with the experimental data.
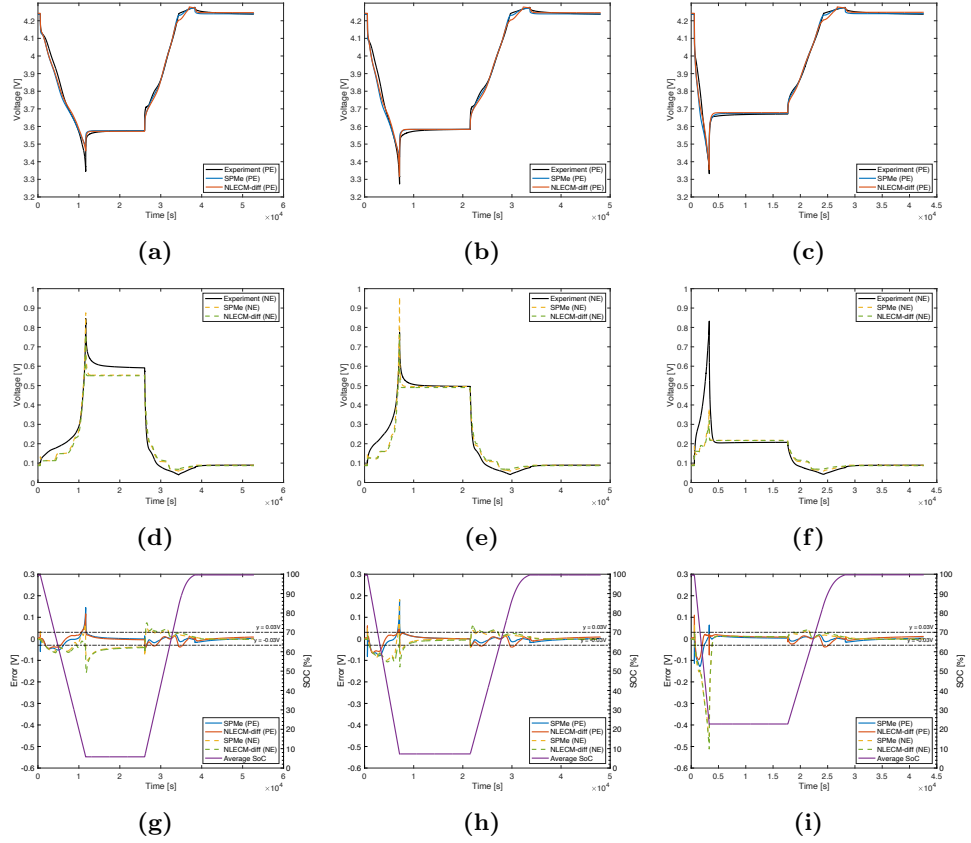
Figure 6.8: Positive electrode (PE) and negative electrode (NE) potential estimations and voltage error results of SPMe and NLECM-diff (Electrode) in CC-CV discharge and charge test with different discharge current values: (a, d, g) under 0.3C discharge current; (b, e, h) under 0.5C discharge current; (c, f, i) under 1C discharge current.

The estimated voltage error of the positive and negative electrode models are plotted in Figure 6.8g, 6.8h, and 6.8i. Note that the error is determined by the measured value subtracted by the model estimated value under the same current input, such that a positive error indicates that model overestimate the voltage while a negative error implies underestimation. The black dashed lines in the voltage error figures reflect the 0.03 V and −0.03 V error boundaries. The results show that the estimation error increases as the discharging current rate enhances when the cell discharges. The model results only show comparable small voltage error

132

in the 0.3C and 0.5C cases, however, in the 1C case, a significant error can be noticed in the result of each model. It's worthy to note that the accuracy of the parameterised SPMe model has been validated in previous work [46]. Such that the NLECM-diff model can achieve a high degree of accuracy as SPMe model. During the CC-CV charge duration, all models can maintain a good accuracy within the boundary. In addition, Figure 6.8g presents the underestimation of estimated positive and negative electrode potential during the discharge period, except the positive electrode potential at end of the period. It is worth to note that, during discharging, the larger voltage error of PE models is found in the middle of SOC range, as well as the significant voltage error of NE models is shown in the low SOC region. Furthermore, the error value of NE models is greater than that of the PE models in the low SOC area. The similar phenomena can be more obviously observed in Figure 6.8h and 6.8i. The largest voltage error of positive electrode reaches around $-0.09\,\text{V}$ in the 0.5C case and $-0.11\,\text{V}$ in the 1C case at 65% SOC, and then, the voltage error gradually decreases until the end of discharging. For the negative electrode, it is shown that when the SOC decreases, the voltage inaccuracy increases. The voltage error can reach to $-0.5\,\text{V}$ at end of discharging in Figure 6.8i, where the voltage error of positive electrode is almost neglectable. Moreover, the NE potential in the SPMe with validated parameters also exhibits as large voltage error as the NLECM-diff (NE) model. Such results illustrate that the dominant voltage error source, which leads to poor accuracy of battery models in the low SOC region, is from the negative electrode rather than from the positive electrode.

Table 6.3

Goodness-of-fit (R^2) and voltage RMSE of SPMe (PE), NLECM-diff (PE), SPMe (NE), and NLECM-diff (NE) in 0.3C/0.5C/1.0C discharge and 0.3C CC-CV charge tests.

	R^2 [%]			RMSE [V]		
	0.3C	0.5C	1C	0.3C	0.5C	1C
SPMe (PE)	99.43	99.31	99.46	0.0224	0.0258	0.0204
NLECM-diff (PE)	99.66	99.65	99.58	0.0176	0.0181	0.0181
SPMe (NE)	97.68	96.15	59.23	0.0378	0.0393	0.0680
NLECM-diff (NE)	97.52	96.82	56.78	0.0397	0.0352	0.0701

In addition, the goodness-of-fit (R^2) and voltage RMSE of electrode models under the long time discharge and charge profiles are compared and then listed in Table 6.3. It can be seen that, for two PE models, the maximum difference of R^2 is less than 0.15% and the maximum difference of RMSE values is less than $0.0054\,\text{V}$

in all three validation scenarios, which indicates that the PE models can maintain high accuracy under various current density loads. Furthermore, the NLECM-diff (PE) model shows higher R^2 and lower RMSE than SPMe (PE), which suggests the accuracy of the proposed model is comparable to SPMe in the positive electrode case. On the other hand, the results describe that, in the negative electrode case, the NLECM-diff (NE) model accuracy is difficult to maintain under high current condition, as the R^2 value significantly drops from 96.82% in 0.5C test to 56.78% in the 1C test, and approximately 0.0349 V RMSE value increment exists while the 1C validation profile is applied in comparison with the 0.5C test. Moreover, the minor R^2 and voltage RMSE difference between the NLECM-diff (NE) model and the SPMe (NE) suggests that the fidelity of these two models is still comparable and the estimation error may be not due to the model inaccuracy. Given that the accuracy of both PE models is reasonably high and does not decrease with increasing current load, the estimation inaccuracy should not be attributable to a modelling flaw. Moreover, given both NE models use the same negative electrode OCV and exhibit comparable error in the 1C case, one possible explanation is that the NE inaccuracy may be attributed to the error of negative electrode OCV measurement in the low SOC range, as, refer to [278], the OCV measurements of the negative electrode of LG M50 21700 cells exhibit a relatively large deviation at low SOC range between C/25 charging and discharging, thus the pOCV calculated by average value could result in OCV error at low SOC range.

Table 6.4

Voltage RMSE comparison of SPMe (PE), NLECM-diff (PE), SPMe (NE), and NLECM-diff (NE) at various SOC intervals in the 0.5C discharge test.

	RMSE [V]		
	100%-80%	80%-20%	<20%
SPMe (PE)	0.0435	0.0481	0.0586
NLECM-diff (PE)	0.0394	0.0363	0.0300
SPMe (NE)	0.0447	0.0836	0.0645
NLECM-diff (NE)	0.0401	0.0901	0.0580

To investigate the improvement of NLECM-diff model in low-SOC-area, Table 6.4 presents voltage RMSE comparison of SPMe (PE), NLECM-diff (PE), SPMe (NE), and NLECM-diff (NE) at various SOC intervals (100%-80%, 80%-20%, and <20% SOC) in the 0.5C discharge test. Note that the relaxation period and charge period are excluded from this comparison. It can be observed that the voltage

RMSE in the low SOC range (<20% SOC) for both electrode NLECM-diff models is less than the medium SOC range (80%-20%), which indicates that the low-SOC-error issue has been relieved by the NLECM-diff model. In addition, the voltage RMSE of NLECM-diff model in the low SOC range is lower than that of the SPMe model, indicating that the NLECM-diff model achieves a comparable accuracy to SPMe in the low SOC range (<20% SOC). It is worth noting that, consistent with Figure 6.8h, the voltage RMSE of the NLECM-diff (NE) and SPMe (NE) models in the medium SOC range (80%-20%) is relatively larger than the low and high SOC ranges, which may be attributed to the measurement error of negative electrode OCV as mentioned previously.

In this section, the modelling methodology presented in Section 6.3 was employed to develop the NLECM-diff model for both electrodes, and the performance of the electrode NLECM-diff models was compared with the SPMe. The results indicate that these two models have comparable fidelity, to the point where the NLECM-diff model may be used in place of the SPMe for estimating the battery internal potential variable. Additionally, in comparison to the minor error associated with positive electrode models, both negative electrode models exhibit relatively large low-SOC-area error when is subjected to a high current load, which demonstrates that the negative electrode dynamic response may be the primary reason resulting in the inaccuracy of battery models in the low SOC region.

6.4.2 CC discharge and CC-CV charge profiles - Full-cell

To fulfil the requirement of general practical applications where access to the individual electrode potentials is not possible, a NLECM-diff model for a full cell was developed based on terminal voltage of the three-electrode experimental cell for simulating the dynamic response of commercial cells. The performance of the full cell NLECM-diff model was evaluated and compared to the SPMe terminal voltage in this section.

Figure 6.9 presents the voltage estimation and error of the SPMe and the NLECM-diff model for a full cell in the various validation loads. The results under 0.3C discharge current are shown in Figure 6.9a which suggests both models provide minor voltage error at the high and middle SOC range with the errors less than 0.03 V. For the low SOC range (lower than 20%), the voltage error surpasses the boundary, which indicates the model voltages are overestimated. During the discharge period, the voltage error of the NLECM-diff model is comparable to the SPMe results. Furthermore, when the battery transits to the relaxation period, the largest deviation from the measured voltage gradually decreases due to the battery
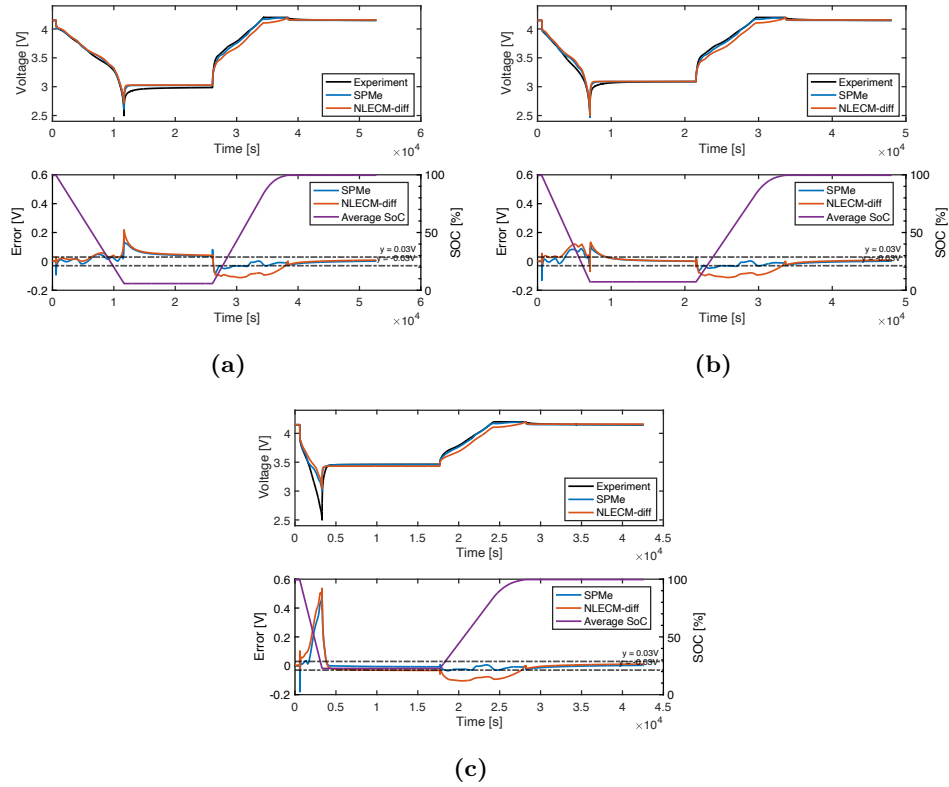
Figure 6.9: Voltage estimation and voltage error results of the SPMe and the NLECM-diff model for a full cell in CC-CV discharge and charge test with different discharge current values: (a) under 0.3C discharge current; (b) under 0.5C discharge current; (c) under 1C discharge current.

diffusion process. It is also noticed that, the voltage error of the NLECM-diff model follows closely the SPMe results which indicates that the NLECM-diff model maintains a comparable fidelity as the SPMe. Moreover, in the 0.3C CC-CV charging period, both models underestimate the terminal voltage. Compared with the around 0.03 V error of SPMe during charging, the NLECM-diff model exhibits poorer accuracy with maximum 0.11 V estimated error. It might be caused due to the fact that the lumped SOC diffusion block, which is calibrated at 0.5C constant current discharge profile, is not suitable for the charge process. At the end of the validation test, the estimated voltage can converge to the measured value with less than 0.007 V error.

The estimated voltage and error under the 0.5C CC discharge and CC-CV charge load are demonstrated in Figure 6.9b. Similar to the electrode model results in the previous section, the error of the two models increases in the discharge period, especially in the low SOC range. The NLECM-diff model overestimates the terminal

voltage, and its error is greater than that of SPMe (Max. 0.118 V versus Max. 0.087 V). However, the voltage error during relaxation are minor, even less than that in the 0.3C case, which might because the models were calibrated under the 0.5C discharge case. Same as the 0.3C case, the NLECM-diff voltage error in the relaxation period has a good agreement with that of the SPMe at around 0.002 V.

Figure 6.9c shows the estimated results of two models in the 1C discharge case where the voltage error remains within the boundaries at the start of discharge, but the large deviation from the experiential data appears from 64% SOC in the discharge process. Not only the NLECM-diff model, the SPMe exhibits a significant voltage error in the low SOC range. Furthermore, it is to noticed that, according to the average SOC (purple line) obtained by current integration method, when the experimental battery voltage is discharged to the minimum limit 2.5 V under 1C constant current, the average SOC only reaches to 22.8% rather than to around 0%. Although the mathematical fit of voltage output is successful, such a result is not expected, as the SOC difference is extremely large. It may be due to the limitation of the SOC dependent diffusion block. Unfortunately, there is no published evidence for this source; in the referenced literature [266], only the mathematical fit of voltage output is presented, but the SOC difference is not mentioned. The dominant battery process which results in a significant error in the low SOC range as well as the unexpected SOC variation will be discussed in Section 6.4.4. It is worthy to note that according to the validation results in this section, the magnitude and appearance time of both full-cell models' error are consistent with those of the negative electrode models for individual electrode models validation. Given that both NLECM-diff and SPMe positive electrode models exhibit relatively minor error, such results support the conclusion mentioned in Section 6.4.1 that the negative electrode dominantly contributes to the low-SOC-area error.

In addition, the goodness-of-fit (R^2) and voltage RMSE under 0.3C/0.5C/1.0C discharge profiles are compared and then listed in Table 6.5. Note that all charge profiles followed by the charge profiles are 0.3C CC-CV charge profile. According to the R^2 results, although the NLECM-diff model has a slightly worse accuracy, the difference between NLECM-diff and SPMe are minor in the 0.3C (0.78%) and 0.5C (0.79%) cases, however, there is a 2.74% reduction than SPMe in accuracy of the NLECM-diff model during the 1C discharge. Likewise, the RMSE results report that the NLECM-diff model has larger voltage error than SPMe in the long time discharge and charge tests.

Overall, by comparing the estimated voltage and error, it is shown that the model estimation error increases as the excitation current enhances and the SOC

Table 6.5

Goodness-of-fit (R^2) and voltage RMSE comparison of SPMe and NLECM-diff in 0.3C/0.5C/1.0C discharge and 0.3C CC-CV charge tests.

	R^2 [%]			RMSE [V]		
	0.3C	0.5C	1C	0.3C	0.5C	1C
SPMe	99.48	99.56	97.05	0.0373	0.0351	0.0624
NLECM-diff	98.70	98.77	94.31	0.0579	0.0541	0.0870

decreases. Furthermore, the accuracy of the NLECM-diff model is slightly lower than the SPMe under CC discharge and CC-CV charge profiles.

6.4.3   NEDC profile - Full-cell

A further model validation was carried out under the New European Driving Cycle (NEDC) load profile. The NEDC is a typical vehicle-level dynamic cycle profile to test the performance of conventional, hybrid, and electric vehicles in the European Union, which consists of periods of constant acceleration, deceleration and speed [279]. The NEDC profile utilised in this section was generated for the three-electrode experimental cell by University of Birmingham collaborators. It's noteworthy that the pack configuration assumptions of certain number of strings in series and number of cell in parallel in a string are critical to determine the C-rates and change in SOC of the cells when scaling from a drive cycle at vehicle level to the cell level. There are different ways of connecting batteries in parallel. Commonly employed topologies include the Z shape or ladder shape configurations being the most common approach [35]. In addition, the size of interconnection resistance between the cells needs to be considered as it can result in a current mismatch [280]. Generally, for simplicity it is assumed that all the resistance values are the same. It is noteworthy that in an actual interconnection resistance system is dependent on the busbar design and they can slightly vary at different locations of the pack. However as they are at the same order, considering identical values for interconnection resistance is a valid assumption [281] when scaling cell level driving cycle.

As shown in Figure 6.10a, the test is performed starting from fully charged until the terminal voltage reaches the cut-off voltage 2.5 V. The zoom-in figure corresponds to the current with average SOC in the 10th cycle, where the SOC changes from 55.9% to 51.3% in a NEDC cycle within 0.33 h. In addition, the estimated voltage of the SPMe and the NLECM-diff model are compared with the measured voltage under the NEDC test as well as the detailed 10th cycle results

138

in Figure 6.10b. A total of nineteen complete plus a partial NEDC cycles are accomplished in this test, and the 10th and 19th cycles are analysed in detail. According to the zoom-in figure in Figure 6.10b, the NLECM-diff model can capture the cell voltage response and has a good agreement with the SPMe, however, the voltage amplitude estimated by the NLECM-diff model is smaller than the SPMe at peak values. Note that, in the end of the NEDC test, the model voltage value, which is less than 2.5 V, is the limitation of mathematical models caused by the extrapolation, which requires to avoid by setting proper saturation.
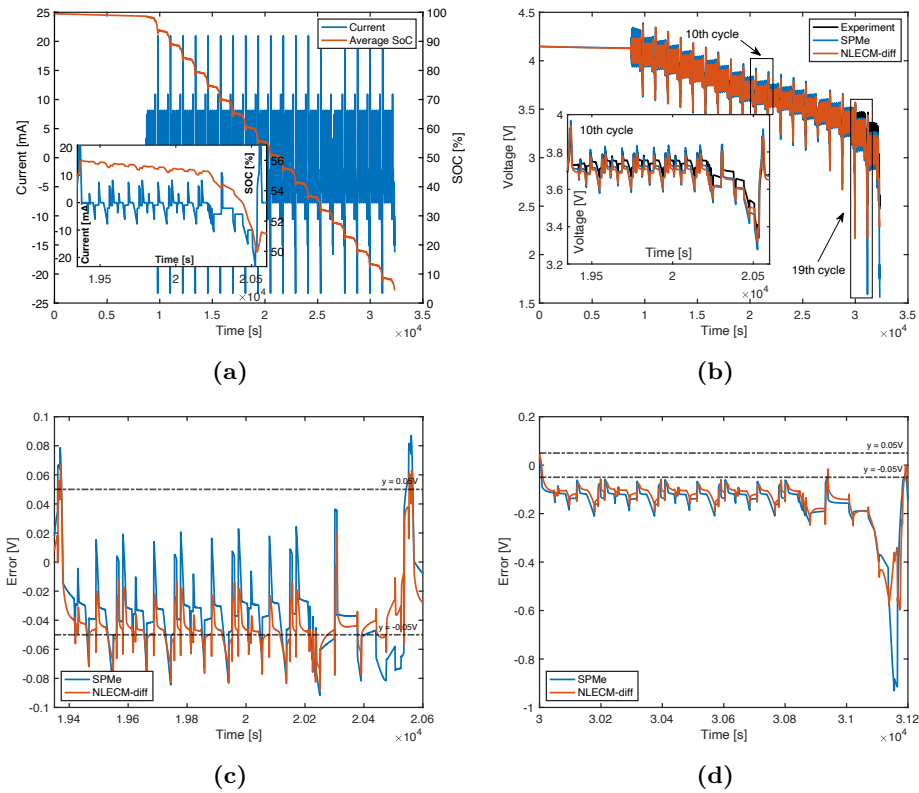
Figure 6.10: Comparison of SPMe and NLECM-diff in NEDC test: (a) Current and SOC variation; (b) Voltage estimation results; (c) Voltage Error in the 10th cycle; (d) Voltage Error in the 19th cycle.

Figure 6.10c illustrates the voltage error in the 10th cycle with the black dashed lines as the ±0.05 V boundaries. Most of the voltage error is within the ±0.05 V range, but an underestimation is noticed for the estimated voltage in the NEDC cycle. Figure 6.10d is related to the 19th cycle in low SOC range with SOC 13.6% − 8.9%. Compared with the results in the 10th cycle, a obvious underestimation, which is out of the boundaries, can be noticed and the largest error appears at the end of each NEDC cycle caused by 22 mA (about 2C) current discharge. Fur-

thermore, the NLECM-diff model shows better performance (smaller error) than the SPMe in this cycle.

The goodness-of-fit (R^2) and voltage RMSE under NEDC are compared and then listed in Table 6.6. The R^2 results illustrate that the NLECM-diff model has 2.78% higher accuracy than the SPMe in the NEDC dynamic profile. According to the RMSE voltage results, the NLECM-diff model shows a 0.11 V RMSE higher accuracy than the SPMe.

Table 6.6

Goodness-of-fit (R^2) and voltage RMSE comparison of SPMe and NLECM-diff in NEDC test.

	R^2 [%]	RMSE [V]
SPMe	92.83	0.0854
NLECM-diff	95.61	0.0744

In this section, the NEDC driving cycle test is carried out for validation and the estimated voltage of two models are compared. The results show that the estimated voltage error increases as the SOC decreases, which is consistent with the results in previous sections.

6.4.4 Dominant electrochemical process under different load profiles

In this section, the fundamental rationale, which leads to the higher accuracy of the NLECM-diff model in the NEDC test rather than in the 1C constant current discharge, was discussed according to the variation of surface SOC and average SOC obtained by the diffusion block. Furthermore, the dominant electrochemical process in a lithium-ion battery under different profiles was determined by analysing voltage losses of the NLECM-diff model.

Figure 6.11a and Figure 6.11b show the comparison between the surface SOC and average SOC under the 1C constant current discharge and the NEDC profile, respectively. It's clear to observe that the difference between surface SOC and average SOC appears in these tests when the excitation starts and the battery equilibrium state no longer exists. In Figure 6.11a, the surface SOC is always less than the average SOC at the same moment during the discharge. According to the purple line, which indicates the difference between the surface SOC and average SOC, termed as ΔSOC, it's shown that the absolute value of ΔSOC increases from 0 to the maximum value of 22.8% within 1287 s of simulation time when the battery is discharged
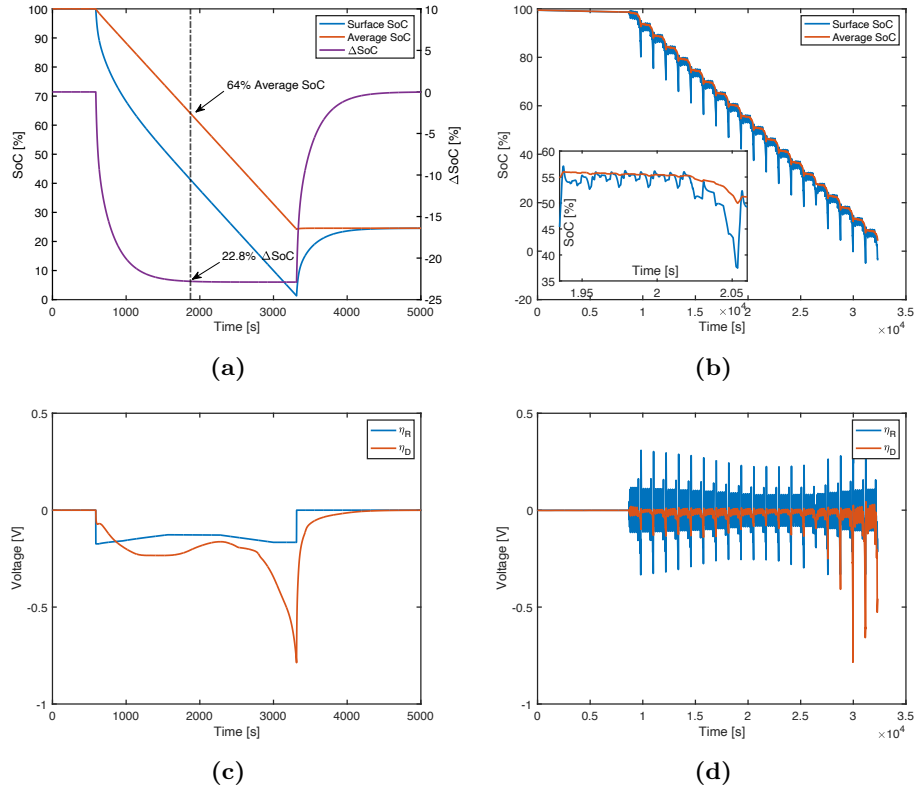
Figure 6.11: Comparison between SOCs and between voltage losses under different load profiles: (a) Comparison between surface SOC and average SOC under 1C discharge; (b) Comparison between surface SOC and average SOC under NEDC profile; (c) Comparison between ohmic and diffusion process voltage loss under 1C discharge; (d) Comparison between ohmic and diffusion process voltage loss under NEDC profile.

to 64% average SOC, and maintains the maximum value until the discharge ends, then decreases to 0 through the relaxation process over 1687 s of simulation time. Recall the estimated voltage results in Figure 6.9c, it is reported that the start of the deviation of estimated voltage also appears at 64% average SOC, and when the measured voltage reaches the cut-off voltage, the remaining 22.8% SOC is exactly same as the maximum difference between the surface SOC and average SOC. Such results illustrate a strong dependence between the large estimated voltage error at 1C discharge and the SOC difference ΔSOC caused by the diffusion process. As described in Section 6.3, Q and τ_D are two parameters which requires to be identified in the diffusion block. In Figure 6.9c, when the battery relaxes to the equilibrium state after 1C discharge, the estimated voltage of the NLECM-diff model is overlapped on the measured experimental voltage data, which indicates the released capacity estimated by the NLECM-diff model is identical to the actual extracted capacity

from the cell in the test, thus it can be confirmed that the parameter Q, which is related to the cell capacity, is accurately identified. On the other side, because the NLECM-diff model is optimised at 0.5C, the significant voltage error observed during discharging could be caused by the fact that the variation of the diffusion-related characteristics results in the identified diffusion-related time constant τ_D is inappropriate for the case of the 1C discharge. Taking into account that the voltage error and the maximum ΔSOC concurrently appear, the reason may be attributed to the value of τ_D in adequately simulating the greater ΔSOC caused by the diffusion process under large current loads. Note that, as described in Section 6.4.1, the negative electrode is determined as the origin of the low-SOC-area error, the dominant factor is thus determined as the diffusion-related characteristic changes of the negative electrode, which leads to the considerable error in the low SOC region under high current load. Refer to [24], the effective diffusion coefficient needs to be adjusted for a given current profile, due to the concentration depends on the applied current profile. In the future work, to improve the accuracy of NLECM-diff model under large current loads, several diffusion-related time constants, especially for the negative electrode, may need to be identified under different typical CC discharge tests (i.e., 0.3C/0.5C/1.0C/1.5C) and tabulated in a look-up table for interpolation, rather than only the parameter under 0.5C discharge test is identified in this case. Then, while a current load is applied on the NLECM-diff model, the diffusion-related time constant, which is corresponding to the magnitude of the current load, will be selected and employed in the model. Such that the situation of insufficient diffusion block under large current load will be addressed.

In addition, Figure 6.11b reports the variation of the surface SOC and average SOC in the NEDC test and the 10th cycle shown in detailed. It's demonstrated that the variation of surface SOC is more drastic than average SOC in the whole test, and the maximum 12.4% SOC difference is found within a single NEDC cycle. Given that the maximum SOC difference which can be provided by the identified NLECM-diff model is 22.8% larger than 12.4%, the diffusion block with the identified parameter τ_D is sufficient to provide the dynamic response caused by diffusion processes, which may be the reason that the NLECM-diff shows high accuracy under the strong dynamic NEDC profile.

In order to understand the role of electrochemical processes inside a lithium-ion battery, the dominant battery losses under different current loads was determined using the NLECM-diff model. Figure 6.11c and Figure 6.11d exhibit the variation of the ohmic voltage loss with charge-transfer reaction effect η_R and the voltage loss caused by diffusion process η_D under different load profiles. During the 1C constant

current discharge, it's noticed that both η_R and η_D exist when the discharge starts. The η_R is shown as the dominant voltage loss contributor at the beginning, then, as the discharge duration increases, the η_D replaces η_R to contribute most voltage loss in the estimated voltage output. At the end of discharge process, the voltage loss contributed by the η_D is 4.93 times than that by the η_R. Contrary to the constant current discharge, it's obviously shown that the η_R is the dominant voltage loss contributor in most of the NEDC test in Figure 6.11d, except for several peak current moments within the low SOC range. It can therefore be concluded that the diffusion process is the behaviour dominating the battery voltage under the large current load profile, but in the strong dynamic load profile, e.g. NEDC, the ohmic voltage loss with charge-transfer reaction effect becomes to the dominant contributor. The conclusion that the dominant voltage loss varies depending on different load profiles is supported by observations in [282].

6.5 Conclusions

To address **Research Objective (3)** defined in Chapter 1, a non-linear equivalent circuit model with diffusion dynamics, termed as a NLECM-diff model, is proposed in this chapter, which is identified with a multisine-based nonlinear characterisation method and a constant current discharge test. The NLECM-diff model is able to account for the battery electrochemical processes, in which a 2nd order linear equivalent circuit model (ECM) presents the battery impedance, a sigmoid function accounts for any non-linearity, and a lumped SOC dependent diffusion block accounts for the diffusion processes. Furthermore, the surface SOC and average SOC are calculated by the diffusion model, thus the voltage losses due to diffusion processes and the open circuit potential can be determined correspondingly. Taking advantage of the three-electrode cell used in this work, not only the NLECM-diff model for a full cell but also for individual electrodes are developed. The accuracy of the NLECM-diff models is validated in two types current load experiments as well as compared with the widely-used single particle model with electrolyte dynamics (SPMe).

The validation results highlight that, by involving the diffusion block at the cost of adding two extra identifiable parameters, the voltage estimation error in the low SOC range is significantly reduced by employing the NLECM-diff model, and the RMSE value decreases by more than 49.6% in comparison of the conventional NLECM as a benchmark. From the perspective of battery modelling, unlike a total of 35 parameters in the SPMe which requires extensive experimental experi-

ments, the NLECM-diff model needs only 9 easily-identifiable parameters obtained by 2 characterisation tests, but it can achieve a comparable accuracy with the electrochemical model. In addition, as the computational cost is well controlled with 10 equations, the NLECM-diff model can be a suitable candidate for accurately predicting battery voltage in real-world BMS applications. Furthermore, the dominant behaviour contributing to the total voltage loss is determined by applying the NLECM-diff model under different current loads, in which the diffusion process is the dominant voltage loss when under the long time current discharge, and the ohmic voltage loss is the dominant dynamic when under a dynamic NEDC profile. Overall, this chapter demonstrates that the developed NLECM-diff model can achieve a comparable accuracy to the SPMe by accounting for battery nonlinearity and diffusion dynamic, which fulfils the requirement of "**Research Objective (3): Develop a battery mathematical model which requires minimal identification cost while achieving a high level of accuracy over the entire SOC range.**"

To extend the conventional ECM function to simulate the battery internal behaviours, the decoupled electrode NLECM-diff models are established for the positive and negative electrodes by utilising voltage data from individual electrodes of a three-electrode configuration experimental cell acquired during the same identification tests. The validation results indicate that the developed model can achieve comparable accuracy to the SPMe model for the full-cell and individual electrodes. Such that the decoupled electrode NLECM-diff model can be used similarly to electrochemical models to estimate internal electrode potential variables, and it enables the applications of state observer or controller for real-time estimation and control of the physical states inside the battery [46, 283], but significantly reduces computational and parameterisation costs. In addition, by comparing with the SPMe electrodes voltage response under the identical current load, the variation of the diffusion-related characteristics of the negative electrode is determined as the primary reason of the battery models' low-SOC-area error under different applied current intensities. This discovery extends knowledge that the role of individual electrodes contributing to full-cell voltage estimation error and suggests that future lithium-ion battery modelling research should place a greater emphasis on investigating the model of battery anode under different operating conditions for a comprehensive and reliable battery model.

The NLECM-diff model exhibits a favourable trade-off between accuracy and identifiability in comparison to the regular ECM and electrochemical models, making it well-suited for usage in real-world applications. In Chapter 7, both local and internet distributed Hardware-in-the-Loop platform setups involving a battery

144

model and a simplified battery management system are established as well as the applicability of the NLECM-diff model to the HIL application is evaluated to fulfil the requirements of VCHV project outlined in Chapter 1.

Chapter 7

An Initial Investigation of Cloud-based Battery Management System[†]

7.1 Introduction

This chapter presents three case studies of Hardware-in-the-Loop (HIL) applications to address "**Research Objective (4):** Evaluate the applicability of the proposed battery model to Hardware-in-the-Loop simulations." As mentioned in Chapter 1, this PhD research is aligned with the externally funded project 'Virtually Connected Hybrid Vehicle (VCHV)'. The goal of VCHV is to build a real-time simulation framework with an internet distributed Hardware-in-the-Loop (ID-HIL) platform spread across different geographical locations. There are six UK universities simultaneously working on this project, and every facility holds one essential hardware component of a hybrid electric vehicle (HEV), as known as Unit-Under-Test (UUT) and shown in Figure 7.1, which needs to communicate with each other in real-time. The author is responsible for the HIL applications of the virtual vehicle's electrical energy storage and battery management system. As required by VCHV project, this chapter records the establishment of HIL and ID-HIL platforms and the performance of the developed battery model in Chapter 6 in HIL applications serving as contributions to VCHV project.

Over the last two decades, the HIL simulation technique has been proposed and widely used as a revolutionary simulation and hardware testing technique [284]. HIL simulation can be used for a system which combines controller hardware with

---

[†]Parts of this chapter have been published in [4]
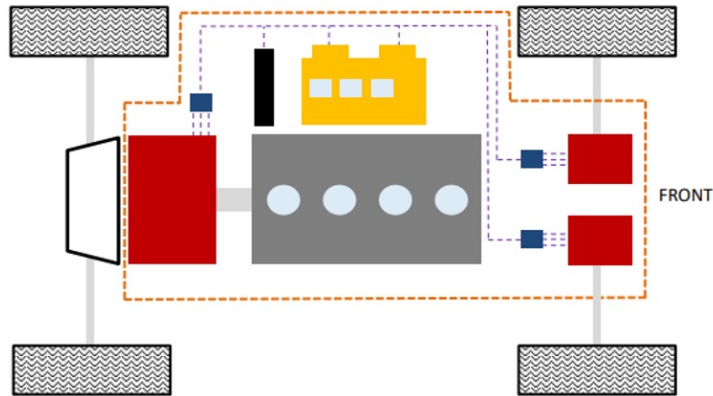
Figure 7.1: Possible configuration and in-scope components within orange dotted lines. Each spoke is represented with a different colour: Bath (Internal Combustion Engines), DETC, Loughborough (Hybrid Controls and Communications), Newcastle (Electric Motors), Nottingham (Power Electronics), UCL (Fuel Cells), and Warwick (Batteries).

mathematical models of the system to be controlled (plant model). By this technique, the cost of simulation and the hardware testing can be maintained efficiently, especially in automotive industry research and development work. Most hardware-in-the-loop (HIL) simulation are physically allocated in the same place or laboratory. However, it will require researchers to transport the test rigs from different places to the same one. Due to the expenses of transporting scenarios over vast distances, researchers have been investigating the feasibility of connecting physical test rigs and mathematical simulation models located in separate locations and then running the HIL simulation in real-time.

The early researchers, who connected two geographically separated Hardware-in-the-Loop testing rigs together, are Ersal et al. in 2009-2013 [285, 286]. This is an illustration of the notion of Internet-distributed hardware-in-the-loop (ID-HIL) simulation. The objective is to integrate physical and virtual prototypes of a system over the Internet, allowing for system simulations to be conducted independent of the location of the system's components. Two HIL rigs used in this work were a 6L V8 diesel engine-in-the-loop simulation setup located at the University of Michigan (UM) in Ann Arbor, MI, USA, and a virtual human operator driver-in-the-loop ride motion simulator located at the TARDEC Simulation Laboratory in Warren, MI, USA [285]. Additionally, the UDP (User Datagram Protocol) has been used to transmit the signals between two rigs. In [285], the authors summarised the most-widely known negative factors such as the Internet's time-delay, jitter, and message loss with the numerical expressions. In addition, the concept of "trans-

parency" is proposed in [286], which means a measure of closeness to ideal coupling. A higher transparency indicates the more accurate and useful the results. Ersal et al. concluded that transparency and how it is affected by delay, jitter, and loss associated with the Internet network is dependent on the signal of interest [286]. They asserted that the effect of distributed simulation is greater than that of the Internet network. In a recent project, a feasibility check for sufficient real-time connectivity is presented for remote and shared experiments, where testing parts are allocated in different geographical places [287]. However, in this study, Schreiber et al. investigated the feasibility of shared and distributed hardware-in-the-loop testing techniques for automotive systems, and a preliminary attempt using test setups located in different countries (South Africa, United States of America, The Netherlands, and Germany) have been performed through UDP communication. Another recent project was conducted on internet-distributed vehicle-in-the-loop simulation for Hybrid Electric Vehicles that has been published in [288]. The feasibility of a centralised internet-distributed hardware-in-the-loop configuration is exploited in that study to co-simulate the entire vehicle's performance with diverse subsystems. To the best of the author's knowledge, the Internet-distributed Hardware-in-the-Loop (ID-HIL) simulation has not been employed in the battery related field.

From the perspective of automotive engineering, a battery management system is physically integrated into the battery pack to provide critical services such as SOC/SOH/SOP estimates and control algorithms in real-time. However, with the rapid growth of cloud computing and big data techniques, an avant-garde concept of cloud-based BMS is recently suggested to make effective use of massive data sets from EVs [51]. Xiong et al. proposed a framework of cloud-based combining BMS with big data platform as shown in Figure 7.2 [51]. Voltage, current, temperature, and other data are constantly transferred to a big data platform built on cloud technology during the daily driving process of EVs. Machine learning systems may be trained in a practical context using the data obtained to produce more accurate predictions. In comparison to the embedded BMS microprocessors' limited computational power, cloud computing technology facilitates the execution of procedures that need a high level of computation and memory. The findings of the data processing will be transmitted to a battery monitoring centre, such that the battery state and fault information throughout the duration of the battery's life can be recorded and stored in the monitoring centre for further analysis. Remote diagnosis and maintenance will be accomplished by transferring real-time battery state and legible fault information to electric vehicles.

Although fully realising this cloud-based BMS is impractical during this
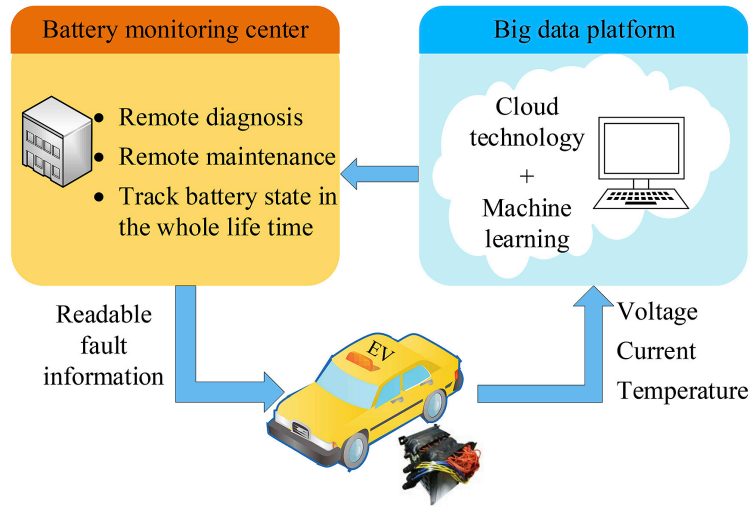
Figure 7.2: A framework of cloud-based combining BMS with big data platform [51].

PhD period due to the methods need massive hardware and large computation, the internet-distributed Hardware-in-the-Loop simulation platform in this chapter enables an initial investigation of the remote network-connected BMS's feasibility. Additionally, the ID-HIL configuration, which comprises of a battery model and a cloud-based BMS, can be viewed as a prototype for simulating network communication across universities as part of VCHV project by alternating the Unit-Under-Test.

The remainder of this chapter, as shown in Figure 7.3, is organised as follows: To establish a HIL platform for VCHV project, Section 7.2 presents a classic local HIL simulation case study in which an SPMe model (as a battery plant) and a Kalman Filter-based state-of-charge observer (as a simplified BMS) were implemented in two HIL rigs physically positioned in the same laboratory. In this chapter, this local HIL platform was the foundation of the other two case studies. Section 7.3 is an extension of Section 7.2 to establish a ID-HIL platform for VCHV project, in which the HIL rigs for the SPMe model and simplified BMS were remotely communicated with each other in two separate campus buildings. Note that, due to the lack of battery model and parameters at the beginning of this PhD, the SPMe model with a general parameter set, which leads to a 25 A h rated capacity, was employed in Section 7.2 and 7.3 for testing. In addition, to demonstrate the applicability of the NLECM-diff model proposed in Chapter 6 to VCHV project, Section 7.4 presents real-time model validations under various current loads in the local HIL platform established in Section 7.2. Conclusions of three case studies in this chapter are summarised and presented in Section 7.5.
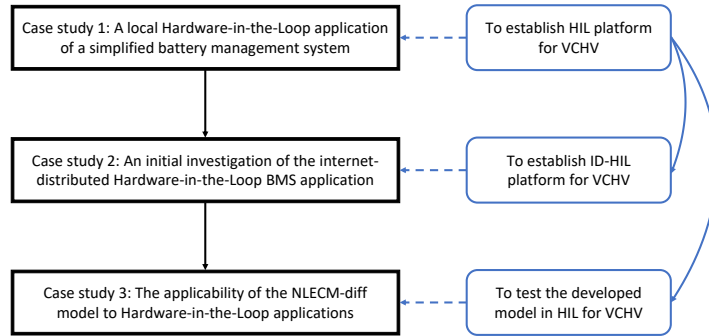
Figure 7.3: Block diagram of organisation and motivations in Chapter 7.

7.2 Case study 1: A local Hardware-in-the-Loop application of a simplified battery management system

7.2.1 Motivation

As described in Chapter 2, different types of battery models demand various degrees of computational complexity, which may be a constraint in real-time Hardware-in-the-Loop applications. In the case of the dSPACE HIL simulation platform, which is commonly used in real-world automobile industrial testing, each iterative operation step must be computed precisely within the specified simulation period. If the system model is overly sophisticated or has an excessive number of computations, HIL rigs will overrun and fail. While equivalent circuit models are frequently used in practical applications due to their low computational complexity, electrochemical models are rarely used in real-time applications. In this case study, an electrochemical battery model and a SOC observer are implemented in the dSPACE Hardware-in-the-Loop platform to act as a battery plant and a simplified BMS, respectively, for the purpose of evaluating the system's applicability to HIL simulations.

7.2.2 Methodology

To build up a real-time simulation framework with distributed Hardware-in-the-Loop platform for VCHV project, the dSPACE hardware platform was selected, which requires battery Simulink model to achieve HIL simulation in real-time. Considering the eventual goal in the future may be not only about SOC, but also about SOH estimation, the electrochemical model proposed in [38], named 'single particle model with electrolyte (SPMe)', was selected to be applied in this work, as the physical phenomena of this model can be presented. In addition, the Kalman Filter-based SOC observer was developed based on a reduced order model of SPMe to further

reduce computational cost for real-time applications. Eventually, the SPMe and SOC observer model were respectively implemented into the SCALEXIO for the real-time HIL simulation. Note that, in this Section, the setup of HIL platform, model implementation, as well as data collection and analysis were the author's original work. The driving cycle (FTP-75) profile was provided by collaborators from Energy Systems Group, WMG, University of Warwick.

Reduced Order Model

To further reduce the computational cost of the SOC observer, the reduced-order model (ROM) was derived from the SPMe introduced in Chapter 2. The idea here is to approximate the linear concentrations dynamics in Equation (2.24) and (2.25) with low order models, while maintaining the nonlinear voltage output equation. Equation (2.24) and (2.25) are simplified to Equation (7.1) and (7.2), respectively, using the balanced truncation method in [97]. Here, the truncated Hankel values should account for no more than 0.5% of the sum of all system Hankel values.

$$
\begin{aligned}
\dot{x}^{\pm}_{s,\mathrm{rom}}(t) &= A^{\pm}_{s,\mathrm{rom}} x^{\pm}_{s,\mathrm{rom}}(t) + B^{\pm}_{s,\mathrm{rom}} I(t) \\
c^{\pm}_{ss,\mathrm{rom}}(t) &= C^{\pm}_{s,\mathrm{rom}} x^{\pm}_{s,\mathrm{rom}}(t) + D^{\pm}_{s,\mathrm{rom}} I(t)
\end{aligned}
\tag{7.1}
$$

$$
\begin{aligned}
\dot{x}_{e,\mathrm{rom}}(t) &= A_{e,\mathrm{rom}} x_{e,\mathrm{rom}}(t) + B_{e,\mathrm{rom}} I(t) \\
c_{e,\mathrm{rom}}(0^{+}, t) &= C^{+}_{e,\mathrm{rom}} x_{e,\mathrm{rom}}(t) + D^{+}_{e,\mathrm{rom}} I(t) \\
c_{e,\mathrm{rom}}(0^{-}, t) &= C^{-}_{e,\mathrm{rom}} x_{e,\mathrm{rom}}(t) + D^{-}_{e,\mathrm{rom}} I(t)
\end{aligned}
\tag{7.2}
$$

The voltage output is calculated using the concentration outputs of the ROM as following,

$$
\begin{aligned}
V(t) =\ & U^{+}(c^{+}_{ss,\mathrm{rom}}(t)/c^{+}_{s,\mathrm{max}}) - U^{-}(c^{-}_{ss,\mathrm{rom}}(t)/c^{-}_{s,\mathrm{max}}) \\
& + k_{\mathrm{conc}} \left[\ln\left(c_{e,\mathrm{rom}}(0^{+}, t) \right) - \ln\left(c_{e,\mathrm{rom}}(0^{-}, t) \right) \right] \\
& + \left[\frac{L^{+} + 2L^{\mathrm{sep}} + L^{-}}{2\bar{\kappa}} - \left(\frac{R^{+}_{f}}{a^{+}L^{+}} + \frac{R^{-}_{f}}{a^{-}L^{-}} \right) \right] I(t) \\
& + \frac{RT}{aF} \left[\sinh^{-1}\left(-\frac{I(t)}{2a^{+}L^{+}i^{+}_{0,\mathrm{rom}}(t)} \right) - \sinh^{-1}\left(\frac{I(t)}{2a^{-}L^{-}i^{-}_{0,\mathrm{rom}}(t)} \right) \right]
\end{aligned}
\tag{7.3}
$$

where $i^{\pm}_{0,\mathrm{rom}}(t) = k^{\pm} \left[c^{\pm}_{ss,\mathrm{rom}}(t) \right]^{\alpha_{c}} \times \left[c_{e,\mathrm{rom}}(0^{\pm}, t)(c^{\pm}_{s,\mathrm{max}} - c^{\pm}_{ss,\mathrm{rom}}(t)) \right]^{\alpha_{a}}$.

Note that the accuracy of the reduced order model is relatively degraded due to the numerical approximation during order reduction, despite the reduced order model's ability to considerably lower calculation cost [289].

State estimation method

The SOC observer acting as a simplified BMS comprises two subsystems: Output Function inversion and the solid phase concentration Kalman Filter. In this work, the observer schematic is shown in Figure 7.4.
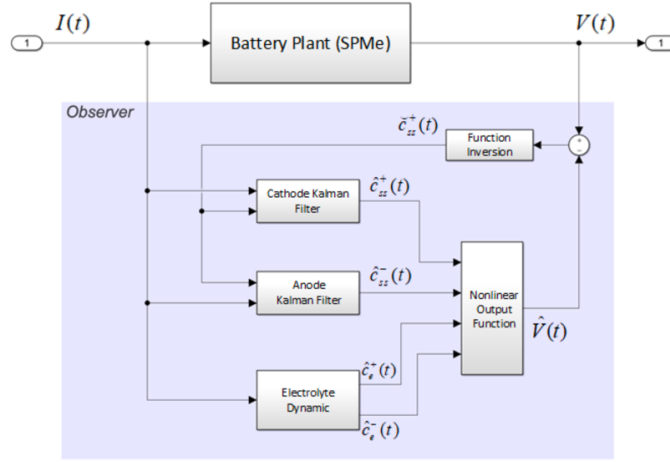
Figure 7.4: The Schematic of SOC observer.

The procedure of SOC observer design is listed as follow,

(i) The voltage error is calculated from cell terminal voltage $V(t)$ and the observer estimated voltage $\hat{V}(t)$, the output function inversion calculates the inversion cathode surface concentration $\breve{c}_{ss}^+(t)$. Consequently, with the assumption of conservation of mass*, the anode surface concentration $\breve{c}_{ss}^-(t)$ can be calculated.

(ii) With the inversion estimated concentrations and input current, the standard Kalman filters based on ROM for both electrode concentration dynamic subsystems can be implemented. Next, the electrodes estimated surface concentration $c_{ss}^\pm(t)$ and bulk concentration $\overline{c}_s^\pm(t)$ can be observed by each Kalman filter.

(iii) Finally, the estimated solid phase surface concentrations and electrolyte concentrations are fed into the observer nonlinear output function subsystem

---

*The total moles of lithium in the solid phase, $n_{Li,s}$, are assumed known beforehand. If we consider initial estimates corresponding to a steady-state condition, the relationship between cathode Li concentration c_{ss}^+ and anode Li concentration c_{ss}^- is shown as following: $n_{Li,s} = \varepsilon_s^+ L^+ c_{ss}^+ + \varepsilon_s^- L^- c_{ss}^-$.

which is same as the function as in the SPMe to produce the observer estimated output voltage $\hat{V}(t)$ (Equation 7.3).

In this part, a nonlinear gradient algorithm is developed to calculate cathode concentration from the measured $I(t)$ and $V(t)$ by inverting the nonlinear output function (7.3).

To focus on the task at hand, the output function is rewritten as

$$V(t) = g(c_{\mathrm{ss}}^+(t), t) \tag{7.4}$$

where the dependence on $c_{\mathrm{ss}}^-(t)$, $c_{\mathrm{e}}^-(0^-, t)$ and $c_{\mathrm{e}}^+(0^+, t)$ has been suppressed into a singular dependence on t.

The inversion result from output function can be represented as $\breve{c}_{\mathrm{ss}}^+(t)$. And then, expand the output function by Taylor series with respect to the difference between $c_{\mathrm{ss}}^+(t)$ and $\breve{c}_{\mathrm{ss}}^+(t)$ about zero. Finally, rewrite the nonlinear output function in 'Gradient Method' form [290], and the gradient update law for $\breve{c}_{\mathrm{ss}}^+(t)$ to minimise cost function $J = \frac{1}{2}\lambda(g(c_{\mathrm{ss}}^+(t), t) - g(\breve{c}_{\mathrm{ss}}^+(t), t))^2$ is given by,

$$\frac{d}{dt}\breve{c}_{\mathrm{ss}}^+(t) = \lambda \cdot (g(c_{\mathrm{ss}}^+(t), t) - g(\breve{c}_{\mathrm{ss}}^+(t), t)) \cdot \frac{\partial}{\partial c_{\mathrm{ss}}^+(t)} g(\breve{c}_{\mathrm{ss}}^+(t), t) \tag{7.5}$$

where λ is the gain to compromise between accuracy and speed.

Kalman Filter

Kalman filter is a widely applied algorithm for state and parameter estimation, which utilises a system's input and output data to seek for the optimal state of linear systems under process and measurement white noise [14]. The discrete-time system can be represented as follow:

$$\begin{aligned} X_k &= AX_{k-1} + BU_{k-1} + w_{k-1} \\ Y_k &= CX_k + v_k \end{aligned} \tag{7.6}$$

Where X represents the states of system, Y denotes the output of estimation, u is the model input and here is the current, A represents the state transition matrix, B denotes control-input matrix, C denotes measurement matrix, and index $k, k-1$ denote time steps of system, while w_k represents the system process noise and v_k represents measurement noise, respectively. These two variables are defined as white noise and with Gaussian probability distributions:

$$p(w_k) \sim N(0, Q)$$
$$p(v_k) \sim N(0, R)$$
(7.7)

where Q and R represents process noise and measurement noise covariance matrices.

Then, the state vector $\hat{X}_k$ and output $\hat{Y}_k$ estimated by Kalman filter algorithm can be mathematically expressed as 'Prediction Time Update' and 'Measurement Update'. In addition, the symbol '$^-$' means the priori variables in each time step.

Prediction Time Update:

$$\hat{X}_k = A\hat{X}_{k-1} + BU_{k-1} + w_{k-1}$$
$$P_k^- = A_k P_{k-1} A_k^T + Q_{k-1}$$
$$\hat{Y}_k = C\hat{X}_k^- + v_k$$
(7.8)

Measurement Update:

$$K_k = P_k^- C_k^T (C_k P_k^- C_k + R_{k-1})$$
$$\hat{X}_k = \hat{X}_k^- + K_k(Y_k - \hat{Y}_k)$$
$$P_k = (I - K_k C_k)P_k^-$$
(7.9)

The Kalman filter can provide the optimal state estimations, and its error elimination ability is suitable for practical real-time application. The readers can refer to [14] for more details.

As the battery plant and SOC observer are to start from equilibrium states, the solid phase surface concentration is set as bulk concentration. Therefore, the initial conditions along the radius are identical in each electrode of the SPMe model. As for the SOC observer, two bulk concentration states require to be set as the initial conditions. In order to evaluate the observer's ability of tracking actual state, various initial conditions are set in different models, as listed in Table 7.1. Note that the total moles of lithium in the electrolyte in the battery and observer are known beforehand and might be provided by the manufacturer [38].

The battery model SPMe and Kalman filter based observer are implemented in 'MATLAB/Simulink 2017b'. In addition, these models are downloaded in the hardware device 'SCALEXIO' from 'dSPACE' for hardware-in-the-loop simulation in real-time. In this work, the reference current profile of the simulations are the city

Table 7.1

Initial conditions of battery plant and SOC observer variables. Note that the value of initial conditions and parameters in this work are the general battery parameters determined artificially.

	Initial lithium ion concentration (mol/m^3)	
	Positive Electrode	Negative Electrode
Battery plant (SPMe)	3000	30000
SOC observer	3900	21000
Output Inversion	2700	/

drive cycle 'FTP-75' (EPA Federal Test Procedure) with capped current magnitude at 1.5C, as shown in Figure 7.5. Note that the primary purpose of this section is to construct the HIL platform; hence, the testing profile was arbitrarily chosen, and the driving cycle was provided by our research group and scaled specifically for this 25 A h battery model.
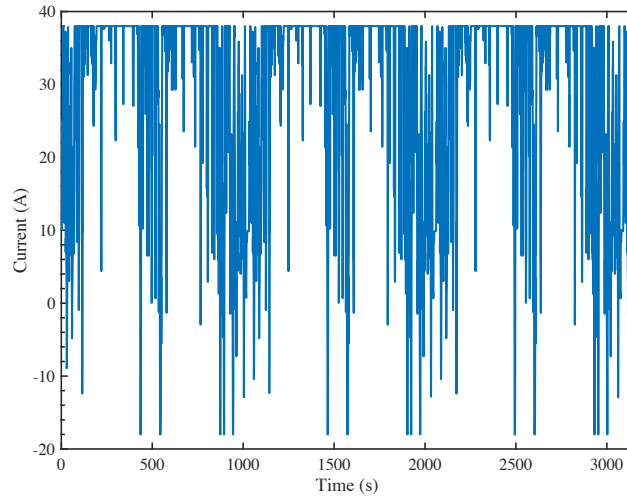
Figure 7.5: The 'FTP-75' city driving cycle profile with capped current magnitude at 1.5C.

7.2.3 Results and discussions

Figure 7.6 presents the output voltage of the observer and the voltage error compared with battery plant's voltage. Even the initial voltage output of the observer was different from battery plant, the observer can still closely converge to plant's output. The reason of the fluctuation in the end should be from the model reduction error

155

and the anode surface concentration conversion process. But the voltage error is acceptable with a maximum error of less than $10\,\mathrm{mV}$ for the real-time electric vehicle application [291].
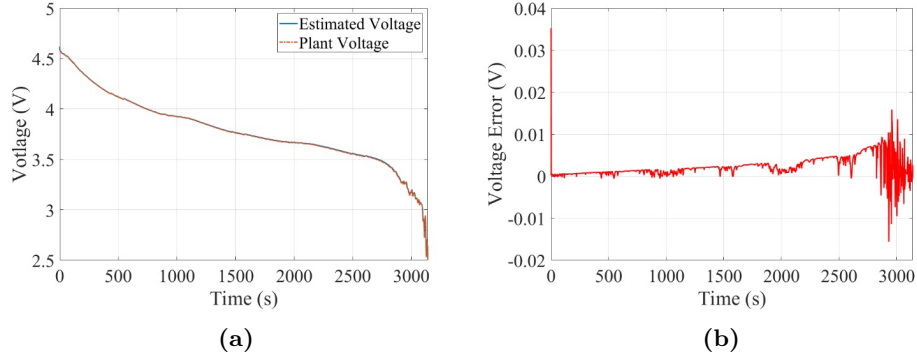
Figure 7.6: Voltage and error profiles of battery plant and SOC observer.

Figure 7.7 shows the performance of the SOC observer in estimating solid phase surface lithium ion concentration. While the initial conditions of lithium ion concentrations were set differently as shown in Table 7.1, the observer can promptly track to the actual surface concentration state and roughly fit the plant's concentration profile. In Figure 7.7b, the surface concentration mole errors between the plant and observer were indicated, and after the beginning of observer tracking process, the cathode error could retain less than 1% in the all discharge regime. Furthermore, in practice, in order to improve battery life, batteries should be designed not to discharge to out of charge. Therefore, the proposed observer can offer reasonable accuracy for the solid phase surface concentration estimation.
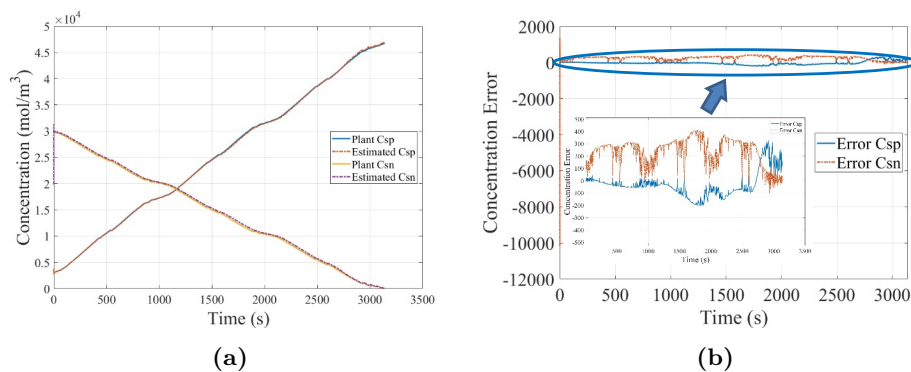
Figure 7.7: Surface lithium ion concentration and error profiles of battery plant and SOC observer.

Additionally, in Figure 7.8, the other objective of the proposed observer SOC

estimation in both electrodes is shown. Since in the ROM, the electrode bulk lithium concentration state is designed. And the change of SOC is directly related to the change of Lithium ion bulk concentration in the electrodes [25]. According to the bulk concentration, the SOC can be estimated for each electrode by the following SOC definition equation:

$$\text{SOC}^{\pm} = \frac{\overline{c}_s^{\pm} - c_{s,\text{SOC}=0\%}^{\pm}}{c_{s,\text{SOC}=100\%}^{\pm} - c_{s,\text{SOC}=0\%}^{\pm}} \tag{7.10}$$

After short transient process, both electrodes SOC were almost overlapped in the whole operational process, and the SOC error between these two electrode observers were less than 0.5%, as shown in Figure 7.8b.
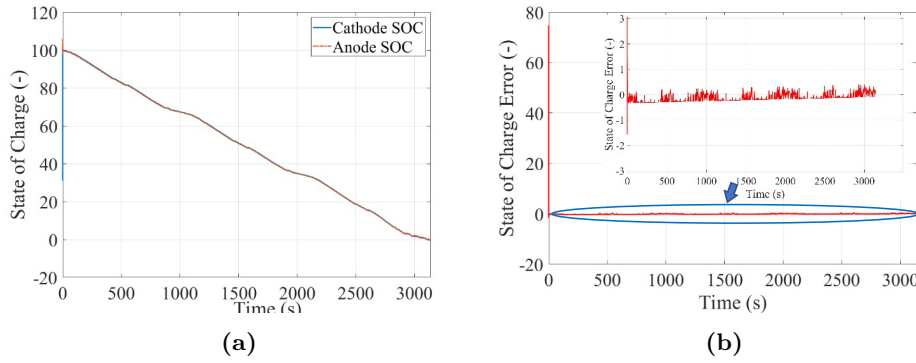
Figure 7.8: Estimated SOC and error profiles of SOC observer.

In this work, the battery plant and simplified BMS are implemented in hardware-in-the-loop simulation device 'SCALEXIO' from dSPACE. In the dSPACE platform, the Run-Time Behaviour 'Period' controls the period of a periodic task or the period constraint of a runnable function. In addition, the 'Step Size' in the Simulink specifies the fundamental sample time used by the selected fixed-step solver. These two configuration parameters control the resolution of the proposed system in the real-time HIL simulation.

Table 7.2 presents the availability of the SPMe and Kalman Filter in various configuration setups of Run-Time Behaviour 'Period' and Simulink 'Step Size'. The results of this case study suggest that the proposed system comprises of battery plant and BMS is successfully employed in the Hardware-in-the-Loop simulation platform, which makes it a potential choice for VCHV project. Furthermore, due to the computational cost, a maximum 0.1 s resolution is available in the real-time HIL application for the proposed system. In the real-world, the BMS should have a higher resolution to promptly respond to emergencies and record batteries operating

Table 7.2

Availability of the SPMe and SOC observer system in the various HIL configuration setups

Simulink 'Step Size'	HIL platform 'Period'		
	0.01 s	0.1 s	1 s
0.01 s	✗	✓	✓
0.1 s	✗	✓	✓
1 s	✗	✓	✓

behaviours.

7.3 Case study 2: An initial investigation of the internet-distributed Hardware-in-the-Loop BMS application

7.3.1 Motivation

The SPMe and SOC observer have been examined in Section 7.2 for their applicability to classic Hardware-in-the-Loop simulation in order to meet the requirements of VCHV project. In this case study, an internet-distributed Hardware-in-the-Loop (ID-HIL) configuration was established on the campus of University of Warwick to emulate the circumstance of network communication between VCHV partners. Not only can this case study contribute a potential network communication approach to VCHV project, but it can also serve as an initial investigation of the cloud-based BMS mentioned in Section 7.1 from an engineering practise standpoint. The idea of the cloud-based BMS in the ID-HIL configuration was to allocate the battery plant and simplified BMS to two geographically distinct buildings instead of the physically connection in the classic HIL configuration. Additionally, the network communication was utilised to remotely transmit data between the battery plant and the remote BMS. If the remote BMS functions properly, it is demonstrated that the ID-HIL configuration is feasible for deployment in VCHV project, as well as the practicality of constructing a cloud-based BMS.

7.3.2 Methodology

This section describes the implementation of the ID-HIL configuration on campus, as shown in Figure 7.9, in which a 'relay' method is devleoped to connect two dSPACE HIL devices, 'MicroAutoBox' and 'SCALEXIO', assigned to two buildings (IDL and IARC) on campus, as well as the system models which are modified for the network

communication. In addition, a 'Virtual Local Area Network (VLAN)' is built to enable real-time data transmission by applying UDP protocol, and the internet quality of the network communication in the ID-HIL configuration is evaluated. Note that, in this Section, the setup of ID-HIL platform, model implementation, network characterisation, as well as data collection and analysis were the author's original work. The driving cycle (FTP-75) profile was provided by collaborators from Energy Systems Group, WMG, University of Warwick.
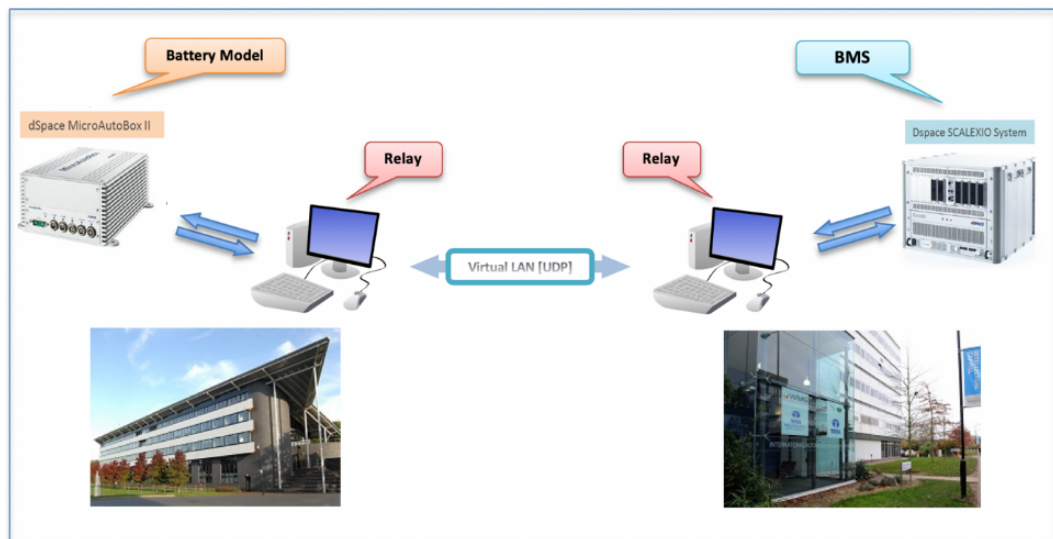
Figure 7.9: Diagram of the internet-distributed Hardware-in-the-Loop configuration on campus.

Description of the 'Relay' method

Generally, the simplest way to connect two dSPACE devices is plugged these two devices into the same sub-network. By this way, the dSPACE inherent system can find each other and connect these two devices, and then the real-time data generated from the HIL simulations can be transmitted directly. However, because of the campus network distribution, the IDL and IARC buildings are set in the distinct sub-networks, such that the direct network connection cannot be applied. Therefore, a 'Relay' method is developed to connect dSPACE devices for data transmission in this case.

In the 'Relay' method, two Host PCs are used not only as monitors for the real-time simulation results from dSPACE devices, but also as the relay modules for network connection via MATLAB/Simulink. Even though the dSPACE devices cannot communicate with each other across multiple sub-networks, MAT-

159

LAB/Simulink is capable of connecting to and transmitting signal data to another MATLAB/Simulink instance located in a different sub-network. To achieve the data transmission, the relay module is implemented in the MATLAB/Simulink of the Host PC, and an example in the IDL building is shown in Figure 7.10. The 'Home' subsystem is used to receive the data from the dSPACE device, and the 'Away' subsystem is employed to send the data over to the other Host PC in the ID-HIL configuration. The IP addresses utilised in the IDL building's relay module is tabulated in Table 7.3. For the other relay module in the IARC building, the IP addresses in the two subsystems are required to be swapped to configure the setup.
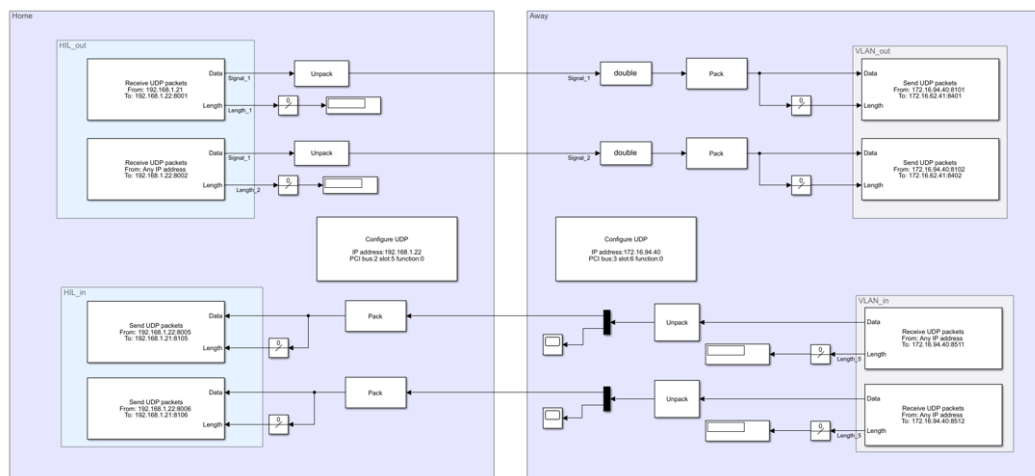
Figure 7.10: Example of the relay module MATLAB/Simulink implementation in the IDL building.

Table 7.3

IP addresses of the dSPACE devices and Host PCs in the ID-HIL configuration.

Location	Device	
	dSPACE device	Host PC
IDL	192.168.1.21	192.168.1.22
IARC	172.16.62.41	172.16.94.40

Description of the models

The SPMe and SOC observer in Section 7.2 were employed and implemented in the dSPACE devices in this work. Practically, each dSPACE device was connected with the Host PC by two network wires. A wire was used for the normal dSPACE-Host

160

PC connection setup and simulation monitor, and the other one was utilised as a network channel for data transmission between the dSPACE device and the Host PC's MATLAB/Simulink. In addition to the original Simulink models, some blocks, which were related to the Network communication, were required to be added into the models. The 'Ethernet Setup', 'Ethernet UDP/IP Setup', 'Ethernet UDP/IP RX', 'Ethernet UDP/IP TX', 'Ethernet decode' and 'Pack' blocks are necessary for this 'relay' method, especially the 'Ethernet decode' and 'Pack' blocks were required for the data type and byte packing normalisation. Thus, the final Simulink model of the battery plant and simplified BMS, which were implemented in the dSPACE devices, were shown in Figure 7.11 and Figure 7.12.
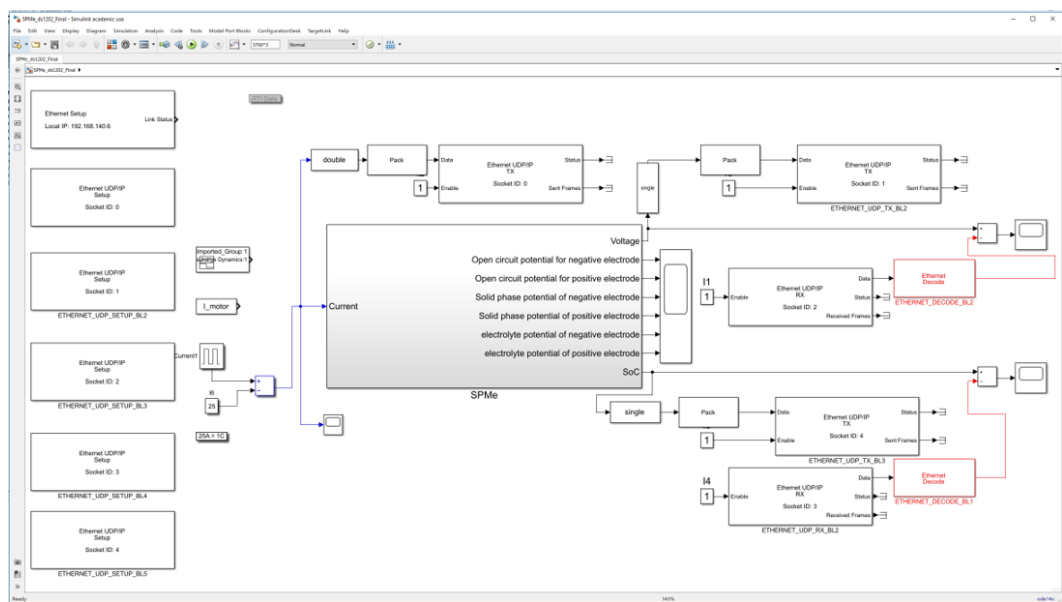
Figure 7.11: Battery Model Simulink Setup with Network Communication

Description of the network characteristics

As required by VCHV project, the User Datagram Protocol (UDP) was utilised for data transmission between two Host PCs. The User Datagram Protocol (UDP) is a data communication protocol that is primarily used to build low-latency and loss-tolerant connections between internet-connected applications. UDP speeds up transfers by allowing data to be transferred prior to the receiving side providing an agreement. As a result, UDP is advantageous for time-sensitive communications such as voice over IP (VoIP), DNS search, and video or audio playback. UDP is a protocol that is an alternative to the Transmission Control Protocol (TCP). Both UDP and TCP are protocols that run on top of IP and are referred to as UDP/IP or

161
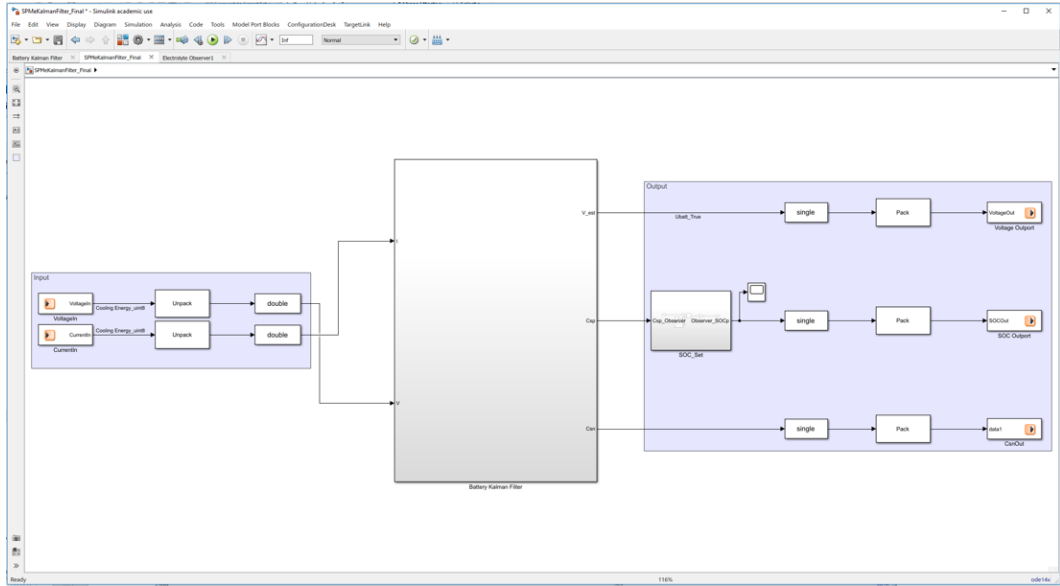
Figure 7.12: BMS Simulink Setup with Network Communication

TCP/IP. However, significant distinctions exist between the two. For instance, UDP provides communication between processes, whereas TCP enables communication between hosts. TCP transmits data in individual packets and is regarded as a reliable transport method to mitigate the data loss during transmission, however, such protocol increases the delay and is not suit for real-time applications. On the other hand, UDP communicates through messages called datagrams and is considered a best-effort communications. This means that UDP makes no promises about the delivery of data or on the availability of special features for retransmitting lost or corrupted messages, but this protocol is recommended for control purpose real-time applications since the control algorithm is time-sensitive but more tolerable to data loss [285, 292].

To characterise the VLAN network quality between IDL and IARC, a series of time delay experiments were conducted between a computer the IDL building and a computer at the IARC building in one week using UDP/IP protocol. A typical result for round trip time delay vs. time of seven days recorded from the tests is shown in Figure 7.13. The figure clearly shows a character in the sense that some packets experience a delay around 1.5 ms, and some around 12 ms (spikes), while others are dropped (shown as 0 delay in the figure). A packet is considered dropped in this case if it does not arrive within 1 s. Table 7.4 provides some statistics of the results shown in Figure 7.13.

The statistics of Figure 7.13 is shown in Table 7.4. Compared to the network
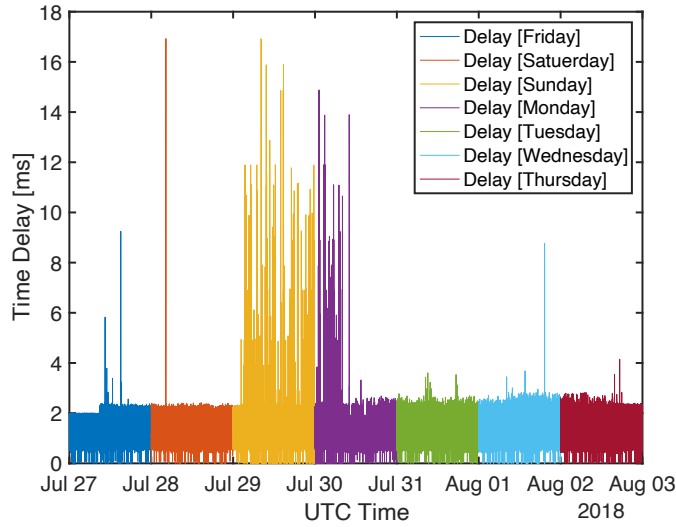
Figure 7.13: Characterisation of VLAN network quality between IDL and IARC in one week. Note that the network testing software 'WireShark' is applied to characterise the network quality.

Table 7.4

Statistics for the results in Figure 7.13.

Number of packets	586089
Avg. delay	1.5 ms
Min. delay	0.5 ms
No of spikes	159(0.021%)
No of drops	71(0.012%)

characteristics in [286] with a delay around 25 ms and some around 350 ms spikes, the variation around 1.5 ms in this case being small makes this network suitable for the purposes of ID-HIL applications.

7.3.3   Results and discussions

In this section, the real-time experimental results of the ID-HIL configuration under different current loads are presented, and the performance of the cloud-based BMS is evaluated. As with the HIL system in Section 7.2, the SPMe was considered to be a battery plant, and the SOC observer was supposed to be a simplified BMS but allocated independently in this study. In addition, the effect of the internet distribution in the ID-HIL was determined by comparing with the results of the Model-in-the-loop and local Hardware-in-the-loop configurations.

Performance of the cloud-based BMS in the ID-HIL configuration

The performance of the cloud-based BMS in the ID-HIL configuration was evaluated under two widely-used current loads, referred to as the constant current charge/discharge profile and the dynamic driving with charge profile. The constant current charge and discharge profile was set at 1C (25 A for the general battery model used in this work) to emulate a general battery test situation, and the FTP-75 city driving cycle*was applied to emulate an actual driving situation. Note that the FTP-75 in this work was from our research group and specifically scaled for this 25 A battery model. A total three cycles of each profile, as shown in Figure 7.14, is applied in this work to evaluate the performance of the BMS in the ID-HIL configuration.
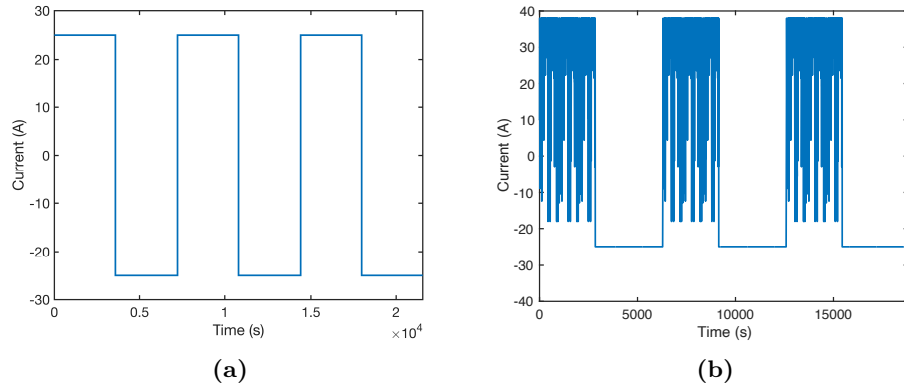
Figure 7.14: Two current loads for the performance evaluation of ID-HIL configuration. (a) 1C constant current discharge and charge profile, and (b) FTP-75 driving cycle with 1C charge profile.

Figure 7.15 presents the voltage and SOC results of the battery plant and BMS throughout the first cycle of the experiments. Note that the experimental results are recorded on the Host PC of the battery plant in the IDL building. Due to the fact that two dSPACE devices are distributed over two buildings and the "Relay" blocks in MATLAB must be manually initiated, it is not possible to initiate a simultaneous start. In this work, the BMS end is started manually first, followed by the battery plant end, which results in the BMS's estimated voltage remaining zero for the first few seconds (7 s in Figure 7.15a and 6 s in Figure 7.15c). The BMS then functions normally, estimating the battery plant's voltage and tracking the battery plant's SOC. Even though the BMS's initial conditions differed from those of the battery plant, resulting in a rather high inaccuracy at first, the BMS's esti-

---

*The FTP-75 city driving cycle is a series of tests defined by the US Environmental Protection Agency (EPA) to measure tailpipe emissions and fuel economy of passenger cars.

mated voltage and SOC eventually mirrored the battery plant's actual states. In the constant current case, the estimated voltage of the BMS overlaps with the battery plant's voltage at 97 s as illustrated in Figure 7.15a. Meanwhile, the BMS's SOC converges to that of the battery plant as shown in Figure 7.15b, which indicates the cloud-based BMS in the ID-HIL configuration can estimate the SOC remotely. In the rest of the experiment duration, the cloud-based BMS can continuously estimate the battery plant's voltage and SOC. Additionally, as presented in Figure 7.15c and Figure 7.15d, the cloud-based BMS is capable of estimating the battery plant's voltage and SOC within around 100 s during driving cycle current load. However, due to the internet distribution of ID-HIL configuration, the BMS's estimated voltage and SOC show relatively larger error than the results from local HIL configuration, as will be discussed in greater detail below.
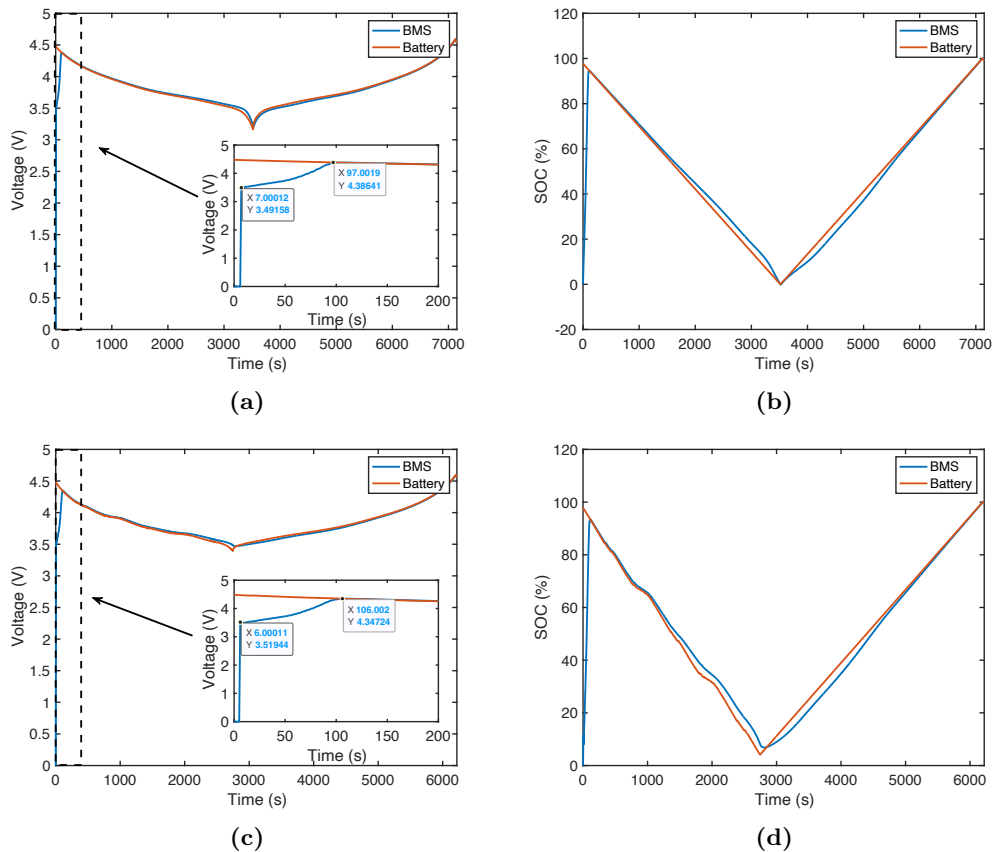
Figure 7.15: Experimental results of the battery-BMS system under the first cycle of two current loads: (a) voltage results in the constant current discharge and charge profile, (b) SOC results in the constant current discharge and charge profile, (c) voltage results in the driving cycle profile, and (d) SOC results in the driving cycle profile.

Effect of internet distribution

To ascertain the effect of internet distribution on the ID-HIL configuration, two current profiles are applied on the the Model-in-the-Loop (MIL) and HIL configurations, respectively, and the ID-HIL simulation results are compared to those of the Model-in-the-Loop (MIL) and HIL configurations. The MIL simulation is used to test the developed model while it is operating in a simulation environment like as Simulink. The MIL configuration captures the majority of the critical features of the hardware system and has the potential ability to improve convenience and minimize costs [293]. Note that the MIL simulation runs in processor-time, which is frequently significantly faster than real-time and does not require a fixed time step, and the results of the MIL simulation can be used as a baseline for validation, as the entire system is assumed to operate in an ideal state without any delay or disturbance caused by data transmission or environment [294]. Additionally, the HIL simulation described in Section 7.2 is employed for comparative purposes in this work. In comparison to the ID-HIL simulation, the HIL simulation omits only the network communication component; the rest of the configuration is identical. Thus, by comparing these two HIL configurations, it is possible to deduce the effect of internet distribution on the real-time battery-BMS system.

Figure 7.16 presents the voltage and SOC error profiles of MIL, HIL, and ID-HIL configurations under the constant current charge/discharge and the dynamic driving with charge loads. The error values are derived by subtracting the corresponding data of the battery plant from the data of the BMS, and the positive value indicates the BMS overestimates the corresponding variable. Due to the fact that the devices cannot be started concurrently in the ID-HIL configuration, the experiment's first period data are discarded; hence, the second and third experiment periods are chosen to analyse the influence of network communication. Taken as a whole, both voltage error and SOC error in Figure 7.16 increases as the battery SOC decreases, which might be related to the inaccuracy of the mathematical model employed in the SOC observer. Furthermore, the error profiles in the second and third periods are identical which indicates the good stability of the systems in all three configurations. In addition, it is clearly observed that the voltage and SOC error of the MIL (blue curves) and HIL (red curves) configurations are quite small and almost overlapped in Figure 7.16, which indicates that the implementation of the HIL configuration has nearly no effect on the performance of the BMS. However, the BMS's estimated voltage and SOC in the ID-HIL configuration (yellow curves) shows significant error in both current load cases. Attributed to the fact that the main difference between the HIL and ID-HIL configurations is the internet distribu-
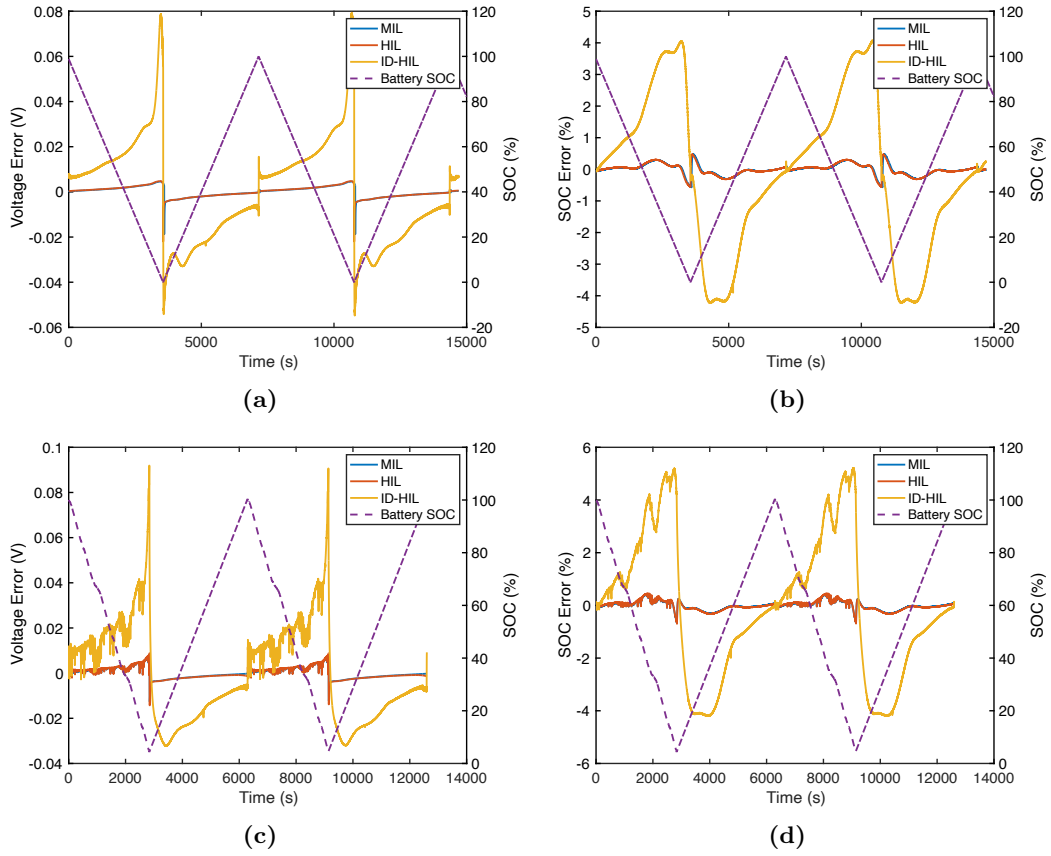
Figure 7.16: Voltage and SOC error profiles of MIL, HIL, and ID-HIL configuration under two current loads: (a) voltage error in the constant current discharge and charge profile, (b) SOC error in the constant current discharge and charge profile, (c) voltage error in the driving cycle profile, and (d) SOC error in the driving cycle profile.

tion, these results show that the internet distribution in the ID-HIL configuration results in the poor accuracy of the BMS.

Table 7.5 presents the maximum error and RMSE of the BMS estimated voltage and SOC in each configuration. Consistent with the Figure 7.16, the BMSs in MIL and HIL configurations exhibits comparable and great accuracy in the voltage and SOC estimations under each current load. However, under the constant current discharge and charge load, the BMS in the ID-HIL configuration exhibits an estimated voltage RMSE almost tenfold that of the HIL configuration and a maximum error fourfold that of the HIL configuration. The SOC maximum error increases from 0.56% to 4.08%, and the RMSE of SOC grows from 0.17% to 2.45%. Similarly, the accuracy of the BMS in the ID-HIL deceases significantly under the driving cycle load and RMSE SOC increases from 0.18% to 2.72%. In both cases, the SOC RMSE is more than the 2% criterion for the accuracy of a state-of-the-art

Table 7.5

Maximum error and RMSE of the BMS estimated voltage and SOC in the experiments of three configurations under two current loads.

	MIL		HIL		ID-HIL	
	Max. Error	RMSE	Max. Error	RMSE	Max. Error	RMSE
Voltage [CC] (mV)	18.7	2.2	22.0	2.3	79.4	23.2
SOC [CC] (%)	0.57	0.17	0.56	0.17	4.08	2.45
Voltage [FTP-75] (mV)	12.7	2.4	14.3	2.6	92.9	21.9
SOC [FTP-75] (%)	0.67	0.16	0.70	0.18	5.22	2.72

SOC estimator [295].

This case study establishes an internet-distributed Hardware-in-the-Loop configuration to emulate the circumstance of network communication between VCHV partners. The cloud-based BMS experimental results demonstrate that the suggested ID-HIL configuration is capable of real-time data transmission, indicating that it could be used in VCHV project. However, the accuracy of the cloud-based BMS is relatively poor due to the internet distribution. Thus, advanced state estimate algorithms, that are tolerant of data loss and time delay, are suggested to be utilised in the future work to improve the accuracy of the cloud-based BMS. For example, in [296], one straightforward extension of Extended Kalman Filter which can handle time-delays was proposed. In this method, the key point is to return to the time step of the delay measurement to incorporate the delay measurement, and then, re-compute the entire estimation progress till the newest step which is without time-delay. The simulation results of this study show that this approach is more reliable than existing approaches for state estimation using measurements with unknown time delays.

7.4 Case study 3: The applicability of the NLECM-diff model to Hardware-in-the-Loop applications

7.4.1 Motivation

This case study presents the HIL validation of the NLECM-diff model to fulfil "**Research Objective (4):** Evaluate the applicability of the proposed battery model in the internet distributed Hardware-in-the-Loop simulation platform." As specified in VCHV research proposal, the author was responsible for developing and providing an accurate battery mathematical model for the internet distributed

Hardware-in-the-Loop applications. In Chapter 6, a unique battery model, termed as nonlinear equivalent circuit model with dynamics (NLECM-diff), was proposed and parameterised for the LG M50 experimental three-electrode cell. Taking advantages of the experimental cell, the NLECM-diff models for the full-cell and for individual electrodes were developed, and the accuracy of the NLECM-diff models has been examined in a software simulation environment. However, the applicability of the NLECM-diff model to the ID-HIL applications has not been evaluated yet. In addition, the terminal voltage of the battery models can be provided by either the full-cell model or a combination of individual electrode models named the decoupled-electrode model. To select the appropriate battery model for VCHV project, the accuracy of these two types of NLECM-diff models in the HIL applications must be evaluated under a diversity of current loads. Thus, in this case study, both the NLECM-diff full-cell model and the decoupled-electrode NLECM-diff model were implemented in the HIL platform to assess their applicability to HIL applications as well as their accuracy for terminal voltage estimation. Note that, due to facility access restrictions, the NLECM-diff models were not demonstrated on the ID-HIL platform.

7.4.2 Methodology

The ID-HIL configuration was developed by evolving from the local HIL configuration in Section 7.3, and the feasibility of the ID-HIL configuration has been evaluated. Taking advantage of the flexibility of the HIL simulation, it is sufficient to replace the mathematical models in the hardware devices when testing a new model of the Unit-Under-Test. In this work, the NLECM-diff model proposed in Chapter 6 was implemented in the dSPACE device 'MicroLabBox' for the HIL validation, as shown in Figure 7.17. To be consistent with the simulation validation of the NLECM-diff model in Chapter 6, the successive CC discharge and CC-CV charge and the NEDC current profiles were applied on the NLECM-diff model and the actual LG M50 21700 battery cell in the HIL validation. Note that the current loads were normalised to the rate capacity of the NLECM-diff model which is parameterised for the experimental cell with $11.5\,\mathrm{mA\,h}$ capacity, as the the current profile was designed for the experiments on the LG M50 21700 $5\,\mathrm{A\,h}$ cell. The measured terminal voltage data of the LG cell (V_Experiment) was then utilised to validate that of the NLECM-diff model generated from the HIL device. As presented in Chapter 6, not only the full-cell model, but also the models of the individual electrodes were developed. Thus, the NLECM-diff model was capable of providing three estimations in terms of full-cell terminal voltage (V_HIL), cathode voltage (Vwe_HIL),

169

and anode voltage (Vce_HIL) while excited by the current loads. According to the relationship between battery cell and individual electrodes, an alternative estimation of the full-cell terminal voltage V_HIL[we-ce] can be represented by the voltage difference between the cathode and anode follows Equation (7.11),

$$V\_HIL[we\text{-}ce] = Vwe\_HIL - Vce\_HIL \tag{7.11}$$

Therefore, two estimated terminal voltage profiles obtained by the NLECM-diff can be validated with the measured experimental terminal voltage data. The voltage of individual electrodes in Equation (7.11) are obtained by using three-electrode experimental configuration, which means the voltage drops across separator and electrolyte are already included [24]. Note that, in this Section, model implementation, data collection and analysis, as well as HIL validation were the author's original work. Three-electrode configuration experimental cells and the driving cycle (NEDC) profile were provided by collaborators from University of Birmingham.
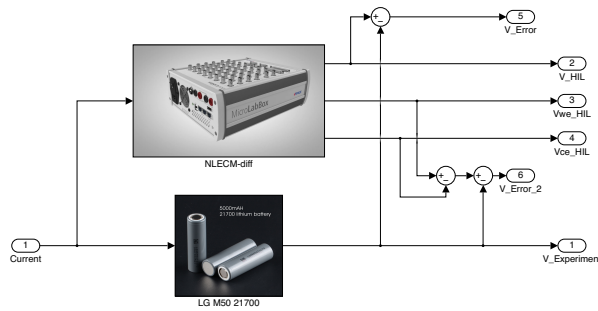
Figure 7.17: Diagram of the NLECM-diff model HIL validation.

7.4.3 Results and discussions

Figure 7.18 shows two current loads applied in this work for examining the applicability of the NLECM-diff to HIL applications. The successive CC discharge and CC-CV charge current profile between 4.2 V and 2.5 V, which consists of a 0.3C CC discharge and 0.3C CC-CV charge, a 0.5C CC discharge and 0.3C CC-CV charge,

and a 1C CC discharge profile, is applied to emulate the voltage response of the NLECM-diff model in stable driving and charging conditions, as shown in Figure 7.18a. The NEDC driving cycle profile employed in Chapter 6 is utilised in this work as shown in Figure 7.18b. The blue curves in Figure 7.18 are the current profile recorded from the LG cell experiments, but the amplitude of the current data has been normalised for the NLECM-diff model with 11.5 mA h rated capacity. The red curves, which represent the current profiles recorded by the HIL device, are seen to overlap with the normalised experimental current signal. This results indicate that the hardware device has the ability to accurately reproduce the imported experimental current signal. Due to a system problem during the experiment, the 15th cycle of the NEDC driving profile in Figure 7.18b is incomplete; however, the current signal employed in the HIL device remains unchanged for consistency.
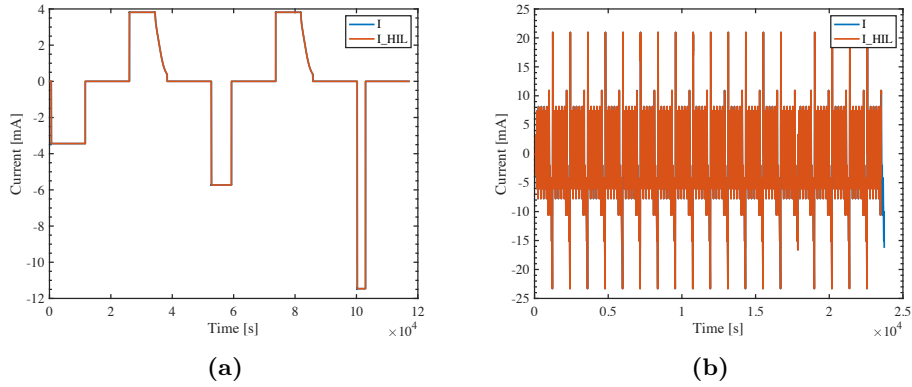
Figure 7.18: Two current loads for examining the applicability of the NLECM-diff model in the HIL applications. (a) Successive CC discharge and CC-CV charge profile, and (b) NEDC driving cycle profile.

Voltage and error profiles of the model estimated full-cell terminal voltage under the successive CC discharge and CC-CV charge current load are presented in Figure 7.19. By and large, the NLECM-diff model is capable of being applied in the HIL applications, and the model estimated voltage has a good agreement with the experimental data as shown in Figure 7.19a. Similar with the results demonstrated in Chapter 6, the NLECM-diff model shows the best performance with around 0.12 V error in the 0.5C discharge duration, as the model is optimised with 0.5C discharge current. However, the estimated voltage error up to 0.5 V in the 1C discharge duration, which is deserved to be improved in the future. In addition, Figure 7.19b presents the voltage error obtained from full-cell terminal voltage estimations of two NLECM-diff models; V_HIL for full-cell NLECM-diff model and V_HIL[we-ce] for decoupled-electrode NLECM-diff model. It is observed that the NLECM-diff model

overestimates the full-cell terminal voltage during discharge and underestimates it during charge time. Furthermore, the lower value of V_HIL[we-ce] illustrates that the estimated full-cell voltage calculated from individual electrodes is slightly more accurate than the full-cell model, particularly while charging. Given the conclusion reached in Chapter 6 that the diffusion dynamics is dominating in long time constant charge and discharge processes, this result could be explained by the fact that two diffusion blocks for both electrodes in decoupled-electrode model provide one more degree of freedom than the full-cell NLECM-diff model.
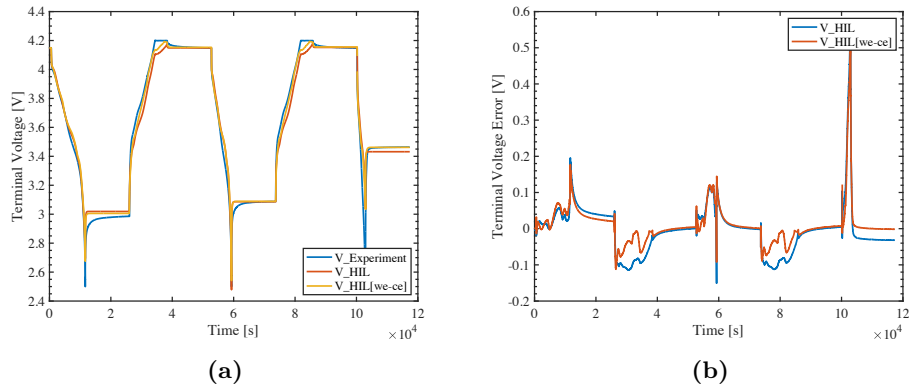
Figure 7.19: Voltage and error profiles of the estimated full-cell terminal voltage under the successive CC discharge and CC-CV charge current load. (a) Voltage profile of the NLECM-diff model estimation, and (b) voltage error profile of the NLECM-diff model estimation.

Figure 7.20 demonstrates the voltage and error profiles of the model estimated full-cell terminal voltage under the NEDC driving cycle current load. The voltage profile obtained from the HIL device agrees well with the experimental data, indicating that the NLECM-diff model is appropriate to HIL applications in driving scenarios. Similar with the simulation validation results in Chapter 6, the NLECM-diff model shows a relative large voltage error at extreme low SOC area, which could be improved by introducing the output limitation into the model. As illustrated in Figure 7.20b, there is no discernible difference in the estimated voltage error between the full-cell and decoupled-electrode models, which might indicate that the improvement achieved by combining individual electrode models is insignificant in dynamic driving scenarios driven by ohmic and polarisation dynamics.

Goodness-of-fit (R^2) of the NLECM-diff full-cell and decoupled-electrode models are calculated and tabulated in Table 7.6. Consistent with the results demonstrated in Figure 7.19 and 7.20, the decoupled-electrode model only exhibits the improvement of the accuracy in the successive CC discharge and CC-CV charge profile. Thus, a trade-off between model complexity and accuracy must be undertaken while
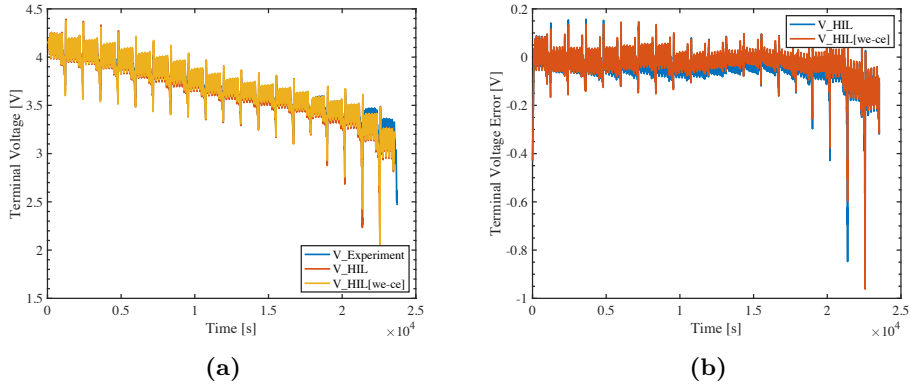
Figure 7.20: Voltage and error profiles of the estimated full-cell terminal voltage under NEDC driving cycle current load. (a) Voltage profile of the NLECM-diff model estimation, and (b) voltage error profile of the NLECM-diff model estimation.

selecting a model that is appropriate for real-world applications.

Table 7.6

Goodness-of-fit (R^2) comparison of the NLECM-diff model estimated terminal voltage between the full-cell and decoupled-electrode model.

	R^2 [%]	
	CC	NEDC
Full-cell model	97.9	96.7
Decoupled-electrode model	98.7	96.7

7.5 Conclusions

This chapter demonstrates three engineering practical case studies to fulfil "**Research Objective (4):** Evaluate the applicability of the proposed battery model to Hardware-in-the-Loop simulations." which the author, on behalf of WMG, University of Warwick, has determined to contribute to VCHV project. In Section 7.2, the virtual battery-BMS system, comprised of the SPMe battery model and a Kalman filter-based SOC observer, has been implemented in the dSPACE HIL hardware devices to evaluate the electrochemical battery model's suitability for VCHV project. On the basis of the success of the HIL configuration, an internet distributed Hardware-in-the-Loop configuration for the battery-clouded-BMS system has been proposed and implemented on the University of Warwick's campus in Section 7.3. This configuration replaces the HIL configuration's communication method from wires to

the internet network to remove the geographical constraints used to emulate the circumstance of the distributed HIL network connection across VCHV partners. Given that the limitations of existing battery models for the practical applications, the advanced NLECM-diff model proposed in Chapter 6 is implemented in the HIL configuration to evaluate the applicability to the ID-HIL applications in Section 7.4. To select the appropriate battery model, the accuracy of the NLECM-diff full-cell and decoupled-electrode models is evaluated and compared under successive CC discharge and CC-CV charge, as well as the NEDC current profile loads.

The following conclusions can be drawn according to the experimental results; Firstly, in Section 7.2, the battery-BMS system, consisting of the simplified electrochemical battery model SPMe and the Kalman filter-based SOC observer, is demonstrated to be available for VCHV project. However, due to the massive computational cost, the resolution of the HIL simulations has to be limited as $0.1\,\mathrm{s}$ for a single battery cell, as demonstrated in this Chapter, which may not be sufficient for algorithms that consider multiple battery cell models for battery modules or packs. Further, in Section 7.3, the ID-HIL configuration with 'relay' modules is proven as a feasible solution for data transmission between geographically dispersed HIL devices. However, the decrease of observer accuracy due to the effect of internet distribution is fairly significant, even in the case of a high-quality network, which is deserved to further investigation. Furthermore, Section 7.4 demonstrates the applicability of the NLECM-diff model to HIL applications, and the real-time simulation results exhibit a good agreement with the experimental data under various current loads. In addition, the NLECM-diff decoupled-electrode model slightly outperforms the full-cell model in the successive CC discharge and CC-CV charge current profile cases; nevertheless, in the NEDC profile scenario, the two models exhibit equal accuracy. While the full-cell model performs similarly to the decoupled-electrode model in terms of accuracy but at a lower computing cost, the decoupled-electrode model has the advantage of being able to estimate the voltage of individual electrodes, and hence merits consideration for VCHV project, such that the state estimation and control algorithms that require internal electrode potential variables can be achieved for optimising charging strategy and preventing lithium-ion plating [46, 278]. Overall, this chapter demonstrates that the developed NLECM-diff models (full-cell model and decoupled-electrode model) can be utilised in both local HIL and ID-HIL simulations for VCHV project, which fulfils the requirement of "**Research Objective (4):** Evaluate the applicability of the proposed battery model to Hardware-in-the-Loop simulations."

Chapter 8

Conclusions and future work

The motivation underpinning this thesis, as described in Chapter 1, is to develop a unique battery mathematical model which requires minimal identification cost while achieving a high level of accuracy over the entire SOC range for Hardware-in-the-Loop applications aligned with the externally funded project "Virtually Connected Hybrid Vehicle (VCHV)". Following a critical review of the existing literature relating to battery mathematical models within Chapter 2, it was concluded that the existing battery models obtained from previous research are developed either by interpreting battery dynamics at a high expense of identification or by fitting the battery current-voltage relationship without regard for physical significance. In terms of practical applications, the former class model is difficult to employ for original equipment manufacturers due to a lack of extensive laboratory conditions, while the latter class model is believed to result in a relatively large voltage estimation error at low SOC range due to nonlinear distortions caused by battery dynamics. Therefore, a lack of a high computational efficiency and easily implementable model, which also can describe battery physical meaning and nonlinearity, for practical applications was identified as a first knowledge gap.

Furthermore, it was found that the absence of the aforementioned battery model could be partially attributed to a lack of nonlinear characterisation methods suitable for battery modelling. As such, developing a novel nonlinear characterisation method is a precondition for building a battery model that performs as expected. To address this, Chapter 3 critically reviewed characterisation methods for battery modelling. It was found that no systematic approach exists for capturing battery nonlinearity while also providing information for battery modelling. Based on these shortcomings, it was concluded that the existing system identification approaches for a lithium-ion battery cell are insufficient for practical applications, and

a second knowledge gap is described as the absence of such nonlinear characterisation method .

8.1 Contributions to knowledge

Innovations and key contributions to knowledge corresponding to research objectives proposed in Chapter 1 are summarised in Figure 8.1. In brief, the innovation of this work is to develop a comprehensive system identification methodology of a lithium-ion battery cell for BMS applications, which includes the nonlinear characterisation method, battery system modelling, and practical implementation.

Research objective	Innovation	Key contribution	Contribution to academia	Chapter in thesis
(1) Design a characterisation method capable of capturing battery nonlinearity.	A new multisine-based nonlinear characterisation method capable of capturing battery nonlinearity while obtaining the necessary information for parameterisation	Odd and even nonlinearities are captured and separated by random phase odd multisine signal.	Published in [1] [2]	4 and 5
(2) Understand the electrochemical processes contributing to nonlinearity.	A model-based procedure to investigate the origins of the battery nonlinearity	Charge transfer kinetic is determined as the most sensitive to nonlinearity at a SOC level.	Published in [1]	4
	An experimental procedure to investigate the dominant electrochemical process contributing to nonlinearity	Diffusion process mainly contributes nonlinearity at low SOC range.	Published in [2]	5
(3) Develop a battery mathematical model which requires low identification cost while achieving a high level of accuracy over the entire SOC range.	A new ECM model with low identification and computational costs that achieves a high level of accuracy over the entire SOC range by accounting for battery nonlinearity and diffusion dynamic	The developed NLECM-diff model achieves a comparable accuracy to the SPMe. The diffusion characteristic of the anode is identified as the cause of low-SOC-error.	Published in [3]	6
(4) Evaluate the applicability of the proposed battery model to Hardware-in-the-Loop simulations.	An internet distributed Hardware-in-the-Loop platform which enables real time co-test across different geographical locations	The decoupled-electrode NLECM-diff model is determined to be a suitable substitute for the SPMe in real-time applications.	Published in [4]	7

Figure 8.1: Summary of innovations and key contributions to knowledge.

This development and implementation of the system identification methodology on the use case of VCHV project has addressed the research gaps identified within Chapter 2 and 3 through the accomplishment of a series of four research objectives.

The first process was defined in "**Research Objective (1):** Design a characterisation method capable of capturing battery nonlinearity." As battery nonlinearity, which is required to be included in the predicted model, is a relatively new topic, it is vital to develop a feasible nonlinear characterisation approach and to analyse and comprehend the corresponding results. In Chapter 4, an odd random-phase multisine signal, the basis of the innovative frequency domain nonlinear characterisation method, is designed, and the method is employed on a widely used electrochemical

battery model (DFN) and an experimental battery cell to investigate the nonlinearity of a lithium-ion battery. The proposed nonlinear characterisation method offers an efficient and rapid approach to access and capture battery nonlinearity for further analysis and application, and lays the groundwork for the development of new system identification methods for lithium-ion batteries.

In Chapter 4, the dominant linear, odd and even order nonlinearities from experimental data and the DFN model are analysed and compared in the frequency domain, and a significant difference in the nonlinearities between the mathematical model and the real battery is observed. Furthermore, the most sensitive parameter to battery nonlinearities is determined as the charge transfer coefficient α by applying a global sensitivity analysis, and thus the charge-transfer reactions are determined as the main contributor to the nonlinearities of a lithium-ion battery at a SOC level. In addition, results of the nonlinearity RMSE show that, rather than the commonly used value of 0.5, α_a set as 0.8 or 0.9 provides a good model agreement with the experimental data while the commercial cell is at 10% SOC. This phenomenon indicates that the charge-transfer reactions in a lithium-ion battery is an asymmetrical behaviour, rather than the commonly assumed perfect symmetrical reaction. Lastly, this study demonstrates the ability of the multisine-based characterisation method to estimate the charge transfer coefficients α by relying on the battery even and odd order nonlinearities in the frequency domain rather than only using measured current-voltage curves. Overall, this chapter demonstrates the feasibility of the developed nonlinear characterisation method, which is based on random phase odd multisine signal to capture and separate odd and even nonlinearities, in the analysis of battery nonlinearity, which fulfils the requirement of "**Research Objective (1):** Design a characterisation method capable of capturing battery nonlinearity." In addition, this chapter enhances the understanding of lithium-ion battery nonlinear dynamic response through the model-based investigation that charge transfer kinetic is the most sensitive to battery nonlinearity at a SOC level, which indicates that lack of charge transfer kinetic interpretation could lead to inaccuracy of battery model. Thus it provides a theoretical basis for the development of the NLECM-diff model in Chapter 6. The resulting methodology including the signal design and simulation data analysis were published in Transactions of the Institute of Measurement and Control [1].

The second stage of the process was defined in "**Research Objective (2):** Understand the electrochemical processes contributing to nonlinearity." This task is a representation of the data collection stage of the system identification procedure, and the completion of this study fulfils the knowledge gap relating to a lack of the

understanding of battery nonlinearity. Chapter 5 presents the successful experimental investigation that was conducted employing the proposed frequency domain nonlinear characterisation method on battery cells, which allows for the capture of battery nonlinearity and the collection of the necessary experimental data for the following model identification step. The feasibility of the proposed characterisation method for capturing battery nonlinearity is thus experimentally demonstrated, as well as the source of battery nonlinearity and the dominant electrochemical process contributing to the nonlinearity are determined in this work.

Overall conclusions of Chapter 5 are summarised as following: First, it can be concluded that nonlinearities are very low at high SOCs (>10%), as such the battery current to voltage relationship is behaving linearly in these regions. Moreover, at low SOCs ($\leqslant 10\%$), the nonlinearities of a lithium-ion battery significantly increase, and the dominant contributor to lithium-ion battery nonlinearity was determined as the cathode even order nonlinearity. Additionally, the dominance of the even nonlinearity indicates that an even order nonlinear characteristic function may be required for modelling non-linear behaviour of a lithium-ion battery. Lastly, the dynamics of the anode changes at 2% SOC and starts to contributes with a significant even-order nonlinear distortion comparable to that of the cathode. Overall, this chapter experimentally investigates the contribution of battery diffusion process and charge transfer kinetics to nonlinearity by employing the developed multisine-based nonlinear characterisation method, which fulfils the requirement of "**Research Objective (2):** Understand the electrochemical processes contributing to nonlinearity." In addition, this chapter concludes that diffusion process mainly contributes nonlinearity at low SOC range, which indicates that lack of interpretation of diffusion process could be the reason of linear ECM models' inaccuracy in the low SOC area. Thus it suggests that the nonlinearity-related diffusion process merits to be modelled during the battery system identification in Chapter 6. The characterisation methodology, results, and explanation for the battery nonlinearity from this experimental work have been published in Journal of Energy Storage [2].

By employing the multisine-based method, Chapter 6 addressed "**Research Objective (3):** Develop a battery mathematical model which requires minimal identification cost while achieving a high level of accuracy over the entire SOC range." It describes the experimental characterisation procedures, the identification methodology, and the validation process. The nonlinear equivalent circuit model with diffusion dynamics (NLECM-diff), as listed in Table 8.1, is proposed, which takes into accounts of diffusion dynamics and nonlinearity interpretation caused by charge-transfer reactions. The validation results shown in Figure 8.2 and Table 8.2

highlight that, by involving the diffusion block at the cost of adding one extra identification test, the voltage estimation error of the NLECM-diff model in both the entire SOC range and the low SOC range is significantly reduced in comparison of the linear 2nd order ECM, and the proposed NLECM-diff model achieves comparable accuracy to the SPMe model but with much less computational time cost, which conforms to the accuracy requirements proposed in Section 1.3. Furthermore, the dominant behaviour contributing to the total voltage loss is determined by applying the NLECM-diff model under different current loads, in which the diffusion process is the dominant voltage loss when under the long time current discharge, and the ohmic voltage loss is the dominant dynamic when under a dynamic NEDC profile. Additionally, the validation results from the decoupled electrode NLECM-diff models suggest that, during discharging, a relatively large voltage estimation error is shown in the negative electrode NLECM-diff model during the low SOC range, and the variation of the diffusion-related characteristics of the negative electrode is determined as the primary reason of the battery models' low-SOC-error under different applied current intensities. This discovery extends knowledge that the role of individual electrodes contributing to full-cell voltage estimation error, and this finding suggests that future lithium-ion battery modelling research should place a greater emphasis on investigating the model of battery negative electrode under different operating conditions for a comprehensive and reliable battery model. Overall, this chapter demonstrates that the developed NLECM-diff model can achieve a comparable accuracy to the SPMe by accounting for battery nonlinearity and diffusion dynamic, which fulfils the requirement of "**Research Objective (3):** Develop a battery mathematical model which requires minimal identification cost while achieving a high level of accuracy over the entire SOC range." The modelling methodology, validation results and analysis have been published in Applied Energy [3].

Table 8.1
Contribution of this work to knowledge of equivalent circuit battery models for BMS applications.

Model	Characterisation Tests	Nonlinearity Interpretation	Diffusion Dynamics	Ref.
ECM	HPPC, OCV	✗	✗	[40]
FOM	EIS, OCV	✗	✔	[139]
NLECM	Multisine test, OCV	✔	✗	[152]
NLECM-diff	Multisine test, CC test, OCV	✔	✔	[3]

The results of the practical implementations and their analysis are presented within Chapter 7 and fulfil "**Research Objective (4):** Evaluate the applicability
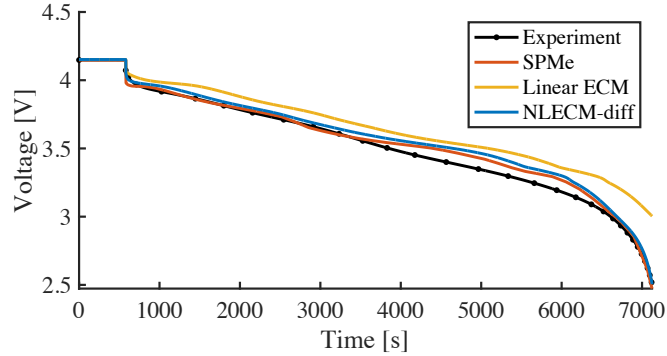
Figure 8.2: Voltage predictions of the linear 2nd order ECM, the SPMe model, and the proposed NLECM-diff model discharged from 100% SOC to 0% SOC at 0.5C constant current load.

Table 8.2
Features of three battery models at 0.5C constant current load.

Model	100%-0% RMSE [V]	20%-0% RMSE [V]	Parameterisation tests	Computational Time [s]
Linear ECM	0.172	0.493	2	2.30
SPMe	0.048	0.036	7	301.33
NLECM-diff	0.047	0.057	3	4.89

of the proposed battery model to Hardware-in-the-Loop simulations." As this PhD is aligned with the externally funded project VCHV, the Hardware-in-the-loop applications required by the project proposal are implemented in the form of three related case studies in this chapter, which is linked to the model application step of the system identification procedure. The experimental results provide a straightforward demonstration that the simplified electrochemical model, named single particle model with electrolyte dynamics (SPMe), is employable in HIL applications to estimate battery cell's voltage response with regards to the corresponding current load. In the same local HIL configuration, the applicability of the NLECM-diff model for HIL applications is examined, which fulfils the demand of VCHV project. From the experimental results obtained within this work, it is inconclusive about the amount of computational cost savings gained by substituting the NLECM-diff model for the SPMe in HIL applications. However, in terms of model parameterisation, in comparison to the 30 parameters required by the SPMe, the NLECM-diff with only 9 parameters is projected to be more advantageous for usage in practical BMS applications. In additional, by utilising the decoupled-electrode NLECM-diff model, it is possible to determine the potential of individual electrodes concurrently with the battery terminal voltage during operation. Such that, for certain practical BMS

operations that require access to individual electrode behaviour, such as preventing lithium plating during fast charging, the decoupled-electrode model may be a better candidate than the sophisticated electrochemical models. Furthermore, this chapter discusses a possible approach for constructing an internet distributed Hardware-in-the-Loop simulation platform as a contribution to the VCHV project, which can be regarded as a working hypothesis of cloud-based BMS applications. However, a relatively poor accuracy caused by the internet distribution in the cloud-based BMS system is observed, which requires to be investigated in further studies. This chapter discusses three practical instances (MIL, HIL, and ID-HIL) from the standpoint of engineering practice that may be of interest to engineers in the automotive sector. Overall, this chapter demonstrates that the developed NLECM-diff models can be utilised in both local HIL and ID-HIL simulations as contributions to VCHV project, which fulfils the requirement of "**Research Objective (4):** Evaluate the applicability of the proposed battery model to Hardware-in-the-Loop simulations." The model selection, HIL implementation, and results from parts of this chapter have been published in 2019 IEEE Vehicle Power and Propulsion Conference [4].

This thesis contributes a multisine-based nonlinear characterisation approach as well as an ECM-based battery model (NLECM-diff model) that may be of interest to LIB-related researchers in specific scenarios. Concrete steps for use of those contributions are listed respectively: As for the nonlinear characterisation method, this thesis suggests that the multisine-based method should be utilised for quick battery nonlinearity analysis using throughout characteristic frequency range of $10\,\mathrm{mHz}$ to $10\,\mathrm{Hz}$ in a room temperature laboratory environment. Furthermore, as for the battery model, this thesis recommends that the NLECM-diff model should be employed in the HIL simulation case where the current rate is not larger than 1C throughout 100% to 0% SOC at room temperature.

In addition, this thesis has a number of implications for the broader scientific community. Due to the fact that the peak value of the current signal for the multisine-based method is few times greater than the designed RMS value, compared to conventional nonlinear characterisation methods, the implementation of which is not always feasible for commercialised vehicles due to the equipment involved. Secondly, from the perspective of battery modelling, the unequal anodic and cathodic charger transfer coefficients indicate that the nonlinear characteristic of a battery cell should be modelled using alternative functions (such as polynomial, logistic and hyperbolic tangent) rather than the sigmoid function with the symmetrical "S"-shape characteristic. Finally, given the critical nature of a diffusion process model for modelling large time constant dynamics, constant current profiles are essential

in identifying equivalent circuit battery models, and mathematical models (such as the NLECM-diff) with diffusion processes are required to account for the variation in diffusion voltage loss under various current intensity cases.

8.2　Future direction and further work

Both the proposed nonlinear characterisation method and battery model provide opportunities for additional research and further work.

Pertaining to the battery characterisation method, further work can be conducted in two directions: parameter estimation and degradation characterisation. In Chapter 4, the initial capability of the multisine-based nonlinear characterisation approach to estimate charge-transfer coefficient parameters has been demonstrated by minimising the total nonlinearity error through the frequency range between the model simulation and experimental results. Although the conclusion of the unequal anodic and cathodic charge transfer coefficients is consistent with literature, the precise values of charge transfer coefficients has not been determined by this characterisation method yet. By optimising the algorithm to take the distribution of characterised nonlinearity into account, the values of charge transfer coefficients would be precisely estimated, which will be beneficial for improving the accuracy of electrochemical models. Furthermore, as described in Chapter 3, nonlinear characterisation methods has been employed in the study of battery cell degradation. However, within this thesis, the experimental database is obtained through the tests on fresh battery cells. As such, the capability of the proposed multisine-based method in degradation characterisation cannot be evaluated. Thus, conducting ageing tests on commercial batteries and applying the multisine non-linear characterisation method is necessary in the future work, and the usefulness of the multisine-based method to degradation characterisation would be investigated by analysing the nonlinearity variation as the battery cell degrades.

From the perspective of battery models, the battery model scale-up and SOC estimation deserve further research. The system identification research within this thesis is limited to cell level because this is the most practical route given the available resources and research risks. For example, identifying a system at a battery pack level requires specialised testing equipment capable of containing the battery pack, and the risk associated with the battery pack's high voltage and power necessitates additional safety precautions. However, for actual BMS applications in EVs, it is important to construct an efficient mathematical model at the scaled-up battery module or pack level for monitoring and controlling the vehicle's power

storage system. A common pattern in theory to achieve the model scale-up objective is connecting multiple battery cell models in series and parallel, which may emphasis the proposed model's advantage of low computational cost. However, it is unknown whether this design is applicable in practice. Thus, scaling up the battery model from cell level to module or pack level needs to be studied in further work. Additionally, SOC estimation algorithm plays a key role in the BMS applications, but, unfortunately, it is not involved within the thesis. In contrast to the SOC estimation methods for numerous conventional equivalent circuit models that are associated with the Coulomb counting and Kalman filter, the proposed model incorporates a lumped diffusion block inspired by electrochemical models in electrode particles' lithium ion concentration distribution which can be related to battery SOC. As a result, a novel SOC estimation algorithm based on the diffusion block needs to be developed specifically for the proposed model and implemented in the practical applications to evaluate the efficiency in the future.

Appendix A

Discrete Chebyshev-Gauss-Lobatto orthogonal collocation method

Refer to [274], in the orthogonal collocation method, the grid points are defined by

$$y_j = \cos\frac{j\pi}{N}, \qquad j = 0, ..., N \tag{A.1}$$

where j is the index of grid points. Mathematically, y_j represents the locations of the extrema of the first kind Chebyshev polynomials, $T_N(l) = \cos(N\arccos(l))$. The $(N+1) \times (N+1)$ Chebyshev derivative matrix D at the quadrature points is:

$$D = (d_{jk})_{0 \leq j \leq N, 0 \leq k \leq N} \tag{A.2}$$

with

$$\begin{cases} d_{00} = \dfrac{2N^2 + 1}{6} \\ d_{jj} = -\dfrac{x_j}{2(1 - y_j^2)} \qquad 1 \leq j \leq N - 1 \\ d_{NN} = -\dfrac{2N^2 + 1}{6} \end{cases}$$

For $0 \leq j \leq N, 0 \leq k \leq N$ with $j \neq k$, the element d_{jk} is

$$d_{jk} = \frac{c_j(-1)^{j+k}}{c_k(y_j - y_k)}$$

with

$$\begin{cases} c_0 = 2 \\ c_j = 1 & 1 \leq j \leq N - 1 \\ c_k = 1 & 1 \leq k \leq N - 1 \\ c_N = 2 \end{cases}$$

If v is the vector formed by the values of the function $u(y)$ at the locations $y_j, j = 0, ..., N$, the values of the approximations v' and v'' of the derivates u' and u'' of u at the grid points y_j are calculated as follows:

$$v' = Dv; \qquad v'' = D^2 v$$

where D is the differentiation matrix. .

Bibliography

[1] C. Fan, T. R. Grandjean, K. O'Regan, E. Kendrick, and W. D. Widanage, "Understanding non-linearity in electrochemical systems using multisine-based non-linear characterization," Transactions of the Institute of Measurement and Control, p. 01423312211045991, 2021.

[2] C. Fan, K. O'Regan, L. Li, E. Kendrick, and W. Widanage, "Frequency domain non-linear characterization and analysis of lithium-ion battery electrodes," Journal of Energy Storage, vol. 36, p. 102371, 2021.

[3] C. Fan, K. O'Regan, L. Li, M. D. Higgins, E. Kendrick, and W. D. Widanage, "Data-driven identification of lithium-ion batteries: A nonlinear equivalent circuit model with diffusion dynamics," Applied Energy, vol. 321, p. 119336, 2022.

[4] C. Fan, M. D. Higgins, and W. D. Widanage, "Real-time state of charge estimation of electrochemical model for lithium-ion battery," in 2019 IEEE Vehicle Power and Propulsion Conference (VPPC), pp. 1–6, IEEE, 2019.

[5] K. Liu, K. Li, Q. Peng, and C. Zhang, "A brief review on key technologies in the battery management system of electric vehicles," Frontiers of mechanical engineering, vol. 14, no. 1, pp. 47–64, 2019.

[6] Z. Li, A. Khajepour, and J. Song, "A comprehensive review of the key technologies for pure electric vehicles," Energy, vol. 182, pp. 824–839, 2019.

[7] T. Horiba, T. Maeshima, T. Matsumura, M. Koseki, J. Arai, and Y. Muranaka, "Applications of high power density lithium ion batteries," Journal of Power Sources, vol. 146, no. 1-2, pp. 107–110, 2005.

[8] J.-M. Tarascon and M. Armand, "Issues and challenges facing rechargeable lithium batteries," Nature, vol. 414, no. 6861, pp. 359–367, 2001.

186

[9] R. Schmuch, R. Wagner, G. Hörpel, T. Placke, and M. Winter, "Performance and cost of materials for lithium-based rechargeable automotive batteries," Nature Energy, vol. 3, no. 4, pp. 267–278, 2018.

[10] MRFR, "Power Battery Management System Market to Post 18.59% CAGR," 2021.

[11] M. Hannan, M. M. Hoque, A. Mohamed, and A. Ayob, "Review of energy storage systems for electric vehicle applications: Issues and challenges," Renewable and Sustainable Energy Reviews, vol. 69, pp. 771–789, 2017.

[12] G. L. Plett, Battery management systems, Volume II: Equivalent-circuit methods, vol. 2. Artech House, 2015.

[13] L. Lu, X. Han, J. Li, J. Hua, and M. Ouyang, "A review on the key issues for lithium-ion battery management in electric vehicles," Journal of power sources, vol. 226, pp. 272–288, 2013.

[14] G. L. Plett, "Extended kalman filtering for battery management systems of lipb-based hev battery packs: Part 3. state and parameter estimation," Journal of Power sources, vol. 134, no. 2, pp. 277–292, 2004.

[15] C. Kleijn, "Introduction to hardware-in-the-loop simulation," Control Lab, vol. 7521, 2014.

[16] N. N, "Schulung und praxis mit flugsimulator," interavia, vol. 19, no. 8, pp. 1104–1107, 1964.

[17] J. Drosdol and F. Panik, "The daimler-benz driving simulator a tool for vehicle development," SAE Transactions, pp. 981–997, 1985.

[18] H. Dai, X. Wei, Z. Sun, and J. Wang, "A hardware-in-the-loop system for development of automotive battery management system," in Measuring Technology and Mechatronics Automation in Electrical Engineering, pp. 27–36, Springer, 2012.

[19] H. Dai, X. Zhang, X. Wei, Z. Sun, J. Wang, and F. Hu, "Cell-bms validation with a hardware-in-the-loop simulation of lithium-ion battery cells for electric vehicles," International Journal of Electrical Power & Energy Systems, vol. 52, pp. 174–184, 2013.

[20] J. V. Barreras, C. Fleischer, A. E. Christensen, M. Swierczynski, E. Schaltz, S. J. Andreasen, and D. U. Sauer, "An advanced hil simulation battery model

for battery management system testing," IEEE Transactions on Industry Applications, vol. 52, no. 6, pp. 5086–5099, 2016.

[21] F. Lacressonnière, A. Varais, X. Roboam, E. Bru, and T. Mullins, "Scale electro-thermal model of a lithium-ion battery for time-accelerated experiments in a hardware in the loop process," Journal of Energy Storage, vol. 39, p. 102576, 2021.

[22] R. Isermann, J. Schaffnit, and S. Sinsel, "Hardware-in-the-loop simulation for the design and testing of engine-control systems," Control Engineering Practice, vol. 7, no. 5, pp. 643–653, 1999.

[23] S. Castano, L. Gauchia, E. Voncila, and J. Sanz, "Dynamical modeling procedure of a li-ion battery pack suitable for real-time applications," Energy Conversion and Management, vol. 92, pp. 396–405, 2015.

[24] C.-H. Chen, F. B. Planella, K. O'regan, D. Gastol, W. D. Widanage, and E. Kendrick, "Development of experimental techniques for parameterization of multi-scale lithium-ion battery models," Journal of The Electrochemical Society, vol. 167, no. 8, p. 080534, 2020.

[25] X. Han, M. Ouyang, L. Lu, and J. Li, "Simplification of physics-based electrochemical model for lithium ion battery on electric vehicle. part i: Diffusion simplification and single particle model," Journal of Power Sources, vol. 278, pp. 802–813, 2015.

[26] R. Matthe, L. Turner, and H. Mettlach, "Voltec battery system for electric vehicle with extended range," SAE International Journal of Engines, vol. 4, no. 1, pp. 1944–1962, 2011.

[27] K. Miyatake, T. Abe, Y. Hisamitsu, T. Kinoshita, Y. Shimoida, and H. Horie, "Research on large capacity, high power lithium-ion batteries," tech. rep., SAE Technical Paper, 2009.

[28] J. Jiang, W. Shi, J. Zheng, P. Zuo, J. Xiao, X. Chen, W. Xu, and J.-G. Zhang, "Optimized operating range for large-format lifepo4/graphite batteries," Journal of The Electrochemical Society, vol. 161, no. 3, p. A336, 2013.

[29] R. Xiong, Y. Pan, W. Shen, H. Li, and F. Sun, "Lithium-ion battery aging mechanisms and diagnosis method for automotive applications: Recent advances and perspectives," Renewable and Sustainable Energy Reviews, vol. 131, p. 110048, 2020.

[30] E. D. Kostopoulos, G. C. Spyropoulos, and J. K. Kaldellis, "Real-world study for the optimal charging of electric vehicles," Energy Reports, vol. 6, pp. 418–426, 2020.

[31] J. Neubauer and E. Wood, "The impact of range anxiety and home, workplace, and public charging infrastructure on simulated battery electric vehicle lifetime utility," Journal of power sources, vol. 257, pp. 12–20, 2014.

[32] Y. Zheng, M. Ouyang, X. Han, L. Lu, and J. Li, "Investigating the error sources of the online state of charge estimation methods for lithium-ion batteries in electric vehicles," Journal of Power Sources, vol. 377, pp. 161–188, 2018.

[33] R. Xiong, J. Huang, Y. Duan, and W. Shen, "Enhanced lithium-ion battery model considering critical surface charge behavior," Applied Energy, vol. 314, p. 118915, 2022.

[34] R. Xiong, F. Sun, X. Gong, and C. Gao, "A data-driven based adaptive state of charge estimator of lithium-ion polymer battery used in electric vehicles," Applied Energy, vol. 113, pp. 1421–1433, 2014.

[35] E. Hosseinzadeh, S. Arias, M. Krishna, D. Worwood, A. Barai, D. Widanalage, and J. Marco, "Quantifying cell-to-cell variations of a parallel battery module for different pack configurations," Applied Energy, vol. 282, p. 115859, 2021.

[36] M. Doyle, T. F. Fuller, and J. Newman, "Modeling of galvanostatic charge and discharge of the lithium/polymer/insertion cell," Journal of the Electrochemical society, vol. 140, no. 6, p. 1526, 1993.

[37] S. J. Moura, N. A. Chaturvedi, and M. Krstić, "Adaptive partial differential equation observer for battery state-of-charge/state-of-health estimation via an electrochemical model," Journal of Dynamic Systems, Measurement, and Control, vol. 136, no. 1, 2014.

[38] S. J. Moura, F. B. Argomedo, R. Klein, A. Mirtabatabaei, and M. Krstic, "Battery state estimation for a single particle model with electrolyte dynamics," IEEE Transactions on Control Systems Technology, vol. 25, no. 2, pp. 453–468, 2016.

[39] M. Ouyang, G. Liu, L. Lu, J. Li, and X. Han, "Enhancing the estimation accuracy in low state-of-charge area: A novel onboard battery model through

surface state of charge determination," Journal of Power Sources, vol. 270, pp. 221–237, 2014.

[40] X. Hu, S. Li, and H. Peng, "A comparative study of equivalent circuit models for li-ion batteries," Journal of Power Sources, vol. 198, pp. 359–367, 2012.

[41] X. Lin, H. E. Perez, S. Mohan, J. B. Siegel, A. G. Stefanopoulou, Y. Ding, and M. P. Castanier, "A lumped-parameter electro-thermal model for cylindrical batteries," Journal of Power Sources, vol. 257, pp. 1–11, 2014.

[42] H. He, R. Xiong, H. Guo, and S. Li, "Comparison study on the battery models used for the energy management of batteries in electric vehicles," Energy Conversion and Management, vol. 64, pp. 113–121, 2012.

[43] D. Andre, M. Meiler, K. Steiner, H. Walz, T. Soczka-Guth, and D. Sauer, "Characterization of high-power lithium-ion batteries by electrochemical impedance spectroscopy. ii: Modelling," Journal of Power Sources, vol. 196, no. 12, pp. 5349–5356, 2011.

[44] J. Li, J. K. Barillas, C. Guenther, and M. A. Danzer, "A comparative study of state of charge estimation algorithms for lifepo4 batteries used in electric vehicles," Journal of power sources, vol. 230, pp. 244–250, 2013.

[45] W. D. Widanage, A. Barai, G. H. Chouchelamane, K. Uddin, A. McGordon, J. Marco, and P. Jennings, "Design and use of multisine signals for Li-ion battery equivalent circuit modelling. Part 1: Signal design," Journal of Power Sources, vol. 324, pp. 70–78, 2016.

[46] L. Li, Y. Ren, K. O'Regan, U. R. Koleti, E. Kendrick, W. D. Widanage, and J. Marco, "Lithium-ion battery cathode and anode potential observer based on reduced-order electrochemical single particle model," Journal of Energy Storage, vol. 44, p. 103324, 2021.

[47] Y. Firouz, R. Relan, J. Timmermans, N. Omar, P. Van Den Bossche, and J. Van Mierlo, "Advanced lithium ion battery modeling and nonlinear analysis based on robust method in frequency domain: Nonlinear characterization and non-parametric modeling," Energy, vol. 106, pp. 602–617, 2016.

[48] J. Newman and K. E. Thomas-Alyea, Electrochemical systems. John Wiley & Sons, 2012.

190

[49] D. Guo, G. Yang, X. Feng, X. Han, L. Lu, and M. Ouyang, "Physics-based fractional-order model with simplified solid phase diffusion of lithium-ion battery," Journal of Energy Storage, vol. 30, p. 101404, 2020.

[50] R. Xiong, J. Cao, Q. Yu, H. He, and F. Sun, "Critical review on the battery state of charge estimation methods for electric vehicles," Ieee Access, vol. 6, pp. 1832–1843, 2017.

[51] R. Xiong, L. Li, and J. Tian, "Towards a smarter battery management system: A critical review on battery state of health monitoring methods," Journal of Power Sources, vol. 405, pp. 18–29, 2018.

[52] W. Waag, C. Fleischer, and D. U. Sauer, "Adaptive on-line prediction of the available power of lithium-ion batteries," Journal of Power Sources, vol. 242, pp. 548–559, 2013.

[53] Q. Lin, J. Wang, R. Xiong, W. Shen, and H. He, "Towards a smarter battery management system: A critical review on optimal charging methods of lithium ion batteries," Energy, vol. 183, pp. 220–234, 2019.

[54] J. Sun, Q. Ma, C. Tang, T. Wang, T. Jiang, and Y. Tang, "Research on optimization of charging strategy control for aged batteries," IEEE Transactions on Vehicular Technology, 2020.

[55] K. Liu, K. Li, and C. Zhang, "Constrained generalized predictive control of battery charging process based on a coupled thermoelectric model," Journal of Power Sources, vol. 347, pp. 145–158, 2017.

[56] K. Liu, X. Hu, Z. Yang, Y. Xie, and S. Feng, "Lithium-ion battery charging management considering economic costs of electrical energy loss and battery degradation," Energy conversion and management, vol. 195, pp. 167–179, 2019.

[57] M. Nie and B. L. Lucht, "Role of lithium salt on solid electrolyte interface (sei) formation and structure in lithium ion batteries," Journal of the Electrochemical Society, vol. 161, no. 6, p. A1001, 2014.

[58] D. Deng, "Li-ion batteries: basics, progress, and challenges," Energy Science & Engineering, vol. 3, no. 5, pp. 385–418, 2015.

[59] M. M. Thackeray, C. Wolverton, and E. D. Isaacs, "Electrical energy storage for transportation—approaching the limits of, and going beyond, lithium-ion

batteries," <u>Energy & Environmental Science</u>, vol. 5, no. 7, pp. 7854–7863, 2012.

[60] N. Nitta, F. Wu, J. T. Lee, and G. Yushin, "Li-ion battery materials: present and future," <u>Materials today</u>, vol. 18, no. 5, pp. 252–264, 2015.

[61] M. Doeff, J. Goodenough, K. Naoi, and K. Bullock, "Batteries for sustainability," <u>Encyclopedia of Sustainability Science and Technology</u>, pp. 5–49, 2013.

[62] J. W. Fergus, "Recent developments in cathode materials for lithium ion batteries," <u>Journal of power sources</u>, vol. 195, no. 4, pp. 939–954, 2010.

[63] B. Rezaei, M. Saghebdoust, A. M. Sorkhe, and N. Majidi, "Generation of a doxorubicin immunosensor based on a specific monoclonal antibody-nanogold-modified electrode," <u>Electrochimica acta</u>, vol. 56, no. 16, pp. 5702–5706, 2011.

[64] A. Thaler and D. Watzenig, <u>Automotive battery technology</u>. Springer, 2014.

[65] Y. Itou and Y. Ukyo, "Performance of linicoo2 materials for advanced lithium-ion batteries," <u>Journal of Power Sources</u>, vol. 146, no. 1-2, pp. 39–44, 2005.

[66] Y. Wu, E. Rahm, and R. Holze, "Carbon anode materials for lithium ion batteries," <u>Journal of power sources</u>, vol. 114, no. 2, pp. 228–236, 2003.

[67] P. Li, H. Kim, S.-T. Myung, and Y.-K. Sun, "Diverting exploration of silicon anode into practical way: A review focused on silicon-graphite composite for lithium ion batteries," <u>Energy Storage Materials</u>, 2020.

[68] M. Doyle and J. Newman, "The use of mathematical modeling in the design of lithium/polymer battery systems," <u>Electrochimica Acta</u>, vol. 40, no. 13-14, pp. 2191–2196, 1995.

[69] V. Chabot, S. Farhad, Z. Chen, A. S. Fung, A. Yu, and F. Hamdullahpur, "Effect of electrode physical and chemical properties on lithium-ion battery performance," <u>International Journal of Energy Research</u>, vol. 37, no. 14, pp. 1723–1736, 2013.

[70] P. R. Shearing, L. E. Howard, P. S. Jørgensen, N. P. Brandon, and S. J. Harris, "Characterization of the 3-dimensional microstructure of a graphite negative electrode from a li-ion battery," <u>Electrochemistry communications</u>, vol. 12, no. 3, pp. 374–377, 2010.

[71] F. B. Planella, W. Ai, A. M. Boyce, A. Ghosh, I. Korotkin, S. Sahu, V. Sulzer, R. Timms, T. G. Tranter, M. Zyskin, et al., "A continuum of physics-based lithium-ion battery models reviewed," arXiv preprint arXiv:2203.16091, 2022.

[72] S. Raël and M. Hinaje, "Using electrical analogy to describe mass and charge transport in lithium-ion batteries," Journal of Power Sources, vol. 222, pp. 112–122, 2013.

[73] N. Wolff, N. Harting, M. Heinrich, F. Röder, and U. Krewer, "Nonlinear frequency response analysis on lithium-ion batteries: a model-based assessment," Electrochimica Acta, vol. 260, pp. 614–622, 2018.

[74] N. Harting, Nonlinear Frequency Response Analysis of Lithium-Ion Batteries. PhD thesis, TU Braunschweig, 2019.

[75] M. J. Moran, H. N. Shapiro, D. D. Boettner, and M. B. Bailey, Fundamentals of engineering thermodynamics. John Wiley & Sons, 2010.

[76] R. Raccichini, M. Amores, and G. Hinds, "Critical review of the use of reference electrodes in li-ion batteries: A diagnostic perspective," Batteries, vol. 5, no. 1, p. 12, 2019.

[77] E. Keszei, Chemical thermodynamics: an introduction. Springer Science & Business Media, 2013.

[78] A. J. Bard, L. R. Faulkner, et al., "Fundamentals and applications," Electrochemical methods, vol. 2, no. 482, pp. 580–632, 2001.

[79] C. R. Birkl, E. McTurk, M. Roberts, P. G. Bruce, and D. A. Howey, "A parametric open circuit voltage model for lithium ion batteries," Journal of The Electrochemical Society, vol. 162, no. 12, p. A2271, 2015.

[80] A. Berrueta, I. San Martín, P. Sanchis, and A. Ursúa, "Lithium-ion batteries as distributed energy storage systems for microgrids," in Distributed Energy Resources in Microgrids, pp. 143–183, Elsevier, 2019.

[81] M. Doyle, J. Newman, A. S. Gozdz, C. N. Schmutz, and J.-M. Tarascon, "Comparison of modeling predictions with experimental data from plastic lithium ion cells," Journal of the Electrochemical Society, vol. 143, no. 6, p. 1890, 1996.

[82] G. Ning and B. N. Popov, "Cycle life modeling of lithium-ion batteries," Journal of The Electrochemical Society, vol. 151, no. 10, p. A1584, 2004.

[83] X.-G. Yang, Y. Leng, G. Zhang, S. Ge, and C.-Y. Wang, "Modeling of lithium plating induced aging of lithium-ion batteries: Transition from linear to nonlinear aging," Journal of Power Sources, vol. 360, pp. 28–40, 2017.

[84] V. R. Subramanian, V. D. Diwakar, and D. Tapriyal, "Efficient macro-micro scale coupled modeling of batteries," Journal of The Electrochemical Society, vol. 152, no. 10, p. A2002, 2005.

[85] W. Sung and C. B. Shin, "Electrochemical model of a lithium-ion battery implemented into an automotive battery management system," Computers & Chemical Engineering, vol. 76, pp. 87–97, 2015.

[86] S. Atlung, K. West, and T. Jacobsen, "Dynamic aspects of solid solution cathodes for electrochemical power sources," Journal of The Electrochemical Society, vol. 126, no. 8, p. 1311, 1979.

[87] B. S. Haran, B. N. Popov, and R. E. White, "Determination of the hydrogen diffusion coefficient in metal hydrides by impedance spectroscopy," Journal of Power Sources, vol. 75, no. 1, pp. 56–63, 1998.

[88] S. Santhanagopalan, Q. Guo, P. Ramadass, and R. E. White, "Review of models for predicting the cycling performance of lithium ion batteries," Journal of power sources, vol. 156, no. 2, pp. 620–628, 2006.

[89] K. A. Smith, C. D. Rahn, and C.-Y. Wang, "Model order reduction of 1d diffusion systems via residue grouping," Journal of Dynamic Systems, Measurement, and Control, vol. 130, no. 1, 2008.

[90] S. K. Rahimian, S. Rayman, and R. E. White, "Extension of physics-based single particle model for higher charge–discharge rates," Journal of Power Sources, vol. 224, pp. 180–194, 2013.

[91] T. R. Tanim, C. D. Rahn, and C.-Y. Wang, "A temperature dependent, single particle, lithium ion cell model including electrolyte diffusion," Journal of Dynamic Systems, Measurement, and Control, vol. 137, no. 1, 2015.

[92] M. Shen and Q. Gao, "A review on battery management system from the modeling efforts to its multiapplication and integration," International Journal of Energy Research, vol. 43, no. 10, pp. 5042–5075, 2019.

[93] X. Han, M. Ouyang, L. Lu, and J. Li, "Simplification of physics-based electrochemical model for lithium ion battery on electric vehicle. part ii: Pseudo-

two-dimensional model simplification and state of charge estimation," <u>Journal of Power Sources</u>, vol. 278, pp. 814–825, 2015.

[94] J. Li, K. Adewuyi, N. Lotfi, R. G. Landers, and J. Park, "A single particle model with chemical/mechanical degradation physics for lithium ion battery state of health (soh) estimation," <u>Applied energy</u>, vol. 212, pp. 1178–1190, 2018.

[95] J. M. Reniers, G. Mulder, and D. A. Howey, "Review and performance comparison of mechanical-chemical degradation models for lithium-ion batteries," <u>Journal of The Electrochemical Society</u>, vol. 166, no. 14, p. A3189, 2019.

[96] L. Li, C. Zhang, J. Marco, and W. D. Widanage, "Control-oriented implementation and model order reduction of a lithium-ion battery electrochemical model," in <u>2019 IEEE Vehicle Power and Propulsion Conference (VPPC)</u>, pp. 1–5, IEEE, 2019.

[97] M. Jun, K. Smith, and P. Graf, "State-space representation of li-ion battery porous electrode impedance model with balanced model reduction," <u>Journal of Power Sources</u>, vol. 273, pp. 1226–1236, 2015.

[98] J. C. Forman, S. Bashash, J. L. Stein, and H. K. Fathy, "Reduction of an electrochemistry-based li-ion battery model via quasi-linearization and pade approximation," <u>Journal of the Electrochemical Society</u>, vol. 158, no. 2, p. A93, 2010.

[99] C. J. Wen, B. Boukamp, R. A. Huggins, and W. Weppner, "Thermodynamic and mass transport properties of "lial"," <u>Journal of The Electrochemical Society</u>, vol. 126, no. 12, p. 2258, 1979.

[100] Y.-C. Chang, J.-H. Jong, and G. T.-K. Fey, "Kinetic characterization of the electrochemical intercalation of lithium ions into graphite electrodes," <u>Journal of the Electrochemical Society</u>, vol. 147, no. 6, p. 2033, 2000.

[101] V. Johnson, "Battery performance models in advisor," <u>Journal of power sources</u>, vol. 110, no. 2, pp. 321–329, 2002.

[102] H. Chan, "A new battery model for use with battery energy storage systems and electric vehicles power systems," in <u>2000 IEEE power engineering society winter meeting. conference proceedings (Cat. No. 00CH37077)</u>, vol. 1, pp. 470–475, IEEE, 2000.

[103] Y.-H. Chiang, W.-Y. Sean, and J.-C. Ke, "Online estimation of internal resistance and open-circuit voltage of lithium-ion batteries in electric vehicles," Journal of Power Sources, vol. 196, no. 8, pp. 3921–3932, 2011.

[104] H. He, R. Xiong, X. Zhang, F. Sun, and J. Fan, "State-of-charge estimation of the lithium-ion battery using an adaptive extended kalman filter based on an improved thevenin model," IEEE Transactions on vehicular technology, vol. 60, no. 4, pp. 1461–1469, 2011.

[105] X. Lai, Y. Zheng, and T. Sun, "A comparative study of different equivalent circuit models for estimating state-of-charge of lithium-ion batteries," Electrochimica Acta, vol. 259, pp. 566–577, 2018.

[106] M. Verbrugge and E. Tate, "Adaptive state of charge algorithm for nickel metal hydride batteries including hysteresis phenomena," Journal of Power Sources, vol. 126, no. 1-2, pp. 236–249, 2004.

[107] M. Verbrugge and B. Koch, "Generalized recursive algorithm for adaptive multiparameter regression: Application to lead acid, nickel metal hydride, and lithium-ion batteries," Journal of The Electrochemical Society, vol. 153, no. 1, p. A187, 2006.

[108] M. Verbrugge, "Adaptive, multi-parameter battery state estimator with optimized time-weighting factors," Journal of applied electrochemistry, vol. 37, no. 5, pp. 605–616, 2007.

[109] Y. Hu, S. Yurkovich, Y. Guezennec, and B. Yurkovich, "Electro-thermal battery model identification for automotive applications," Journal of Power Sources, vol. 196, no. 1, pp. 449–457, 2011.

[110] R. Khatib, A.-L. Dalverny, M. Saubanère, M. Gaberscek, and M.-L. Doublet, "Origin of the voltage hysteresis in the cop conversion material for li-ion batteries," The Journal of Physical Chemistry C, vol. 117, no. 2, pp. 837–849, 2013.

[111] S. Nejad, D. Gladwin, and D. Stone, "A systematic review of lumped-parameter equivalent circuit models for real-time estimation of lithium-ion battery states," Journal of Power Sources, vol. 316, pp. 183–196, 2016.

[112] B. Powell, K. Bailey, and S. Cikanek, "Dynamic modeling and control of hybrid electric vehicle powertrain systems," IEEE Control Systems Magazine, vol. 18, no. 5, pp. 17–33, 1998.

[113] S. Abu-Sharkh and D. Doerffel, "Rapid test and non-linear model characterisation of solid-state lithium-ion batteries," Journal of Power Sources, vol. 130, no. 1-2, pp. 266–274, 2004.

[114] G. L. Plett, "Extended Kalman filtering for battery management systems of LiPB-based HEV battery packs - Part 1. Background," Journal of Power Sources, vol. 134, pp. 252–261, aug 2004.

[115] G. L. Plett, "Extended kalman filtering for battery management systems of lipb-based hev battery packs: Part 2. modeling and identification," Journal of power sources, vol. 134, no. 2, pp. 262–276, 2004.

[116] W. Shen, C. C. Chan, E. W. Lo, and K. Chau, "Adaptive neuro-fuzzy modeling of battery residual capacity for electric vehicles," IEEE Transactions on Industrial Electronics, vol. 49, no. 3, pp. 677–684, 2002.

[117] C. Zhang, W. Allafi, Q. Dinh, P. Ascencio, and J. Marco, "Online estimation of battery equivalent circuit model parameters and state of charge using decoupled least squares technique," Energy, vol. 142, pp. 678–688, 2018.

[118] J. K. Barillas, J. Li, C. Günther, and M. A. Danzer, "A comparative study and validation of state estimation algorithms for li-ion batteries in battery management systems," Applied Energy, vol. 155, pp. 455–462, 2015.

[119] I.-S. Kim, "The novel state of charge estimation method for lithium battery using sliding mode observer," Journal of Power Sources, vol. 163, no. 1, pp. 584–590, 2006.

[120] S. Tong, M. P. Klein, and J. W. Park, "On-line optimization of battery open circuit voltage for improved state-of-charge and state-of-health estimation," Journal of Power Sources, vol. 293, pp. 416–428, 2015.

[121] J. Kim and B.-H. Cho, "State-of-charge estimation and state-of-health prediction of a li-ion degraded battery based on an ekf combined with a per-unit system," IEEE Transactions on Vehicular Technology, vol. 60, no. 9, pp. 4249–4260, 2011.

[122] J. Bi, T. Zhang, H. Yu, and Y. Kang, "State-of-health estimation of lithium-ion battery packs in electric vehicles based on genetic resampling particle filter," Applied energy, vol. 182, pp. 558–568, 2016.

[123] L. Pei, C. Zhu, T. Wang, R. Lu, and C. Chan, "Online peak power prediction based on a parameter and state estimator for lithium-ion batteries in electric vehicles," Energy, vol. 66, pp. 766–778, 2014.

[124] J. Tian, R. Xiong, W. Shen, and F. Sun, "Fractional order battery modelling methodologies for electric vehicle applications: Recent advances and perspectives," Science China Technological Sciences, pp. 1–20, 2020.

[125] D. C. Robertson, J. P. Christophersen, T. Bennett, L. K. Walker, F. Wang, S. Liu, B. Fan, and I. Bloom, "A comparison of battery testing protocols: Those used by the us advanced battery consortium and those used in china," Journal of Power Sources, vol. 306, pp. 268–273, 2016.

[126] J. Huang, Z. Li, B. Y. Liaw, and J. Zhang, "Graphical analysis of electrochemical impedance spectroscopy data in bode and nyquist representations," Journal of Power Sources, vol. 309, pp. 82–98, 2016.

[127] E. Kuhn, C. Forgez, and G. Friedrich, "Modeling diffusive phenomena using non integer derivatives," The European Physical Journal-Applied Physics, vol. 25, no. 3, pp. 183–190, 2004.

[128] B. Wang, S. E. Li, H. Peng, and Z. Liu, "Fractional-order modeling and parameter identification for lithium-ion batteries," Journal of Power Sources, vol. 293, pp. 151–161, 2015.

[129] J. Gómez-Aguilar, H. Yépez-Martínez, R. Escobar-Jiménez, C. Astorga-Zaragoza, and J. Reyes-Reyes, "Analytical and numerical solutions of electrical circuits described by fractional derivatives," Applied Mathematical Modelling, vol. 40, no. 21-22, pp. 9079–9094, 2016.

[130] J. F. G. AGUILAR, "Behavior characteristics of a cap-resistor, memcapacitor, and a memristor from the response obtained of rc and rl electrical circuits described by fractional differential equations," Turkish Journal of Electrical Engineering & Computer Sciences, vol. 24, no. 3, pp. 1421–1433, 2016.

[131] V. F. Morales-Delgado, J. F. Gómez-Aguilar, M. A. Taneco-Hernández, and R. F. Escobar-Jiménez, "Fractional operator without singular kernel: Applications to linear electrical circuits," International Journal of Circuit Theory and Applications, vol. 46, no. 12, pp. 2394–2419, 2018.

[132] M. E. Orazem and B. Tribollet, "Electrochemical impedance spectroscopy," New Jersey, pp. 383–389, 2008.

[133] K. S. Cole and R. H. Cole, "Dispersion and absorption in dielectrics i. alternating current characteristics," The Journal of chemical physics, vol. 9, no. 4, pp. 341–351, 1941.

[134] A. Maheshwari, M. Heck, and M. Santarelli, "Cycle aging studies of lithium nickel manganese cobalt oxide-based batteries using electrochemical impedance spectroscopy," Electrochimica Acta, vol. 273, pp. 335–348, 2018.

[135] J. Li, D. Sun, Z. Chai, H. Jiang, and C. Sun, "Sinusoidal alternating current heating strategy and optimization of lithium-ion batteries with a thermo-electric coupled model," Energy, vol. 186, p. 115798, 2019.

[136] C. A. Monje, Y. Chen, B. M. Vinagre, D. Xue, and V. Feliu-Batlle, Fractional-order systems and controls: fundamentals and applications. Springer Science & Business Media, 2010.

[137] Y. Zheng, Z. Shi, D. Guo, H. Dai, and X. Han, "A simplification of the time-domain equivalent circuit model for lithium-ion batteries based on low-frequency electrochemical impedance spectra," Journal of Power Sources, vol. 489, p. 229505, 2021.

[138] J. Sabatier, P. Lanusse, P. Melchior, and A. Oustaloup, "Fractional order differentiation and robust control design," Intelligent systems, control and automation: science and engineering, vol. 77, pp. 13–18, 2015.

[139] C. Zou, L. Zhang, X. Hu, Z. Wang, T. Wik, and M. Pecht, "A review of fractional-order techniques applied to lithium-ion batteries, lead-acid batteries, and supercapacitors," Journal of Power Sources, vol. 390, pp. 286–296, 2018.

[140] A. Oustaloup, F. Levron, B. Mathieu, and F. M. Nanot, "Frequency-band complex noninteger differentiator: characterization and synthesis," IEEE Transactions on Circuits and Systems I: Fundamental Theory and Applications, vol. 47, no. 1, pp. 25–39, 2000.

[141] X. Liao, J. Yu, and L. Gao, "Electrochemical study on lithium iron phosphate/hard carbon lithium-ion batteries," Journal of Solid State Electrochemistry, vol. 16, no. 2, pp. 423–428, 2012.

[142] C. Zou, X. Hu, S. Dey, L. Zhang, and X. Tang, "Nonlinear fractional-order estimator with guaranteed robustness and stability for lithium-ion batteries,"

IEEE Transactions on Industrial Electronics, vol. 65, no. 7, pp. 5951–5961, 2017.

[143] B. Wang, Z. Liu, S. E. Li, S. J. Moura, and H. Peng, "State-of-charge estimation for lithium-ion batteries based on a nonlinear fractional model," IEEE Transactions on Control Systems Technology, vol. 25, no. 1, pp. 3–11, 2016.

[144] J. Zhu, Z. Sun, X. Wei, and H. Dai, "An alternating current heating method for lithium-ion batteries from subzero temperatures," International Journal of Energy Research, vol. 40, no. 13, pp. 1869–1883, 2016.

[145] R. Yang, R. Xiong, H. He, and Z. Chen, "A fractional-order model-based battery external short circuit fault diagnosis approach for all-climate electric vehicles application," Journal of cleaner production, vol. 187, pp. 950–959, 2018.

[146] M. Hu, Y. Li, S. Li, C. Fu, D. Qin, and Z. Li, "Lithium-ion battery modeling and parameter identification based on fractional theory," Energy, vol. 165, pp. 153–163, 2018.

[147] A. Ehsani, M. G. Mahjani, and M. Jafarian, "Electrochemical impedance spectroscopy study on intercalation and anomalous diffusion of $alcl_4^-$ions into graphite in basic molten salt," Turkish Journal of Chemistry, vol. 35, no. 5, pp. 735–743, 2011.

[148] W. D. Widanage, J. Stoev, A. Van Mulders, J. Schoukens, and G. Pinte, "Nonlinear system-identification of the filling phase of a wet-clutch system," Control Engineering Practice, vol. 19, no. 12, pp. 1506–1516, 2011.

[149] J. E. Stephen, S. S. Kumar, and J. Jayakumar, "Nonlinear modeling of a switched reluctance motor using lssvm-abc," Acta Polytechnica Hungarica, vol. 11, no. 6, pp. 143–158, 2014.

[150] A. F. Esfahani, P. Dreesen, K. Tiels, J.-P. Noël, and J. Schoukens, "Polynomial state-space model decoupling for the identification of hysteretic systems," IFAC-PapersOnLine, vol. 50, no. 1, pp. 458–463, 2017.

[151] Y. Firouz, S. Goutam, M. C. Soult, A. Mohammadi, J. Van Mierlo, and P. Van den Bossche, "Block-oriented system identification for nonlinear modeling of all-solid-state li-ion battery technology," Journal of Energy Storage, vol. 28, p. 101184, 2020.

200

[152] W. D. Widanage, A. Barai, G. H. Chouchelamane, K. Uddin, A. McGordon, J. Marco, and P. Jennings, "Design and use of multisine signals for Li-ion battery equivalent circuit modelling. Part 2: Model estimation," Journal of Power Sources, vol. 324, pp. 61–69, 2016.

[153] W. Allafi, K. Uddin, C. Zhang, R. M. R. A. Sha, and J. Marco, "On-line scheme for parameter estimation of nonlinear lithium ion battery equivalent circuit models using the simplified refined instrumental variable method for a modified wiener continuous-time model," Applied energy, vol. 204, pp. 497–508, 2017.

[154] S. Tian, M. Hong, and M. Ouyang, "An experimental study and nonlinear modeling of discharge i–v behavior of valve-regulated lead–acid batteries," IEEE transactions on Energy Conversion, vol. 24, no. 2, pp. 452–458, 2009.

[155] T. Hu and H. Jung, "Simple algorithms for determining parameters of circuit models for charging/discharging batteries," Journal of power sources, vol. 233, pp. 14–22, 2013.

[156] T. Kim and W. Qiao, "A hybrid battery model capable of capturing dynamic circuit characteristics and nonlinear capacity effects," IEEE Transactions on Energy Conversion, vol. 26, no. 4, pp. 1172–1180, 2011.

[157] J. Schoukens, R. Pintelon, T. Dobrowiecki, and Y. Rolain, "Identification of linear systems with nonlinear distortions," Automatica, vol. 41, no. 3, pp. 491–504, 2005.

[158] J. Schoukens, J. Swevers, R. Pintelon, and H. Van Der Auweraer, "Excitation design for frf measurements in the presence of non-linear distortions," Mechanical Systems and Signal Processing, vol. 18, no. 4, pp. 727–738, 2004.

[159] R. Pintelon and J. Schoukens, "Measurement and modelling of linear systems in the presence of non-linear distortions," Mechanical systems and signal processing, vol. 16, no. 5, pp. 785–801, 2002.

[160] J. Paduart, L. Lauwers, J. Swevers, K. Smolders, J. Schoukens, and R. Pintelon, "Identification of nonlinear systems using polynomial nonlinear state space models," Automatica, vol. 46, no. 4, pp. 647–656, 2010.

[161] F. Giri and E.-W. Bai, Block-oriented nonlinear system identification, vol. 1. Springer, 2010.

[162] S. A. Billings, <u>Nonlinear system identification: NARMAX methods in the time, frequency, and spatio-temporal domains</u>. John Wiley & Sons, 2013.

[163] M. Schoukens and K. Tiels, "Identification of block-oriented nonlinear systems starting from linear approximations: A survey," <u>Automatica</u>, vol. 85, pp. 272–292, 2017.

[164] E. Zhang, M. Schoukens, and J. Schoukens, "Structure detection of wiener–hammerstein systems with process noise," <u>IEEE Transactions on Instrumentation and Measurement</u>, vol. 66, no. 3, pp. 569–576, 2017.

[165] M. Schoukens, E.-W. Bai, and Y. Rolain, "Identification of hammerstein-wiener systems," <u>IFAC Proceedings Volumes</u>, vol. 45, no. 16, pp. 274–279, 2012.

[166] A. Barai, K. Uddin, M. Dubarry, L. Somerville, A. McGordon, P. Jennings, and I. Bloom, "A comparison of methodologies for the non-invasive characterisation of commercial li-ion cells," <u>Progress in Energy and Combustion Science</u>, vol. 72, pp. 1–31, 2019.

[167] J. Lu, T. Wu, and K. Amine, "State-of-the-art characterization techniques for advanced lithium-ion batteries," <u>Nature Energy</u>, vol. 2, no. 3, pp. 1–13, 2017.

[168] C. Pastor-Fernández, T. F. Yu, W. D. Widanage, and J. Marco, "Critical review of non-invasive diagnosis techniques for quantification of degradation modes in lithium-ion batteries," <u>Renewable and Sustainable Energy Reviews</u>, vol. 109, pp. 138–159, 2019.

[169] J.-M. Tarascon and M. Armand, "Issues and challenges facing rechargeable lithium batteries," <u>Materials for sustainable energy: a collection of peer-reviewed research and review articles from Nature Publishing Group</u>, pp. 171–179, 2011.

[170] S. S. Zhang, "The effect of the charging protocol on the cycle life of a li-ion battery," <u>Journal of power sources</u>, vol. 161, no. 2, pp. 1385–1391, 2006.

[171] A. Barai, K. Uddin, W. Widanalage, A. McGordon, and P. Jennings, "The effect of average cycling current on total energy of lithium-ion batteries for electric vehicles," <u>Journal of Power Sources</u>, vol. 303, pp. 81–85, 2016.

[172] T. Ashwin, A. McGordon, W. D. Widanage, and P. A. Jennings, "Modified electrochemical parameter estimation of ncr18650bd battery using implicit finite volume method," <u>Journal of Power Sources</u>, vol. 341, pp. 387–395, 2017.

[173] J. C. Forman, S. J. Moura, J. L. Stein, and H. K. Fathy, "Genetic identification and fisher identifiability analysis of the doyle–fuller–newman model from experimental cycling of a lifepo4 cell," Journal of Power Sources, vol. 210, pp. 263–275, 2012.

[174] J. Moskon, J. Jamnik, and M. Gaberscek, "In depth discussion of selected phenomena associated with intrinsic battery hysteresis: Battery electrode versus rubber balloons," Solid State Ionics, vol. 238, pp. 24–29, 2013.

[175] W. Dreyer, C. Guhlke, and R. Huth, "The behavior of a many-particle electrode in a lithium-ion battery," Physica D: Nonlinear Phenomena, vol. 240, no. 12, pp. 1008–1019, 2011.

[176] V. Srinivasan and J. Newman, "Existence of path-dependence in the lifepo4 electrode," Electrochemical and solid-state letters, vol. 9, no. 3, p. A110, 2006.

[177] V. Srinivasan and J. Newman, "Discharge model for the lithium iron-phosphate electrode," Journal of the Electrochemical Society, vol. 151, no. 10, p. A1517, 2004.

[178] T. Huria, G. Ludovici, and G. Lutzemberger, "State of charge estimation of high power lithium iron phosphate cells," Journal of Power Sources, vol. 249, pp. 92–102, 2014.

[179] A. Barai, G. H. Chouchelamane, Y. Guo, A. McGordon, and P. Jennings, "A study on the impact of lithium-ion cell relaxation on electrochemical impedance spectroscopy," Journal of Power Sources, vol. 280, pp. 74–80, 2015.

[180] W. Weppner and R. A. Huggins, "Determination of the kinetic parameters of mixed-conducting electrodes and application to the system li3sb," Journal of The Electrochemical Society, vol. 124, no. 10, p. 1569, 1977.

[181] W. Weppner and R. A. Huggins, "Electrochemical methods for determining kinetic properties of solids," Annual Review of Materials Science, vol. 8, no. 1, pp. 269–311, 1978.

[182] A. Li, S. Pelissier, P. Venet, and P. Gyan, "Fast characterization method for modeling battery relaxation voltage," Batteries, vol. 2, no. 2, p. 7, 2016.

[183] F. M. Kindermann, A. Noel, S. V. Erhard, and A. Jossen, "Long-term equalization effects in li-ion batteries due to local state of charge inhomogeneities and their impact on impedance measurements," Electrochimica Acta, vol. 185, pp. 107–116, 2015.

[184] A. Nyman, T. G. Zavalis, R. Elger, M. Behm, and G. Lindbergh, "Analysis of the polarization in a li-ion battery cell by numerical simulations," Journal of The Electrochemical Society, vol. 157, no. 11, p. A1236, 2010.

[185] Z. Mao, M. Farkhondeh, M. Pritzker, M. Fowler, and Z. Chen, "Dynamics of a blended lithium-ion battery electrode during galvanostatic intermittent titration technique," Electrochimica Acta, vol. 222, pp. 1741–1750, 2016.

[186] C. Delacourt, M. Ati, and J. Tarascon, "Measurement of lithium diffusion coefficient in $li_y feso_4 f$," Journal of the Electrochemical Society, vol. 158, no. 6, p. A741, 2011.

[187] D. W. Dees, D. P. Abraham, W. Lu, K. G. Gallagher, M. Bettge, and A. N. Jansen, "Electrochemical modeling and performance of a lithium-and manganese-rich layered transition-metal oxide positive electrode," Journal of the Electrochemical Society, vol. 162, no. 4, p. A559, 2015.

[188] C. Bohnke, J.-L. Fourquet, N. Randrianantoandro, T. Brousse, and O. Crosnier, "Electrochemical insertion of lithium into the ramsdellite-type oxide $li_2 ti_3 o_7$: influence of the $li_2 ti_3 o_7$ particle size," Journal of Solid State Electrochemistry, vol. 6, no. 6, pp. 403–411, 2002.

[189] M. Petzl and M. A. Danzer, "Advancements in ocv measurement and analysis for lithium-ion batteries," IEEE Transactions on energy conversion, vol. 28, no. 3, pp. 675–681, 2013.

[190] C. Truchot, M. Dubarry, and B. Y. Liaw, "State-of-charge estimation and uncertainty for lithium-ion battery strings," Applied Energy, vol. 119, pp. 218–227, 2014.

[191] Y. Xing, W. He, M. Pecht, and K. L. Tsui, "State of charge estimation of lithium-ion batteries using the open-circuit voltage at various ambient temperatures," Applied Energy, vol. 113, pp. 106–115, 2014.

[192] M. Dubarry and B. Y. Liaw, "Development of a universal modeling tool for rechargeable lithium batteries," Journal of Power Sources, vol. 174, no. 2, pp. 856–860, 2007.

[193] G. B. Less, J. H. Seo, S. Han, A. M. Sastry, J. Zausch, A. Latz, S. Schmidt, C. Wieser, D. Kehrwald, and S. Fell, "Micro-scale modeling of li-ion batteries: parameterization and validation," Journal of The Electrochemical Society, vol. 159, no. 6, p. A697, 2012.

[194] P. Bai, D. A. Cogswell, and M. Z. Bazant, "Suppression of phase separation in lifepo4 nanoparticles during battery discharge," Nano letters, vol. 11, no. 11, pp. 4890–4896, 2011.

[195] A. Lasia, "Electrochemical impedance spectroscopy and its applications," in Modern aspects of electrochemistry, pp. 143–248, Springer, 2002.

[196] M. Urquidi-Macdonald, S. Real, and D. D. Macdonald, "Applications of kramers—kronig transforms in the analysis of electrochemical impedance data—iii. stability and linearity," Electrochimica Acta, vol. 35, no. 10, pp. 1559–1566, 1990.

[197] C. Pastor-Fernández, K. Uddin, G. H. Chouchelamane, W. D. Widanage, and J. Marco, "A comparison between electrochemical impedance spectroscopy and incremental capacity-differential voltage as li-ion diagnostic techniques to identify and quantify the effects of degradation modes within battery management systems," Journal of Power Sources, vol. 360, pp. 301–318, 2017.

[198] D. K. Kampouris, X. Ji, E. P. Randviir, and C. E. Banks, "A new approach for the improved interpretation of capacitance measurements for materials utilised in energy storage," Rsc Advances, vol. 5, no. 17, pp. 12782–12791, 2015.

[199] D. Andre, M. Meiler, K. Steiner, C. Wimmer, T. Soczka-Guth, and D. Sauer, "Characterization of high-power lithium-ion batteries by electrochemical impedance spectroscopy. i. experimental investigation," Journal of Power Sources, vol. 196, no. 12, pp. 5334–5341, 2011.

[200] W. Waag, S. Käbitz, and D. U. Sauer, "Experimental investigation of the lithium-ion battery impedance characteristic at various conditions and aging states and its influence on the application," Applied energy, vol. 102, pp. 885–897, 2013.

[201] S. Rodrigues, N. Munichandraiah, and A. Shukla, "Ac impedance and state-of-charge analysis of a sealed lithium-ion rechargeable battery," Journal of Solid State Electrochemistry, vol. 3, no. 7-8, pp. 397–405, 1999.

[202] V. Sauvant-Moynot, J. Bernard, R. Mingant, A. Delaille, F. Mattera, S. Mailley, J.-L. Hognon, and F. Huet, "Alidissi, a research program to evaluate electrochemical impedance spectroscopy as a soc and soh diagnosis tool for li-ion batteries," Oil & Gas Science and Technology–Revue de l'Institut Français du Pétrole, vol. 65, no. 1, pp. 79–89, 2010.

[203] L. Raijmakers, D. Danilov, J. Van Lammeren, M. Lammers, and P. Notten, "Sensorless battery temperature measurements based on electrochemical impedance spectroscopy," Journal of Power Sources, vol. 247, pp. 539–544, 2014.

[204] J. Zhu, Z. Sun, X. Wei, and H. Dai, "A new lithium-ion battery internal temperature on-line estimate method based on electrochemical impedance spectroscopy measurement," Journal of Power Sources, vol. 274, pp. 990–1004, 2015.

[205] I. N. Bronshtein and K. A. Semendyayev, Handbook of mathematics. Springer Science & Business Media, 2013.

[206] M. Kiel, O. Bohlen, and D. Sauer, "Harmonic analysis for identification of nonlinearities in impedance spectroscopy," Electrochimica Acta, vol. 53, no. 25, pp. 7367–7374, 2008.

[207] K. Darowicki, "Linearization in impedance measurements," Electrochimica acta, vol. 42, no. 12, pp. 1781–1788, 1997.

[208] F. Fasmin and R. Srinivasan, "Nonlinear electrochemical impedance spectroscopy," Journal of The Electrochemical Society, vol. 164, no. 7, p. H443, 2017.

[209] K. Darowicki, "Fundamental-harmonic impedance of first-order electrode reactions," Electrochimica acta, vol. 39, no. 18, pp. 2757–2762, 1994.

[210] K. Darowicki, "The amplitude analysis of impedance spectra," Electrochimica acta, vol. 40, no. 4, pp. 439–445, 1995.

[211] K. Darowicki, "Corrosion rate measurements by non-linear electrochemical impedance spectroscopy," Corrosion science, vol. 37, no. 6, pp. 913–925, 1995.

[212] K. Darowicki and J. Orlikowski, "Fast method for the determination of the charge transfer coefficient of an electrode reaction," Electrochimica acta, vol. 44, no. 2-3, pp. 433–436, 1998.

[213] J.-P. Diard, B. Le Gorrec, and C. Montella, "Deviation from the polarization resistance due to non-linearity i-theoretical formulation," Journal of electroanalytical chemistry, vol. 432, no. 1-2, pp. 27–39, 1997.

[214] J.-P. Diard, B. Le Gorrec, and C. Montella, "Deviation of the polarization resistance due to non-linearity ii-application to electrochemical reactions," Journal of electroanalytical chemistry, vol. 432, no. 1-2, pp. 41–52, 1997.

[215] J.-P. Diard, B. Le Gorrec, and C. Montella, "Deviation of the polarization resistance due to non-linearity. iii-polarization resistance determination from non-linear impedance measurements," Journal of electroanalytical chemistry, vol. 432, no. 1-2, pp. 53–62, 1997.

[216] G. E. Mog and E. P. Ribeiro, "Total harmonic distortion calculation by filtering for power quality monitoring," in 2004 IEEE/PES Transmision and Distribution Conference and Exposition: Latin America (IEEE Cat. No. 04EX956), pp. 629–632, IEEE, 2004.

[217] Q. Mao, U. Krewer, and R. Hanke-Rauschenbach, "Total harmonic distortion analysis for direct methanol fuel cell anode," Electrochemistry communications, vol. 12, no. 11, pp. 1517–1519, 2010.

[218] Q. Mao and U. Krewer, "Sensing methanol concentration in direct methanol fuel cell with total harmonic distortion: Theory and application," Electrochimica Acta, vol. 68, pp. 60–68, 2012.

[219] Q. Mao and U. Krewer, "Total harmonic distortion analysis of oxygen reduction reaction in proton exchange membrane fuel cells," Electrochimica Acta, vol. 103, pp. 188–198, 2013.

[220] M. D. Murbach and D. T. Schwartz, "Extending newman's pseudo-two-dimensional lithium-ion battery impedance simulation approach to include the nonlinear harmonic response," Journal of The Electrochemical Society, vol. 164, no. 11, p. E3311, 2017.

[221] M. D. Murbach, V. W. Hu, and D. T. Schwartz, "Nonlinear electrochemical impedance spectroscopy of lithium-ion batteries: experimental approach, analysis, and initial findings," Journal of the Electrochemical Society, vol. 165, no. 11, p. A2758, 2018.

[222] M. D. Murbach and D. T. Schwartz, "Analysis of li-ion battery electrochemical impedance spectroscopy data: An easy-to-implement approach for physics-based parameter estimation using an open-source tool," Journal of The Electrochemical Society, vol. 165, no. 2, p. A297, 2018.

[223] N. Harting, N. Wolff, F. Röder, and U. Krewer, "Nonlinear frequency response analysis (nfra) of lithium-ion batteries," Electrochimica Acta, vol. 248, pp. 133–139, 2017.

[224] N. Harting, N. Wolff, and U. Krewer, "Identification of lithium plating in lithium-ion batteries using nonlinear frequency response analysis (nfra)," Electrochimica Acta, vol. 281, pp. 378–385, 2018.

[225] N. Harting, R. Schenkendorf, N. Wolff, and U. Krewer, "State-of-health identification of lithium-ion batteries based on nonlinear frequency response analysis: First steps with machine learning," Applied Sciences, vol. 8, no. 5, p. 821, 2018.

[226] N. Harting, N. Wolff, F. Röder, and U. Krewer, "State-of-health diagnosis of lithium-ion batteries using nonlinear frequency response analysis," Journal of The Electrochemical Society, vol. 166, no. 2, p. A277, 2019.

[227] N. Wolff, N. Harting, M. Heinrich, and U. Krewer, "Nonlinear frequency response analysis on lithium-ion batteries: Process identification and differences between transient and steady-state behavior," Electrochimica Acta, vol. 298, pp. 788–798, 2019.

[228] N. Wolff, N. Harting, F. Röder, M. Heinrich, and U. Krewer, "Understanding nonlinearity in electrochemical systems," The European Physical Journal Special Topics, vol. 227, no. 18, pp. 2617–2640, 2019.

[229] J. Schoukens, R. Pintelon, and Y. Rolain, Mastering system identification in 100 exercises. John Wiley & Sons, 2012.

[230] E. Evans, D. Rees, and L. Jones, "Nonlinear disturbance errors in system identification using multisine test signals," IEEE Transactions on Instrumentation and Measurement, vol. 43, no. 2, pp. 238–244, 1994.

[231] W. D. Widanage, J. Stoev, and J. Schoukens, "Design and application of signals for nonlinear system identification," IFAC Proceedings Volumes, vol. 45, no. 16, pp. 1605–1610, 2012.

[232] J. Schoukens and T. Dobrowiecki, "Design of broadband excitation signals with a user imposed power spectrum and amplitude distribution," in IMTC/98 Conference Proceedings. IEEE Instrumentation and Measurement Technology Conference. Where Instrumentation is Going (Cat. No. 98CH36222), vol. 2, pp. 1002–1005, IEEE, 1998.

[233] R. Pintelon and J. Schoukens, System Identification: A Frequency Domain Approach. John Wiley and Sons, apr 2012.

[234] H. Zappen, F. Ringbeck, and D. U. Sauer, "Application of time-resolved multi-sine impedance spectroscopy for lithium-ion battery characterization," Batteries, vol. 4, no. 4, p. 64, 2018.

[235] R. Relan, Y. Firouz, J.-M. Timmermans, and J. Schoukens, "Data-driven non-linear identification of li-ion battery based on a frequency domain nonpara-metric analysis," IEEE Transactions on Control Systems Technology, vol. 25, no. 5, pp. 1825–1832, 2016.

[236] C. D. Rahn and C.-Y. Wang, Battery systems engineering. John Wiley & Sons, 2013.

[237] A. Saltelli, "Sensitivity Analysis for Importance Assessment," Risk Analysis, vol. 22, pp. 579–590, jun 2002.

[238] X. Lai, S. Wang, S. Ma, J. Xie, and Y. Zheng, "Parameter sensitivity analysis and simplification of equivalent circuit model for the state of charge of lithium-ion batteries," Electrochimica Acta, vol. 330, p. 135239, 2020.

[239] Z. Deng, X. Hu, X. Lin, Y. Kim, and J. Li, "Sensitivity analysis and joint estimation of parameters and states for all-solid-state batteries," IEEE Transactions on Transportation Electrification, vol. 7, no. 3, pp. 1314–1323, 2021.

[240] T. R. Grandjean, L. Li, M. X. Odio, and W. D. Widanage, "Global sensitivity analysis of the single particle lithium-ion battery model with electrolyte," in 2019 IEEE Vehicle Power and Propulsion Conference (VPPC), pp. 1–7, IEEE, 2019.

[241] V. Czitrom, "One-factor-at-a-time versus designed experiments," American Statistician, vol. 53, no. 2, pp. 126–131, 1999.

[242] Z. Khalik, M. Donkers, and H. J. Bergveld, "Model simplifications and their impact on computational complexity for an electrochemistry-based battery modeling toolbox," Journal of Power Sources, vol. 488, p. 229427, 2021.

[243] J. Li, N. Lotfi, R. G. Landers, and J. Park, "A single particle model for lithium-ion batteries with electrolyte and stress-enhanced diffusion physics," Journal of The Electrochemical Society, vol. 164, no. 4, p. A874, 2017.

[244] M. D. Morris, "Factorial sampling plans for preliminary computational experiments," Technometrics, vol. 33, no. 2, pp. 161–174, 1991.

[245] M. Balesdent, L. Brevaul, S. Lacaze, S. Missoum, and J. Morio, "Methods for high-dimensional and computationally intensive models," in Estimation of Rare Event Probabilities in Complex Aerospace and Other Systems: A Practical Approach, pp. 109–136, Elsevier Inc., 2016.

[246] M. K. Scharrer, B. Suhr, and D. Watzenig, "A new space mapping parameter surrogate optimization for lithium-ion cell models," in 4th Inverse Problems, Design and Optimization Symposium, pp. 26–28, 2013.

[247] M. Ye and M. Hill, "Global sensitivity analysis for uncertain parameters, models, and scenarios," in Sensitivity analysis in earth observation modelling, pp. 177–210, Elsevier, 2017.

[248] M. Andersson, M. Streb, J. Y. Ko, V. L. Klass, M. Klett, H. Ekström, M. Johansson, and G. Lindbergh, "Parametrization of physics-based battery models from input–output data: A review of methodology and current research," Journal of Power Sources, vol. 521, p. 230859, 2022.

[249] A. Saltelli and P. Annoni, "How to avoid a perfunctory sensitivity analysis," Environmental Modelling & Software, vol. 25, no. 12, pp. 1508–1517, 2010.

[250] B. Iooss and P. Lemaître, "A review on global sensitivity analysis methods," Operations Research/ Computer Science Interfaces Series, vol. 59, pp. 101–122, 2015.

[251] J. O. Bockris and Z. Nagy, "Symmetry factor and transfer coefficient: A source of confusion in electrode kinetics," Journal of Chemical Education, vol. 50, no. 12, pp. 839–843, 1973.

[252] B. Rowden and N. Garcia-Araez, "Estimating lithium-ion battery behavior from half-cell data," Energy Reports, vol. 7, pp. 97–103, 2021.

[253] A. Nickol, T. Schied, C. Heubner, M. Schneider, A. Michaelis, M. Bobeth, and G. Cuniberti, "Gitt analysis of lithium insertion cathodes for determining the lithium diffusion coefficient at low temperature: Challenges and pitfalls," Journal of the Electrochemical Society, 2020.

[254] S. S. Zhang, "Is li/graphite half-cell suitable for evaluating lithiation rate capability of graphite electrode?," Journal of the Electrochemical Society, 2020.

[255] E. McTurk, T. Amietszajew, J. Fleming, and R. Bhagat, "Thermo-electrochemical instrumentation of cylindrical li-ion cells," Journal of Power Sources, vol. 379, pp. 309–316, 2018.

[256] S. P. Rangarajan, Y. Barsukov, and P. P. Mukherjee, "In operando impedance based diagnostics of electrode kinetics in li-ion pouch cells," Journal of The Electrochemical Society, vol. 166, no. 10, p. A2131, 2019.

[257] D. Juarez-Robles, C.-F. Chen, Y. Barsukov, and P. P. Mukherjee, "Impedance evolution characteristics in lithium-ion batteries," Journal of The Electrochemical Society, vol. 164, no. 4, p. A837, 2017.

[258] M. Wünsch, R. Füßler, and D. U. Sauer, "Metrological examination of an impedance model for a porous electrode in cyclic aging using a 3-electrode lithium-ion cell with NMC111 — Graphite," Journal of Energy Storage, vol. 20, pp. 196–203, 2018.

[259] EL-CELL GmbH, "EL-CELL - electrochemical test equipment," 2021.

[260] A. U. Schmid, M. Kurka, and K. P. Birke, "Reproducibility of li-ion cell re-assembling processes and their influence on coin cell aging," Journal of Energy Storage, vol. 24, p. 100732, 2019.

[261] M. Rashid, A. McGordon, L. Somerville, and W. D. Widanage, "Effect of formation cycling schemes on li-ion cell capacity," in ECS Meeting Abstracts, no. 1, p. 123, IOP Publishing, 2018.

[262] Q. Gao, H. Dai, X. Wei, and B. Jiang, "Impedance modeling and aging research of the lithium-ion batteries using the EIS technique," SAE Technical Papers, vol. 2019-April, no. April, 2019.

[263] J. Costard, M. Ender, M. Weiss, and E. Ivers-Tiffée, "Three-electrode setups for lithium-ion batteries," Journal of The Electrochemical Society, vol. 164, no. 2, p. A80, 2016.

[264] X.-G. Yang, S. Ge, T. Liu, Y. Leng, and C.-Y. Wang, "A look into the voltage plateau signal for detection and quantification of lithium plating in lithium-ion cells," Journal of Power Sources, vol. 395, pp. 251–261, 2018.

[265] S. Wang, M. Verbrugge, J. S. Wang, and P. Liu, "Power prediction from a battery state estimator that incorporates diffusion resistance," Journal of Power Sources, vol. 214, pp. 399–406, 2012.

[266] H. Ekström, B. Fridholm, and G. Lindbergh, "Comparison of lumped diffusion models for voltage prediction of a lithium-ion battery cell during dynamic loads," Journal of Power Sources, vol. 402, pp. 296–300, 2018.

[267] R. Pintelon, J. Schoukens, G. Vandersteen, and K. Barbé, "Estimation of non-parametric noise and frf models for multivariable systems—part i: Theory," Mechanical Systems and Signal Processing, vol. 24, no. 3, pp. 573–595, 2010.

[268] I. Kollár, R. Pintelon, and J. Schoukens, "Frequency domain system identification toolbox for matlab," IFAC Proceedings Volumes, vol. 24, no. 3, pp. 1243–1247, 1991.

[269] A. Jossen, "Fundamentals of battery dynamics," Journal of power sources, vol. 154, no. 2, pp. 530–538, 2006.

[270] B. Pattipati, B. Balasingam, G. Avvari, K. Pattipati, and Y. Bar-Shalom, "Open circuit voltage characterization of lithium-ion batteries," Journal of Power Sources, vol. 269, pp. 317–333, 2014.

[271] G. I. El-Baghdady and M. El-Azab, "Chebyshev-gauss-lobatto pseudo-spectral method for one-dimensional advection-diffusion equation with variable coefficients," Math, vol. 3, no. 1, pp. 1–8, 2016.

[272] D. Di Domenico, A. Stefanopoulou, and G. Fiengo, "Lithium-ion battery state of charge and critical surface charge estimation using an electrochemical model-based extended kalman filter," Journal of dynamic systems, measurement, and control, vol. 132, no. 6, 2010.

[273] S. Gottlieb and D. Gottlieb, "Spectral methods," Scholarpedia, vol. 4, no. 9, p. 7504, 2009. revision #91796.

[274] H. Binous, A. A. Shaikh, and A. Bellagi, "Chebyshev orthogonal collocation technique to solve transport phenomena problems with matlab® and mathematica," Computer Applications in Engineering Education, vol. 23, no. 3, pp. 422–431, 2015.

[275] S. Kirkpatrick, C. D. Gelatt, and M. P. Vecchi, "Optimization by simulated annealing," science, vol. 220, no. 4598, pp. 671–680, 1983.

[276] F. Busetti, "Simulated annealing overview," World Wide Web URL www. geocities. com/francorbusetti/saweb. pdf, vol. 5, 2003.

[277] C. Liu, Y. Gao, and L. Liu, "Toward safe and rapid battery charging: Design optimal fast charging strategies thorough a physics-based model considering lithium plating," International Journal of Energy Research, vol. 45, no. 2, pp. 2303–2320, 2021.

[278] C. Zhang, T. Amietszajew, S. Li, M. Marinescu, G. Offer, C. Wang, Y. Guo, and R. Bhagat, "Real-time estimation of negative electrode potential and state of charge of lithium-ion battery based on a half-cell-level equivalent circuit model," Journal of Energy Storage, vol. 51, p. 104362, 2022.

[279] T. Barlow, S. Latham, I. Mccrae, and P. Boulter, "A reference book of driving cycles for use in the measurement of road vehicle emissions," tech. rep., Department for Transport, 2009.

[280] E. Hosseinzadeh, J. Marco, and P. Jennings, "Combined electrical and electrochemical-thermal model of parallel connected large format pouch cells," Journal of Energy Storage, vol. 22, pp. 194–207, 2019.

[281] B. Wu, V. Yufit, M. Marinescu, G. J. Offer, R. F. Martinez-Botas, and N. P. Brandon, "Coupled thermal–electrochemical modelling of uneven heat generation in lithium-ion battery packs," Journal of Power Sources, vol. 243, pp. 544–554, 2013.

[282] V. Ovejas and A. Cuadras, "State of charge dependency of the overvoltage generated in commercial li-ion cells," Journal of Power Sources, vol. 418, pp. 176–185, 2019.

[283] B. Suthar, P. W. Northrop, R. D. Braatz, and V. R. Subramanian, "Optimal charging profiles with minimal intercalation-induced stresses for lithium-ion batteries using reformulated pseudo 2-dimensional models," Journal of The Electrochemical Society, vol. 161, no. 11, p. F3144, 2014.

[284] D. Maclay, "Simulation gets into the loop," IEE Review, vol. 43, no. 3, pp. 109–112, 1997.

[285] T. Ersal, M. Brudnak, A. Salvi, J. L. Stein, Z. Filipi, and H. K. Fathy, "Development of an internet-distributed hardware-in-the-loop simulation platform for an automotive application," in Dynamic Systems and Control Conference, vol. 48937, pp. 73–80, 2009.

[286] T. Ersal, M. Brudnak, A. Salvi, J. L. Stein, Z. Filipi, and H. K. Fathy, "Development and model-based transparency analysis of an internet-distributed

hardware-in-the-loop simulation platform," <u>Mechatronics</u>, vol. 21, no. 1, pp. 22–29, 2011.

[287] V. Schreiber, V. Ivanov, K. Augsburg, M. Noack, B. Shyrokau, C. Sandu, and P. S. Els, "Shared and distributed x-in-the-loop tests for automotive systems: Feasibility study," <u>IEEE Access</u>, pp. 1–1, 2018.

[288] Y. Zhang, S. Lu, Y. Yang, and Q. Guo, "Internet-distributed vehicle-in-the-loop simulation for hevs," <u>IEEE transactions on Vehicular Technology</u>, vol. 67, no. 5, pp. 3729–3739, 2018.

[289] G. Fan, K. Pan, and M. Canova, "A comparison of model order reduction techniques for electrochemical characterization of lithium-ion batteries," in <u>2015 54th IEEE Conference on Decision and Control (CDC)</u>, pp. 3922–3931, IEEE, 2015.

[290] P. A. Ioannou and J. Sun, <u>Robust adaptive control</u>. Courier Corporation, 2012.

[291] R. Klein, N. A. Chaturvedi, J. Christensen, J. Ahmed, R. Findeisen, and A. Kojic, "Electrochemical model based observer design for a lithium-ion battery," <u>IEEE Transactions on Control Systems Technology</u>, vol. 21, no. 2, pp. 289–301, 2012.

[292] C. Zhang, Y. Zhao, L. Zhu, Y. Liu, E. Farantatos, M. Patel, H. Hooshyar, C. Pisani, R. Zaottini, and G. Giannuzzi, "Implementation and hardware-in-the-loop testing of a wide-area damping controller based on measurement-driven models," in <u>2021 IEEE Power & Energy Society General Meeting (PESGM)</u>, pp. 1–5, IEEE, 2021.

[293] A. R. Plummer, "Model-in-the-loop testing," <u>Proceedings of the Institution of Mechanical Engineers, Part I: Journal of Systems and Control Engineering</u>, vol. 220, no. 3, pp. 183–199, 2006.

[294] J. Nibert, M. E. Herniter, and Z. Chambers, "Model-based system design for mil, sil, and hil," <u>World Electric Vehicle Journal</u>, vol. 5, no. 4, pp. 1121–1130, 2012.

[295] P. Shen, M. Ouyang, X. Han, X. Feng, L. Lu, and J. Li, "Error analysis of the model-based state-of-charge observer for lithium-ion batteries," <u>IEEE Transactions on Vehicular Technology</u>, vol. 67, no. 9, pp. 8055–8064, 2018.

[296] K. Lee and E. N. Johnson, "State and parameter estimation using measurements with unknown time delay," in <u>2017 IEEE Conference on Control Technology and Applications (CCTA)</u>, pp. 1402–1407, IEEE, 2017.